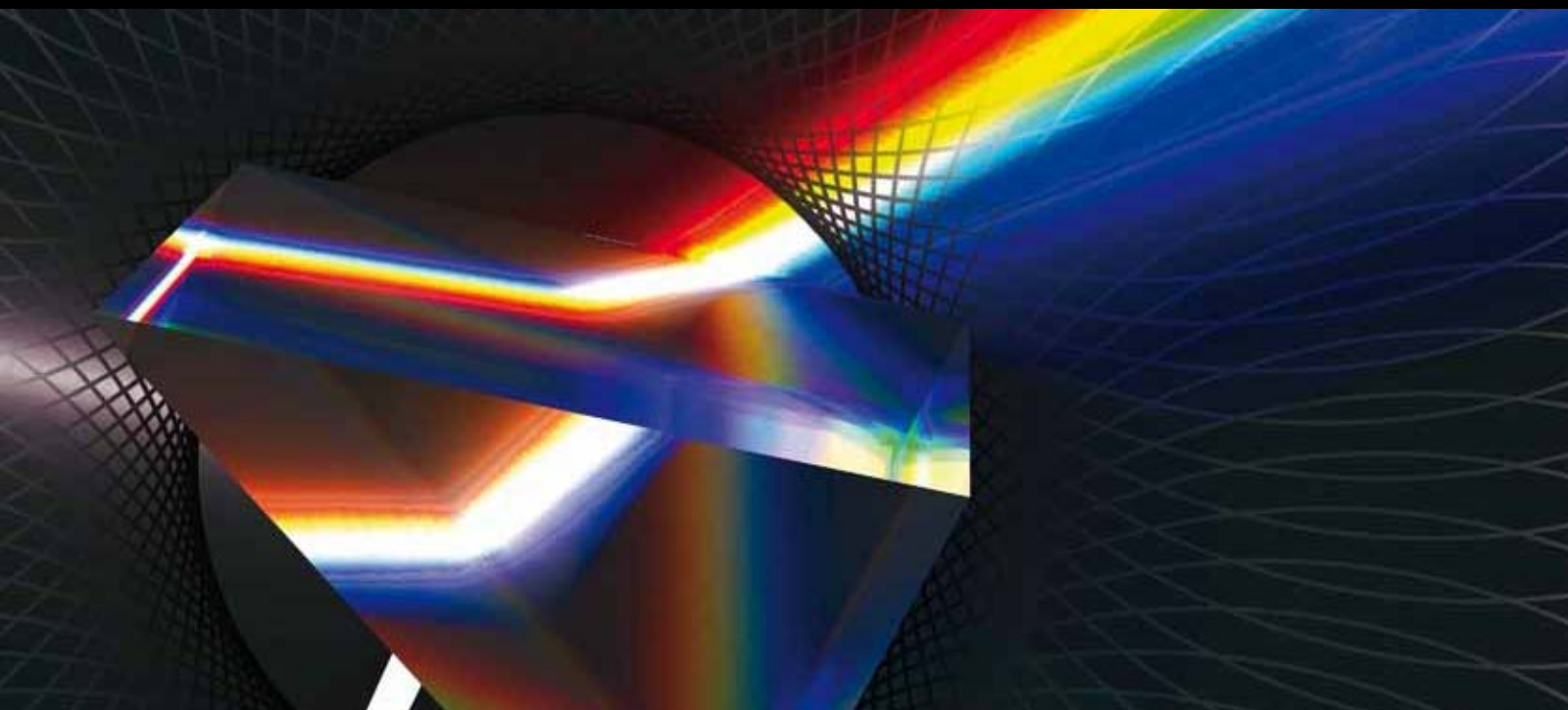


Optical ANTENNAS

GUEST EDITORS: NICOLAS BONOD, ALEXANDRE BOUHELIER,
A. FEMIUS KOENDERINK, AND ALI PASSIAN





Optical Antennas

International Journal of Optics

Optical Antennas

Guest Editors: Nicolas Bonod, Alexandre Bouhelier,
A. Femius Koenderink, and Ali Passian



Copyright © 2012 Hindawi Publishing Corporation. All rights reserved.

This is a special issue published in “International Journal of Optics.” All articles are open access articles distributed under the Creative Commons Attribution License, which permits unrestricted use, distribution, and reproduction in any medium, provided the original work is properly cited.

Editorial Board

Alejandro Aceves, USA
Fortunato Tito Arcchi, Italy
Victor Arrizon, Mexico
Gaetano Assanto, Italy
Jose Azana, Canada
Ole Bang, Denmark
Randy A. Bartels, USA
Augusto Belendez, Spain
E. Bernabeu, Spain
Le Nguyen Binh, Germany
Keith J. Blow, UK
A. D. Boardman, UK
Wojtek J. Bock, Canada
Neil Broderick, UK
Hrvoje Buljan, Croatia
A. Cartaxo, Portugal
Giulio Cerullo, Italy
K. S. Chiang, Hong Kong
W. C. H. Choy, Hong Kong
David Coutts, Australia
Ilaria Cristiani, Italy
Michael J. Damzen, UK
Vittorio Degiorgio, Italy
Cornelia Denz, Germany
Ivan Djordjevic, USA
Niloy K. Dutta, USA
Robert G. Elliman, Australia

Charles M. Falco, USA
Mahmoud Fallahi, USA
Pietro Ferraro, Italy
Mário F. Ferreira, Portugal
Rashid A. Ganeev, Uzbekistan
Hooshang Ghafouri-Shiraz, UK
Ivan Glesk, UK
Qihuang Gong, China
N. A. Halliwell, UK
Sang-Kook Han, Republic of Korea
Sulaiman Wadi Harun, Malaysia
W. F. Hsieh, Taiwan
Mark Humphrey, Australia
Nicusor Iftimia, USA
Mohammed N. Islam, USA
Chennupati Jagadish, Australia
Wonho Jhe, Korea
Mirosław A. Karpierz, Poland
Yu S. Kivshar, Australia
Wieslaw Krolikowski, Australia
Nayot Kurukitkoson, Thailand
R. Leitgeb, Switzerland
Gong Ru Lin, Taiwan
Michael E. Marhic, UK
Lorenzo Marrucci, Italy
John McInerney, Ireland
Andrea Melloni, Italy

Adam Miranowicz, Poland
Roberto Morandotti, Canada
Uwe Morgner, Germany
Dragomir Neshev, Australia
Jean-Michel Nunzi, Canada
Takashige Omatsu, Japan
Wolfgang Osten, Germany
Ben Ovryn, USA
Nicolae C. Panoiu, UK
Vittorio M. N. Passaro, Italy
Gang-Ding Peng, Australia
Reji Philip, India
Armando Nolasco Pinto, Portugal
Adrian Podoleanu, UK
Jianan Qu, Hong Kong
Chenggen Quan, Singapore
Marek Samoc, Poland
John T. Sheridan, Ireland
Ping Shum, Singapore
Mohammad Taghizadeh, UK
R. P. Tatam, UK
Markus E. Testorf, USA
Mustapha Tlidi, Belgium
Stefano Trillo, Italy
Stefan Wabnitz, Italy
Boris Y. Zeldovich, USA

Contents

Optical Antennas, Nicolas Bonod, Alexandre Bouhelier, A. Femius Koenderink, and Ali Passian
Volume 2012, Article ID 365109, 4 pages

Novel Directional Nanoantennas for Single-Emitter Sources and Wireless Nano-Links, Maciej Klemm
Volume 2012, Article ID 348306, 7 pages

Surface Plasmon States in Inhomogeneous Media at Critical and Subcritical Metal Concentrations, Katyayani Seal and Dentcho A. Genov
Volume 2012, Article ID 519509, 9 pages

Gap Nanoantennas toward Molecular Plasmonic Devices, Aude L. Lereu, Jacob P. Hoogenboom, and Niek F. van Hulst
Volume 2012, Article ID 502930, 19 pages

Antenna Design for Directivity-Enhanced Raman Spectroscopy, Aftab Ahmed, Yuanjie Pang, Ghazal Hajisalem, and Reuven Gordon
Volume 2012, Article ID 729138, 8 pages

Absorption by an Optical Dipole Antenna in a Structured Environment, E. Castanié, R. Vincent, R. Pierrat, and R. Carminati
Volume 2012, Article ID 452047, 8 pages

Digital Heterodyne Holography Reveals the Non-Quasi-Static Scattering Behaviour of Transversally Coupled Nanodisk Pairs, Sarah Y. Suck, Sébastien Bidault, Nicolas Bonod, Stéphane Collin, Nathalie Bardou, Yannick De Wilde, and Gilles Tessier
Volume 2012, Article ID 532576, 8 pages

Gold Nanoparticles as Probes for Nano-Raman Spectroscopy: Preliminary Experimental Results and Modeling, V. Le Nader, J.-Y. Mevellec, T. Minea, and G. Louarn
Volume 2012, Article ID 591083, 8 pages

Mie Plasmons: Modes Volumes, Quality Factors, and Coupling Strengths (Purcell Factor) to a Dipolar Emitter, G. Colas des Francs, S. Derom, R. Vincent, A. Bouhelier, and A. Dereux
Volume 2012, Article ID 175162, 8 pages

Nanocrosses with Highly Tunable Double Resonances for Near-Infrared Surface-Enhanced Raman Scattering, Ye Jian and VanDorpe Pol
Volume 2012, Article ID 745982, 5 pages

Optimization of s-Polarization Sensitivity in Apertureless Near-Field Optical Microscopy, Yuika Saito, Yoshiro Ohashi, and Prabhat Verma
Volume 2012, Article ID 962317, 6 pages

Water-Based Assembly and Purification of Plasmon-Coupled Gold Nanoparticle Dimers and Trimers, Sébastien Bidault and Albert Polman
Volume 2012, Article ID 387274, 5 pages



Plasmonic-Resonant Bowtie Antenna for Carbon Nanotube Photodetectors, Hongzhi Chen, Ning Xi, King Wai Chiu Lai, Liangliang Chen, Carmen Kar Man Fung, and Jianyong Lou
Volume 2012, Article ID 318104, 9 pages

Ultrafast Plasmonic Nanoantenna-ITO Hybrid Switches, Martina Abb and Otto L. Muskens
Volume 2012, Article ID 132542, 5 pages

Fluorescence Enhancement Factors on Optical Antennas: Enlarging the Experimental Values without Changing the Antenna Design, Jérôme Wenger
Volume 2012, Article ID 828121, 7 pages

Editorial

Optical Antennas

Nicolas Bonod,¹ Alexandre Bouhelier,² A. Femius Koenderink,³ and Ali Passian⁴

¹*Institut Fresnel, Domaine Universitaire de Saint-Jérôme, CNRS, Aix-Marseille Université, Ecole Centrale Marseille, 13397 Marseille, France*

²*Laboratoire Interdisciplinaire Carnot de Bourgogne UMR 6303, CNRS, Université de Bourgogne, 9, Avenue Alain Savary, 21078 Dijon, France*

³*Center for Nanophotonics, FOM Institute AMOLF, Science Park 104, 1098 XG Amsterdam, The Netherlands*

⁴*Oak Ridge National Laboratory, 1 Bethel Valley Rd. Oak Ridge, TN 37831-6075, USA*

Correspondence should be addressed to Nicolas Bonod, nicolas.bonod@fresnel.fr

Received 13 February 2012; Accepted 13 February 2012

Copyright © 2012 Nicolas Bonod et al. This is an open access article distributed under the Creative Commons Attribution License, which permits unrestricted use, distribution, and reproduction in any medium, provided the original work is properly cited.

1. Introduction

This special issue features contributing and invited papers from leading groups in the field of optical antennas. Fourteen papers address some of the most challenging aspects of these photonic components aimed to increase at a nanometer scale and at room temperature the light/matter interaction.

Optical antennas feature the property to strongly enhance light matter interaction at a nanometer scale, at room temperature, and over spectrally broad bandwidths. Interaction between localized light emitters and optical antennas has been deeply investigated in order to (i) enhance the radiative time constants and radiative efficiency of emitters and also (ii) to redirect the electromagnetic radiation. Reciprocally, when illuminated from the far field, optical antennas can focus light into tiny spots which permits to probe the local environment with a high resolution. Consequently, optical antennas have been embraced by many researchers for improved spectroscopy techniques but also to enhance photovoltaic devices, or to realize single-photon nonlinearities in quantum optics.

All these progresses have been permitted on the one hand by an emerging dialogue between physicists and electrical engineers that provides a new understanding of nanooptics, and on the other hand by the recent advances of top-down (FIB, e-beam lithography) and bottom-up nanofabrication technologies. In this context, it is expected that chemical functionalization and self-assembled nanoantennas will play a key role in the near future to realize new nano-antenna designs.

This special issue addresses some of the most exciting challenges of this research field. It contains 14 papers

combining experimental and theoretical works from leading groups in the field. These contributions are tentatively classified in four sections surveying the different aspects of the topic: (i) antenna efficiencies, (ii) antenna devices, (iii) coupled antennas and (iv) antenna enhanced spectroscopy.

2. Coupled Antennas

Realizing the full power of plasmonic antennas for any linear or nonlinear application in spectroscopy, light generation or detection naturally requires that we understand coupled plasmonic systems. Firstly, only upon combining single plasmonic scatterers in coupled oligomers do we obtain full control over near-field enhancements, polarization response and far-field directivity in scattering and emission. Secondly, controlling and understanding the coupling of plasmonics to molecular light sources or nanoscale detectors is of the essence to realize the promised enhanced functionalities. The valuable contributions in this section focus on strategies to fabricate coupled systems controllably on the smallest scale and on how to quantify the coupling in optical measurements.

A. Lereu et al. present a study of plasmonic dimer antennas in which high field enhancements are obtained as a consequence of the high field in a narrow gap of a dimer coupled mode. Their study focuses on how to fully quantify the field enhancement in nano-antennas, firstly by linear and nonlinear spectroscopy of the luminescence that especially Au metal antennas generate intrinsically. Secondly they show how a very dilute random sprinkling of single fluorescent molecules on such antennas can be used

as ultimate vectorial nonperturbative probes. By collecting statistics on emission polarization, spectra, and lifetime, one can obtain statistical information on antenna performance beyond the diffraction limit and ensemble averaging intrinsic to traditional studies with dense fluorescent films. Finally they show how nanolithography could be used to truly localize single fluorophores.

Some of the most exciting proposals to reach ultimately high field enhancements rely on the fabrication of dimers, trimers and self-similar chains of metal particles of different size and with ultrasmall gaps. At the typical desired dimensions where gaps are just nanometers in size and particles below 40 nm are desired, only bottom-up fabrication strategies can be employed. S. Bidault et al. describe the realization of exactly such a strategy, in which gold particles are assembled in dimers and trimers using a simple one-step water-based scheme. Via appropriate selection of a short dithiol linker molecule, the spacing between particles is reduced to the nanometer scale. The controlled fabrication of dimers and trimers with spacings of just 1.0 to 1.5 nm shows large promise for SERS applications.

S. Suck et al. present experiments and simulations that explore the distance regime in which plasmonic coupling reaches outside the familiar quasistatic limit. For very small coupled antennas well below $\lambda/2\pi$ in size, the characteristic near-field $1/r^3$ coupling is often assumed, without any phase retardation over the object. However, in actual structures this quasistatic assumption usually does not hold. Firstly, phase retardation modifies the coupled eigenmodes, and secondly, quasistatics intrinsically ignores all interaction with the far field. Thus retardation determines scattering. However, exactly where and how the cross-over from quasistatic to retarded behaviour occurs is a matter of debate. S. Suck et al. present measurements of the radiation strength and directionality for the hybridized modes of plasmon disk dimers. Importantly, retardation in their structure with a coupling distance below $\lambda/4$ is directly evident from the fact that the supposedly dark mode is in practice as bright as the nominally bright mode.

Application of plasmonic antennas to detection brings the challenge of coupling optical field enhancements with electrically connected detection elements. H. Chen et al. describe the integration of plasmonic bow tie antennas for large field enhancements with electrically connected carbon nanotubes that act as the actual photodetectors. As the nanotube diameter is comparable to the antenna gap width, these structures form a perfect match. Importantly, H. Chen et al. report an order-of-magnitude photocurrent enhancement as compared to bare carbon nanotube photodetectors at wavelengths in the near infrared. Their structure could thus be a promising candidate for future nanoscale detectors.

3. Antenna Efficiencies

Metallic optical antennas resonantly interact with incident light through the excitation of localized surface plasmon polaritons. This electromagnetic resonance offers moderate quality factors due to the intrinsic metallic losses but permits

to confine light into very small volumes. The absorption losses of a single spherical metallic particle can be analytically derived but E. Castanié et al. highlight in their paper the fundamental role played by the environment. They use a rigorous scattering theory based on the Green dyadic function formalism to show that the absorption of light by lossy metallic particles is not an intrinsic property of the metallic particle but depends on its surrounding environment. More precisely, they demonstrate that an increase of the local density of photonic states around the particle permits to decrease the absorption losses. When a particle is excited by incident light, the electron gas oscillates and its relaxation can take place either through the scattering of light (radiative decay rates) or through electron-phonon collisions (non-radiative channels). An increase of the local density of photonic states permits to privilege the relaxation through radiative channels. They illustrate this result by considering a single metallic particle coupled with a perfect mirror. They plot on the same graph the local density of states and the absorption losses of the particle when varying the particle/mirror distance and nicely reveal the link between those parameters.

The efficiency of optical antennas is also questioned by J. Wenger when dealing with fluorescent molecules. The author shows that the fluorescent enhancement factors offered by an optical antenna is not a trivial issue and depends on several parameters such as the antenna geometry and the spectral overlap of its resonance with the emission spectrum of the molecule. Emphasis is placed in this paper on collection efficiency and also emitter's quantum yield. J. Wenger shows how the fluorescence enhancement can be highly modulated by tuning the setup of the experiment but without modifying the design of the plasmonic antenna. He finally gives the ingredients that will offer high fluorescence enhancements but also draws our attention to the fact that high fluorescence enhancement is not synonymous of bright photon sources.

It is now well known that spontaneous emission is not an intrinsic property of quantum emitters and strongly depends on the surrounding environment. G. Colas des Francs et al. derive the Purcell factor of quantum emitters coupled with a single metallic particle. In a first part, they clearly formulate, in the case of an electric dipolar assumption, the quality factor of the plasmon resonance, before deriving the spontaneous emission decay rates when the electric dipolar transition moment is normal to the surface of the particle. Identification with the Purcell factor gives the effective volume of the metallic particle dipolar mode. In a second part, this work is extended and generalized to the case of multipolar modes, and explicit formulations of the quality factors and effective volumes are given as a function of the multipolar order n . The last part of the paper addresses the coupling strength between a quantum emitter and a given mode n compared with all the other deexcitation channels.

4. Antenna Devices

Optical antennas are often considered as essential units of the photonics toolbox for controlling light-matter interaction.

Major research efforts are focused on the development of functionalities at the nanoscale in order to realize optical devices or advanced investigation tools. In their paper, M. Abb et al. report on an all-optical mechanism enabling control over the spectral response of an optical gap antenna. Their approach consists in loading the optical antenna with a nonlinear material. The authors experimentally showed that Indium Tin Oxide (ITO), a common material traditionally used as a thin conductive layer in electron-beam lithography, features a Kerr nonlinearity governed by the free carrier concentration. Optically depleting the material in a pump-probe configuration induces a local change of the refractive index which consequently shifts the antenna resonance. Potential exploitation of this ultrafast antenna switch is discussed.

Another important functionality is approached by M. Klemm. Very much like their radiofrequency counterparts, optical antennas are increasingly used to control the emission diagram of nanoscale light sources. In this contribution, the author describes a novel antenna design with a computed directivity better than state-of-the-art optical Yagi-Uda structures. The concept, based on the travelling wave notion, could enable efficient intrachip wireless optical transmission providing that the emitting and receiving antennas are embedded in the same optical medium.

The role of an optical antenna is essential to interface near-field information to a detectable far-field signal. Scanning near-field optical microscopy is largely taking advantage of antenna characteristics to increase lateral resolution, enhance weak signals, and map optical fields. Because of geometrical considerations, metal tip antennas are usually sensitive to field polarization aligned with the main axis of the tip, limiting thus the detectable information. In their article, Y. Saito et al. demonstrate that, with proper polarization conditions and controlled tip shape, efficient scattering of in-plane optical fields can occur. They demonstrate their approach by mapping the focal point of azimuthal polarized laser beam using different tips and quantified their in-plane efficiencies.

5. Antenna-Enhanced Spectroscopy

Surface modes, in particular those sustained by noble metals, as a result of the excitation of polaritons and plasmons in their surface regions, have played a fundamental role in the so-called surface-enhanced spectroscopies. A myriad of materials and morphologies have emerged in an effort to understand the role of surface excitations and to further exploit the observed enhancement in the applications of molecule-metal substrate systems. The nanoscale curvature and roughness associated with these morphologies yield electromagnetic scattering properties that can elegantly be embraced by the concept of optical nanoantennas. As a receiver, the large number of available modes at the optical frequencies possessed by these antennas facilitates flexible collective electronic excitation. As an emitter, the near- and far-field patterns of the antennas offer a superb platform for nanooptics investigations. Here in an effort to elucidate

the enhancement effect of nanoantennas in spectroscopic studies, the authors have treated a series of morphologies with emphasis on their plasmonic properties. Particularly, dipole antennas (A. Ahmed et al.), semicontinuous films (K. Seal et al.), nanocrosses (J. Ye et al.), and nanospheres (V. Le Nader et al.) all support plasmon excitation and as such have been implicated in a form of enhancement process. Typically, either the molecules of interest are brought into the vicinity or contact with the nanostructure making up the antenna, or the antenna is brought near the molecules as in the so-called tip enhancement effect. Consequently, the responses of both nanoantennas and molecules couple to create new scattering properties.

Directing the radiation to the molecules optimally can greatly enhance the signal regardless of what may be provided by surface enhancement due to plasmonic processes. By designing a set of auxiliary structures to serve as reflectors, A. Ahmed et al. fabricated nanoantennas with improved directivity that was quantified employing Raman spectroscopy. Apart from directivity, a desired capability is the flexibility of the spectral placement of the plasmonic resonances of the antenna toward targeting specific vibrational transitions during surface enhanced spectroscopies. To this end J. Ye et al. propose a four-piece gold nanostructure in form of a cross where two of the arms are allowed to vary in length to provide spectral tunability. In doing so, they numerically predict useful levels of enhancement delivered at two resonance positions, a relevant feature in the context of Raman spectroscopy. The utility of nanoantennas in spectroscopy can also be appreciated in structures with less stringent a priori design parameters. The first example herein capitalizes on the controlled deposition of metals below a threshold (typically below 10 nm), which results in the formation of islands. By capturing the near-field of a series of discontinuous silver films with varying surface coverage but random distribution, K. Seal et al. discuss localized as well as delocalized plasmon excitation in describing the measured field distribution, which is of importance in spectroscopic measurements of adsorbates residing on such substrates. In a second example, V. Le Nader et al. describe a chemical immobilization technique for attaching gold nanoparticles from a colloidal solution at the apex of a tapered optical fiber. The sharp optical probe fabricated is subsequently shown to randomly host a number of gold nanoparticles. Owing to their plasmonic properties the particles can resonantly deliver localized energy to a Raman active sample of carbon nanotubes. This tip-enhanced spectroscopy then permits the study of the various Raman bands as a function of the nanoantenna-nanotube distance.

Acknowledgments

The guest editors thank all the authors for their valuable contribution to this special issue. The high quality papers united in this special issue address some of the most important issues in optical antenna theory and design. All the papers are open access which we anticipate will stimulate

the rapid dissemination and wide application of these state-of-the-art findings.

Nicolas Bonod
Alexandre Bouhelier
A. Femius Koenderink
Ali Passian

Research Article

Novel Directional Nanoantennas for Single-Emitter Sources and Wireless Nano-Links

Maciej Klemm

Department of Electrical and Electronic Engineering, University of Bristol, Woodland Road, Bristol BS1 8UB, UK

Correspondence should be addressed to Maciej Klemm, m.klemm@bristol.ac.uk

Received 30 September 2011; Revised 19 December 2011; Accepted 20 December 2011

Academic Editor: Nicolas Bonod

Copyright © 2012 Maciej Klemm. This is an open access article distributed under the Creative Commons Attribution License, which permits unrestricted use, distribution, and reproduction in any medium, provided the original work is properly cited.

Optical nanoantennas are emerging as one of the key components in the future nanophotonic and plasmonic circuits. The first optical nanoantennas were in a form of simple spherical nanoparticles. Recently more complex Yagi-Uda nanoantenna structures were demonstrated. These nanoantennas enhance radiation of single emitters and provide well-defined directional radiation. In this contribution, we present the novel design of the directional nanoantenna, which is excited from the propagating mode of the plasmonic waveguide. The nanoantenna design is based on the *travelling wave* principle, well known at RF/microwave frequencies. By properly designing the propagating parts of the nanoantenna, a very efficient coupling to free space wave impedance can be achieved. Furthermore, the control over the radiation direction and beam width is relatively easy with this nanoantenna. Compared to the previously published Yagi-Uda designs, the new nanoantenna presented in this work has directivity three times higher.

1. Introduction

In the future we foresee the development of optical wireless communication networks at the nanoscale [1]. In this work we will focus on one specific problem in the development of the physical layer of such wireless networks—design of novel nanoantennas (often also referred to as *optical antennas*, or *plasmonic antennas* in the open literature). Nanoantennas are key components and enabling technology for the future wireless connectivity at the nanoscale, coupling light from external world to nanoscale circuits and vice versa.

Nanoantennas have their origins in the field of physics and more precisely in near-field microscopy. Wessel in 1985 was the first to mention explicitly the analogy of local microscopic light sources to classical antennas [2]—a concept that has since been thoroughly explored. History of nanoantennas can be found in [3].

As one of the main applications for novel nanoantennas we envisage (a) on-chip and intrachip wireless nano-links in future micro- and nanodevices and (b) single-emitter sources coupled to the directional nanoantenna.

The coupling of the nanoantenna to single-emitter light sources has been investigated by several groups theoretically

[4–7] as well as experimentally [8, 9]. Nanoantenna in this application is used mainly to direct and focus light. Due to the lack of true nanoscale light sources, the coupling of the emitter (e.g., quantum dot) to the nanoantenna has been achieved by proximity coupling (near-field coupling) which is rather inefficient. Ideally, one would like to connect the source and the nanoantennas by efficient transmission line (waveguide), similarly as at RF and microwave frequencies. When designing nanoantenna, it is important to consider not only the radiating part but also the feeding arrangement.

Nanoantenna-enabled wireless nano-links could be considered as an alternative solution to the problem of an *interconnect bottleneck* in the next generation-integrated circuits (ICs). Currently *silicon photonics* is being actively researched in academia and by many electronic manufacturers, who see it as a means for keeping up with Moore's law by using optical interconnects to provide faster data transfers between and within microchips. However, size of dielectric waveguides used in silicon photonics is fundamentally limited by diffraction optics, posing a limit on the maximum achievable density of such interconnect technology. To tackle this problem, *plasmonic integrated circuits* have been most recently proposed [10] to achieve true nanoscale integration

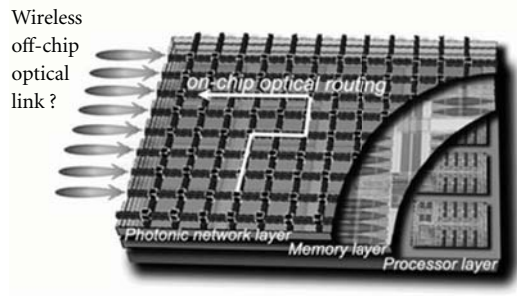


FIGURE 1: A concept of using directional nanoantennas as means of providing wireless on-chip and intrachip communication. Photo is modified from IBM.

in future ICs. Unfortunately, the price to pay for extremely high density of plasmonic interconnects is relatively high loss in such waveguides (compared to silicon photonics). We would like to propose another approach to the optical interconnect problem—*wireless connectivity using nanoantennas*. We can imagine a very high data rate chip-to-chip and intrachip links supported mainly by nanoantennas with very few interconnects needed. Moreover, besides providing a “simple” on-/intrachip connections, nanoantennas could offer an advantage of having an extra wireless functionality in future integrated circuits.

2. Differences between RF/Microwave Antennas and Plasmonic Nanoantennas

Theory of RF/microwave antennas was being developed for well over 100 years. Several design rules for antenna engineers exist, and probably tens of textbooks are at their disposal. However, if one wishes to design a nanoantenna, not even a single book on a subject is available. Unfortunately, due to different underlying physics at optical wavelengths, based on *plasmon resonance* (specific electromagnetic solution of Maxwell’s equations at the metal-dielectric interface at optical wavelengths [11]), most design rules for RF/microwave antennas cannot be simply used in nanoantennas. Even for the simplest possible antenna, a dipole, there is a significant difference in radiation patterns of the plasmonic nanoantenna and the RF antenna [12], as shown in Figure 2.

3. Nanoantenna Design

The design of the new directional nanoantenna was performed using commercial electromagnetic finite integration technique (FIT) solver-CST Microwave Studio [13]. In all studies antennas were assumed to be made of gold. We used gold permittivity values as measured by Johnson and Christy [14], which were fitted as the fourth-order polynomial in the numerical solver. Comparison between values from [14] and those used in simulations is shown in Figure 3.

For the proposed new directional nanoantenna, shown in Figure 4, we have chosen a design based on the travelling-wave principle [15]. This nanoantenna can be seen as a hybrid between a well-known V-antenna and Vivaldi-antenna. In the study we assumed free-space operation only.

The first directional nanoantennas were based on the Uda-Yagi design. However unlike at the RF/microwave frequencies, these nanoantennas were excited either by near-field coupling of the dipole source (quantum dot in [8]) or by far-field laser radiation [16]. Obviously for our targeted application, integrated on-chip plasmonic circuits, it is desired to excite antennas using a waveguide. As shown in Figure 4(a), our proposed design is easy to integrate with the traditional metal-insulator-metal (MIM) plasmonic waveguide. We used the same MIM waveguide as presented in [17], composed of two 50 nm by 50 nm gold stripes, with the gap of 20 nm. The calculated impedance is 449Ω . The complex effective index of the feeding plasmonic waveguide is $n_{\text{eff}} = 2.19 + i0.068$.

The leaky nature of propagating plasmons in the proposed design makes the operation of the nanoantenna similar to the V-antenna (composed of two wires over a ground plane). The main difference between RF and nanoversion is that in plasmonics the ground plane is not used (due to the very nature of the plasmonic mode), and the concept of the termination (used in the RF V-antenna) does not exist at the nanoscale. For these two reasons the proposed nanoantenna can be seen being close to another travelling wave RF design-Vivaldi antenna.

During the design of our nanoantennas we did not aim at any particular wavelength. Results presented hereinafter are for the wavelength of 780 nm. However, this nanoantenna is fairly broadband in its operation and can be used at other wavelengths. The major difference in operation will be due to the dispersive permittivity of gold.

In Figure 5(a) we present the radiation pattern for the designed nanoantennas at 780 nm. The calculated radiation efficiency at this wavelength is 48%. Considering a lossy nature of plasmonic structures this is a relatively good result (it also includes losses in the feeding waveguide).

The most important result of the new design is a high maximum directivity value of around 24 (linear scale). This is a major improvement over previously designed Yagi-Uda nanoantennas. To obtain a more quantitative comparison we have simulated gold Yagi-Uda nanoantenna (shown in Figure 5(b)) similar to this presented in [18]. We could therefore compare only radiation patterns and not efficiencies between these two designs. As clearly seen in Figure 5 the nanoantenna proposed in this work has a maximum directivity of 24, more than three times higher directivity achieved by Yagi-Uda (around 7).

When analysing results for traditional RF/microwave antennas, the input matching (or return loss) is often considered as one of the main performance measures. At the nanoscale however, although the concept of nanoantenna impedance has been investigated [19, 20], because of the lack of *integrated nanoscale sources* the input matching is not being considered at the moment. By “integrated nanoscale sources” we mean the sources similar to those found at

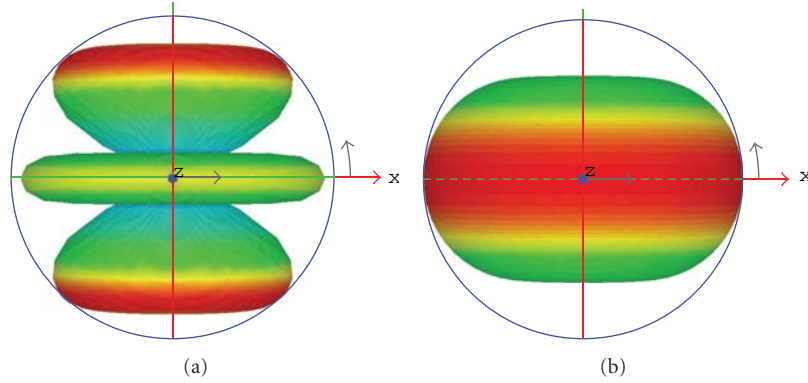


FIGURE 2: Radiation pattern of dipole antenna in third-order resonance: (a) standard RF dipole and (b) nanoantenna.

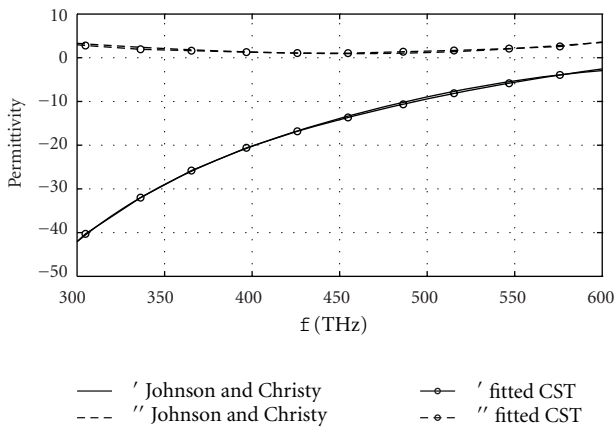


FIGURE 3: Complex permittivity of gold used in EM simulations (CST Microwave Office). Values are based on measured data from [14] and fitted using fourth-order polynomial.

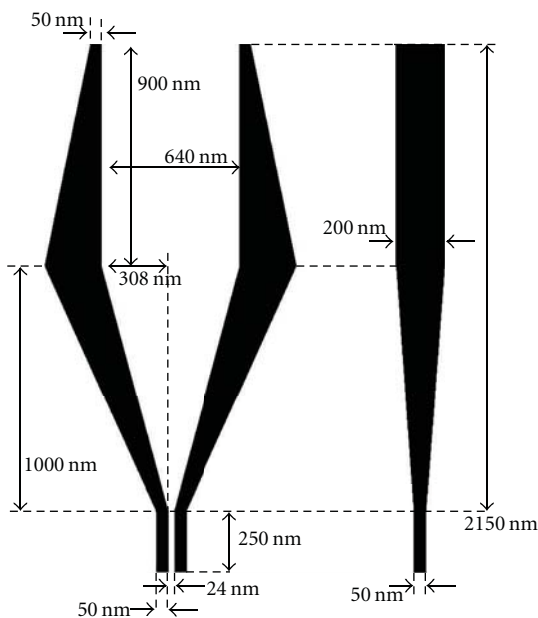


FIGURE 4: Geometry of the proposed new directional nanoantenna: top view (left) and side view (right).

RF/microwave frequencies, which can be simply “plugged” to the antenna or transmission line. Also a concept of “standard” impedance (usually 50Ω for RF/microwave circuits and antennas) is currently not defined for nanocircuits.

4. Nanoantenna Coupled to the Single Emitter Source

Directional nanoantennas could also be used for extracting light from single photon sources. This was recently demonstrated in [8], where Yagi-Uda nanoantenna was used to direct light from the quantum dot (QD). Because both the QD and nanoantenna were placed on the surface of the high-index material, main radiation was directed in the substrate. In Figure 6 we present the example of our new directional nanoantennas coupled to the dipolar emitter as well as the reference result of the stand-alone dipole emitter embedded in high-index material. Dipole is oriented along the x -axis (to excite the plasmonic waveguide) and placed $2.15 \mu\text{m}$ below the surface of the material with $n = 1.5$. This distance was dictated solely by the size of the nanoantenna. Figures 6(c) and 6(d) present the electric field produced by the stand-alone and nanoantenna-coupled dipole, respectively. Due to the reflection off the interface between materials, most radiation goes into the high index substrate for the single dipole. The calculated far-field radiation for this case is shown in Figure 6(e). However, unidirectional emission was achieved when the dipole was coupled to the new directional nanoantenna. The light generated by the dipole is propagated along the plasmonic structure and efficiently radiated into the low-index material (free space). The radiation pattern of the dipole-nanoantenna-coupled system is shown in Figure 6(f). Most importantly, in the direction of the main radiation beam the amplitude of the electric field is more than 30 dB higher when the dipole emitter is coupled to the nanoantenna. Exact electric field (E_x) values taken $1 \mu\text{m}$ above the interface between materials (see Figure 6(b) for exact location of the E-field probe) are presented in Figure 7.

Naturally, the nanoantenna embedded in the high-index material (Figure 6(b)) and its directional radiation into the free space (Figures 6(d) and 6(f)) could be used to provide wireless connectivity in the intrachip and board-to-board

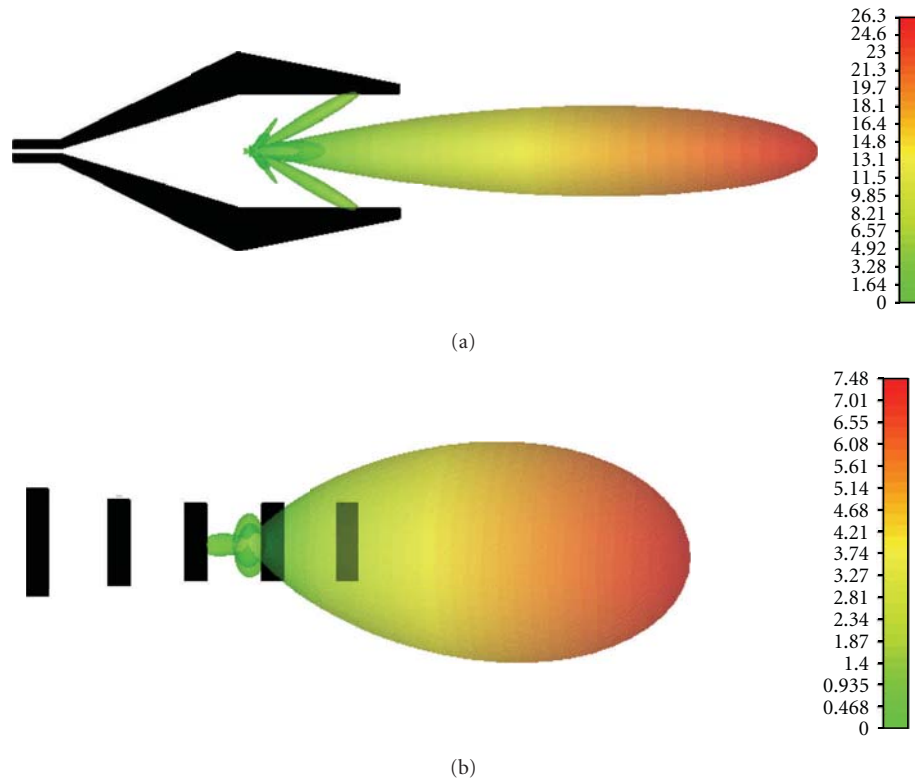


FIGURE 5: Comparison of simulated directivity (linear scale) far-field radiation patterns for (a) new directional nanoantennas designed in this work, and (b) Yagi-Uda type nanoantennas from [18]. Both nanoantennas are shown in top view.

optical links (as shown in, e.g., Figure 1). Moreover, we believe that in future 3D-integrated circuits with optical interconnects, the presented directional nanoantenna could be used as an “*optical via*”, providing vertical connection between different chip layers. Currently proposed solutions of 3D optical integration involve microlenses and micromirrors [21].

5. Nanoantennas for Wireless Optical Nano-links

In the future we foresee the development of optical wireless communication networks at the nanoscale. Nanoantennas are key components and an enabling technology for future optical wireless connectivity at the nanoscale, coupling light from external world to nanoscale circuits and vice versa. As one of the main applications for novel nanoantennas we envisage a provision of on-chip and intrachip wireless nano-links in future micro- and nanodevices.

One of the main challenges in using nanoantennas fabricated on high-index substrates is the problem with most of the radiated power going into the substrate [8]. This is presented in Figure 8 for the nanolink composed of our new nanoantennas on glass. The distance between antennas is $4\ \mu\text{m}$. Figure 8 shows the amplitude of electric field as radiated by the transmitting antenna on the left-hand side. Most of the radiation goes straight into the glass, which is obviously not desired in achieving efficient transmission between antenna.

To overcome the problem of radiation to the substrate, we have embedded our nanoantennas in high-index material and placed on the edge of the substrate, as shown in Figure 9. The distance between antennas is again $4\ \mu\text{m}$ and the medium between them is free space. Practically, this scenario could be realized in the case of end-fire on-chip nanoantennas for interchip interconnects (see, e.g., Figure 1). In this case we can observe symmetrical radiation with the maximum in the direction of the receiving antenna on the right-hand side, where we can clearly see the propagation of the guided wave along the nanoantenna.

The last example of the nanolink is presented in Figure 10 where both nanoantennas are again embedded in the high-index material, which is also acting as the propagation medium. This scenario could practically be considered in multilayered integrated circuits, where nanoantennas could in-plane connectivity, as well as connections between layers on multiple chip levels. As expected, because of the homogeneous environment the nanoantenna radiates horizontally towards the receiving antenna. This is an efficient wireless link.

The quantitative comparison of transmission efficiency of all three nano-links is shown in Figure 11. We compare the magnitude of the scattering parameter S_{21} , indicating the power captured by the receiving antenna. At 300 THz we can see that the best transmission is achieved using the link from Figure 10, with both antennas embedded in glass. Slightly less efficient is the end-fire-like nano-link shown in Figure 9. The worst result is achieved with nanoantennas

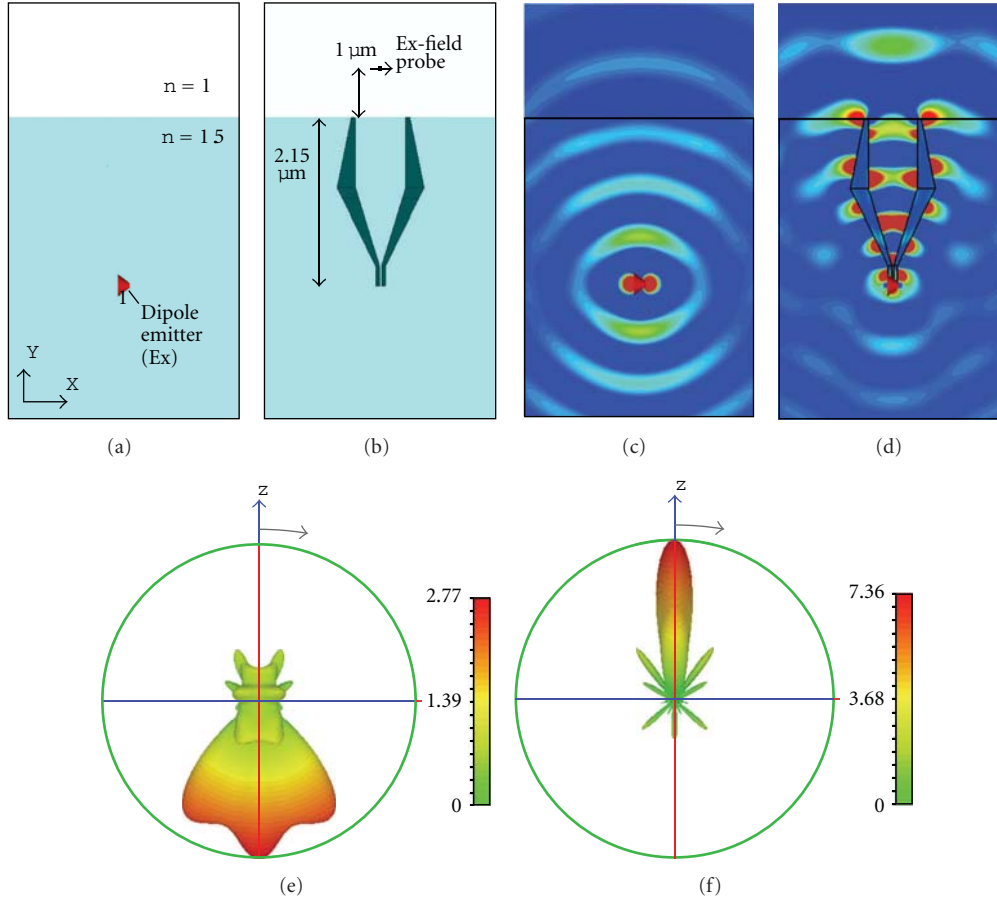


FIGURE 6: Comparison of far-field radiation of the dipole emitter embedded in high-index material with and without the nanoantenna. (a) Dipole emitted embedded $2.15 \mu\text{m}$ below the surface of $n = 1.5$ material, (b) dipole coupled to the nanoantenna, (c) E-field of the dipole emitter, (d) E-field of the coupled dipole-nanoantenna system, (e) far-field radiation pattern of the dipole in high-index material, and (f) far-field of the dipole coupled to the directional nanoantenna. All results are presented at the wavelength $1 \mu\text{m}$.

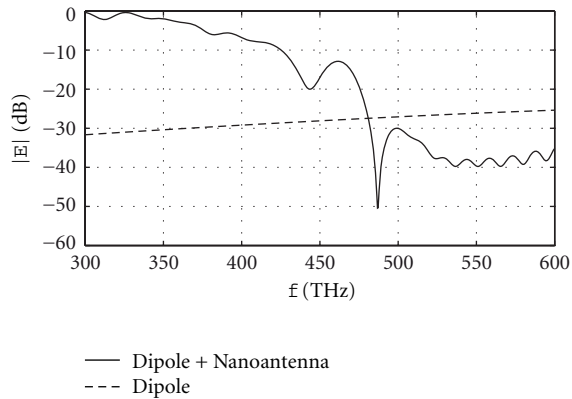


FIGURE 7: Comparison of the amplitude of the radiated Ex electric field taken 1 mm above the material interface (see Figure 6(b)).

placed on glass (Figure 8), with the $|S_{21}|$ smaller by more than 20 dB, compared with the other two cases. These results clearly show that for most efficient transmission nanoantennas should be placed in homogeneous dielectric on top (superstrate) and below.

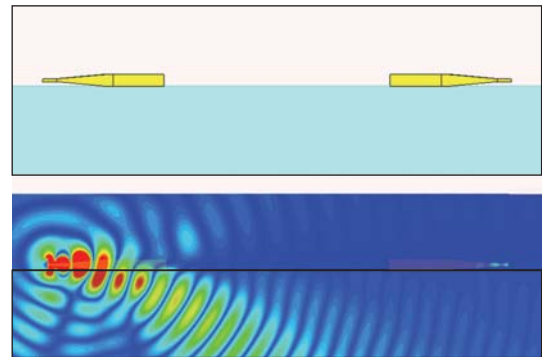


FIGURE 8: Optical wireless link between nanoantennas on glass substrate and corresponding radiated E-field. Distance between nanoantennas is $4 \mu\text{m}$; frequency is 300 THz.

6. Fabrication of Nanoantennas

After very encouraging design results of the new nanoantennas, we made the first attempts at fabricating them. In Figure 12 we can see two examples of different nanoantenna

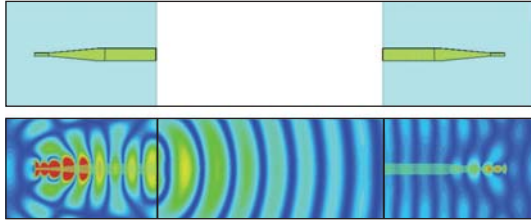


FIGURE 9: Optical wireless link between nanoantennas embedded in glass substrate and corresponding radiated E-field. Distance between nanoantennas is $4\ \mu\text{m}$, frequency is 300 THz, and propagation medium is free space.

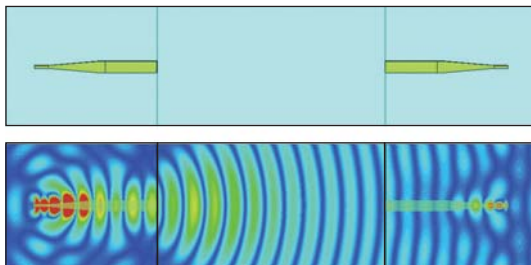


FIGURE 10: Optical wireless link between nanoantennas embedded in glass substrate and corresponding radiated E-field. Distance between nanoantennas is $4\ \mu\text{m}$, frequency is 300 THz, and propagation medium is glass.

samples. They were fabricated in 50 nm gold deposited on thick glass slides using focused ion beam milling.

We are currently in a phase of improving our fabrication process and building a measurement setup. All final nanoantenna designs will need to be optimized for operation on a glass substrate.

7. Conclusions

In this contribution we presented the novel design of the directional nanoantenna, which is excited from the MIM plasmonic waveguide. The nanoantenna design is based on the *travelling wave* principle and can be considered as a hybrid between a well-known V-antenna and Vivaldi-antenna. The most important result of the new design is a high maximum directivity value of around 24 (linear scale), more than three times higher than that achieved by previously published Yagi-Uda (directivity of 7). First samples of designed nanoantennas were fabricated and measurements are currently being set up. This novel nanoantenna could be used in the end-fire configuration in the intrachip and board-to-board free space optical links or in efficient directional extraction of light emitted by single-photon sourced.

Acknowledgment

The authors acknowledge the support of the UK's Engineering and Physical Sciences Research Council (EPSRC),

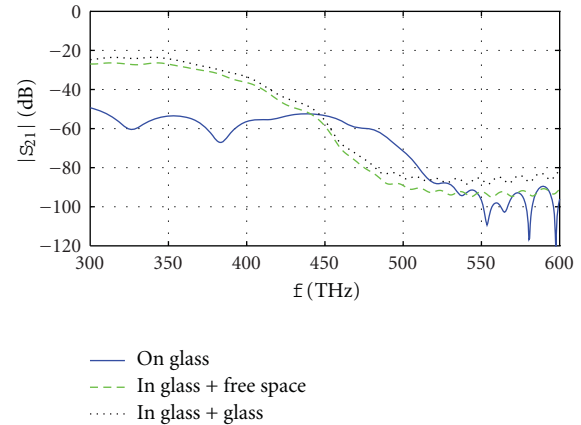
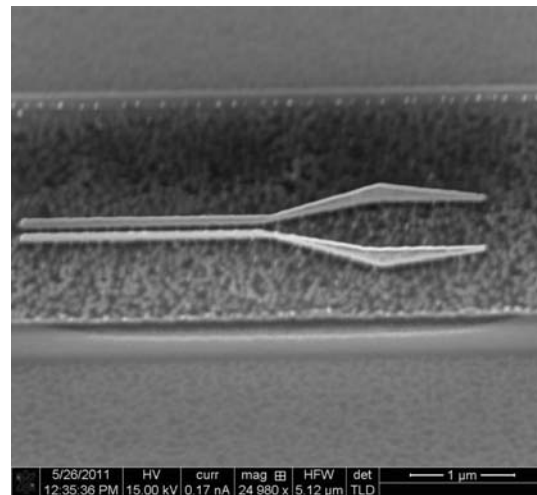
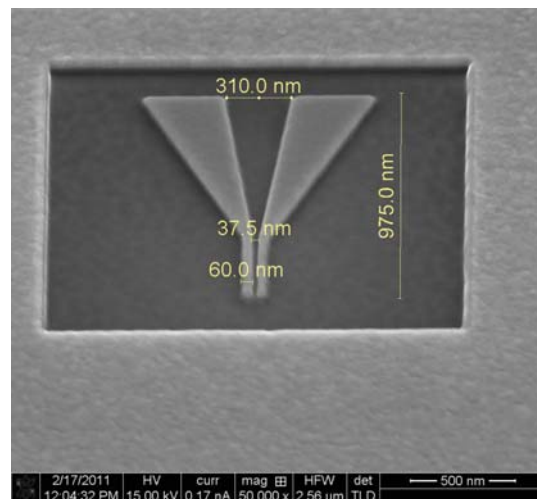


FIGURE 11: Transmission coefficient $|S_{21}|$ for three different scenarios of the optical wireless links from Figures 8–10. Distance between nanoantennas is $4\ \mu\text{m}$.



(a)



(b)

FIGURE 12: Example of gold nanoantennas fabricated using dual beam focused ion beam (FIB) milling. Nanoantennas were fabricated in 50 nm gold on thick glass slides.

Cross-Disciplinary Interfaces Programme (C-DIP) Fellowship Fund, Grant EP/I017852/1.

References

- [1] PhotonicsRoadmapSME (EU FP7 project), "Photonics in ICT: A Technology Roadmap for SMEs on new photonic devices, materials and fabrication technologies," technology roadmap, http://www.photonicroad.eu/upload/PhotonicRoadSME_Technology%20Roadmap%20on%20Photonic%20in%20ICT.pdf.
- [2] J. Wessel, "Surface-enhanced optical microscopy," *Journal of the Optical Society of America B*, vol. 2, pp. 1538–1540, 1985.
- [3] P. Bharadwaj, B. Deutsch, and L. Novotny, "Optical antennas," *Advances in Optics and Photonics*, vol. 1, pp. 438–483, 2009.
- [4] T. H. Taminiau, F. D. Stefani, and N. F. Van Hulst, "Optical nanorod antennas modeled as cavities for dipolar emitters: evolution of sub- and super-radiant modes," *Nano Letters*, vol. 11, no. 3, pp. 1020–1024, 2011.
- [5] B. Stout, A. Devilez, B. Rolly, and N. Bonod, "Multipole methods for nanoantennas design: applications to Yagi-Uda configurations," *Journal of the Optical Society of America B*, vol. 28, no. 5, pp. 1213–1223, 2011.
- [6] K. C. Y. Huang, Y. C. Jun, M.-K. Seo, and M. L. Brongersma, "Power flow from a dipole emitter near an optical antenna," *Optics Express*, vol. 19, no. 20, pp. 19084–19092, 2011.
- [7] V. Giannini, J. A. Sánchez-Gil, O. L. Muskens, and J. G. Rivas, "Electrodynamic calculations of spontaneous emission coupled to metal nanostructures of arbitrary shape: nanoantenna-enhanced fluorescence," *Journal of the Optical Society of America B*, vol. 26, no. 8, pp. 1569–1577, 2009.
- [8] A. G. Curto, G. Volpe, T. H. Taminiau, M. P. Kreuzer, R. Quidant, and N. F. Van Hulst, "Unidirectional emission of a quantum dot coupled to a nanoantenna," *Science*, vol. 329, no. 5994, pp. 930–933, 2010.
- [9] Y. Alaverdyan, N. Vamivakas, J. Barnes, C. Leboeuf, J. Hare, and M. Atature, "Spectral tunability of a plasmonic antenna with a dielectric nanocrystal," *Optics Express*, vol. 19, no. 19, pp. 18175–18181, 2011.
- [10] S. A. Maier, M. L. Brongersma, P. G. Kik, S. Meltzer, A. A. G. Requicha, and H. A. Atwater, "Plasmonics—a route to nanoscale optical devices," *Advanced Materials*, vol. 13, no. 19, pp. 1501–1505, 2001.
- [11] S. Maier, *Plasmonics: Fundamentals and Applications*, Springer, Berlin, Germany, 2007.
- [12] J. Dorfmueller, R. Vogelgesang, W. Khunsin, C. Rockstuhl, C. Etrich, and K. Kern, "Plasmonic nanowire antennas: experiment, simulation, and theory," *Nano Letters*, vol. 10, no. 9, pp. 3596–3603, 2010.
- [13] <http://www.cst.com/>.
- [14] P. B. Johnson and R. W. Christy, "Optical constants of the noble metals," *Physical Review B*, vol. 6, no. 12, pp. 4370–4379, 1972.
- [15] C. Balanis, *Antenna Theory: Analysis and Design*, John Wiley & Sons, New York, NY, USA, 2005.
- [16] T. Kosako, Y. Kadoya, and H. F. Hofmann, "Directional control of light by a nano-optical Yagi-Uda antenna," *Nature Photonics*, vol. 4, no. 5, pp. 312–315, 2010.
- [17] A. Alù and N. Engheta, "Wireless at the nanoscale: optical interconnects using matched nanoantennas," *Physical Review Letters*, vol. 104, no. 21, Article ID 213902, 2010.
- [18] T. H. Taminiau, F. D. Stefani, and N. F. Van Hulst, "Enhanced directional excitation and emission of single emitters by a nano-optical Yagi-Uda antenna," *Optics Express*, vol. 16, no. 14, pp. 10858–10866, 2008.
- [19] A. Alù and N. Engheta, "Input impedance, nanocircuit loading, and radiation tuning of optical nanoantennas," *Physical Review Letters*, vol. 101, no. 4, Article ID 043901, 2008.
- [20] J. J. Greffet, M. Laroche, and F. Marquier, "Impedance of a nanoantenna and a single quantum emitter," *Physical Review Letters*, vol. 105, no. 11, Article ID 117701, 2010.
- [21] B. Ciftcioglu, R. Berman, J. Zhang et al., "A 3-D integrated intrachip free-space optical interconnect for many-core chips," *IEEE Photonics Technology Letters*, vol. 23, no. 3, pp. 164–166, 2011.

Research Article

Surface Plasmon States in Inhomogeneous Media at Critical and Subcritical Metal Concentrations

Katyayani Seal¹ and Dentcho A. Genov²

¹Department of Physics and Astronomy, University of Tennessee, Knoxville, TN 37996, USA

²College of Engineering and Science, Louisiana Tech University, Ruston, LA 71270, USA

Correspondence should be addressed to Katyayani Seal, sealk@ornl.gov

Received 30 September 2011; Accepted 14 December 2011

Academic Editor: Ali Passian

Copyright © 2012 K. Seal and D. A. Genov. This is an open access article distributed under the Creative Commons Attribution License, which permits unrestricted use, distribution, and reproduction in any medium, provided the original work is properly cited.

Semicontinuous metal-dielectric films are composed of a wide range of metal clusters of various geometries—sizes as well as structures. This ensures that at any given wavelength of incident radiation, clusters exist in the film that will respond resonantly, akin to resonating nanoantennas, resulting in the broad optical response (absorption) that is a characteristic of semicontinuous films. The physics of the surface plasmon states that are supported by such systems is complex and can involve both localized and propagating plasmons. This chapter describes near-field experimental and numerical studies of the surface plasmon states in semicontinuous films at critical and subcritical metal concentrations and evaluates the local field intensity statistics to discuss the interplay between various eigenmodes.

1. Introduction

Random metal-dielectric composites, such as nanoscaled semicontinuous metallic structures, exhibit unique optical and electrical transport properties [1–26]. One of the most remarkable properties of such composites is the enhancement of electric and magnetic fields in the visible and infrared spectral ranges [1, 8–22]. These materials show promise in wide ranging photonics technologies including applications in negative index materials [27–29], biosensing [30, 31], and nonlinear optics [10] spectroscopy [32, 33] broadband optical amplifiers and optical absorbers [10, 34, 35].

The synthesis of metal-dielectric composites typically involves the deposition of metal particles onto a dielectric substrate [14, 21–23]. At low metal concentrations, mutually separated nanometer-sized grains are formed at random locations. Self-similar clusters form as the metal surface concentration increases [1, 3, 10]. At a certain metal concentration (p_c), that is, the percolation threshold, the metal clusters interconnect to form an infinite “backbone cluster”, setting off an insulator-to-metal phase transition. This is marked by a sharp drop in dc resistivity [14, 23] and

anomalous absorption at visible and near-infrared wavelengths [1, 10, 11, 14–19, 21–23]. At even higher metal concentrations, the sample becomes mostly metallic with dielectric voids, ultimately resulting in a uniform metal film.

From both theoretical predictions and experimental corroboration, it has been observed that under illumination with light at optical and near infrared frequencies, strong local field enhancement of up to 10^4 can be achieved on the surface of two-dimensional metal-dielectric composites [1, 10–22, 36]. This light trapping effect is facilitated by the excitation of collective electron oscillations, that is, surface plasmons (SP). Surface plasmon modes are morphological resonances governed by the structural inhomogeneities inherent in the fractal clusters formed within the random metal-dielectric films. The observed local fields appear to be strongly localized [1, 10, 11, 17–19] with relatively high Q-factors dependent on the intrinsic dissipation in the metal. This phenomenon has been observed in rough and semicontinuous metal films [8, 9, 15, 16, 23]. Notably, due to the geometry of the clusters, the spatial distribution of the field maxima is sensitive to the polarization, wavelength and angle of incidence of the applied field [1, 2, 10]. Thus the

metal clusters in a semicontinuous film that support SP modes may be thought of as resonating nanoantennas with a range of resonant frequencies and Q-factors. The accumulation and subsequent dissipation of electromagnetic energy in these localized SP modes result in the anomalous absorption characteristic of semicontinuous metal films [1, 2, 5–10, 14–22].

The near-field intensity distribution across a semicontinuous metal film near the “percolation threshold” has been observed to be extremely inhomogeneous with giant local field maxima [15, 16, 20–22], that vary not only in size by orders of magnitude from subwavelength to multiple wavelengths, but also vary strongly in intensity. In the early theoretical studies on percolating metal-dielectric composites, an observed similarity between the Kirchhoff Hamiltonian used to model random metal dielectric systems and the Anderson Hamiltonian [37] led to the expectation that all surface plasmon eigenmodes are localized [10]. Follow-up numerical simulations subsequently suggested that a planar disordered nanosystem can simultaneously have localized and delocalized states [18]. This concept of “inhomogeneous localization” was originally introduced for metal fractal aggregates, where self-similarity in the structural geometry can result in a mode consisting of multiple hot spots spread over the entire system [10]. Later calculations have shown that in an infinitely large semicontinuous metal film, delocalized SP modes exist only at one point in the eigenvalue spectrum and their measure is zero [19]. The conceptual origin for these delocalized states lies in the short-range correlations in the governing Kirchhoff Hamiltonian, which are absent in the Anderson Hamiltonian [37]. Remarkably, even though they have a zero measure, delocalized modes can affect the local field statistics by modifying the critical indices for the high-order field moments [19, 22] and thus influence the optical properties. The interplay between localized and delocalized states in semicontinuous films and their role in the transport properties therein remain a topic of interest and speculation.

For disordered systems with a range of possible eigenmodes and transport paths, studies of field and intensity statistics are a valuable avenue to uncover the system’s dominant response and the nature of wave transport. In disordered metallic nanostructures in particular, the intensity statistics are more complex because of the excitation of surface plasmons and resulting inhomogeneous localization [18]. In the study of random metal-dielectric composites, both numerically [2, 14, 17–19] and experimentally [5–7, 15, 16, 19–23] obtained near-field intensity statistics are often used to characterize the local field fluctuations in various metal aggregates, fractal structures, and rough and semicontinuous metal films.

This chapter provides a comprehensive view of the interplay between localized and delocalized plasmon excitations in metal semicontinuous films through the analysis of experimentally and numerically obtained near-field intensity statistics.

2. Synthesis of Semicontinuous Films and Near-Field Statistics

Semicontinuous silver films on glass substrates are typically synthesized by thermal evaporation [5–9] or by pulsed laser deposition [16]. Transmission electron microscope (TEM) images from a silver-glass semicontinuous film grown by pulsed laser deposition are shown in Figure 1(a). From the images, it is evident that these samples are composed of individual silver grains of average size about 20–30 nm. An increase in deposition time (surface concentration of silver) induces a structural transition from isolated metal grains ($p < 0.4$) to interconnected metal clusters ($p = 0.6$) and finally to a nearly continuous metal film with dielectric voids ($p > 0.8$) [16]. For these samples, the percolation threshold was found to be at $p_c = 0.65$ from previous work [16]. The 2D structural correlation functions were found to be isotropic. The correlation radius, defined as the half width at half maximum (HWHM) of the structural correlation function, is close to the grain size ~ 20 nm.

Near-field optical microscopy (NSOM) is a powerful tool to image the near-field intensity distribution over the surface of a sample [15, 16]. Figure 1(b) shows NSOM images for silver on glass semicontinuous films with metal concentration $p = 0.36, 0.45, 0.65, 0.75,$ and 0.83 at a probe wavelength of 543 nm. The samples were illuminated by the evanescent field (in the total internal reflection geometry) of “ \mathbf{p} ” polarized laser light. The projection of the incident beam’s \mathbf{k} -vector on the film plane (x - y plane), \mathbf{k}_{\parallel} , is along the vertical y axis. The local optical signal was collected by a tapered, uncoated optical fiber of tip radius of about 50 nm. The tip-to-sample distance, controlled by shear-force feedback, was approximately 10 nm. The tip resolution is estimated to be of the order of 150 nm from the smallest features in the near-field images [16, 22]. The images exhibit inhomogeneous intensity distributions with intensity maxima (or optical “hot spots”) of various sizes. At $p = 0.36$, there is an indication of interference fringes parallel to the horizontal x axis, which are weakened at $p = 0.45$, completely lost at $p = 0.65$, and reappear at $p = 0.83$.

To understand the role of the eigenmodes supported by various clusters in the semicontinuous film, it is instructive to study the near-field intensity statistics for different metal concentrations p . Specifically, the variance $\text{var}(I) = \langle I(x, y)^2 \rangle / \langle I(x, y) \rangle^2 - 1$ and higher-order moments $M_{2n} = \langle I(x, y)^n \rangle / I_0^n$ can be obtained from the NSOM images, where $I(x, y)$ is the intensity over the sample surface as a function of x and y coordinates. Figure 2 shows the experimentally obtained values of $\text{var}(I)$ as a function of $\Delta p = p - p_c$ at a probe wavelength of 633 nm calculated from the NSOM images similar to the ones in Figure 1(b). Each data point was obtained from approximately 300,000 near-field intensity values. The error bar was evaluated as the standard error of data collected from several NSOM images of different parts of the samples. Counterintuitively, the intensity fluctuations do not maximize at p_c ($\Delta p = 0$), where scattering is the strongest. Instead, a local minimum appears at p_c . Away from p_c , $\text{var}(I)$ has two maxima at $\Delta p = -0.2$ and $\Delta p = +0.1$. A similar dependence of $\text{var}(I)$

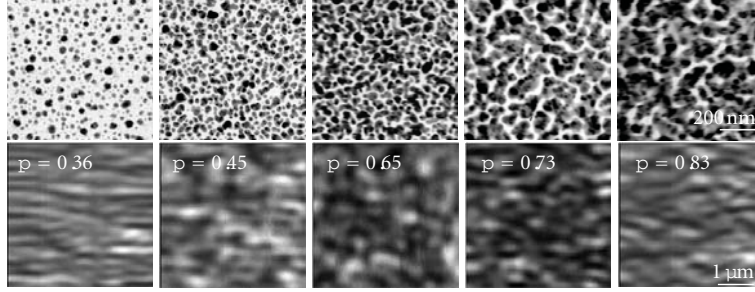


FIGURE 1: TEM micrographs of silver semicontinuous films on glass substrates showing the metal nanostructure geometry for various metal concentrations in the first row. The second row shows the inhomogeneous distribution of the near-field intensity for corresponding samples.

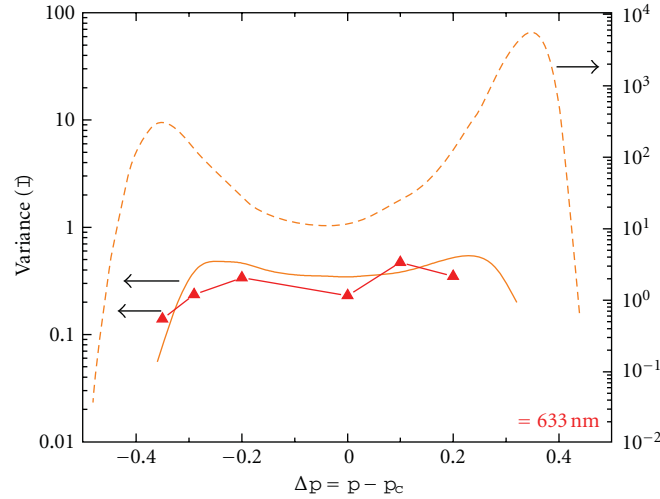


FIGURE 2: Near-field intensity variance $\text{var}(I)$ as a function of silver concentration $\Delta p = p - p_c$, obtained experimentally (solid line with triangles) and numerically with (dotted line) and without (dashed line) spatial averaging [22, Figure 1].

on p is also observed at lower probe wavelengths (543 nm). However, the absolute value of $\text{var}(I)$ at $\lambda = 543$ nm is lower than that at $\lambda = 633$ nm, indicating that the intensity fluctuations are stronger at longer wavelengths.

The variance of intensity fluctuations is proportional to the inverse participation ratio (IPR) of the local field, often used to describe the spatial extent of eigenstates [2]. In the experimental set up described, where the incident field excites a number of SP modes, IPR gives a qualitative measure of the surface area occupied by hot spots. Similar to $\text{var}(I)$, IPR has a minimum at p_c . Larger values of IPR at $|p - p_c| = 0.1$ and 0.2 indicate that a smaller percentage of the film surface is occupied by hot spots. This is consistent with the direct observation that away from p_c , there are fewer hot spots but each is brighter.

The experimentally observed dip in IPR suggests a weakening of the SP localization strength at p_c . For the calculation of the high-order moments of intensity enhancement M_{2n} , the incident light intensity I_0 obtained from the near-field measurement of a clean glass substrate can be used as a standard normalizing factor. Figure 3(a) is a plot of M_{2n} versus Δp for $n = 2, 3, 4$, and 5 obtained from the same NSOM images (at a probe wavelength of 633 nm) as were

used in Figure 2. The error bars were obtained by the same method as for $\text{var}(I)$ in Figure 2. The M_{2n} exhibit a prominent dip near p_c , which becomes more pronounced for higher n . This observation once more confirms that the local field fluctuations are weakened at the percolation threshold.

3. Numerical Model of a Semicontinuous Film

In order to understand the experimental findings, it is useful to perform numerical simulations to simulate the semicontinuous film. In the visible frequency regime, metal-dielectric composites can be viewed as a system of lumped RLC circuits [2, 10], and the bond percolation model can be employed to describe their electromagnetic response. The bond model has a percolation threshold $p_c = 0.5$, which differs slightly from the experimental observation. This deviation, however, should not preclude a direct mapping between experiment and theory because the scaling properties of random metal films do not depend on the absolute value of p_c [3].

The inhomogeneous metal dielectric composite is a random system of metal nanoparticles incorporated within a dielectric host and can be modeled as a strongly coupled lumped $R-L-C$ network. Provided the feature sizes along

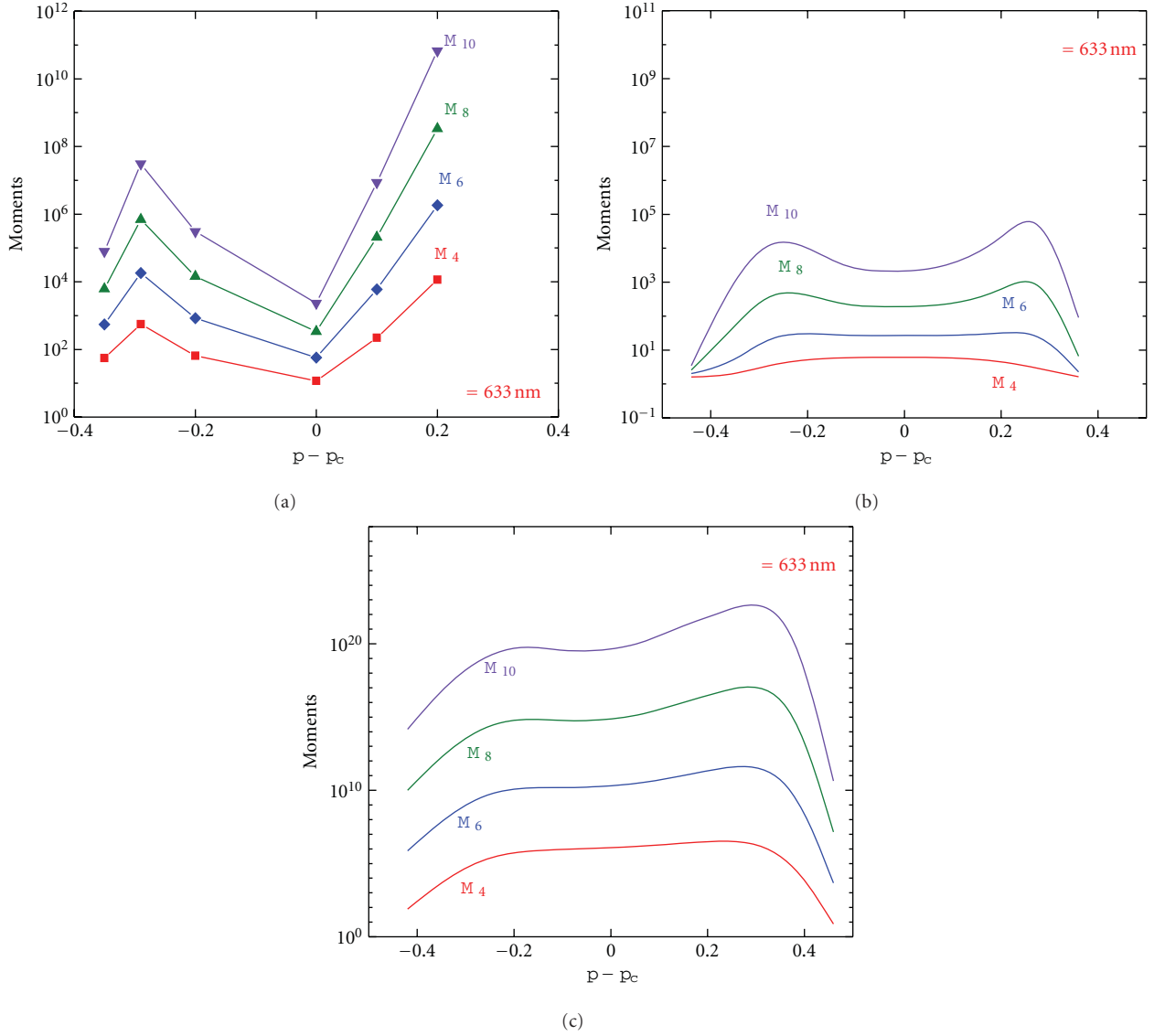


FIGURE 3: High-order moments of near-field intensity enhancement M_{2n} as a function of silver concentration $\Delta p = p - p_c$, obtained experimentally (a) and numerically with (b) and without (c) spatial averaging [22, Figure 2].

the direction of illumination are small compared to the incident wavelength $\lambda = 2\pi c/\omega$, the impinging electric field \vec{E}_0 couples with the metal dielectric composite quasistatically, with a local electric potential $\varphi(\omega)$ given as

$$\vec{\nabla} \cdot [\sigma(\omega, \vec{r}) \vec{\nabla} \varphi(\vec{r})] = \vec{E}_0 \cdot \vec{\nabla} \sigma(\omega, \vec{r}), \quad (1)$$

where the local conductivity $\sigma(\omega, \vec{r})$ is a discontinuous random function across the composite taking discrete values $\sigma_m = -i\omega\epsilon_m$ for the metal particles and $\sigma_d = -i\omega\epsilon_d$ for the dielectric voids with probabilities p and $1 - p$, respectively [14]. Equation (1) describes a generalized Kirchhoff problem and can be solved numerically by discretization of the electric potential on a cubic lattice, with the metal and dielectric constituents represented by randomly distributed metal/dielectric bonds connecting each lattice site. The resulting linear system of equations is written in short form

$\hat{H} \cdot \vec{\varphi} = \hat{W} \cdot \hat{E}_0$, where \hat{H} is a complex value Kirchhoff Hamiltonian (KH), $\vec{\varphi} = \{\varphi_{i,j}\}$ is a vector containing the values of the potential at each lattice side (i, j) , and \hat{W} is the incident field projection operator. The Kirchhoff Hamiltonian is a random matrix with diagonal elements $H_{nn} = \sum \sigma_{\{i,j\}_n}$, where the summation is over all bond conductivities connecting the n th site with its nearest neighbors, and correlated off-diagonal elements proportional to the respective bond conductivities $\sigma_{\{i,j\}_n}$. Traditional numerical methods such as Gaussian eliminations require $O(L^6)$ floating point operations and $O(L^4)$ operational memory to achieve solution (here L is the lateral size of the composite). For the system sizes of interest (a few μm^2 or up to a million metal particles), these algorithms are not feasible even with high performance computing. To overcome this computational problem, a block elimination method has been developed that splits the Kirchhoff Hamiltonian on $L \times L$ block matrixes

and performs triangulation on these separated block of matrixes [2]. This effectively allows the reduction of this two-dimensional problem to an equivalent 4/3-dimensional problem, resulting in dramatic improvement in performance with solution obtained in only $O(L^4)$ floating point operations and operational memory requirement of the order of $O(L^3)$.

The numerical results based on the Block Elimination procedure are shown in Figures 2, 3(b), and 3(c), where the local field distribution is calculated for $2\mu\text{m} \times 2\mu\text{m}$ -sized semicontinuous films of different silver concentrations, followed by calculations of $\text{var}(I)$ and M_{2n} . Detailed information on the method of calculation used is provided in [2, 10]. At the percolation threshold a highly inhomogeneous local field distribution is observed, with peak intensities surpassing the incident laser light intensity by factors of 10^3 – 10^4 .

The experimentally obtained local field enhancements are considerably lower in comparison because of the finite spatial resolution of NSOM. For optimal comparison with the experimental data, the local fields at a distance equal to the tip-sample separation (~ 10 nm for the NSOM configuration used) from the sample surface can be estimated numerically and then averaged using the NSOM aperture function (in this case, corresponding to a tip resolution of ~ 150 nm). Numerical data for $\text{var}(I)$ and M_{2n} before and after the spatial averaging are provided in Figures 2, 3(b), and 3(c). These curves were obtained from 100 realizations of the semicontinuous film surface for each p . As shown in Figure 2, the $\text{var}(I)$ calculated without spatial averaging exhibits a wider and deeper dip near p_c . The spatial averaging not only reduces the value of $\text{var}(I)$ but also partially smooths out the dip at p_c . After the resolution limit of the NSOM is taken into account, the numerical data closely mimic the experimental $\text{var}(I)$. However, some of the numerical values fall outside the experimental error bars because of inevitable approximations used in the calculations such as uncertainty in the value of dielectric constant of silver, the tip-sample distance, and the spatial averaging parameter. In Figure 3, the calculated local field moments M_{2n} exhibit a p -dependence similar to the measured one, that is, M_{2n} reaches a local minimum at p_c and has two distinct maxima at $|\Delta p| \leq 0.3$. The above numerical uncertainties also contribute to the discrepancies between experimental and numerical (spatially averaged) data shown in Figure 2.

4. A Qualitative Understanding of the Variations in Localization Strength

The observed decrease of $\text{var}(I)$ and M_{2n} at $|\Delta p| \geq 0.3$ can be qualitatively explained by considering the resonant nature of SP excitation. According to percolation theory [3], the largest metal cluster in the random composite has a size $l_m(p) = ap_c^\nu/|p - p_c|^\nu$, where a is the average metal particle size and ν is a critical exponent. Resonant SP modes can be excited by incident light of a wavelength λ if $l_m(p) \geq l_r = a(|\epsilon'_m|/\epsilon_d)^{\nu/(s+t)}$, where $\epsilon'_m + i\epsilon''_m$ and ϵ_d are the dielectric constants of the metal particles and dielectric host,

respectively [10]. The critical exponents s and t correspond to the scaling of the composite's static conductivity and dielectric constant, respectively, with the sample size. For the planar systems under consideration, $s = \nu = t = 4/3$ [3]. Thus the SP resonance wavelength in a cluster of size $l \geq l_r$ scales as $\lambda_r \approx \lambda_p(l/a)^{\nu/(s+t)} \approx \lambda_p\sqrt{l/a}$, where λ_p is the plasma wavelength [10]. This unique property of localized SPs is distinct from resonances in the retarded (nonquasistatic) regime where $\lambda_r \approx l$.

When the metal concentration p differs considerably from p_c , there is a decrease in the maximum cluster size l_m . If $l_m(p) < l_r$, SP modes in the semicontinuous metal film can no longer be excited by the external field, leading to a dramatic decrease in the local electromagnetic response. The cutoff metal concentrations are estimated from the condition $l_r = l_m(p_\pm)$ as $p_\pm = p_c[1 \pm (\epsilon_d/|\epsilon'_m|)^{1/(s+t)}]$. At $\lambda = 633$ nm, $\Delta p_\pm = |p_\pm - p_c| \approx 0.3$. For concentrations in the range $|\Delta p| > \Delta p_\pm$, both $\text{var}(I)$ and M_{2n} are expected to decrease sharply. Estimates for the cutoff concentrations Δp agree well with the experimental and numerical results shown in Figures 2 and 3. The presence of cutoff metal concentrations also manifests itself as an anomalous absorption band in semicontinuous metal films [23]. Specifically, when $\kappa = |\epsilon''_m/\epsilon'_m| \ll 1$, the buildup of giant local fields and storage of electromagnetic energy in the films leads to strong light absorption, which occurs for metal concentrations inside the band $p_c - \Delta p_- < p < p_c + \Delta p_+$ [26]. The quantity Δp_\pm , calculated as $\sqrt{|\epsilon'_m|/\epsilon_d/(|\epsilon'_m| + \epsilon_d)}$ from effective medium theory, gives values close to the cutoff concentration estimates based on the resonant cluster size.

5. Density of States and Localization Length from the SP Eigenproblem

To further understand the behavior of $\text{var}(I)$ and M_{2n} at p_c , it is instructive to solve the SP eigenproblem. In order to model the local electric response of a random system comprised of a large number of metal particles, one can work in the quasistatic limit. The general solution of the current conservation (1) can be described completely by examining the underlying eigenproblem [10, 19]

$$\bar{\nabla} \cdot \left[\sigma(\vec{r}) \bar{\nabla} \Psi_\Lambda(\vec{r}) \right] = \Lambda \Psi_\Lambda(\vec{r}). \quad (2)$$

Reduction of (2) on a square lattice leads to a system of linear equations $\hat{H}_{\text{KH}}|n\rangle = \Lambda_n|n\rangle$, where again the Kirchhoff Hamiltonian $\hat{H}_{\text{KH}} = \sum_n h_{nn}|n\rangle\langle n| + \sum_{n \neq k} h_{nk}|n\rangle\langle k|$ is a random matrix with correlated diagonal and off-diagonal elements and $|n\rangle$ are the SP eigenstates [5–7, 19, 16]. The existence of short range correlations in the SP eigenproblem makes it substantially different than the corresponding quantum mechanical case where the random Hamiltonians are noncorrelated [19]. The correlations in the KH are due to the local current conservation and exist for all spatial dimensions.

The statistical properties of the solution to the SP eigenproblem can be investigated in terms of the density of states $\rho(\lambda)$ and SP localization lengths $\xi(\lambda)$. These are plotted

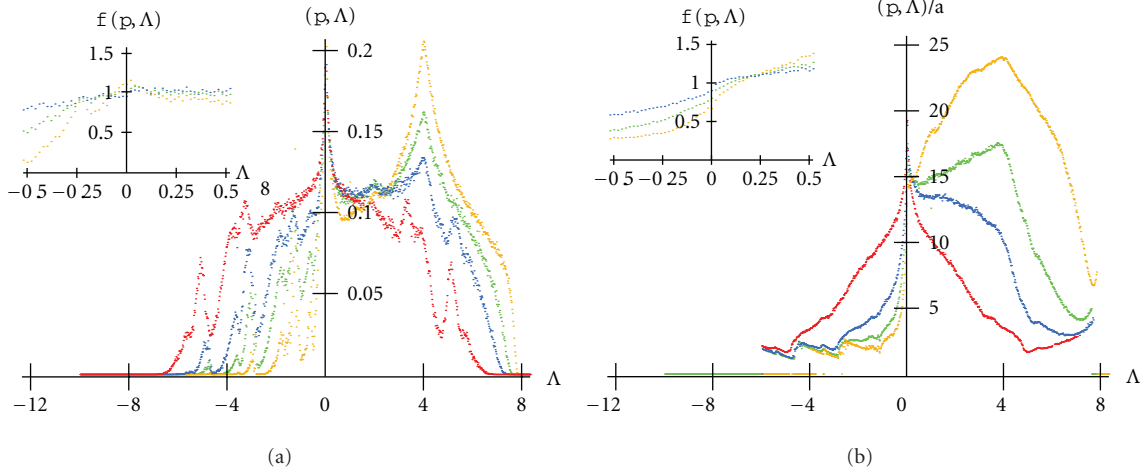


FIGURE 4: The surface plasmons density of states (DOS) (a) and localization length (b) are calculated for an ensemble of 100 metal-dielectric films each with size $1 \mu\text{m}$. Four different metal filling fractions are investigated: $p = 0.1$ (yellow color), $p = 0.2$ (green color), $p = 0.3$ (blue color), and $p = 0.5$ (red color). The singularity at the band center and its dependence on the metal concentration is closely inspected in the insets [24, Figure 2].

for different metal concentrations in Figures 4(a) and 4(b), respectively. At the band center, and concentrations close to percolation, the density of states exhibits a singularity as shown in Figure 4(a). In the first approximation the density of states seems to diverge as a power law $\rho(\Lambda) \sim |\Lambda|^{-\gamma}$ at $p = p_c$ (red curve), where $\gamma = 0.14 \pm 0.01$ [17] is a critical exponent. The localization length for each eigenmode (presented in Figure 4(b)) is also calculated using the gyration radius $\xi^2(p, \Lambda) = \int (\vec{r} - \langle \vec{r} \rangle_\Lambda)^2 |\Psi_\Lambda(\vec{r}, p)|^2 d\vec{r}$, where $\langle \vec{r} \rangle_\Lambda = \int \vec{r} |\Psi_\Lambda(\vec{r}, p)|^2 d\vec{r}$ is the “mass center” of the n th mode and the integration is performed over the film surface. Similar to the density of states, there is a singularity at the band center. At p_c , the localization length diverges logarithmically for $\Lambda \rightarrow 0$, but also can be fitted with a power law $\xi(\Lambda) \sim |\Lambda|^{-\alpha}$, where $\alpha = 0.15 \pm 0.02$.

Relying on the SP eigenproblem (2), it is possible to estimate the optical response of the random metal films for an incident frequency ω_r corresponding to the single particle resonance $\text{Re } \varepsilon_m(\omega_r) = -\varepsilon_d$. Specifically, the local potential is expanded over the SP eigenspace [10] to obtain an integral relationship for the local field moments

$$M_{2n} = \frac{1}{S|E_0|^{2n}} \left\langle \int |E(\vec{r}, p)|^{2n} d\vec{r} \right\rangle \quad (3)$$

$$\cong \int_{-\infty}^{\infty} \frac{\rho(p, \Lambda) [a/\xi(p, \Lambda)]^{2(2n-1)}}{(\Lambda^2 + \kappa^2)^n} d\Lambda,$$

where $\kappa = |\varepsilon_m''/\varepsilon_m'| \ll 1$ is the intrinsic loss factor, S is the sample area, and the brackets correspond to ensemble averaging over large numbers of system realizations.

The integral in (3) can be analyzed as follows. Close to the band center ($|\Lambda| \ll 1$), the properties of the generalized SP eigenstates can be modeled (see inserts in Figure 4) by simplified expressions for the SP DOS $f_p(p, \lambda) = \rho(p, \lambda)/\rho(p_c, \lambda) \approx 1$ and the SP localization length $f_\xi(p, \Lambda) = \xi(p, \Lambda)/\xi(p_c, \Lambda) \approx g(p) + \theta(\Lambda)(1 - g(p))$, where $\theta(\Lambda)$ is a step function and $g(p) < 1$. Since only the SP eigenmodes in the

vicinity of the band center have a dominant contribution to the moments, the p dependence from the integral (3) can then be taken out to give $M_{2n}(p) \approx M_{2n}(p_c)[1 + g^{4(1+n)}(p)]$, where $M_{2n}(p_c)$ are the local field moments at percolation [19]. Using $g(p) < 1$, the limiting condition $M_{2n}(p) > M_{2n}(p_c)g^{4(1+n)}(p) > M_{2n}(p_c)$ is obtained, which implies that at p_c and for $n > 1$, the local field moments have a minimum. This simple reasoning based on the general properties of the SP eigenstates provides a qualitative explanation of the observed dip in the field moments as per Figure 3.

From Figure 4(a), it is also clear that for $p < p_c$ the localization lengths of the excited SP eigenstates, predominantly those with $\Lambda < 0$, is lower as compared to the critical case ($p = p_c$). This suggests that at noncritical metal concentrations the role of the localized states in the local field statistics becomes stronger. Moreover, since current conservation holds in all cases, one may expect maxima in $\rho(\lambda)$ and $\xi(\lambda)$ at noncritical metal concentrations as well, as shown in Figures 4(a) and 4(b). With the decrease of p , a shift in the DOS is observed with an increase of the number of eigenstates with positive eigenvalues. This phenomenon corresponds to the fact that the eigenproblem maps the underlying film geometry with positive eigenvalues corresponding to eigenstates situated mostly in the dielectric host. It should be pointed out that although Figure 4 presents only the results for $p < p_c$, the properties of the SP eigenstates at high and low metal concentrations are equivalent due to symmetry. Thus, the relationships $\rho(\Lambda, p_c + \Delta p) = \rho(\Lambda, p_c - \Delta p)$ and $\xi(\Lambda, p_c + \Delta p) = \xi(\Lambda, p_c - \Delta p)$ hold for any given $\Delta p \leq p_c$.

6. Behavior of the Slope of the Higher-Order Moments (M_{2n})

The increased contribution of the localized states at $p \neq p_c$, or alternatively the increase of SP delocalization at p_c , is revealed through the dependence of $\ln[M_{2n}(p)]$ on the order

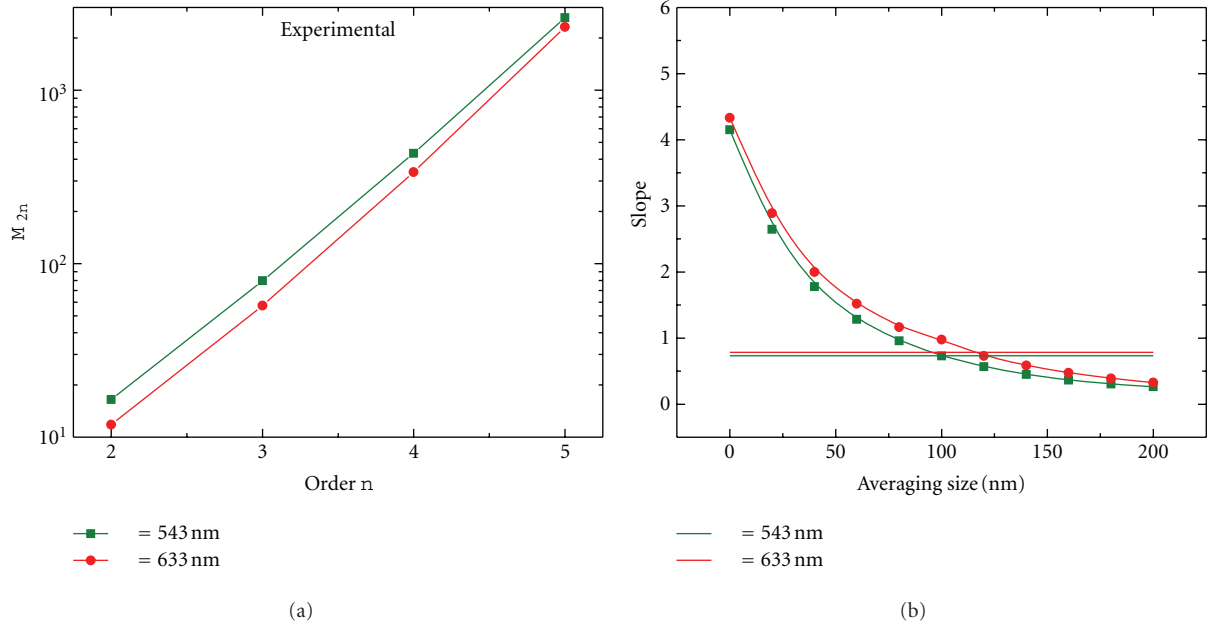


FIGURE 5: (a) Log-linear plot of measured high-order moments of near-field intensity enhancement M_{2n} versus n . (b) Slope of $\log(M_{2n})$ over n at the percolation threshold obtained numerically after spatial averaging versus averaging parameter d . The measured slopes are marked by horizontal lines with the standard error given in the legend [22, Figure 3].

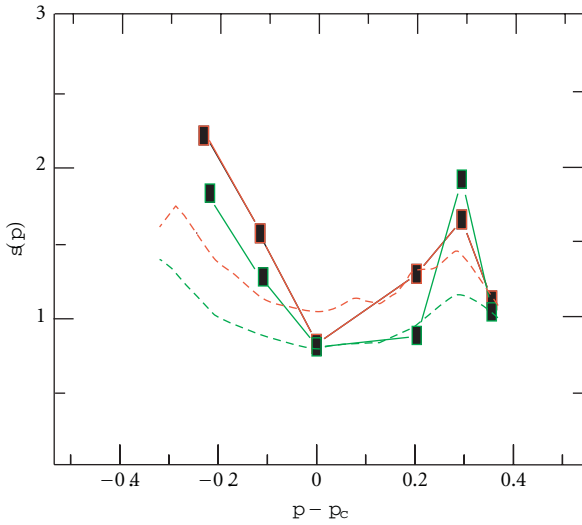


FIGURE 6: Slope versus metal concentration for numerical (dashed line) and experimental (solid line and square symbols) data. The wavelengths of the incident light are $\lambda = 543$ nm (green color) and $\lambda = 633$ nm (red color) [24, Figure 3].

n . According to the scaling theory described above, a linear dependence of the form $\ln[M_{2n}(p)] \sim 2ns(p)$ is to be expected, with the slope $s(p) = s(p_c) + 4 \ln[1/g(p)] \geq s(p_c)$ increasing for metal concentrations away from the percolation threshold. Figure 5(a) is a log-linear plot of the measured M_{2n} versus order n at p_c for two probe wavelengths 543 nm and 633 nm. Clearly, a linear dependence on the field moment n is observed. However, due to the limited NSOM

resolution, the slopes obtained experimentally were found to be considerably lower than those obtained numerically. To account for the effect of the finite spatial resolution in the experiment, the calculated local field distribution was first averaged over an area of dimension d , and then M_{2n} was computed to extract the slope of $\ln[M_{2n}(p)]$ versus n . Figure 5(b) shows that the slope decreases as d increases. When the slope is reduced to the experimental values (marked by horizontal lines), the averaging parameter d is found to be very close to the NSOM resolution limit estimated from the smallest features in the near-field images. The same value of d also leads to good agreement between the calculated $\text{var}(I)$ and the experimental data.

To extend this result for metal concentrations away from p_c , Figure 6 plots the slope as described above for various metal concentrations. In the calculations, the local field is again spatially averaged to account for the finite NSOM resolution. Figure 6 shows a similar trend with respect to p for both experiment and numerical calculations, with a clear minimum at p_c . Although the exact numerical values of the slope at $p \neq p_c$ cannot be easily interpreted based only on the SP eigenproblem, the observed increase in slope away from p_c clearly indicates a transition at p_c . The analysis following (3) suggests that stronger SP localization is favored at these metal concentrations, which leads to stronger local field fluctuations. The higher-order moments are more sensitive to those fluctuations, a fact that is manifested by the increase in the slope. It must be pointed out that for $p > p_c$, apart from the quasistatic SP modes caused by the sub-wavelength features in the system, the medium could support propagating surface waves and surface plasmon polaritons [20]. However, the local fields modulations that are associated with those propagating modes are weaker

compared to the quasistatic resonances and should have a relatively small effect on the local field distributions. This conclusion is indirectly supported by the good correlation between the numerical calculations and experiment.

7. Conclusion

The implications of the above statistical analysis in practical applications are wide-ranging. The high-order local field moments M_{2n} correspond to the enhancement of multiphoton optical processes due to the excitation of SP resonances in the substrate. For instance, M_4 relates to the electromagnetic enhancement of Raman-scattering provided that Raman active molecules are deposited on the metal surface. Since $M_{2n}(p) \geq M_{2n}(p_c)$, one may conclude that contrary to common practice, a highly effective surface enhanced Raman substrate can be achieved at low and high metal concentration. A similar conclusion can be made for the higher-order optical processes such as hyper-Raman scattering, Kerr optical nonlinearity, and n th harmonic generation.

To conclude, the near-field intensity statistics in semi-continuous silver films over a range of metal concentrations is effective in providing an overview of the various eigenstates supported by the film and the interplay between localized and delocalized SP eigenmodes. The variance of intensity fluctuations and the high-order moments of intensity enhancement exhibit local minima at the percolation threshold. Experimental observations, through theoretical corroboration, indicate a decrease of the SP localization in metal composites at critical concentrations with maxima in localization at concentrations away from the critical metal concentration. This effect runs opposite to the intuitive notion that stronger interactions lead to increase in localization. A possible explanation for this behavior is the existence of delocalized SP states, due to the local current conservation. Those states are present in the spectra for all metal concentrations and for metal-dielectric systems of any dimension. The possibility for this coexistence of both localized and delocalized SP modes has important ramifications in the understanding and applications of random metal films. Fine tuning the geometrical structure of the metal composites may allow for tuning of the localization properties of the excited SP modes, which may improve the enhancement of various linear and nonlinear optical processes.

Acknowledgments

Research partly supported by the U.S. Department of Energy, Basic Energy Sciences, Materials Sciences and Engineering Division, through Oak Ridge National Laboratory, U.S. Department of Energy (KS) and the Louisiana Board of Regents and NSF under Contracts nos. LEQSF(2011-14)-RD-A-18 and NSF(2010)-PFUND-20 (DAG).

References

[1] V. M. Shalaev, *Nonlinear Optics of Random Media*, Springer, Berlin, Germany, 2000.

- [2] D. A. Genov, A. K. Sarychev, and V. M. Shalaev, "Plasmon localization and local field distribution in metal-dielectric films," *Physical Review E*, vol. 67, no. 5, Article ID 056611, 10 pages, 2003.
- [3] D. Stauffer and A. Aharony, *Introduction to Percolation Theory*, Taylor & Francis, London, UK, 2nd edition, 1992.
- [4] V. M. Markel and T. F. George, Eds., *Optics of Nanostructured Materials*, John Wiley & Sons, New York, NY, USA, 2001.
- [5] D. P. Tsai, J. Kovacs, Z. Wang et al., "Photon scanning tunneling microscopy images of optical excitations of fractal metal colloid clusters," *Physical Review Letters*, vol. 72, no. 26, pp. 4149–4152, 1994.
- [6] S. Grésillon, L. Aigouy, A. C. Boccarda et al., "Experimental observation of localized optical excitations in random metal-dielectric films," *Physical Review Letters*, vol. 82, no. 22, pp. 4520–4523, 1999.
- [7] S. Ducourtieux, V. A. Podolskiy, S. Grésillon et al., "Near-field optical studies of semicontinuous metal films," *Physical Review B*, vol. 64, no. 16, Article ID 165403, pp. 1654031–16540314, 2001.
- [8] S. I. Bozhevolnyi, I. I. Smolyaninov, and A. V. Zayats, "Near-field microscopy of surface-plasmon polaritons: localization and internal interface imaging," *Physical Review B*, vol. 51, no. 24, pp. 17916–17924, 1995.
- [9] S. I. Bozhevolnyi, V. S. Volkov, and K. Leosson, "Localization and waveguiding of surface plasmon polaritons in random nanostructures," *Physical Review Letters*, vol. 89, no. 18, Article ID 186801, 4 pages, 2002.
- [10] A. K. Sarychev and V. M. Shalaev, "Electromagnetic field fluctuations and optical nonlinearities in metal-dielectric composites," *Physics Report*, vol. 335, no. 6, pp. 275–371, 2000.
- [11] M. I. Stockman, "Local fields' localization and chaos and nonlinear-optical enhancement in clusters and composites," in *Optics of Nanostructured Materials*, V. A. Markel and T. F. George, Eds., pp. 313–354, John Wiley & Sons, New York, NY, USA, 2000.
- [12] J. A. Sánchez-Gil, J. V. García-Ramos, and E. R. Méndez, "Near-field electromagnetic wave scattering from random self-affine fractal metal surfaces: spectral dependence of local field enhancements and their statistics in connection with surface-enhanced Raman scattering," *Physical Review B*, vol. 62, no. 15, pp. 10515–10525, 2000.
- [13] L. Zekri, R. Bouamrane, N. Zekri, and F. Brouers, "Localization and absorption of the local field in two-dimensional composite metal-dielectric films at the percolation threshold," *Journal of Physics Condensed Matter*, vol. 12, no. 3, pp. 283–291, 2000.
- [14] D. A. Genov, A. K. Sarychev, V. M. Shalaev, and A. Wei, "Resonant Field Enhancements from Metal Nanoparticle Arrays," *Nano Letters*, vol. 4, no. 1, pp. 153–158, 2004.
- [15] S. I. Bozhevolnyi and V. Coello, "Statistics of local field intensity enhancements at nanostructured surfaces investigated with a near-field optical microscope," *Physical Review B*, vol. 64, no. 11, Article ID 115414, pp. 1154141–1154147, 2001.
- [16] K. Seal, M. A. Nelson, Z. C. Ying, D. A. Genov, A. K. Sarychev, and V. M. Shalaev, "Growth, morphology, and optical and electrical properties of semicontinuous metallic films," *Physical Review B*, vol. 67, no. 3, Article ID 035318, 13 pages, 2003.
- [17] A. K. Sarychev, V. A. Shubin, and V. M. Shalaev, "Anderson localization of surface plasmons and nonlinear optics of metal-dielectric composites," *Physical Review B*, vol. 60, no. 24, pp. 16389–16408, 1999.
- [18] M. I. Stockman, S. V. Faleev, and D. J. Bergman, "Localization versus delocalization of surface plasmons in nanosystems: can

- one state have both characteristics?" *Physical Review Letters*, vol. 87, no. 16, Article ID 167401, 4 pages, 2001.
- [19] D. A. Genov, V. M. Shalaev, and A. K. Sarychev, "Surface plasmon excitation and correlation-induced localization-delocalization transition in semicontinuous metal films," *Physical Review B*, vol. 72, no. 11, Article ID 113102, 4 pages, 2005.
- [20] K. Seal, A. K. Sarychev, H. Noh et al., "Near-field intensity correlations in semicontinuous metal-dielectric films," *Physical Review Letters*, vol. 94, no. 22, Article ID 226101, 4 pages, 2005.
- [21] Y. Yagil, P. Gadenne, C. Julien, and G. Deutscher, "Optical properties of thin semicontinuous gold films over a wavelength range of 2.5 to 500 μm ," *Physical Review B*, vol. 46, no. 4, pp. 2503–2511, 1992.
- [22] K. Seal, D. A. Genov, A. K. Sarychev et al., "Coexistence of localized and delocalized surface plasmon modes in percolating metal films," *Physical Review Letters*, vol. 97, no. 20, Article ID 206103, 2006.
- [23] M. Kunz, G. A. Niklasson, and C. G. Granqvist, "Optical and electrical properties of sputter-deposited Al films close to the percolation threshold," *Journal of Applied Physics*, vol. 64, no. 7, pp. 3740–3742, 1988.
- [24] D. A. Genov, K. Seal, X. Zhang et al., "Collective electronic states in inhomogeneous media at critical and subcritical metal concentrations," *Physical Review B*, vol. 75, no. 20, Article ID 201403, 2007.
- [25] M. Gadenne, P. Gadenne, and J. Lafait, "Infrared optical absorption and fractal structure of granular media at percolation," *Optics Communications*, vol. 71, no. 5, pp. 273–278, 1989.
- [26] F. Brouers, J. P. Clerc, G. Giraud, J. M. Laugier, and Z. A. Randriamantany, "Dielectric and optical properties close to the percolation threshold. II," *Physical Review B*, vol. 47, no. 2, pp. 666–673, 1993.
- [27] J. B. Pendry, "Negative refraction makes a perfect lens," *Physical Review Letters*, vol. 85, no. 18, pp. 3966–3969, 2000.
- [28] R. A. Shelby, D. R. Smith, and S. Schultz, "Experimental verification of a negative index of refraction," *Science*, vol. 292, no. 5514, pp. 77–79, 2001.
- [29] N. Fang, H. Lee, C. Sun, and X. Zhang, "Sub-diffraction-limited optical imaging with a silver superlens," *Science*, vol. 308, no. 5721, pp. 534–537, 2005.
- [30] Y. Lu, G. L. Liu, and L. P. Lee, "High-density silver nanoparticle film with temperature-controllable interparticle spacing for a tunable surface enhanced Raman scattering substrate," *Nano Letters*, vol. 5, no. 1, pp. 5–9, 2005.
- [31] X. Xu, K. Seal, X. Xu et al., "High tunability of the surface-enhanced Raman scattering response with a metal-multiferroic composite," *Nano Letters*, vol. 11, no. 3, pp. 1265–1269, 2011.
- [32] J. E. Rowe, C. V. Shank, D. A. Zwemer, and C. A. Murray, "Ultrahigh-vacuum studies of enhanced Raman scattering from pyridine on Ag surfaces," *Physical Review Letters*, vol. 44, no. 26, pp. 1770–1773, 1980.
- [33] K. Kneipp, Y. Wang, H. Kneipp et al., "Single molecule detection using surface-enhanced Raman scattering (SERS)," *Physical Review Letters*, vol. 78, no. 9, pp. 1667–1670, 1997.
- [34] T. V. Teperik, F. J. García De Abajo, A. G. Borisov et al., "Omnidirectional absorption in nanostructured metal surfaces," *Nature Photonics*, vol. 2, no. 5, pp. 299–301, 2008.
- [35] C. Hu, Z. Zhao, X. Chen, and X. Luo, "Realizing near-perfect absorption at visible frequencies," *Optics Express*, vol. 17, no. 13, pp. 11039–11044, 2009.
- [36] V. N. Pustovif and G. A. Niklasson, "Observability of resonance optical structure in fractal metallic clusters," *Journal of Applied Physics*, vol. 90, no. 3, pp. 1275–1279, 2001.
- [37] P. W. Anderson, "Absence of diffusion in certain random lattices," *Physical Review*, vol. 109, no. 5, pp. 1492–1505, 1958.

Review Article

Gap Nanoantennas toward Molecular Plasmonic Devices

Aude L. Lereu,¹ Jacob P. Hoogenboom,² and Niek F. van Hulst^{3,4}

¹ CINaM-CNRS, Campus de Luminy, 13288 Marseille, France

² Department of Imaging Science and Technology, Faculty of Applied Sciences, Delft University of Technology, Lorentzweg 1, 2628 CJ Delft, The Netherlands

³ ICFO—Institut de Ciències Fotòniques, Mediterranean Technology Park, Castelldefels, 08860 Barcelona, Spain

⁴ ICREA—Institut Catalana de Recerca i Estudis Avançats, 08015 Barcelona, Spain

Correspondence should be addressed to Aude L. Lereu, lereu@cinam.univ-mrs.fr

Received 30 September 2011; Revised 16 December 2011; Accepted 16 December 2011

Academic Editor: Ali Passian

Copyright © 2012 Aude L. Lereu et al. This is an open access article distributed under the Creative Commons Attribution License, which permits unrestricted use, distribution, and reproduction in any medium, provided the original work is properly cited.

Recently we have demonstrated that single fluorescent molecules can be used as non-perturbative vectorial probes of the local field. Here, we expand on such experiments exploiting fluorescence lifetime of single molecules to probe various types of gap nanoantennas. First, studies of the nanoantennas are carried out to evaluate the electric field. We then investigate hybrid systems composed by nanoantennas and randomly positioned fluorescent molecules. Finally, we present a fabrication scheme for the controlled placement of fluorescent molecules at welldefined positions with respect to the dimer nanoantenna, which is a more direct route to probe the local field in an *a priori* determined way.

1. Introduction to Gap Nanoantennas: Dimers and Nanorods

Metallic nanoantennas (also called optical antennas) have been, over the past ten years, at the heart of numerous investigations ([1–7] and references therein) due to their optical properties, like strong enhancement and subwavelength confinement of the electrical field [8–17]. The coupling between photons and electrons in these nano-objects is the origin of their extraordinary optical properties. In such 3D structures, the electrons oscillate with (spatial) periods smaller than the wavelength of the incident photons, raising plasmon resonances. Such resonances can then give rise to a strongly localized field enhancement. In addition, nanoantennas permit to couple propagative optical waves into evanescent waves and vice versa. They are therefore promising as intermediary between nanoscale optical and electronic devices and optical fields. Their applications include different fields such as nanoscale imaging and spectroscopy [18–25], light-emitting devices [26–31], photovoltaics [32–41], microfluidics [42, 43], and metamaterials in the infrared [44, 45].

Here, we concentrate on gap nanoantennas that can be defined as two symmetric metallic particles (of specific

shape and size) separated by a fabricated gap ranging from no gap up to a few tenths of nanometers. In the particular case of gap nanoantennas, the field enhancement and resonance modes have been theoretically predicted [46–57] and experimentally studied [8–17, 58–64]. Numerous works have been reported on luminescence spectroscopy of gold nanoparticles such as nanorods [9, 10, 58] and dimers [12, 57, 60, 61] (see Section 3). Two-photon luminescence (TPL) has also been employed and proven particularly sensitive to local fields near metallic nano-objects [12, 58]. Moreover, TPL spectroscopy permits to measure the plasmon resonances of such nanostructures by evaluating the TPL as a function of excitation wavelengths [61, 62]. Near-field scanning optical microscopy (NSOM) is also extensively used to explore such nano-objects either by locally mapping the field enhancements [9, 10, 25, 63, 64] or by grafting an individual nanoantenna at the apex of an NSOM probe [65–70]. However, in these studies, the influence of the near-field probe onto the nanostructures can induce a complex coupling response which has to be taken into account. In particular, plasmonics mode detailed mapping of nanoantennas has been achieved with “apertureless” NSOM using Si-tips [71–74]. Other studies have also looked

at the fundamental understanding of resonant processes in such nanostructures by means of Raman imaging [75–77] or nonlinear effects [78]. In parallel, analytical and numerical models have been developed in an approach to unify the experimental observations [46–54].

Finally, one alternative approach to study nanoantennas, is to probe their near fields using single molecules (SM) [79–81]. By doing so, one can access the local mapping of the nanoantenna fields in a nonperturbative way. Furthermore, integrating SM together with metallic nanoantennas is an ultimate step in terms of applications for the technological miniaturization drive. In most cases, the functionality of SM is inherently defined by the electronic or optical properties of the molecules. However, the construction of active molecular-scale devices often requires embedding the molecule in a nanostructured environment that provides a means to address, tailor, or control the molecular functionality. Gap nanoantennas are particularly promising interfaces, because of their strongly localized electromagnetic field modes, both in the spatial and the frequency domain. Consequently, the emerging field of molecular plasmonics [82] holds great promise for applications in areas like sensing, light harvesting and energy conversion, single-photon sources, all-optical components, and electronic-optical interfacing. However, a major task remains in the mutually well-defined positioning of both functional molecules and metallic nanostructures with nanometer-scale precision. Different approaches have been developed relying on random deposition of functional molecules, for example, by spin-coating [83], bulk overcoating of a metallic structure [84], or plasmonic micropositioning [42, 43]. In highly symmetric nanoparticle systems, one degree of positional control has been achieved by employing a spacer layer that can be functionalized [85–87]. The full exploitation of molecular functionality requires localized and designed molecular positioning at arbitrary locations with respect to a tailored plasmonic nanostructure. Recently, encouraging progress in this direction has been made by double e-beam lithography, positioning a single quantum dot on the feed element of an array antenna [88].

Here, we will describe the full characterization of antennas needed to realize resonant nanoantenna structures overcoated with low (“single molecule”) concentrations of fluorescent molecules. This characterization serves to extract the individual optical response of the nanoantennas in an effort to match the fluorescence spectra of molecules. Parts of this work have been described previously [63, 64, 79]. After these introductory results, we will present fluorescence measurements on nanoantennas overcoated with ultralow concentrations of molecules. We will address measurement of the fluorescence lifetime, to map the local density of states around the nanoantennas [80], in direct competition with the intrinsic luminescence of the antennas. Finally, a fabrication procedure that allows for the controlled positioning of molecules with respect to the antenna, together with initial related results, will be presented.

The subject matter is divided over the various sections in the following way: in Section 2, we introduce the nanoantenna samples (dimer and nanorod arrays), explaining the

fabrication process and characterizing their spectroscopic response. In Section 3, we describe one photon luminescence of dimer antennas. These first two sections lay the basis to first evaluate the optical response of the nanoantennas, without (dye) molecules but under excitation conditions typical for single-molecule spectroscopy. In Section 4, we discuss the response of randomly scattered single molecules over dimers. Finally, molecular probing will be refined using a well-controlled molecular probing in Section 5. Section 6 gathers our conclusions.

2. Nanofabrication and Spectroscopic Insights of Gold Dimers and Nanorods Arrays

The nanoantenna electromagnetic response is known to depend highly on size, geometry, and even chemical treatment. A large panel of sizes, shapes, and compositions has therefore been fabricated at the nanoscale either by bottom-up colloidal chemistry [89–94] or by top-down nanofabrication techniques [11, 61–64, 95, 96] with the use of electron beam lithography or ion beam milling. A multitude of shapes is emerging offering a wide range of field pattern and strength. Here, we will report on dimer and nanorod-like structures.

The parameters specifying the geometry of the dimer and nanorod-like structures are the aspect ratio (AR), defined as the ratio of length to width, the gap separation distance between the two nanoparticles constituting the gap nanoantenna, and the thickness. The single nanoantennas in these studies have an AR in the range from 1.0 (dimers) to 4.5 (nanorods), as illustrated in insets of Figure 1. We mainly kept the width around 100 nm and varied the length of the structures. The different fabrication steps are depicted in Figure 1. We used conventional e-beam lithography (FEI-QUANTA 200 electron microscope associated with a Raith ELPHY) and metal depositions followed by a lift-off process to realize periodic arrays ($100 \times 100 \mu\text{m}$) of nanoantennas. Prior to any investigation, we calculated the spectroscopic response (in the excitation wavelength range of 400 nm to 700 nm) for the given geometry and performed far-field spectroscopic measurements on the arrays of fabricated nanostructures. This is illustrated in Figure 2 for the dimers and Figure 3 for the nanorods.

In this section, we focus on and quantify the different resonant modes in the visible, a spectral range spanned by our excitation sources. Therefore, we carried out local spectroscopic measurements on distinct arrays of nanoantennas, under white light illumination and two orthogonal linear polarization states. Throughout this paper, the p-polarization state will be referred to as the polarization excitation along the long axis of the structures, whereas the s-polarization state will be associated with the perpendicular one. In parallel, we have calculated the specific spectral response at the gap region of an individual pair of nanoantennas for each involved AR. While the presented 2D simulations (insets of Figures 2 and 3) seek to illustrate the overall field distribution under defined excitation conditions (polarization state and excitation wavelength), it is not to be directly confronted to the measurements.

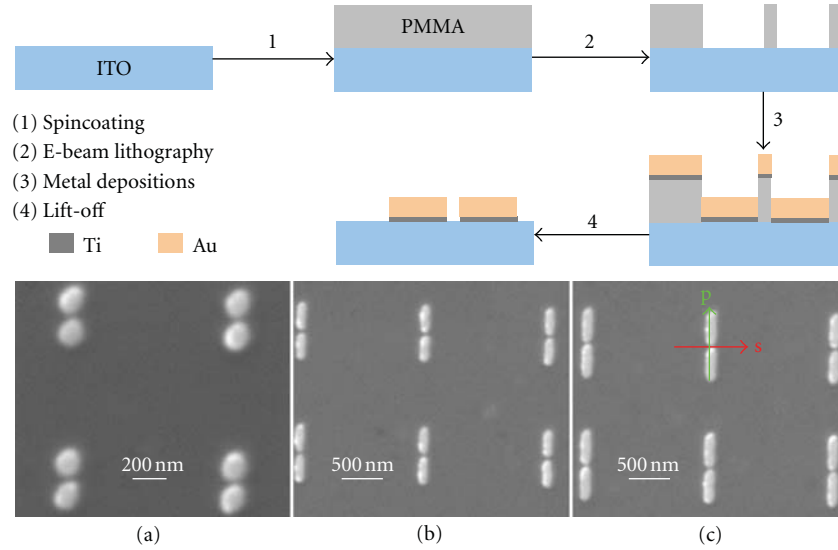


FIGURE 1: Fabrication steps of nanoantenna arrays using e-beam lithography and metal depositions. SEM images of selected nanoantenna arrays, used in the reported studies, are presented in (a) for dimers, and in (b) and (c) for nanorods with different lengths and therefore different ARs. The arrows in (c) define the used excitation polarizations, with p-polarization along the long axis of the nanostructures and s-polarization perpendicular to the long axis.

In Figure 2, the measured scattering spectra of dimers, for both excitation s and p-polarization states, and the calculated spectral response of an individual dimer are displayed. Under p-polarization excitation, the measured peak is close to 635 nm, while the calculation presents a peak at around 655 nm. This experimental blue shift may be explained both by geometrical variations occurring during the fabrication process and by substrate effects. The numerical work was carried out for a single dimer in free standing space. Under s-polarization excitation (electric field perpendicular to the dimer axis), a very weak peak centered on 599 nm is observed. For this wavelength, the simulation does not present any peak as the field distribution is mainly located at the edges of the dimers and not in the gap from where the calculated spectrum is extracted. Finally, secondary peaks are predicted at around 500 nm for both polarization states but were not experimentally observed. Neglecting the effect of the substrate as well as retardation effects (more pronounced for shorter wavelengths) in the simulation may explain the discrepancy over these auxiliary peaks.

In Figure 3, theoretical spectra are presented for nanorods for each excitation polarization state, both in the nonretarded (continuous lines of Figures 3(a) and 3(b)) and the retarded regime (Figures 3(c) and 3(d)). In the retarded regime, the results are the solutions of the wave equation, whereas in the nonretarded regime, the time dependence has been neglected. The experimental spectra are included in Figures 3(a) and 3(b) (dashed lines). Note that the different nanorods' lengths are highlighted in the colors of the curves, red for the 150 nm long, blue for the 350 nm, and green for the 450 nm. For the p-polarization state, a 2- to 4-fold enhancement, defined as the ratio of the electric field in the presence and in the absence of the nanoantennas, is reached, both theoretically (in the retarded

regime) and experimentally. The theoretical values obtained in the quasistatic regime are much higher, apart for the case of a nanoantenna with an AR of 1.5. This is to be expected as the time dependence becomes more important for structures with increasing sizes where the distances can be larger than the excitation wavelength. This is actually illustrated in Figure 3 where the two models can be directly compared. One can see that for the 150 nm long rods the quasistatic and retarded responses are similar, whereas for the 450 nm long rods, this does not hold anymore. Furthermore, if we now compare simulations in the retarded regime with the experiment, we see that the experimentally observed intensities are mainly higher than the simulated ones. This observation can also be rationalized by the contribution of the additional field imaged on the edges of the structures during the measurements or in the field distributions. However, the theoretical spectra concentrate only on the electric field in the gap.

Under s-polarized excitation, the gap region, for each considered AR, shows no predicted field enhancement, except in the retarded regime for the 450 nm long rods in the 465 to 510 nm spectral range. Indeed, an up to 2-fold enhancement is then expected. Experimentally, we obtain a resonance peak around 465 nm for the 450 nm long rods. For the 350 nm and 150 nm long rods, the peaks are centered at 462 nm and 460 nm, respectively, with corresponding enhancement factors between 2 and 4. The differences (in terms of peak wavelength and enhancement factor) with the simulation may result from fabrication inhomogeneities and/or from the fact that the experimental values are retrieved after integration of the field in a region encompassing the whole structure instead of the gap alone. This is also predicted as seen in the insets representing the total field distribution at the point B of Figure 3, where

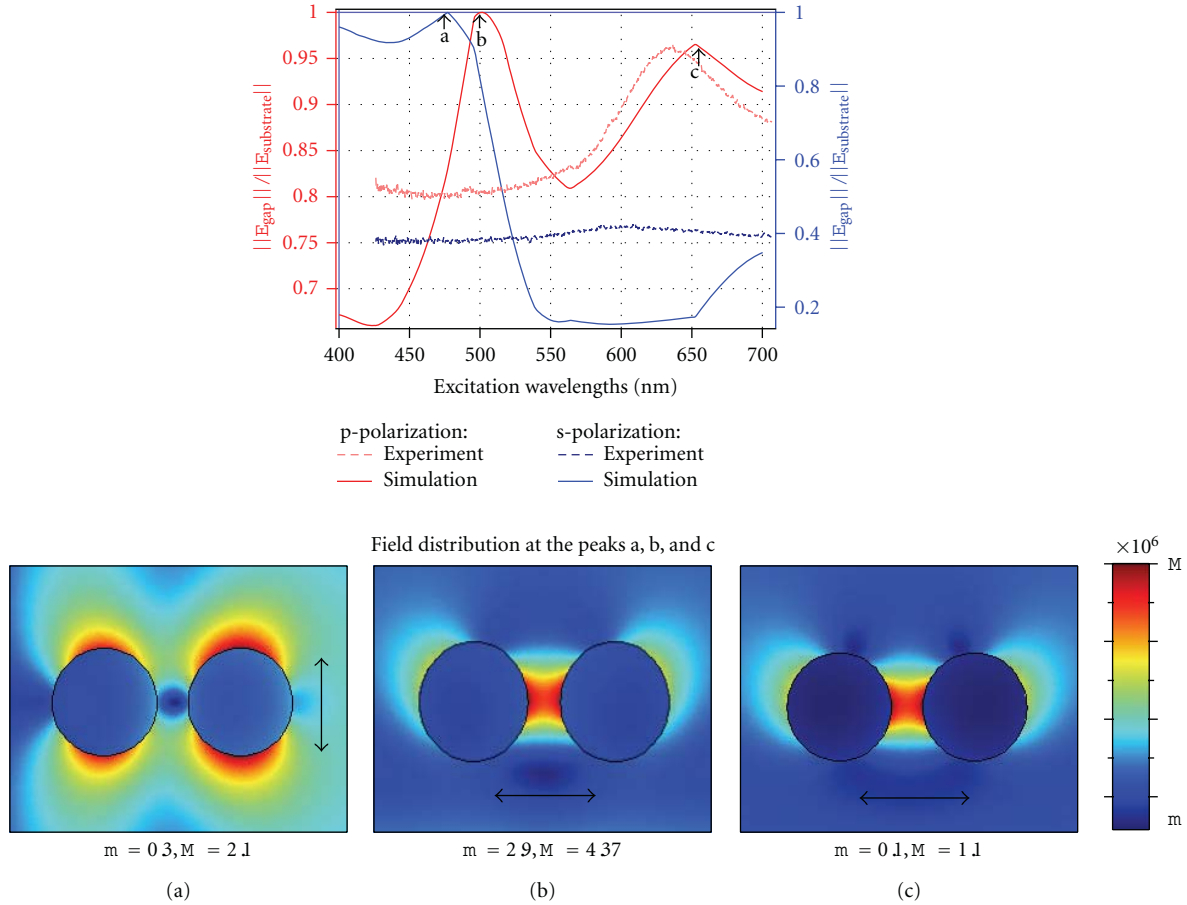


FIGURE 2: Theoretical and experimental spectra of the electric field and extinction for dimers (particles with 100 nm diameter) with 30 nm gap. The (a) to (b) labels indicate the excitation parameters where resonances occur. These are then used in the corresponding insets to display the field distribution under these excitation conditions. The insets (a) to (c) depict the total field fingerprint for each spectral peak (black arrows show the polarization state), to illustrate the resonances and local field enhancement around the dimers.

the strongest fields are mainly located at the edges of the structures and not in the gap.

By linking the geometrical parameters of the nanoantennas with their optical responses, the presented spectroscopic studies served as a guide for subsequent experiments. In the following, we will present experiments aimed at mapping the luminescence distribution in the vicinity of the nanoantennas as a function of incident polarization. These experiments will allow acquiring a complementary insight into the optical response of the nanoantennas. The knowledge of predicted electric fields, presented in the insets of Figures 2 and 3, will assist the analysis of the experimental results.

3. Luminescence of Dimers under Pulsed Excitation

In this section, we present one-photon excitation photoluminescence measurements on nanoantennas. The influence of the polarization state is explored by illuminating the nanoantennas with both p and s-polarized light. As already mentioned, p-polarized incident light is polarized along the

long axis of the dimers, whereas s-polarized incident light is polarized perpendicular to the dimer axis. A comparison between an optimal dimer gap of 30 nm (also referred to as resonant case) and no gap (nonresonant case) is also given.

As mentioned in Section 2, samples were made by e-beam lithography and metal deposition. The sample design consists here of several $100\ \mu\text{m} \times 100\ \mu\text{m}$ arrays of gold nano-objects forming either a dimer or a single particle (monomer) as illustrated in Figure 4(a). In order to make an unambiguous distinction between dimers and monomers in the optical experiments, the global array was fashioned by alternating three lines of dimers and two of monomers. The diameter was chosen as 100 nm and the height as 40 nm, for an optimum gap of 30 nm [23]. Finally, in order to observe any gap effect, similar arrays of dimers with no gap, shown in Figure 4(b), were studied in parallel. The geometric parameters of the gold particles were chosen so that the dimers would be resonant at around 635 nm (see scattering spectrum in Figure 2). The choice of the 635 nm resonant wavelength was aimed at matching the absorption spectrum of the molecular species used

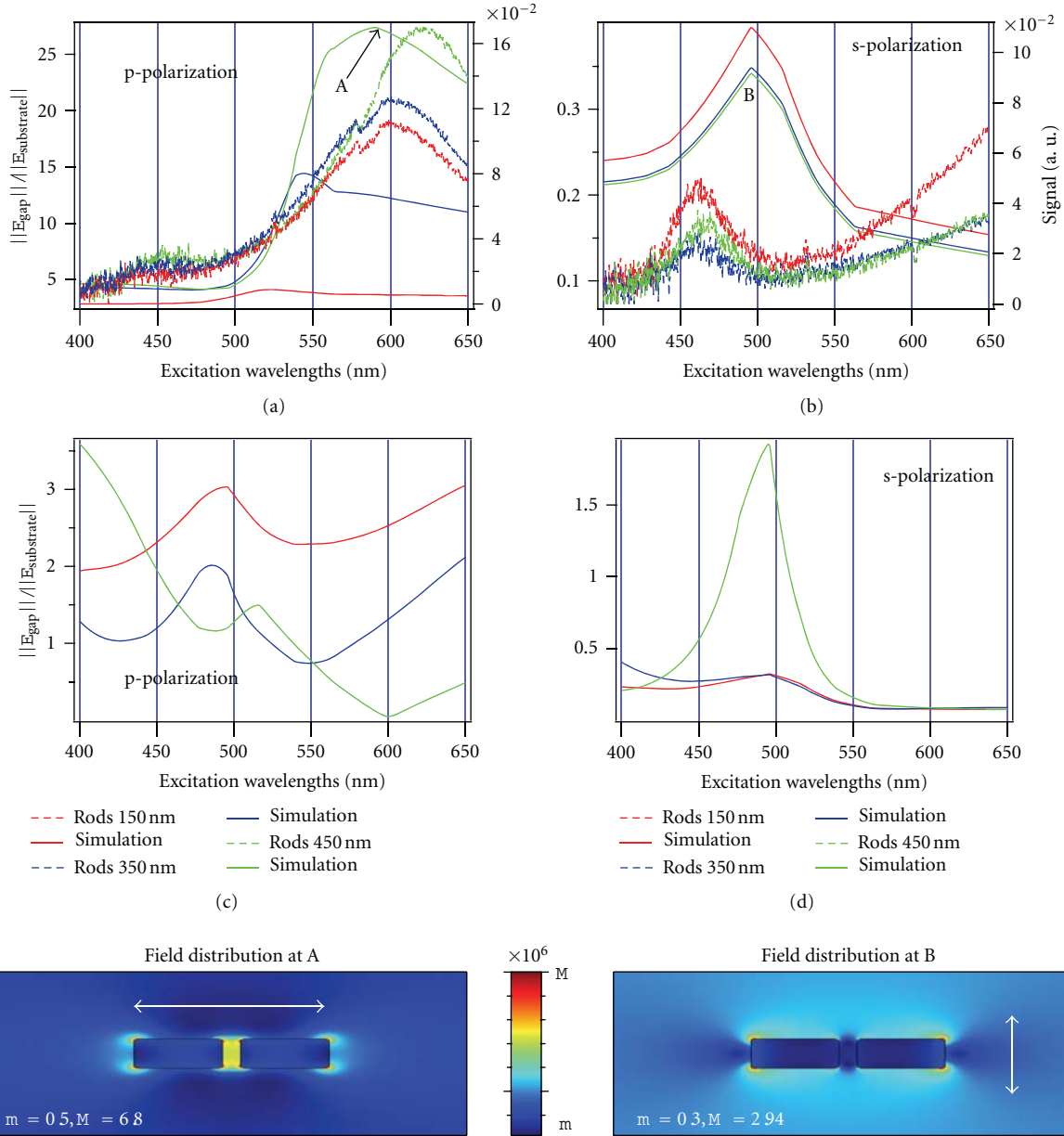


FIGURE 3: Theoretical and experimental spectra of the electric field intensity and extinction for antennas made of nanorods of different lengths and with 30 nm gap. (a) and (b) Plot the experimental and theoretical spectra (in the quasistatic regime), while (c) and (d) show the theoretical spectra in the retarded regime. All spectra are depicted for both excitation polarization states. Note that the theoretical curves depict the electric field in the gap of the structures, whereas the data represent the response of the total structure. The two insets give the total electric field distribution for the 450 nm long rods at the peaks A (at 580 nm) and B (at 500 nm). The white arrows indicate the considered polarization.

as a probe, here DiD (1,1'-dioctadecyl-3,3,3',3'-tetramethylindodicarbocyanine), a photostable molecule commonly used in single-molecule studies.

Luminescence measurements on individual dimers (and monomers) were carried out using a confocal microscope, as shown in Figure 5. A confocal scanning fluorescence microscope with a high numerical aperture (1.3 NA) objective was equipped with two avalanche photodiodes (APDs) detecting the respective (p & s) cross-polarizations using

a polarizing beam splitter [63, 64]. The excitation source was chosen to be a picosecond (ps) laser (90 ps pulses at 20 MHz repetition rate, average power density $\sim 34 \text{ kW/cm}^2$ at $\lambda_{\text{exc}} = 635 \text{ nm}$). The emitted luminescence from the nanostructures (see examples in inset (c) of Figure 5) was collected by the same objective and then directed to the two APDs after discrimination from the excitation light by an appropriate dichroic mirror and a long pass filter. Thereafter, the two luminescence images obtained via the two different

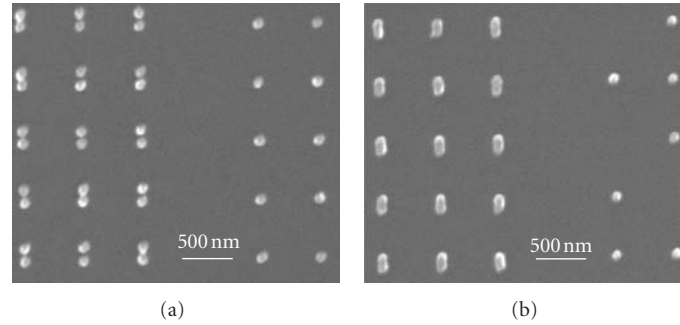


FIGURE 4: SEM images of the specifically designed samples. Alternations between three lines of the investigated dimers and two lines of reference monomers are made. All nanoparticles are 100 nm in diameter. In (a), the dimer's separation gap is 30 nm, and in (b) the dimers have no gap (i.e., contact). The mutual distance between two dimers (center to center) is fixed at 600 nm in both directions.

APDs are recombined to result in a polarization-dependent luminescence image (as insets (d) and (e) of Figure 5). Finally, to simultaneously detect the transmitted excitation light through the sample, a photodiode was mounted on the opposite side of the high NA objective, above the sample plane. An example of such a transmitted image ($10 \times 10 \mu\text{m}$) is given in the inset (a) of Figure 5, where the series of two lines of black dots are associated with the gold monomers, and the series of three black lines are associated with the dimers. The center to center dimer separation of only 600 nm is only slightly larger than the diffraction limit of the confocal microscope, which prevents from fully resolving two neighboring dimers. As a result, the dimers appear as a semicontinuous black strip with dots in the transmission image. Note that the same experimental setup was utilized as a basis for all the results reported further.

The luminescence (Figure 6 and insets (d) and (e) of Figure 5) is always recorded simultaneously with the transmission signal (inset (a) of Figure 5) to ensure the monomers' positioning with respect to the dimers on the luminescence images. Figure 6 outlines the luminescence images as a function of the excitation polarization and the gap size. The color scale gives the polarization state of the detected luminescence going from green pixels for "pure" p-polarization (i.e., along the dimers axis) to red pixels for "pure" s-polarization. The yellow color represents an equal contribution of both p- and s-polarization components. From these images, one can extract different aspects. First, the (expected) isotropic emission in polarization of the monomers is clearly highlighted from its yellow appearance (i.e., $p = s$) on each image. Next, compared to this isotropic emission, the luminescence from the dimers is predominantly p-polarized (green appearance). However, a large variation in luminescence intensity from one nanoantenna to another is observed. This can be mainly explained by the variation in shape and size of each gold particle as introduced by the fabrication process. To take into account the variability between antennas, we made a statistical analysis over the nanoparticles designed to be identical. This statistical analysis serves to study the optical response of metallic structures as a function of fabrication uncertainties.

According to the first qualitative observations on the resonance behavior of such nanoantennas, we oriented the first statistical analysis to extract the peak intensity for each luminescent spot on each image. An intensity distribution is therefore excerpted for the case of a 30 nm gap, and no gap (see columns in Figure 6), and for p- and s-excitation polarizations (see rows in Figure 6). Similar studies on the monomers served as a reference for polarization effects and allowed the suppression of possible substrate effects. The resulting histograms are depicted in insets (a_2-d_2) of Figure 6 for the dimers and insets (a_3-d_3) for the monomers. We thus confirmed the isotropic behavior of the monomers, where the polarization ratio (i.e., the ratio of the p-detected over the s-detected polarization) is extracted to be around unity for both p- and s-polarized excitation.

For the dimers with the two considered gap sizes, the luminescence distribution is shifted toward the higher intensity values for the p-polarized luminescence (with respect to the s-polarized luminescence). This is valid for both excitation polarizations, but the effect is more pronounced for the resonant case (i.e., dimers with a 30 nm gap) with p-polarized illumination and p-polarized detection. This is expected as the localized plasmon excitation is involved in the process as illustrated, in the insets of Figure 2, by the electric field amplitude in the near field of the dimers. Indeed, for the 30 nm gap, the p-polarized excitation leads to a strong coupling between the local charges of each gold particle constituting the nanoantenna. By opposition, the local charges of the individual particles are independently excited under s-polarized excitation. For the no gap dimers, we made similar observations. However, the strong coupling for p-polarized excitation is far less pronounced. This is foreseen as the particles do not couple with each other but act as a unique elongated particle.

In a second statistical analysis, we concentrated on the polarization ratio distribution extrapolated from the luminescence peaks in Figure 6. The polarization ratio is defined as the ratio of the p-polarized over the s-polarized luminescence intensity. We seek here to quantify the polarization effect using the polarization ratio. This is illustrated in Figure 7(a) for the 30 nm gap dimers and (b) for the

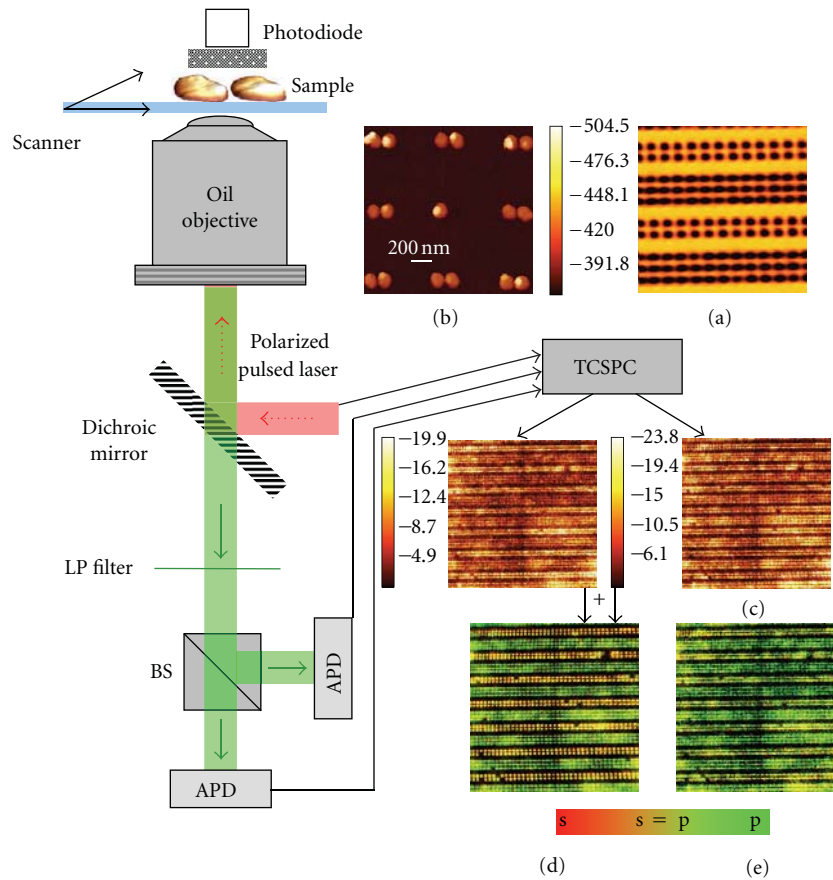


FIGURE 5: Confocal microscope with single-molecule detection capability. A pulsed laser serves as the excitation light incident on the sample via a dichroic mirror and an oil immersed objective (numerical aperture 1.3). The luminescence EPI-generated by the sample is collected through the objective, and then directed through the dichroic mirror and long-pass (LP) filters toward the detectors. The detectors are avalanche photodiodes (APDs), detecting the two crossed-polarization components of the luminescence. These components are formerly separated by a polarizing beam splitter (BS) and recorded via a time-correlated single-photon counting (TCSPC). A photodiode is also placed above the sample, to collect simultaneously the transmitted field as in (a). The piezo scanner, associated with the feedback controller, allows acquiring point-by-point images in the xy -plane of the sample, as illustrated by the two images in (c). A composed image from the images in (c) is then generated for p- (inset d) and for s-polarized (inset e) excitation. The inset (b) is a selected AFM image of one of the explored samples.

no-gap ones. In Figure 7(a), the polarization ratio ranges between 1.2 and 5.7 for p-polarized excitation and between 1.2 and 2.4 for s-polarized excitation, whereas in Figure 7(b), the polarization ratio ranges between 1.3 and 2.9 for p and between 1.1 and 2.5 for s-polarized excitation. This leads to an average ratio for the 30 nm gap of 3.1 for p-polarized excitation against 1.6 for s-polarized excitation, whereas in the no-gap case, the average is 1.8 for p against 1.4 for s.

An averaged 3-fold enhancement is hence shown with respect to the monomers (close to unity, independently of the excitation polarizations), exhibiting a maximum 6-fold enhancement, for some of the dimers. This is in agreement with the reported 100-fold enhancement using two-photon luminescence on bowties [11] and the 10-fold enhancement measured in TPL [61]. The weaker increase also observed for the nonresonant case with p-polarized excitation may be attributed to the elongated shape of the

dimers. For s-polarized excitation, no noticeable difference is seen with respect to the gap size. This can be explained by the excitation of two independent dipoles that do not interact. Furthermore, this statement is reinforced by the actual measurement of values close to 1 in the s-polarized detected luminescence, approaching the monomer behavior.

To conclude, luminescence of dimer-like nanoantennas was measured under picosecond pulsed excitation at relatively high excitation power compared to typical fluorescence measurements, highlighting (i) the low intrinsic luminescence of the nanoantennas and (ii) the wide distribution from one antenna to another. The effect of excitation polarization and gap size was also investigated. This preliminary study provided insights into understanding the local response of such metallic nanoantennas and may help to understand the nanoantenna-single molecule coupling, as reported below.

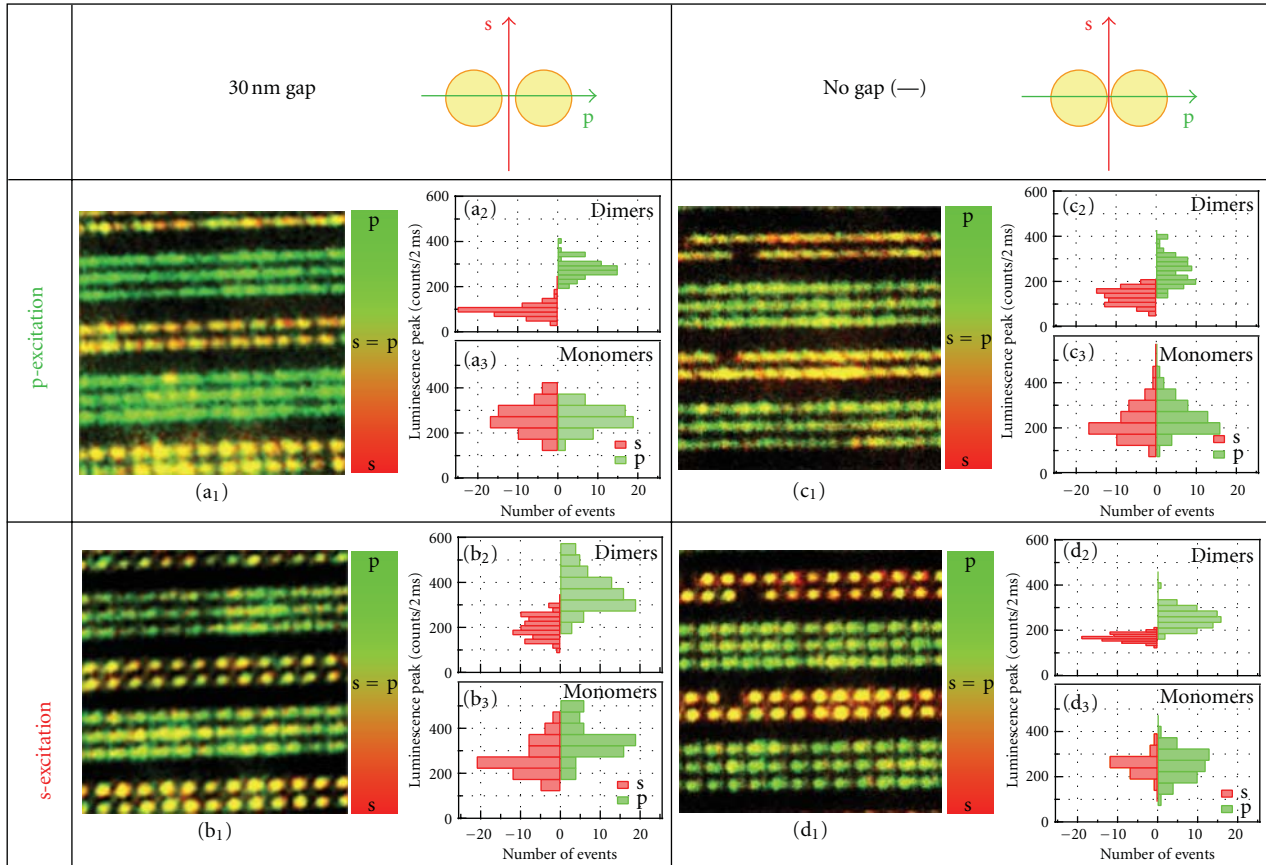


FIGURE 6: Luminescence measurements of single gold dimers with a gap of 30 nm (a and b) and with no gap (c and d). The figures (a and c) illustrate the luminescence of the structures when illuminated with p-polarized light (i.e., parallel to the long axis of the dimers). Figures (b and d) show the same results for s-polarized excitation light (perpendicular to the dimer axis). (a₁ to d₁) Show luminescence images of a $10 \times 10 \mu\text{m}$ scanned area. The color scale gives the polarization state of the detected field. (a₂ to d₂) and (a₃ to d₃) Show distribution of the luminescence peak for dimers (over 60 dimers were considered for each case) and monomers (over 50 monomers were considered for each case), respectively.

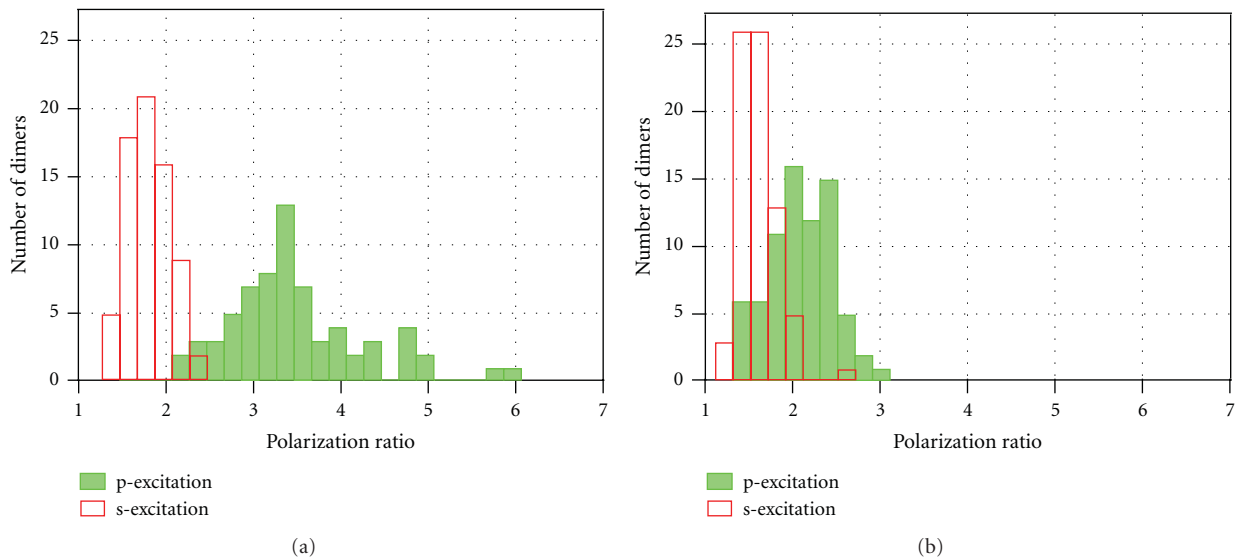


FIGURE 7: Distribution of the polarization ratio in detection (p-polarized over s-polarized luminescence) for about 60 dimers illuminated under p- or s-polarized light. (a) is for the dimers with 30 nm gap and (b) for the dimers with no gap.

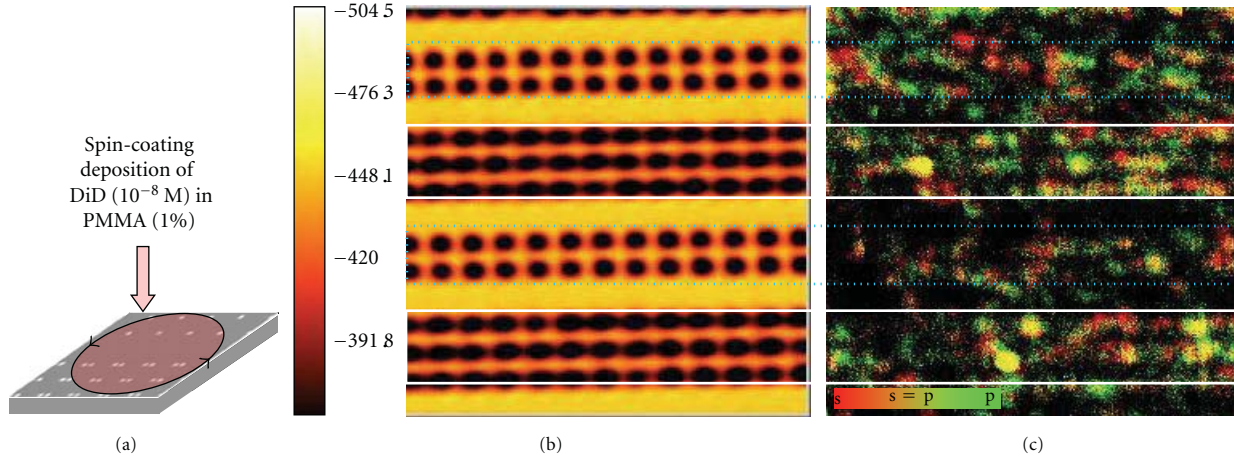


FIGURE 8: (a) Scheme of a random deposition of molecules over samples as described in Figure 4(a). (b) Optical transmission microscopy image and (c) fluorescence microscopy image. The white and blue squares highlight the dimer and monomer regions, respectively. The color scale in (c) indicates the polarization as given in Figure 6.

4. Fluorescence of Molecules at Metallic Nanoantennas

After imaging the luminescence of individual nanoantennas, we exploit single fluorescent molecules as nonperturbative vectorial point detectors to map the local photonic density of states, with nanometric precision [97]. We have previously demonstrated this procedure for a metal Fabry-Pérot-like cavity [80]. In that study, the measured spatial fluorescence lifetime variations were shown to map the local density of states inside the cavity, provided intrinsic molecular lifetime variations were taken into account. Hereto, individual fluorophores are randomly spread over the sample and are studied in terms of molecular position, orientation, and fluorescence brightness.

As already mentioned in Section 2, the plasmon resonances in metallic nanoantennas are associated with an absorption peak and a localized field enhancement. The proximity of a metallic nanoantenna or nanostructured film is likely to affect the excitation and emission processes of a fluorophore, especially under the plasmon resonance conditions.

In this section, we use the fluorophore properties to probe the local field of the metallic gap nanoantennas. The optical characterization was carried out using the same home-built inverted confocal microscopy setup with single-molecule sensitivity described in Section 3. The samples were excited using a pulsed laser (90 ps, 20 MHz repetition rate, 1 kW/cm^2) at a wavelength of 635 nm, optimum to the excitation spectrum of the fluorophore and at a power considerably lower than in Section 3. The collected fluorescence light was separated from the excitation beam using a dichroic mirror and a long-pass filter assembly and subsequently split into two orthogonal polarization directions, each of which was focused onto the detection area of an APD. Transmitted light was simultaneously detected using a photodiode to identify the dimer series from the monomers as in Section 3

and Figure 8(b). On the previously studied nanoantennas arrays, a solution of DiD (1,1'-dioctadecyl-3,3,3',3'-tetramethylindodicarbocyanine) molecules in a PMMA (polymethyl methacrylate) matrix was then spin-coated over the nanoantennas, as seen in Figure 8(a). In the intermediate regions with no antenna in Figure 8(c), the fluorophore emission was evaluated to be at the single-molecule detection level as expected. In the regions where nanoantennas are present, one can observe higher emission intensity. Furthermore, in the dimer regions, the average emission intensity is even higher than in the monomer regions (see Figure 8(c)). This may be due to an enhancement of single-molecule excitation and emission by the antenna. However, the gold luminescence signal, despite the weak excitation power (compared to the excitation power used in Section 3), may be detectable, or the random deposition of the single molecules is not homogeneous because of the topographic presence of nanoantennas.

In order to investigate the separate contributions of dimer nanoantenna intrinsic luminescence and molecular fluorescence in more detail, we turned to a perylene dye that we used in previous studies because of its excellent photostability [98, 99]. This dye allows for observation times up to minutes and in addition shows an on-off switching (blinking) on timescales of seconds [99] which facilitates measuring the separate responses. In order to match the nanoantenna response to the greener (compared to DiD) wavelength spectrum of the perylene dye (excitation around 565 nm), the thickness of the nanoantenna dimers was increased to 60 nm. This shifts the dimer resonance spectrum to the same wavelength range as the perylene fluorescence. We spin-coated a 50 nm layer of perylene in PMMA over the substrate containing the antennas. Samples were then excited using pulsed (280 fs, 80 MHz repetition rate) laser illumination (Coherent Mira 900-F pumped by a Coherent Verdi V-18, with an APE optical parametric oscillator and an APE pulse picker set at a 1 in 20 picking

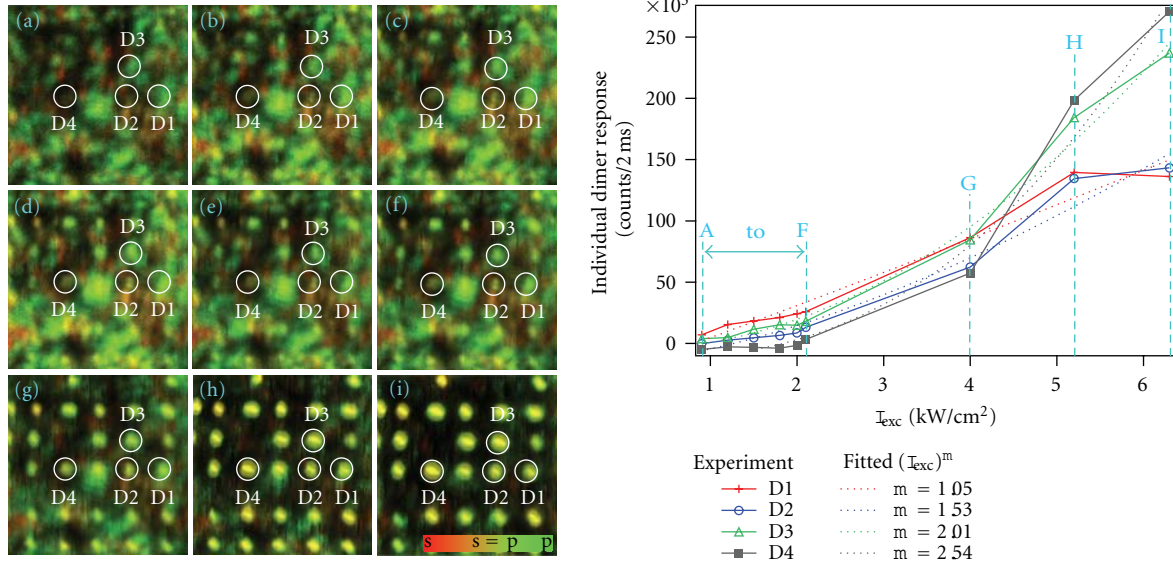


FIGURE 9: Femtosecond pulsed excitation over gold dimers. The excitation wavelength is fixed at 565 nm, and its power density is varied from 0.9 (a) to 6.3 kW/cm² (i). The dedicated sample here is a 100 × 100 μm array of dimers with a 100 nm diameter, a 30 nm gap, and a 60 nm thickness, that matches the excitation wavelength. A 50 nm layer of perylene in PMMA is spin-coated over the gold dimers as in Figure 4(a). The graph displays the individual response of selected dimers (circled on the image series) as a function of the excitation power. From one dimer to another, one can see various power dependences of the signal, going from close to linear behavior (for D1) to overquadratic one (in D3 and D4).

ratio) and with circular polarization. As described above, the collected fluorescence light was separated from the excitation beam using a dichroic mirror and a 575 nm long-pass filter before being routed toward two cross-polarized APDs. Varying power densities from 0.9 kW/cm² (Figure 9(a)) up to 6.3 kW/cm² (Figure 9(i)) were used. In Figure 9, we display a series of images of the same region of the sample illuminated with increasing powers. Note that the molecular concentration used here is slightly higher than what is typically used for single-molecule fluorescence experiments so that several fluorophores may be excited at each position. From these images, we extracted the individual response of four dimer-molecule assemblies D1 to D4 and plotted as a function of incident power density (Figure 9). We clearly highlighted the linear behavior at low power (density < 2 kW/cm²) mainly due to the molecular fluorescence. As the power increases, the dimer contribution is evolving going from linear to quadratic. In addition, at higher powers, the nanoantennas response becomes predominant with behavior from quadratic to supraquadratic varying from antennas to antennas. The broad distribution between dimers induced again a large distribution in the nonlinearity level m (with a main contribution for $m \approx 2$ over all dimers imaged here). This is to be expected, as the local field enhancement is particularly conducive to the enhancement of nonlinear processes such as two-photon absorption. Furthermore, enhancements are expected to be stronger under two-photon excitation since its rate varies as the square of the local field intensity. Non-linear absorption processes also need a high-power density explaining our observation of a non-linear response for high-power density. Thus, an excitation

power sweep may serve to unravel molecular response from the nanoantennas in order to map the latter positions in densely coated samples. We now turn to measurement of the fluorescence lifetime in the low (~2 kW/cm²) excitation regime.

Figure 10 shows a fluorescence image of a sample with a concentration of perylene molecules slightly higher than concentration typically used for resolving fluorescence from single molecules. Many spots in the sample appear single-colored indicating polarized fluorescence emission and thus the presence of only one or few molecules. Upon close inspection, a regular pattern of spots, reminiscent of the array of nanoantennas, appears, some of which are clearly brighter than the average spots. This brighter appearance may result from antenna-enhanced emission, locally higher concentrations of perylene (induced by the topography presented by the dimers during spin-coating), or a joint signal of molecular fluorescence and nanoantenna luminescence. In Figure 10, we present intensity time trajectories recorded at two positions that correlate with positions of dimer nanoantennas. These positions are indicated with numbered circles in the image. Both trajectories show blinking between different intensity levels in the first 10 to 20 seconds, together with discrete, permanent steps to a lower intensity, reminiscent of stepwise photobleaching of each of the perylenes. This blinking and stepwise bleaching is a clear indication of the presence of our perylene molecules [99]. From the number of discrete intensity levels, we can determine the number of molecules excited by the diffraction-limited laser focus. For instance, four separate intensity levels are identified in the first 20 seconds of

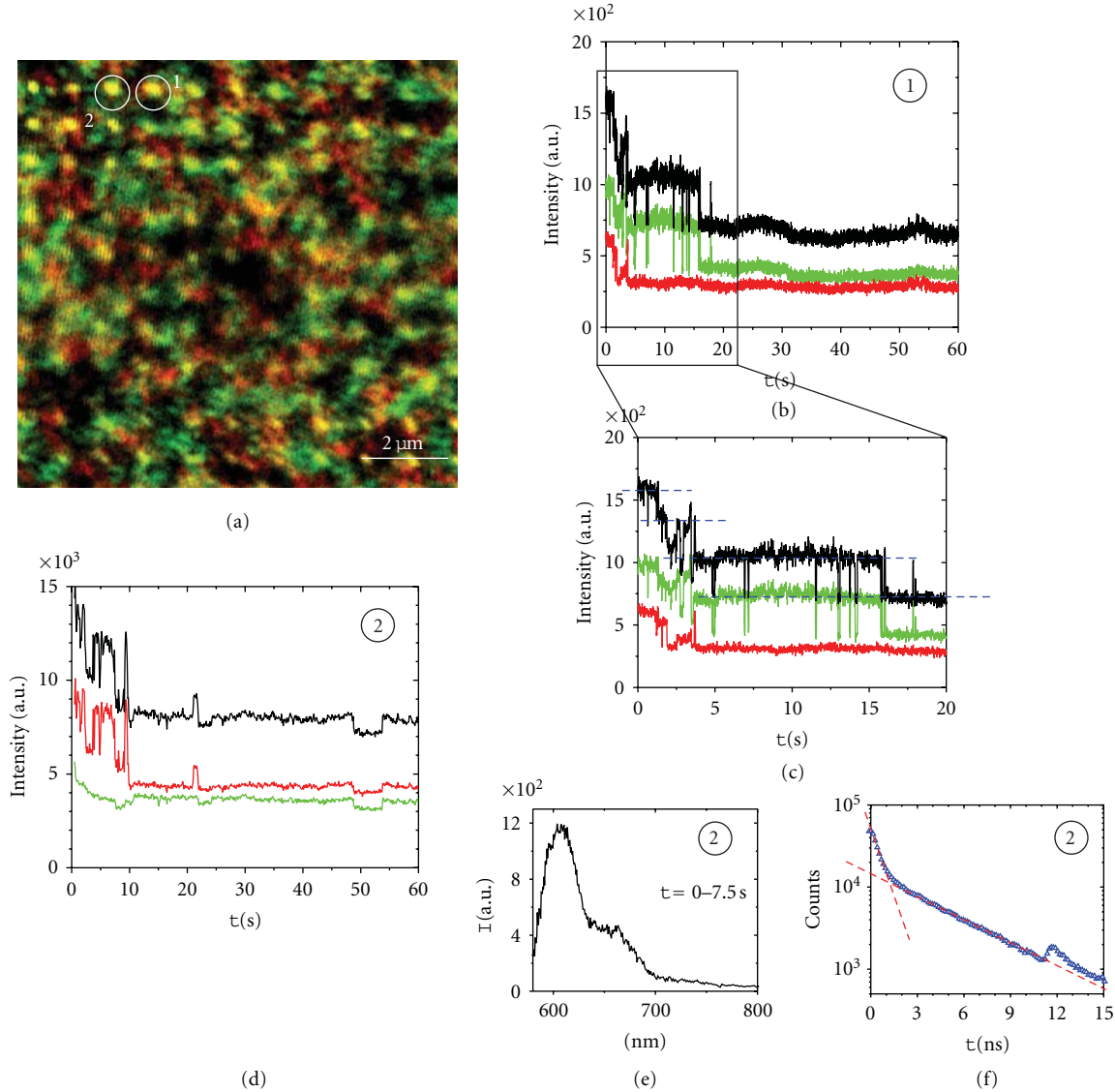


FIGURE 10: (a) Fluorescence image of perylene fluorescent molecules spin-coated on a substrate with dimer and monomer nanoantennas. (b) Fluorescence intensity trajectory measured at the position is indicated with circle numbered 1 in (a). Red and green trajectories indicate signals with orthogonal in-plane polarizations, while the black line indicates the total intensity. The intensity trajectory at position (1) shows a clear multilevel intensity blinking and bleaching reminiscent of molecular fluorescence. (c) Zoom in to the first 20 s where the four intensity levels are indicated with dashed blue lines. (d) The intensity trajectory measured at position number 2 in (a) displays similar blinking. (e) The fluorescence spectrum is recorded in the initial 7.5 s of the trajectory at position 2, with the spectra measured between $t = 30$ and $t = 60$ s subtracted. The resulting spectrum is a typical emission spectrum of our perylene molecule. (f) Fluorescence lifetime is measured at position 2. Dashed lines in the lifetime graph indicate exponential fits with lifetimes of $\tau_1 = 0.4$ ns and $\tau_2 = 5$ ns, respectively.

trajectory (1), as indicated in the figure. Of these, the three highest intensity levels show the discrete switching, while the fourth level remains continuous with broad variations on a 5–10 seconds timescale. We attribute the discrete switching behavior to the presence of three perylene molecules, while the fourth level constitutes a background signal that was present without blinking over observations as long as several minutes. Note also that the polarization anisotropy of the emitted fluorescence is different for the different intensity levels. Due to the fixed molecular orientation, and thus fixed transition dipole orientation, in the polymer matrix, this

again indicates that the discrete intensity steps result from individual molecules switching on and off.

The trajectory recorded at position (2) displays a similar blinking before the signal falls to a continuous background. The small stepwise variations that are present in the background signal at $t \sim 20$ s and $t \sim 50$ s may result from molecules that are at the rim of the laser focus and are thus only weakly excited. In general, we observed similar trajectories with an initial discrete switching between typically one to three intensity levels and a remaining persistent continuous background signal for many different positions. All these

positions coincided with the regular pattern of the nanoantennas array. Measurements at positions outside the antenna array yielded similar molecular fluorescence blinking but without this strong background signal. Thus, we attribute the persistent background signal to the presence of the dimer nanoantenna.

For all positions, fluorescence intensity spectrum and fluorescence lifetime were measured simultaneously with the intensity trajectory. For position (2) in Figure 10, we present the fluorescence spectrum recorded over the first 7.5 seconds of the trajectory. Here, the spectrum recorded for the background signal was subtracted, which yields a typical perylene emission spectrum. This again constitutes a strong indication that the initial intensity switching results from the presence of a perylene molecule. In the lower right panel of Figure 10, also the fluorescence decay curve (recorded from the photon arrival times after the laser trigger pulse) constructed from the 60-second trajectory is indicated. Here, we observe a clear biexponential decay with a fast component (measured lifetime $\tau_1 = 0.4$ ns, close to our instrument response and a slower component with $\tau_2 = 5.0$ ns). The 5.0 ns lifetime is typical for our perylene dye in PMMA [98], while the fast component is attributed to the nanoantenna background signal. Similar decay curves with a fast component limited by our detector response and a slower component with typical perylene fluorescence lifetime were measured for all intensity trajectories that displayed the initial discrete fluorescence switching. From the fact that the measured fluorescence lifetimes are comparable to the regular (i.e., without nanoantennas) perylene lifetime, we conclude that these molecules are not coupled to the nanoantenna. The fast component of course may result from either antenna-coupled molecular emission or from the intrinsic luminescence of the nanoantennas. To resolve this latter issue, we reduced the molecular concentration to $\sim 10^{-8}$ M, a typical concentration for single-molecule fluorescence experiments. In this case, the dye dissolved in toluene was first spin-coated (i.e., without PMMA), while a PMMA solution in toluene was spin-coated afterwards to coat with a protective ~ 50 nm thick layer of polymer. With this procedure, we expect topographic effects, that is, capillary interactions, during spin-coating of the perylene solution to draw the molecules to the nanoantennas. Given the overall low concentration of perylene molecules, even in this case we expect only a few nanoantennas to be coupled with a molecule. In Figure 11, a typical fluorescence image from an area with nanoantennas is shown.

Fluorescence spectra were recorded at different nanoantenna positions as indicated in Figure 11. All spectra show a resonance below 620 nm (overlapping with the molecular excitation and emission wavelength as anticipated) and extend into the red part of the wavelength spectrum. All nanoantenna spectra show a dip at 630 nm. We grouped our measured dimer antenna spectra in two groups based on the appearance of the fluorescence spectra beyond this 630 nm dip. The group indicated with red curves extends deep into the 700 nm range with three broad peaks at equivalent positions between 630 nm and 700 nm. Compared to the molecular fluorescence spectra also indicated in Figure 11,

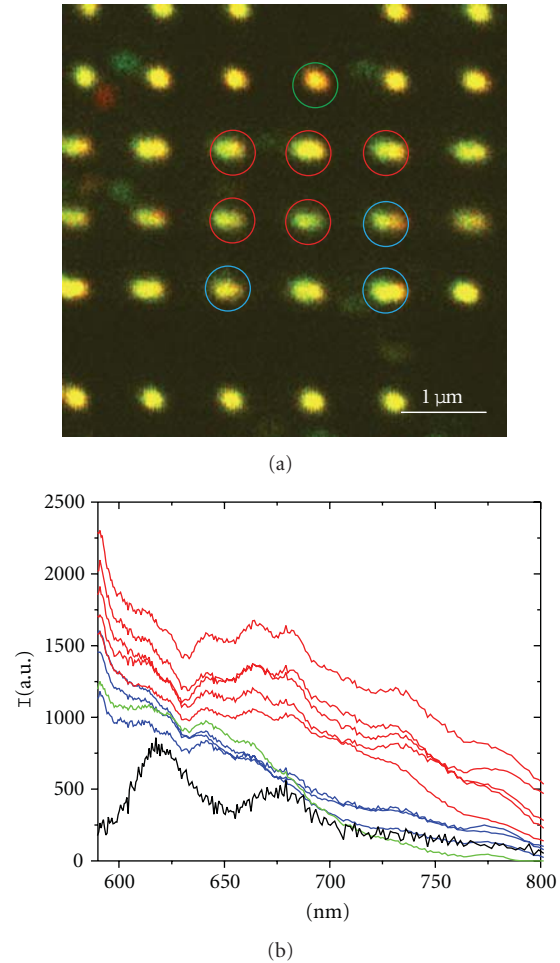


FIGURE 11: (a) Fluorescence image of a nanoantenna array with low concentration of perylene molecules. Bright spots indicate the positions of nanoantennas. First two rows and the lowest row are monomer antennas, while the middle three rows are dimer antennas. (b) Fluorescence spectra for eight dimer positions and one monomer position from the image in (a). The spectra with red lines correspond to red-encircled spots in the image, blue curves to the blue-encircled spots, and the green curve to the monomer position. The black curve indicates a typical perylene fluorescence spectrum recorded for a single molecule outside the nanoantenna array.

we can see that the nanoantenna response shows a good overlap with the molecular resonance. The curves indicated in blue show a faster decay below 700 nm and are reminiscent of the monomer spectra indicated with the green curve. Thus, we attribute these latter to geometrical artifacts (such as fused dimers) and assume the red curves to result from proper gap dimers. For all these positions, fluorescence lifetime was measured simultaneously, and this always resulted in a fast, $\tau \sim 0.5$ ns decay without any sign of slower component resulting from uncoupled molecules. In addition, the intensity trajectories were similar to the background signal presented in the respective panels in Figure 10. Similar behavior was observed for several tens

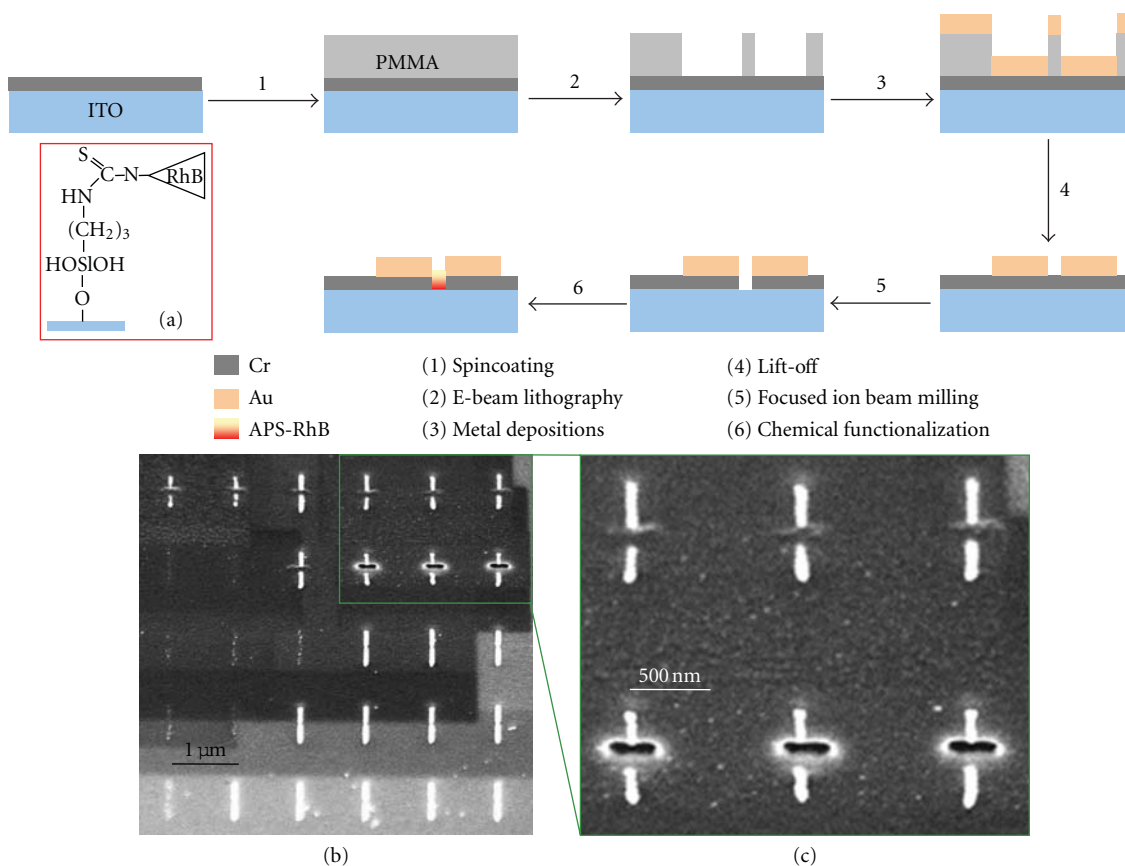


FIGURE 12: Schematic outline of the fabrication procedure of a molecular plasmonic nanoantenna involving the consecutive application of electron-beam lithography, focused ion beam (FIB) milling, and localized chemical surface functionalization. The inset (a) displays the surface grafting of a Rhodamine B (RhB) fluorophore onto the ITO substrate. The FIB step (step 5) is represented by the SEM images in (b) and (c) where the gap is milled either through a few nanometers of chromium only (top row in (c)) or all the way to the ITO layer (bottom row in (c)).

of nanoantenna positions, where statistically a majority of these are expected not to be coupled to molecules. While few of the recorded fluorescence spectra could result from a strongly coupled antenna-molecule system, such fluorescence measurements fail to discriminate between the signal of a coupled system and the intrinsic luminescence of the dimer nanoantennas. Note that the comparatively higher luminescence signal for this system compared to the previous DiD system, may result from the shorter pulse length, and thus higher instantaneous power density, in the perylene experiments (280 fs as compared to 90 ps). Finally, we want to note that in this strong coupling regime, molecules coupled to an antenna would predominantly radiate via the antenna modes. Thus, molecular positions can only be retrieved in a weaker coupling regime. In this case, however, the fact that both molecular lifetime distribution and nanoantenna field strength distribution (see Section 3) have to be statistically accounted for makes that hundreds of positions need to be measured which is a laborious task. Thus, we can conclude that only an a priori positioning of fluorescent molecules at well-defined positions with respect to the nanoantenna can solve these issues. In the next section,

we will present a fabrication scheme with which this could be achieved.

5. Dedicated Positioning of Molecules in the Nanoantenna Gap

To tackle the issues presented above, we devised a fabrication procedure for molecular plasmonic nanostructures where functional molecules can be placed at a predefined position which is the gap of the nanoantennas. Luminescence measurements were thereafter carried out as a proof of principle.

Our methodology relies on the use of two distinct conductive layers which allows the consecutive, high-resolution application of different charged particle lithography techniques, in our case electron-beam lithography and focused ion beam milling. The top conductive layer furthermore serves both as a deposition and adhesion layer for the plasmonic structure and as a mask for a final chemical surface modification step, which functionalizes the exposed parts of the underlying conductive material. An outline of the fabrication procedure is given in Figure 12. First, we

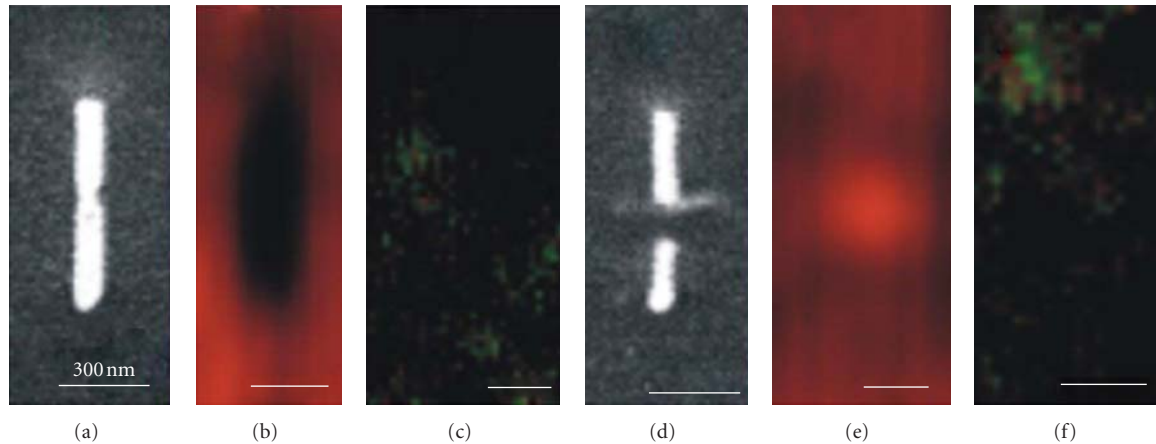


FIGURE 13: (a–c) Gold nanoantenna not exposed to FIB milling after surface functionalization: (a) SEM image, (b) optical transmission microscopy image, and (c) fluorescence microscopy image. (d–f) Same respective images for a gold nanoantenna where the gap size had been increased by FIB milling but without exposing the lower ITO layer.

evaporate a 80 nm thick layer of indium tin oxide (ITO) onto a glass cover slide. The ITO layer is overcoated with an approximately 10 nm layer of chromium by evaporation. The use of optically transparent ITO allows for light microscopy in both reflection and transmission mode and thus makes the fabrication scheme compatible for applications relying on enhanced detection of, for example, fluorescence or Raman scattering signals. Gold nanoantennas were created on the Cr layer with the process described in Section 2 (Figure 1), the Cr layer replacing the Ti adhesion layer. The nanoantennas consist here of two equally sized gold rods ($l \times w \times h = 300 \times 80 \times 40$ nm) with the short ends facing at a separation of 30 nm. Examples of such gold nanoantennas are given in the bottom row of Figure 12(b) or closely in Figure 13(a).

Next, we use focused ion beam (FIB) lithography to mill a rectangular, 200 nm long, 50 nm wide hole into the Cr layer, cutting the nanoantennas halfway, that is, at the gap. This increases the gap size of exposed nanoantennas to approximately 50 nm (see Figure 12(c)). The FIB milling finally uncovers the underlying ITO substrate (step 5 in Figure 12). These exposed ITO areas on the substrate can be selectively functionalized using a surface grafting procedure that exploits the chemical contrast between metal (Cr) and oxide (ITO) areas. If necessary the Cr surface can be passivated by applying a coating reaction prior to FIB milling. We functionalized the exposed ITO area in the gap between both gold bars with a Rhodamine dye derivative. Rhodamine dyes are often used both as fluorescent markers because of their high quantum yield and photostability and as model probes for surface-enhanced Raman scattering studies. First, isothiocyanate Rhodamine B (RhB) was linked to the silane coupling agent 3-aminopropyltriethoxysilane (APS). The ITO areas are then reacted to the APS-RhB construct (see Figure 12(a)) under ammonia-catalyzed conditions [100]. Samples were thoroughly rinsed with ethanol to prevent absorption of APS-RhB onto the Cr surface upon drying.

The resulting nanostructure is indicated in Figure 12 after step 6.

After APS-RhB reaction, gold nanoantennas were analyzed using the previously described high-resolution (single-molecule sensitivity) confocal microscopy setup in both transmission (excitation light) and reflection (fluorescence light) modes. Nanoantennas not exposed to FIB milling are visible due to decreased transmission, but do not show fluorescence (Figures 13(b) and 13(c)). Milling a gap in the nanoantenna and a small indentation in the Cr-layer without exposing the ITO substrate (Figures 13(d), 13(e), and 13(f)) leads to a corresponding small increase in transmission, at the location of the indentation in between the gold rods. However, no change in fluorescence signal from background level is observed, indicating negligible absorption of APS-RhB onto the Cr surface. We have used a range of FIB milling times and beam doses, which leads to various indentation depths in the Cr layer, but a fluorescence signal was only observed when the transmission signal indicated removal of the Cr layer. At this point, transmission increased about 6-fold compared to transmission through the non-FIB-milled Cr areas.

Figure 14 shows results for nanoantennas where FIB milling completely removed the Cr layer, leading to local exposure of ITO. Removal of the Cr layer is evidenced by the increase in the transmission signal, and RhB-functionalization of the ITO in the gap gives rise to a strong fluorescence signal. The width of the Gaussian fluorescence profiles is 310 nm, that is, diffraction limited. This is in correspondence with the projected gap size of 200×50 nm. Note that the alignment of the FIB area with nanoantenna gap is not optimal so that antennas are partly cut. The differences in fluorescence intensity between the functionalized nanoantennas can be caused by variations in the number of RhB molecules. In principle, this could also be caused by the field enhancement variations but given the relatively large gap sizes and the fact that antennas are

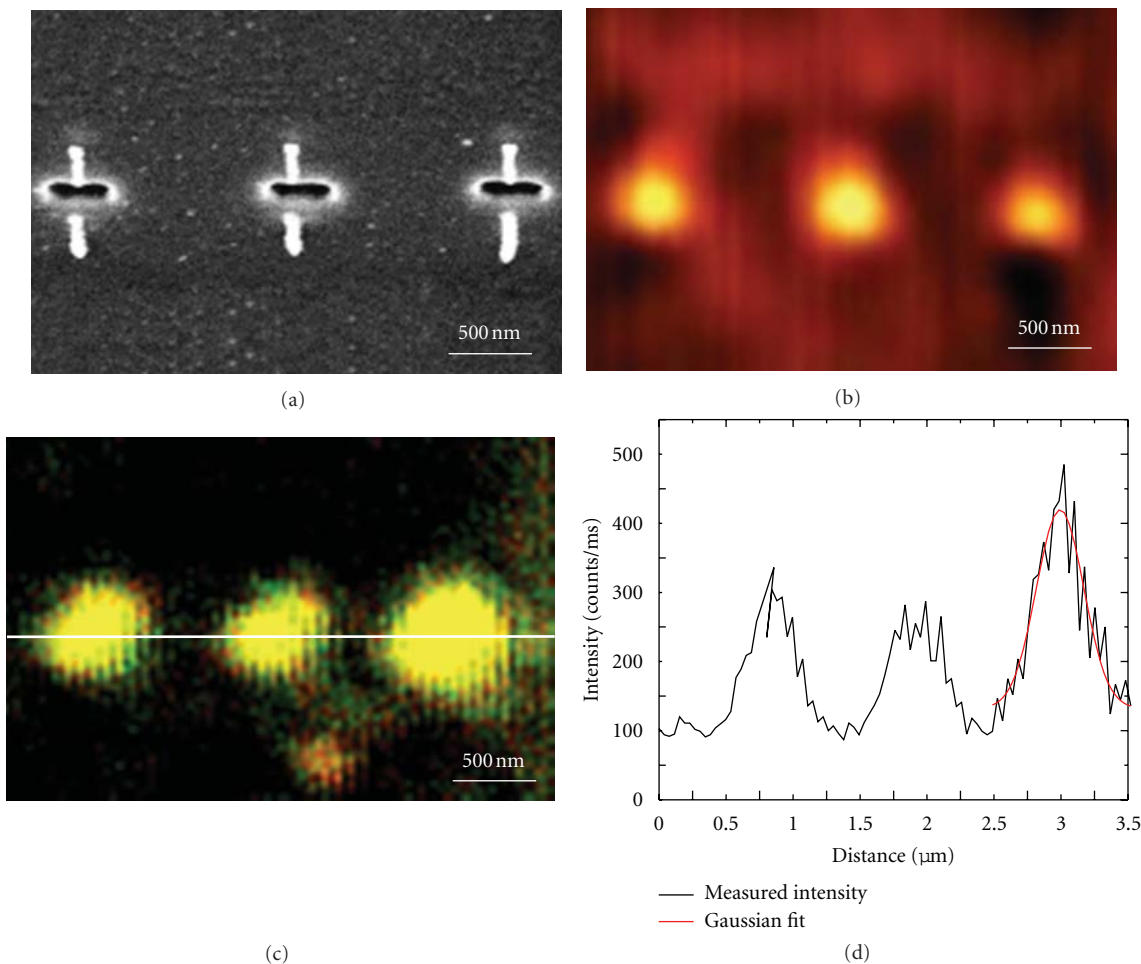


FIGURE 14: (a) SEM image of gold nanoantennas after FIB milling through the Cr layer and the respective images in (b) transmission and (c) fluorescence microscopy. Color scaling in (b, c) is identical to that in Figure 2 to highlight the intensity increase. The fluorescence image has been built from a red and a green channel-denoting orthogonal polarization directions. (d) Intensity profile along the white line drawn in (c) indicating that fluorescence spots are diffraction limited.

partly cut by the FIB procedure, we do not expect significant enhancement. This is also indicated by the unpolarized and thus not-antenna-coupled emission. By adjusting reagent concentrations, surface coating could be tuned to a few or single molecules per nanostructure, which would allow for a detailed and localized mapping of field enhancement properties around plasmonic nanostructures.

In summary, we have presented a fabrication procedure for the localized, sub-diffraction-limit positioning of fluorescent molecules at a designed position with respect to a plasmonic nanoantenna. Initial results indicate the feasibility of the approach, which relies on the combined use of electron-beam and focused ion beam lithography, together with chemical surface modification. The use of two distinct conductive layers, of which the upper one serves as a mask for the chemical functionalization, allows both lithography techniques to be applied at high resolution, opening the way to sub-20 nm patterning. Further work should aim at demonstrating the technique at this resolution and at improving alignment with the nanoantennas. This would give the

possibility to unambiguously map the local field around plasmonic nanostructures, but also provide the way for creating active molecular plasmonic nanodevices for, for example, high-resolution chemical and biological sensing, light harvesting, and nanophotonic components.

6. Conclusions and Perspective

Gap nanoantennas composed of double identical rods separated by a nanometric gap were first fabricated by electron beam lithography before being theoretically investigated and experimentally characterized by far-field spectroscopy. In a preliminary study, arrays of gap nanoantennas with various aspect ratios and gap sizes were considered and their optical response recorded. The local field in the close vicinity of the nanoantennas was then evaluated by luminescent measurements using a confocal microscope with single-molecule detection capability. Polarization effects were then explored. We observed luminescence predominantly polarized along

the dimer axis with an average enhancement up to 3-fold. This is in agreement with previous work reporting 10-fold enhancement on similar arrays using two-photon luminescence measurements. These prior studies give insights into the local response distribution of such metallic nanoantennas and constituted a strong guiding line when tackling the issue of nanoantenna-single molecule coupling.

It is crucial to understand antenna-molecule coupling as these hybrid systems receive increasing attention in fields as diverse as biosensing, imaging, or photovoltaics. As a general strategy, we used single fluorescent molecules as vectorial nonperturbative probes to map the local field of individual nanoantennas. For this task, two types of fluorophores were used. First, common DiD fluorophores were randomly deposited over the nanoantenna arrays. We observed enhancement of the fluorescence intensity caused by the presence of nanoantennas. However, and despite the low excitation power used in the experiment, it was difficult to dissociate the molecular fluorescence from the intrinsic gold luminescence signal. In addition, the presence of the nanoantennas could disturb the homogeneity of the fluorophores on the samples, precluding quantitative analysis. To discriminate between the fluorophore and the nanoantenna contributions to the fluorescence signal, we subsequently utilized perylene molecules as photostable fluorophores. They permitted longer observations (up to minutes). In addition, they exhibit an on-off switching on a timescale of seconds. These combined features eased the discrimination between the molecular and nanoantenna contribution to the fluorescence signal. We then carried out fluorescence measurements at different excitation power. Due to the different power laws followed by linear molecular fluorescence and two-photon excited luminescence from the nanoantennas, we were able to discriminate these two contributions. Fluorescence spectroscopy and lifetime measurements were then carried out on the nanoantenna-molecule system. The lifetime measurements revealed a biexponential decay with a fast component $\tau_1 = 0.4$ ns (close to the system temporal resolution) attributed to the nanoantennas background and a typical $\tau_2 = 5.0$ ns typical of perylene in PMMA. From the insensitivity of the latter decay to the presence of the nanoantennas, we conclude that the molecules under investigation were not coupled to nanoantennas. By cons, the fast component is linked to the nanoantennas whether via antenna-coupled molecular emission or as a result of the intrinsic antenna luminescence. Even working at low concentration, and therefore being less influenced by the topographic artifacts, we expected to have only rare antenna-molecule coupling events. Furthermore, we note that any molecule coupled to an antenna should reemit via the antenna modes, and therefore a large number of positions have to be evaluated to take into account the broad distributions in the molecules' lifetime and in the dimers' luminescence. To overcome this issue, we proposed a hybrid system composed of a nanoantenna and a molecule with well-controlled position. Its feasibility was demonstrated using a process involving electron beam and focused ion beam lithography, followed by chemical surface modification. This opens up new routes toward the local 3D

mapping of local field in the vicinity of metallic nanoantennas as well as active plasmonic nanodevices, where the relative positioning remains a burden. This has tremendous applications in the numerous currently hot topics such as the development of nanophotonic components, bio- and chemical sensing, imaging, light-harvesting mimicking systems, or hybrid photovoltaic cells design.

Acknowledgment

The authors would like to thank: Professor Ali Passian at the Oak Ridge National Laboratory in Tennessee for providing the theoretical results illustrated in Figures 2 and 3 of Section 2; Frans Segerink at University of Twente and M. J. Lopez Bosque at the Parc Científic de Barcelona for FIB-milling; Petru Ghenuche and Gabriel Sanchez-Mosteiro at ICFO-Barcelona for e-beam lithography and confocal microscopy, and A. van Blaaderen for use of laboratory facilities. This work was supported by the EU Network of Excellence Plasm Nano Devices (WP 19.8.2). Niek van Hulst acknowledges funding by the European Specific Target Research Project (STRP) ASPRINT, the Spanish MICINN program CONSOLIDER CSD2007-046, Fundacio CELLEX Barcelona and the EU ERC Grant No. 247330. Aude L. Lereu acknowledges the Centre National de la Recherche Scientifique.

References

- [1] P. Bharadwaj, B. Deutsch, and L. Novotny, "Optical antennas," *Advances in Optics and Photonics*, vol. 1, pp. 438–483, 2009.
- [2] L. Novotny and N. F. van Hulst, "Antennas for light," *Nature Photonics*, vol. 5, pp. 83–90, 2011.
- [3] C. Girard and E. Dujardin, "Near-field optical properties of top-down and bottom-up nanostructures," *Journal of Optics A*, vol. 8, supplement 4, pp. S73–S86, 2006.
- [4] F. Wang and Y. R. Shen, "General properties of local plasmons in metal nanostructures," *Physical Review Letters*, vol. 97, no. 20, Article ID 206806, 2006.
- [5] C. Girard, "Near fields in nanostructures," *Reports on Progress in Physics*, vol. 68, no. 8, pp. 1883–1933, 2005.
- [6] S. A. Maier and H. A. Atwater, "Plasmonics: localization and guiding of electromagnetic energy in metal/dielectric structures," *Journal of Applied Physics*, vol. 98, no. 1, Article ID 011101, pp. 1–10, 2005.
- [7] H. Cang, A. Labno, C. Lu et al., "Probing the electromagnetic field of a 15-nanometre hotspot by single molecule imaging," *Nature*, vol. 469, no. 7330, pp. 385–388, 2011.
- [8] P. Ghenuche, R. Quidant, and G. Badenes, "Cumulative plasmon field enhancement in finite metal particle chains," *Optics Letters*, vol. 30, no. 14, pp. 1882–1884, 2005.
- [9] K. Imura, T. Nagahara, and H. Okamoto, "Near-field two-photon-induced photoluminescence from single gold nanorods and imaging of plasmon modes," *Journal of Physical Chemistry B*, vol. 109, no. 27, pp. 13214–13220, 2005.
- [10] K. Imura, T. Nagahara, and H. Okamoto, "Photoluminescence from gold nanoplates induced by near-field two-photon absorption," *Applied Physics Letters*, vol. 88, no. 2, Article ID 023104, pp. 1–3, 2006.

- [11] P. Mühlischlegel, H. J. Eisler, O. J. F. Martin, B. Hecht, and D. W. Pohl, "Applied physics: resonant optical antennas," *Science*, vol. 308, no. 5728, pp. 1607–1609, 2005.
- [12] P. J. Schuck, D. P. Fromm, A. Sundaramurthy, G. S. Kino, and W. E. Moerner, "Improving the mismatch between light and nanoscale objects with gold bowtie nanoantennas," *Physical Review Letters*, vol. 94, no. 1, Article ID 017402, 2005.
- [13] A. Sundaramurthy, P. J. Schuck, N. R. Conley, D. P. Fromm, G. S. Kino, and W. E. Moerner, "Toward nanometer-scale optical photolithography: utilizing the near-field of bowtie optical nanoantennas," *Nano Letters*, vol. 6, no. 3, pp. 355–360, 2006.
- [14] A. K. Sheridan, A. W. Clark, A. Glidle, J. M. Cooper, and D. R. S. Cumming, "Multiple plasmon resonances from gold nanostructures," *Applied Physics Letters*, vol. 90, no. 14, Article ID 143105, 2007.
- [15] C. E. Talley, J. B. Jackson, C. Oubre et al., "Surface-enhanced Raman scattering from individual Au nanoparticles and nanoparticle dimer substrates," *Nano Letters*, vol. 5, no. 8, pp. 1569–1574, 2005.
- [16] A. M. Michaels, J. Jiang, and L. Brus, "Ag nanocrystal junctions as the site for surface-enhanced raman scattering of single rhodamine 6G molecules," *Journal of Physical Chemistry B*, vol. 104, no. 50, pp. 11965–11971, 2000.
- [17] K. Li, M. I. Stockman, and D. J. Bergman, "Self-similar chain of metal nanospheres as an efficient nanolens," *Physical Review Letters*, vol. 91, no. 22, Article ID 227402, 4 pages, 2003.
- [18] L. Novotny and B. Hecht, *Principles of Nano-Optics*, Cambridge University Press, 2006.
- [19] L. Novotny and S. J. Stranick, "Near-field optical microscopy and spectroscopy with pointed probes," *Annual Review of Physical Chemistry*, vol. 57, pp. 303–331, 2006.
- [20] L. Novotny, "Effective wavelength scaling for optical antennas," *Physical Review Letters*, vol. 98, no. 26, Article ID 266802, 2007.
- [21] A. Hartschuh, M. R. Beversluis, A. Bouhelier, and L. Novotny, "Tip-enhanced optical spectroscopy," *Philosophical Transactions of the Royal Society A*, vol. 362, no. 1817, pp. 807–819, 2004.
- [22] A. Hartschuh, "Tip-enhanced near-field optical microscopy," *Angewandte Chemie*, vol. 47, no. 43, pp. 8178–8191, 2008.
- [23] E. Bailo and V. Deckert, "Tip-enhanced Raman scattering," *Chemical Society Reviews*, vol. 37, no. 5, pp. 921–930, 2008.
- [24] E. Fort and S. Grésillon, "Surface enhanced fluorescence," *Journal of Physics D*, vol. 41, no. 1, Article ID 013001, 2008.
- [25] A. L. Lereu, A. Passian, and P. Dumas, "Near field optical microscopy: a brief review," *International Journal of Nanotechnology*, vol. 8, 2011.
- [26] S. Wedge, J. A. E. Wasey, W. L. Barnes, and I. Sage, "Coupled surface plasmon-polariton mediated photoluminescence from a top-emitting organic light-emitting structure," *Applied Physics Letters*, vol. 85, no. 2, pp. 182–184, 2004.
- [27] C. Liu, V. Kamaev, and Z. V. Vardeny, "Efficiency enhancement of an organic light-emitting diode with a cathode forming two-dimensional periodic hole array," *Applied Physics Letters*, vol. 86, no. 14, Article ID 143501, pp. 1–3, 2005.
- [28] E. Ozbay, "Plasmonics: merging photonics and electronics at nanoscale dimensions," *Science*, vol. 311, no. 5758, pp. 189–193, 2006.
- [29] S. Pillai, K. R. Catchpole, T. Trupke, G. Zhang, J. Zhao, and M. A. Green, "Enhanced emission from Si-based light-emitting diodes using surface plasmons," *Applied Physics Letters*, vol. 88, no. 16, Article ID 161102, 2006.
- [30] G. Sun, J. B. Khurgin, and R. A. Soref, "Plasmonic light-emission enhancement with isolated metal nanoparticles and their coupled arrays," *Journal of the Optical Society of America B*, vol. 25, no. 10, pp. 1748–1755, 2008.
- [31] P. Ball, "Let there be light," *Nature*, vol. 409, no. 6823, pp. 974–976, 2001.
- [32] R. Corkish, M. A. Green, and T. Puzzer, "Solar energy collection by antennas," *Solar Energy*, vol. 73, no. 6, pp. 395–401, 2002.
- [33] P. J. Burke, S. Li, and Z. Yu, "Quantitative theory of nanowire and nanotube antenna performance," *IEEE Transactions on Nanotechnology*, vol. 5, no. 4, Article ID 1652847, pp. 314–334, 2006.
- [34] K. Kempa, J. Rybczynski, Z. Huang et al., "Carbon nanotubes as optical antennae," *Advanced Materials*, vol. 19, no. 3, pp. 421–426, 2007.
- [35] S. Pillai, K. R. Catchpole, T. Trupke, and M. A. Green, "Surface plasmon enhanced silicon solar cells," *Journal of Applied Physics*, vol. 101, no. 9, Article ID 093105, 2007.
- [36] K. Nakayama, K. Tanabe, and H. A. Atwater, "Plasmonic nanoparticle enhanced light absorption in GaAs solar cells," *Applied Physics Letters*, vol. 93, no. 12, Article ID 121904, 2008.
- [37] S. H. Lim, W. Mar, P. Matheu, D. Derkacs, and E. T. Yu, "Photocurrent spectroscopy of optical absorption enhancement in silicon photodiodes via scattering from surface plasmon polaritons in gold nanoparticles," *Journal of Applied Physics*, vol. 101, no. 10, Article ID 104309, 2007.
- [38] C. Hägglund, M. Zäch, G. Petersson, and B. Kasemo, "Electromagnetic coupling of light into a silicon solar cell by nanodisk plasmons," *Applied Physics Letters*, vol. 92, no. 5, Article ID 053110, 2008.
- [39] A. J. Morfa, K. L. Rowlen, T. H. Reilly II, M. J. Romero, and J. Van De Lagemaat, "Plasmon-enhanced solar energy conversion in organic bulk heterojunction photovoltaics," *Applied Physics Letters*, vol. 92, no. 1, Article ID 013504, 2008.
- [40] S. S. Kim, S. I. Na, J. Jo, D. Y. Kim, and Y. C. Nah, "Plasmon enhanced performance of organic solar cells using electrodeposited Ag nanoparticles," *Applied Physics Letters*, vol. 93, no. 7, Article ID 073307, 2008.
- [41] D. Derkacs, W. V. Chen, P. M. Matheu, S. H. Lim, P. K. L. Yu, and E. T. Yu, "Nanoparticle-induced light scattering for improved performance of quantum-well solar cells," *Applied Physics Letters*, vol. 93, no. 9, Article ID 091107, 2008.
- [42] A. Passian, S. Zahrai, A. L. Lereu, R. H. Farahi, T. L. Ferrell, and T. Thundat, "Nonradiative surface plasmon assisted microscale Marangoni forces," *Physical Review E*, vol. 73, no. 6, Article ID 066311, 2006.
- [43] R. H. Farahi, A. Passian, S. Zahrai, A. L. Lereu, T. L. Ferrell, and T. Thundat, "Microscale Marangoni actuation: all-optical and all-electrical methods," *Ultramicroscopy*, vol. 106, no. 8–9, pp. 815–821, 2006.
- [44] V. M. Shalaev, W. Cai, U. K. Chettiar et al., "Negative index of refraction in optical metamaterials," *Optics Letters*, vol. 30, no. 24, pp. 3356–3358, 2005.
- [45] V. M. Shalaev, "Optical negative-index metamaterials," *Nature Photonics*, vol. 1, no. 1, pp. 41–48, 2007.
- [46] G. W. Bryant, I. Romero, F. J. Garcia de Abajo, and J. Aizpurua, "Stimulating electromagnetic response in coupled metallic nanoparticles for nanoscale optical microscopy and spectroscopy: nanorod-end effects," in *Plasmonics: Metallic Nanostructures and their Optical Properties*, vol. 6323 of *Proceedings of SPIE*, pp. 632313–632318, 2006.

- [47] I. Romero, J. Aizpurua, G. W. Bryant, and F. J. García De Abajo, "Plasmons in nearly touching metallic nanoparticles: singular response in the limit of touching dimers," *Optics Express*, vol. 14, no. 21, pp. 9988–9999, 2006.
- [48] J. Aizpurua, G. W. Bryant, L. J. Richter, F. J. García De Abajo, B. K. Kelley, and T. Mallouk, "Optical properties of coupled metallic nanorods for field-enhanced spectroscopy," *Physical Review B*, vol. 71, no. 23, Article ID 235420, 13 pages, 2005.
- [49] I. D. Mayergoyz, Z. Zhang, and G. Miano, "Analysis of dynamics of excitation and dephasing of plasmon resonance modes in nanoparticles," *Physical Review Letters*, vol. 98, no. 14, Article ID 147401, 2007.
- [50] C. Dahmen, B. Schmidt, and G. Von Plessen, "Radiation damping in metal nanoparticle Pairs," *Nano Letters*, vol. 7, no. 2, pp. 318–322, 2007.
- [51] S. Foteinopoulou, J. P. Vigneron, and C. Vandembem, "Optical near-field excitations on plasmonic nanoparticle-based structures," *Optics Express*, vol. 15, no. 7, pp. 4253–4267, 2007.
- [52] I. Olivares, R. Rojas, and F. Claro, "Surface modes of a pair of unequal spheres," *Physical Review B*, vol. 35, no. 5, pp. 2453–2455, 1987.
- [53] L. Gou and C. J. Murphy, "Fine-tuning the shape of gold nanorods," *Chemistry of Materials*, vol. 17, no. 14, pp. 3668–3672, 2005.
- [54] M. Futamata, Y. Maruyama, and M. Ishikawa, "Local electric field and scattering cross section of Ag nanoparticles under surface plasmon resonance by finite difference time domain method," *Journal of Physical Chemistry B*, vol. 107, no. 31, pp. 7607–7617, 2003.
- [55] S. Enoch, R. Quidant, and G. Badenes, "Optical sensing based on plasmon coupling in nanoparticle arrays," *Optics Express*, vol. 12, no. 15, pp. 3422–3427, 2004.
- [56] J. P. Kottmann and O. J. F. Martin, "Plasmon resonant coupling in metallic nanowires," *Optics Express*, vol. 8, no. 12, pp. 655–663, 2001.
- [57] H. Tamaru, H. Kuwata, H. T. Miyazaki, and K. Miyano, "Resonant light scattering from individual Ag nanoparticles and particle pairs," *Applied Physics Letters*, vol. 80, no. 10, p. 1826, 2002.
- [58] A. Bouhelier, R. Bachelot, G. Lerondel, S. Kostchev, P. Royer, and G. P. Wiederrecht, "Surface plasmon characteristics of tunable photoluminescence in single gold nanorods," *Physical Review Letters*, vol. 95, no. 26, Article ID 267405, 2005.
- [59] H. Kuwata, H. Tamaru, K. Esumi, and K. Miyano, "Resonant light scattering from metal nanoparticles: practical analysis beyond rayleigh approximation," *Applied Physics Letters*, vol. 83, no. 22, pp. 4625–4627, 2003.
- [60] A. A. Mikhailovsky, M. A. Petruska, M. I. Stockman, and V. I. Klimov, "Broadband near-field interference spectroscopy of metal nanoparticles using a femtosecond white-light continuum," *Optics Letters*, vol. 28, no. 18, pp. 1686–1688, 2003.
- [61] D. Ten Bloemendal, P. Ghenuche, R. Quidant, I. G. Cormack, P. Loza-Alvarez, and G. Badenes, "Local field spectroscopy of metal dimers by TPL microscopy," *Plasmonics*, vol. 1, no. 1, pp. 41–44, 2006.
- [62] P. Ghenuche, S. Cherukulappurath, T. H. Taminiau, N. F. Van Hulst, and R. Quidant, "Spectroscopic mode mapping of resonant plasmon nanoantennas," *Physical Review Letters*, vol. 101, no. 11, Article ID 116805, 2008.
- [63] A. L. Lereu, G. Sanchez-Mosteiro, P. Ghenuche, R. Quidant, and N. F. Van Hulst, "Individual gold dimers investigated by far- and near-field imaging," *Journal of Microscopy*, vol. 229, no. 2, pp. 254–258, 2008.
- [64] A. L. Lereu, G. Sanchez-Mosteiro, P. Ghenuche et al., "Probing the local field of nanoantennas using single particle luminescence," *Journal of Physics*, vol. 100, no. 5, Article ID 052038, 2008.
- [65] T. Matsumoto, T. Ichimura, T. Yatsui, M. Kourogi, T. Saiki, and M. Ohtsu, "Fabrication of a near-field optical fiber probe with a nanometric metallized protrusion," *Optical Review*, vol. 5, no. 6, pp. 369–373, 1998.
- [66] R. Eckert, J. M. Freyland, H. Gersen et al., "Near-field fluorescence imaging with 32 nm resolution based on microfabricated cantilevered probes," *Applied Physics Letters*, vol. 77, no. 23, pp. 3695–3697, 2000.
- [67] T. Kalkbrenner, M. Ramstein, J. Mlynek, and V. Sandoghdar, "A single gold particle as a probe for apertureless scanning near-field optical microscopy," *Journal of Microscopy*, vol. 202, no. 1, pp. 72–76, 2001.
- [68] H. G. Frey, S. Witt, K. Felderer, and R. Guckenberger, "High-resolution imaging of single fluorescent molecules with the optical near-field of a metal tip," *Physical Review Letters*, vol. 93, no. 20, Article ID 200801, 2004.
- [69] J. N. Farahani, D. W. Pohl, H. J. Eisler, and B. Hecht, "Single quantum dot coupled to a scanning optical antenna: a tunable superemitter," *Physical Review Letters*, vol. 95, no. 1, Article ID 017402, pp. 1–4, 2005.
- [70] T. H. Taminiau, R. J. Moerland, F. B. Segerink, L. Kuipers, and N. F. Van Hulst, " $\lambda/4$ resonance of an optical monopole antenna probed by single molecule fluorescence," *Nano Letters*, vol. 7, no. 1, pp. 28–33, 2007.
- [71] J. Dorfmüller, R. Vogelgesang, R. T. Weitz et al., "Fabry-Pérot resonances in one-dimensional plasmonic nanostructures," *Nano Letters*, vol. 9, no. 6, pp. 2372–2377, 2009.
- [72] J. Dorfmüller, R. Vogelgesang, W. Khunsin, C. Rockstuhl, C. Etrich, and K. Kern, "Plasmonic nanowire antennas: experiment, simulation, and theory," *Nano Letters*, vol. 10, no. 9, pp. 3596–3603, 2010.
- [73] M. Schnell, A. García-Etxarri, A. J. Huber, K. Crozier, J. Aizpurua, and R. Hillenbrand, "Controlling the near-field oscillations of loaded plasmonic nanoantennas," *Nature Photonics*, vol. 3, no. 5, pp. 287–291, 2009.
- [74] P. Alonso-Gonzalez, M. Schnell, P. Sarriugarte et al., "Real-space mapping of Fano interference in plasmonic metamolecules," *Nano Letters*, vol. 11, no. 9, pp. 3922–3926, 2011.
- [75] N. Félijd, G. Laurent, J. Grand et al., "Far-field raman imaging of short-wavelength particle plasmons on gold nanorods," *Plasmonics*, vol. 1, no. 1, pp. 35–39, 2006.
- [76] G. Laurent, N. Félijd, J. Aubard et al., "Evidence of multipolar excitations in surface enhanced Raman scattering," *Physical Review B*, vol. 71, no. 4, pp. 1–6, 2005.
- [77] C. Nobile, V. A. Fonoberov, S. Kudera et al., "Confined optical phonon modes in aligned nanorod arrays detected by resonant inelastic light scattering," *Nano Letters*, vol. 7, no. 2, pp. 476–479, 2007.
- [78] M. Pelton, M. Liu, S. Park, N. F. Scherer, and P. Guyot-Sionnest, "Ultrafast resonant optical scattering from single gold nanorods: large nonlinearities and plasmon saturation," *Physical Review B*, vol. 73, no. 15, Article ID 155419, pp. 1–6, 2006.
- [79] J. P. Hoogenboom, A. L. Lereu, and N. F. van Hulst, "Fabrication of molecular plasmonic devices with localized, subdiffraction-limit control over molecular positions," *Patent*. In press.

- [80] J. P. Hoogenboom, G. Sanchez-Mosteiro, G. C. Des Francs et al., "The single molecule probe: nanoscale vectorial mapping of photonic mode density in a metal nanocavity," *Nano Letters*, vol. 9, no. 3, pp. 1189–1195, 2009.
- [81] A. Kinkhabwala, Z. Yu, S. Fan, Y. Avlasevich, K. Müllen, and W. E. Moerner, "Large single-molecule fluorescence enhancements produced by a bowtie nanoantenna," *Nature Photonics*, vol. 3, no. 11, pp. 654–657, 2009.
- [82] R. P. Van Duyne, "Molecular plasmonics," *Science*, vol. 306, no. 5698, pp. 985–986, 2004.
- [83] O. L. Muskens, V. Giannini, J. A. Sánchez-Gil, and J. Gómez Rivas, "Strong enhancement of the radiative decay rate of emitters by single plasmonic nanoantennas," *Nano Letters*, vol. 7, no. 9, pp. 2871–2875, 2007.
- [84] G. P. Wiederrecht, J. E. Hall, and A. Bouhelier, "Control of molecular energy redistribution pathways via surface plasmon gating," *Physical Review Letters*, vol. 98, no. 8, Article ID 083001, 2007.
- [85] O. G. Tovmachenko, C. Graf, D. J. Van Den Heuvel, A. Van Blaaderen, and H. C. Gerritsen, "Fluorescence enhancement by metal-core/silica-shell nanoparticles," *Advanced Materials*, vol. 18, no. 1, pp. 91–95, 2006.
- [86] F. Tam, G. P. Goodrich, B. R. Johnson, and N. J. Halas, "Plasmonic enhancement of molecular fluorescence," *Nano Letters*, vol. 7, no. 2, pp. 496–501, 2007.
- [87] Y. Fedutik, V. Temnov, U. Woggon, E. Ustinovich, and M. Artemyev, "Exciton-plasmon interaction in a composite metal-insulator-semiconductor nanowire system," *Journal of the American Chemical Society*, vol. 129, no. 48, pp. 14939–14945, 2007.
- [88] A. G. Curto, G. Volpe, T. H. Taminiau, M. P. Kreuzer, R. Quidant, and N. F. Van Hulst, "Unidirectional emission of a quantum dot coupled to a nanoantenna," *Science*, vol. 329, no. 5994, pp. 930–933, 2010.
- [89] G. V. Hartland, M. Hu, O. Wilson, P. Mulvaney, and J. E. Sader, "Coherent excitation of vibrational modes in gold nanorods," *Journal of Physical Chemistry B*, vol. 106, no. 4, pp. 743–747, 2002.
- [90] H. M. Chen, H. C. Peng, R. S. Liu et al., "Controlling the length and shape of gold nanorods," *Journal of Physical Chemistry B*, vol. 109, no. 42, pp. 19553–19555, 2005.
- [91] P. K. Jain, S. Eustis, and M. A. El-Sayed, "Plasmon coupling in nanorod assemblies: optical absorption, discrete dipole approximation simulation, and exciton-coupling model," *Journal of Physical Chemistry B*, vol. 110, no. 37, pp. 18243–18253, 2006.
- [92] P. Mulvaney, J. Pérez-Juste, M. Giersig, L. M. Liz-Marzán, and C. Pecharromán, "Drastic surface plasmon mode shifts in gold nanorods due to electron charging," *Plasmonics*, vol. 1, no. 1, pp. 61–66, 2006.
- [93] R. Zanella, A. Sandoval, P. Santiago, V. A. Basiuk, and J. M. Saniger, "New preparation method of gold nanoparticles on SiO₂," *Journal of Physical Chemistry B*, vol. 110, no. 17, pp. 8559–8565, 2006.
- [94] B. J. Wiley, Y. Chen, J. M. McLellan et al., "Synthesis and optical properties of silver nanobars and nanorice," *Nano Letters*, vol. 7, no. 4, pp. 1032–1036, 2007.
- [95] T. Ito and S. Okazaki, "Pushing the limits of lithography," *Nature*, vol. 406, no. 6799, pp. 1027–1031, 2000.
- [96] C. L. Haynes and R. P. Van Duyne, "Nanosphere lithography: a versatile nanofabrication tool for studies of size-dependent nanoparticle optics," *Journal of Physical Chemistry B*, vol. 105, no. 24, pp. 5599–5611, 2001.
- [97] N. F. Van Hulst, J. A. Veerman, M. F. García-Parajó, and L. Kuipers, "Analysis of individual (macro)molecules and proteins using near-field optics," *Journal of Chemical Physics*, vol. 112, no. 18, pp. 7799–7810, 2000.
- [98] J. Hernando, J. P. Hoogenboom, E. M. H. P. Van Dijk et al., "Single molecule photobleaching probes the exciton wave function in a multichromophoric system," *Physical Review Letters*, vol. 93, no. 23, Article ID 236404, 2004.
- [99] J. P. Hoogenboom, E. M. H. P. Van Dijk, J. Hernando, N. F. Van Hulst, and M. F. García-Parajó, "Power-law-distributed dark states are the main pathway for photobleaching of single organic molecules," *Physical Review Letters*, vol. 95, no. 9, Article ID 097401, pp. 1–4, 2005.
- [100] N. A. M. Verhaegh and A. Van Blaaderen, "Dispersions of rhodamine-labeled silica spheres: synthesis, characterization, and fluorescence confocal scanning laser microscopy," *Langmuir*, vol. 10, no. 5, pp. 1427–1438, 1994.

Research Article

Antenna Design for Directivity-Enhanced Raman Spectroscopy

Aftab Ahmed, Yuanjie Pang, Ghazal Hajisalem, and Reuven Gordon

Department of Electrical and Computer Engineering, University of Victoria, Victoria, BC, Canada V8W 3P6

Correspondence should be addressed to Reuven Gordon, rgordon@uvic.ca

Received 1 October 2011; Revised 22 December 2011; Accepted 4 January 2012

Academic Editor: Nicolas Bonod

Copyright © 2012 Aftab Ahmed et al. This is an open access article distributed under the Creative Commons Attribution License, which permits unrestricted use, distribution, and reproduction in any medium, provided the original work is properly cited.

Antenna performance can be described by two fundamental parameters: directivity and radiation efficiency. Here, we demonstrate nanoantenna designs in terms of improved directivity. Performance of the antennas is demonstrated in Raman scattering experiments. The radiated beam is directed out of the plane by using a ground plane reflector for easy integration with commercial microscopes. Parasitic elements and parabolic and waveguide nanoantennas with a ground plane are explored. The nanoantennas were fabricated by a series of electron beam evaporation steps and focused ion beam milling. As we have shown previously, the circular waveguide nanoantenna boosts the measured Raman signal by 5.5x with respect to a dipole antenna over a ground plane; here, we present the design process that led to the development of that circular waveguide nanoantenna. This work also shows that the parabolic nanoantenna produces a further fourfold improvement in the measured Raman signal with respect to a circular waveguide nanoantenna. The present designs are nearly optimal in the sense that almost all the beam power is coupled into the numerical aperture of the microscope. These designs can find applications in microscopy, spectroscopy, light-emitting devices, photovoltaics, single-photon sources, and sensing.

1. Introduction

Antennas have been widely used in radio communications for more than a century for efficient transmission of information over long distances. Since its discovery in 1895, enormous progress has been made with better control of antenna parameters (for a brief history see [1] and references therein). For example, directional emission was demonstrated by Yagi-Uda in the microwave regime [2] where the radiation from the feed element is directed with the assistance of reflector and director parasitic elements. The directivity of antennas has played a vital role in microwave communication systems, specifically in satellite communication for the realization of high-gain antennas.

Radio antennas provide solutions to communication problems, whereas recent developments for realization of optical antennas were mainly dictated by microscopy and spectroscopy applications [3, 4]. Typically antennas have dimensions of the order of the operating wavelength, requiring antenna dimensions in nanometers for operation in the visible regime. In the visible-IR regime, the metal cannot be taken as a perfect conductor and the nanoantenna design must be modified due to plasmonic properties [5–8]. Recent

developments in the nanotechnology have made the fabrication of such small structures possible, leading to the development of optical single element and Yagi-Uda equivalent nanoantennas [9–20]. Directing the emission from optical emitters is highly desired for efficient detection and, by reciprocity, efficient excitation as well. Typical applications include light-emitting devices [21, 22], photovoltaics [23–27], sensing [28, 29], spectroscopy [30–32], single-photon sources [33, 34], and microscopy [3, 35, 36].

In a recent work, our group has shown that the scattered radiation from nanoparticles can be directed out of the plane of substrate and into the collection microscope using a ground plane reflector [37]. Enhancement of over 50x was observed in the measured Raman signal as compared to nanoprisms over a glass substrate. We also demonstrated recently an experimental work on waveguide nanoantenna to boost the Raman signal by beam forming in the lateral plane [38]. A further 5.5x enhancement was observed with a circular waveguide nanoantenna as compared to a dipole nanoantenna over a ground plane.

The main objective of this work is to present the design of planar nanoantennas for optimal performance in directivity-enhanced Raman scattering (DERS). Here, we present the

details of the design process that led to the development of circular waveguide nanoantenna, the different designs considered for beam forming in the lateral plane, and the possibility of higher local fields for further Raman enhancement. We also show experimentally that the parabolic reflector can enhance the Raman signal by 4x as compared to the circular waveguide nanoantenna owing to its improved directivity and enhanced local fields; however, it is challenging to fabricate.

2. Antenna Design Parameters

The total power radiated by an antenna can be given as

$$P_{\text{rad}} = \int_0^{2\pi} \int_0^\pi p(\theta, \phi) \sin(\theta) d\theta d\phi, \quad (1)$$

where $p(\theta, \phi)$ is the normalized angular power density also known as radiation pattern of an antenna. Directivity is defined as the antennas ability to radiate in a specific direction more efficiently as compared to a hypothetical isotropic radiator [39]:

$$D = \frac{4\pi}{P_{\text{rad}}} p(\theta, \phi). \quad (2)$$

Considering the numerical aperture (NA) of the microscope objective, a more suitable parameter for describing the beam forming ability of an antenna is the beam efficiency (BE):

$$\text{BE} = \frac{\int_0^{2\pi} \int_0^{\theta_0} p(\theta, \phi) \sin(\theta) d\theta d\phi}{P_{\text{rad}}}, \quad (3)$$

where θ_0 is the cone half angle. Cone angle of 30 degrees was calculated from the measured spot size “ d ” of approximately 1.5 μm , using $\theta_0 = \sin^{-1}(\lambda/2d)$. This corresponds to an NA of 0.28.

Radiation patterns of single element nanoantennas are typically dipolar in nature resulting in poor directivity ($D_{\text{max}} = 1.5$). Directive emission at optical wavelengths has been achieved using multielement nanoantennas [11, 13, 40]. Radiation patterns of those antennas reveal that the main beam is directed in the plane of the substrate, thus cannot be readily used in an ordinary microscope setup. Further, vertical Yagi-Uda nanoantenna has been realized using top-down approach [15]. Improved directivity at optical wavelengths can have tremendous impact in areas such as optical microscopy, spectroscopy, sensing, and applications involving single-photon sources, where efficient collection and emission is critical.

Another important factor in the context of Raman measurements is the local field strength. It has been recently shown that maximum field enhancement results when power radiated by the antenna is equal to the power loss in the antenna [41–43]. This is commonly referred to as impedance matching in microwave antenna theory [39]. Even higher local field can be achieved by reducing the mode volume of the antenna by reducing the feed gap between the two elements of the dipole antenna [43].

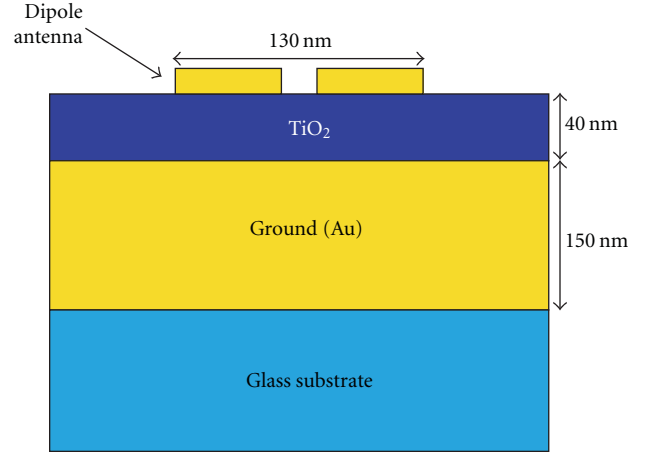


FIGURE 1: Multilayer substrate to control the radiation pattern of a dipole antenna. Thicknesses of ground plane, dielectric (TiO_2) spacer, and top gold layer are 150 nm, 40 nm, and 50 nm, respectively. Dipole antenna length of 130 nm with a 20 nm feed gap was used to operate at wavelength of 840 nm.

3. Design and Fabrication

In this paper we investigate different nanoantenna designs for DERS with the desired features of out-of-plane radiation and enhanced local fields. The introduction of ground plane prevents loss of scattered radiation into the substrate and proper adjustment of antenna distance from the ground plane can result in radiation enhancement out of the plane. Further improvement of directivity is demonstrated by beam shaping in the lateral plane using different designs including parasitic elements, waveguide antennas, and parabolic reflectors. The multilayer substrate is fabricated by electron beam evaporation, and the different designs are milled using focused ion beam (FIB).

Figure 1 illustrates the multilayer substrate used for the fabrication of nanoantennas studied in this work. The antennas were designed to be tested under Raman microscope. The dimensions of different layers and the dipole antenna were calculated to achieve best performance at wavelength of 840 nm (mean of excitation and Raman scattered wavelengths). The antenna consists of a 130 nm long and 50 nm wide dipole. Traditionally, dipole antenna characteristic lengths were of the order of wavelength of operation ($\lambda/2$), but the real metal response requires that shorter effective wavelengths are introduced for the determination of dipole length in infrared and optical regions [7]. A 150 nm thick gold layer was used as ground plane to ensure that it was optically thick.

The optimal thickness of dielectric spacer (TiO_2) was calculated numerically to be 40 nm using finite-difference time-domain (FDTD) simulations. It should be noted that this is smaller than the typical quarter wavelength value due to penetration into the metal, as well as impedance matching effects [43].

The multilayer substrate was fabricated by evaporation of gold and TiO_2 onto glass substrate by means of electron beam evaporation under a pressure of 2×10^{-6} Torr. The

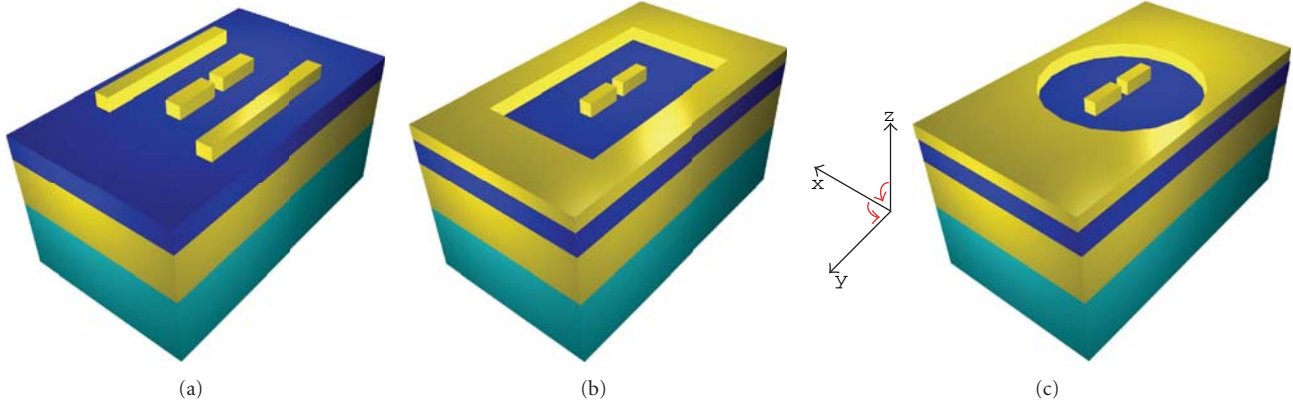


FIGURE 2: (a) Dipole antenna over ground with two parasitic reflectors 150 nm long and 100 nm from the feed element. (b) Dipole antenna over ground plane with a square reflector of length 500 nm (square waveguide antenna). (c) Dipole antenna over ground plane with a circular reflector of radius 250 nm (circular waveguide antenna).

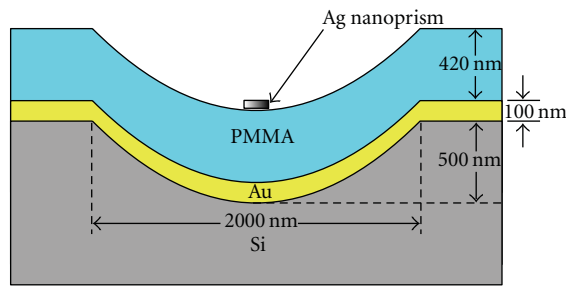


FIGURE 3: The schematic drawing of the proposed parabolic reflector nanoantenna.

proposed nanoantenna structures were milled on the top 50 nm thick gold layer using FIB. Figure 2 shows the different nanoantennas investigated in this work for normal emission. Relative efficiencies of these structures are discussed in the simulation section below, where it is shown that the circular waveguide nanoantenna shown in Figure 2(c) results in best performance in terms of directivity.

Another promising design translated from the microwave antenna theory is that of the parabolic reflector antenna. We demonstrate DERS from the beam forming abilities of a parabolic reflector nanoantenna. Figure 3 shows the schematic of the parabolic nanoantenna. A paraboloid-shaped trench was milled into a silicon wafer using FIB. As shown in the figure, the focal length of this paraboloid was designed to be 500 nm and the diameter of the top circle is 2 μm . A layer of 100 nm thick gold (optically thick) was evaporated onto the silicon wafer by means of electron beam evaporation under a pressure of 2×10^{-6} Torr.

The conformity of the evaporated layer to the hole in silicon creates a parabolic reflector antenna on Au layer. PMMA was then spin-coated on top of the Au layer as a spacing dielectric layer. We chose PMMA and the spin-coating technique to make the spacer layer for reasons of simplicity and repeatable thickness control. Finally, Ag nanoprisms, synthesized in water by white-light assisted conversion of spherical nanoparticles [44], were mixed with

3 μMol rhodamine 6 G dye and drop-coated onto the PMMA surface. The nanoprisms serve as the feed of the parabolic reflector nanoantenna.

The experiments of [37] are first repeated using PMMA for the determination of optimal thickness of the PMMA layer. As a result (not shown), the first- and second-order coherent SERS enhancement peaks are found at 120 nm and 420 nm PMMA thickness. We choose to spin-coat 420 nm PMMA (corresponding to the second-order SERS enhancement) onto our parabolic reflector since this thickness is more compatible with the focal length of our parabolic reflector, bringing the feed Ag nanoprism near the paraboloid focal point.

4. Simulation Results

The proposed structures were simulated using the FDTD method. The simulation domain was terminated by perfectly matched layers (PMLs) for minimal reflections. The antenna structure was enclosed by a set of 2D field monitors forming a box to perform far-field projections and for the determination of field patterns. For the antenna structures shown in Figure 2, an electric dipole source located at the feed gap of the dipole antenna was used to excite the nanoantenna.

FDTD simulations indicate the following parameters for best performance for each type of antenna. Two 150 nm long parasitic reflectors, 100 nm away from the feed element, resulted in a half power beam width (HPBW) of 110 degrees in the xz plane. Radiation patterns of this structure show a very broad HPBW in the yz plane. To further improve the directivity in both planes we introduced reflectors parallel to the x -axis as well. It was demonstrated numerically that a square reflector with length of 500 nm resulted in best performance. The corresponding HPBWs are 85 degrees and 90 degrees in the xz and yz planes, respectively. Even better performance is observed by using a circular waveguide antenna as shown in Figure 2(c), producing a symmetrical beam out of the plane of substrate with HPBW of 85 degrees in both planes. Figures 4(a) and 4(b) shows the radiation

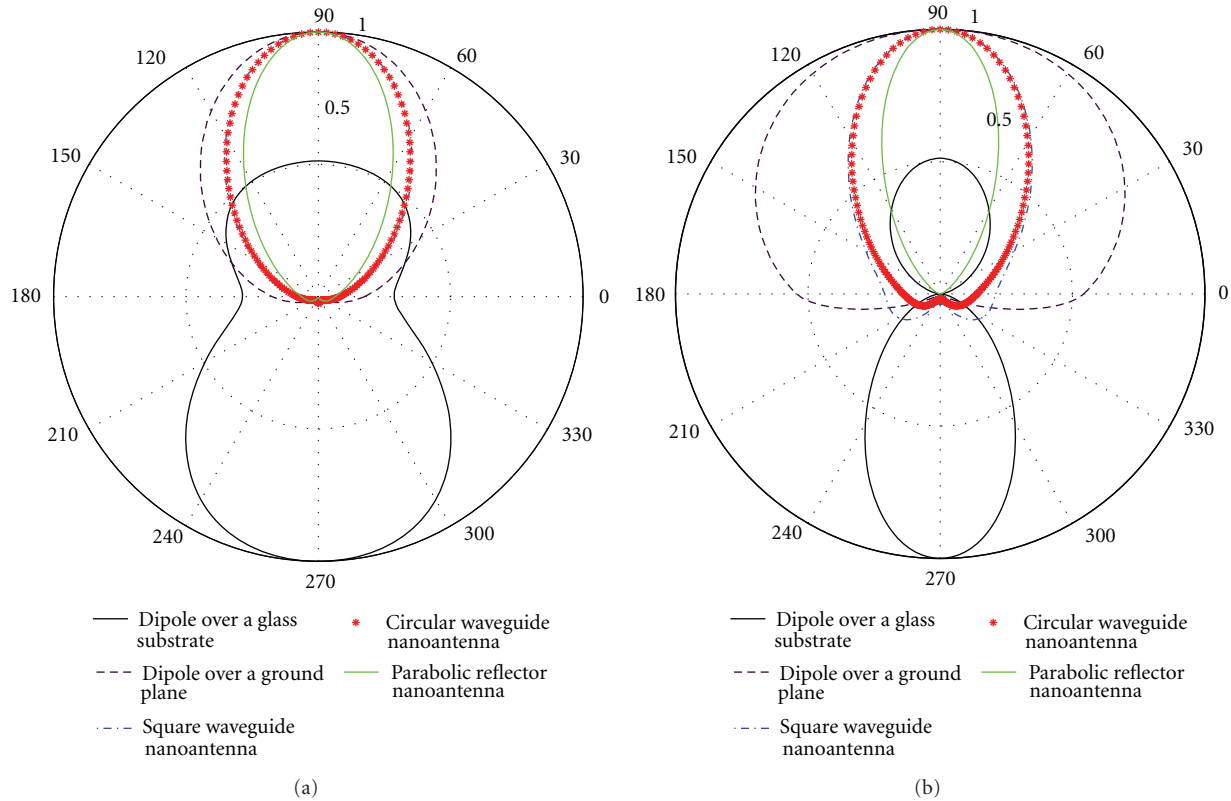


FIGURE 4: Radiation patterns of a dipole antenna on a glass substrate, dipole over ground plane, square waveguide nanoantenna (side length = 500 nm), circular waveguide nanoantenna (radius = 250 nm), and parabolic reflector nanoantenna. Calculated using far-field projections of 3D FDTD simulations, (a) xz plane, (b) yz plane.

pattern in the xz and yz planes, respectively, at the wavelength of 840 nm. It can be seen that in the absence of ground reflector, most of the scattered power is directed into the substrate and away from the microscope objective.

The circular waveguide nanoantenna gives a nearly optimal radiation pattern resulting in the collection of almost all of the scattered light by a numerical aperture of 0.75. The radiation patterns of the parabolic reflector are also plotted in Figure 4 for comparison. It can be seen that the parabolic reflector nanoantenna results in an even better directivity as compared to the circular waveguide nanoantenna.

The ring reflector acts to create a lateral standing wave that reflects light back towards the central dipole antenna structure. This is most similar to the waveguide antenna, which has a lateral resonance when the wavelength is $3.4\times$ the radius of the circular waveguide (i.e., at the lowest order mode cut-off) [39, 45]. Larger and smaller radii do not provide this resonance at the desired wavelength of 840 nm and thus give smaller directivities. The radiation patterns of circular waveguide nanoantenna with slightly smaller and larger radii (not shown) show splitting of the main beam into two lobes, thus lowering the directivity in the normal direction.

Since the present design is optimized to work at around 840 nm, this corresponds to a radius of 250 nm, which is precisely the radius value that was found to give the

greatest DERS in the experiment. The beam forming for this antenna design allows for directive emission into a numerical aperture of approximately 0.75; therefore, it is well suited for microscope setups.

Another parameter dictating the intensity of Raman signal is the local field enhancement that arises from plasmonic resonances, tapers, gaps, and high curvature in the antenna design [46, 47]. Impedance matching and reduction of mode volume of the antenna provide maximum local field enhancement [43]. Figures 5(a) and 5(b) show the local field intensity in the antenna gap for gap sizes of 20 and 5 nm, respectively, at the design wavelength of 840 nm (log scale).

By reducing the gap size from 20 nm to 5 nm, the normalized E field intensity $(|E|/|E_0|)^2$ increases by approximately 1000x. Intensity of Raman signal is proportional to the square of E field intensity, thus we expect an enhancement of 10^6 . The feed gap of the fabricated circular waveguide nanoantenna was 20 nm. Thus, it is clear that the Raman signal can be considerably enhanced by reducing the feed gap, which is a challenging task.

Now we present the simulation results of the parabolic reflector nanoantenna. Figure 6 shows the electric field intensity profile at a vertical segment of the structures at the design wavelength of 840 nm. It can be seen that the local field intensity at the Ag prism over a parabolic reflector is much larger than that over a planar reflector. From the

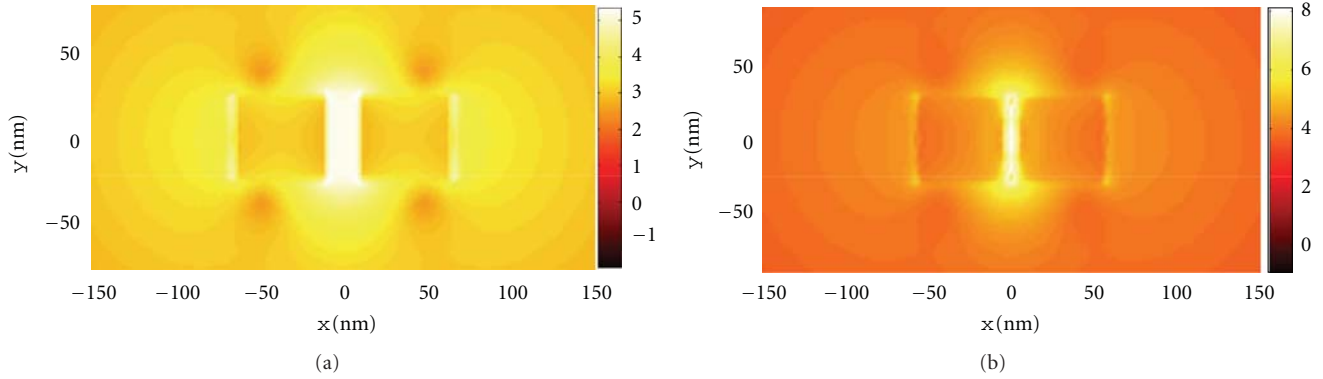


FIGURE 5: E field intensity $(|E|/|E_0|)^2$ at the design wavelength of 840 nm for (a) gap size of 20 nm and (b) gap size of 5 nm (log scale).

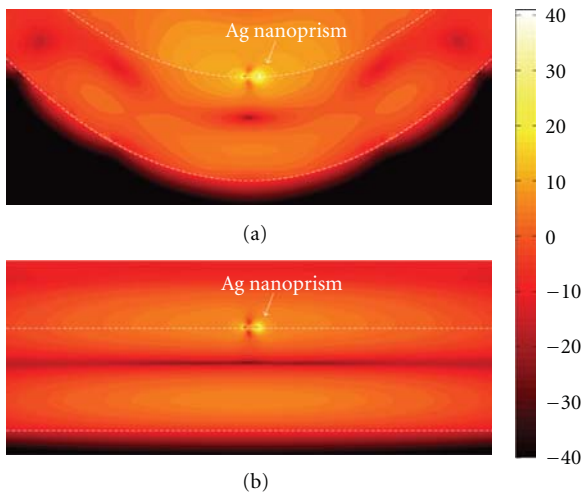


FIGURE 6: FDTD simulation results comparing the vertical segment electric field intensity profiles of an Ag nanoprism above (a) a parabolic reflector and (b) a planar reflector. The white dotted lines show the Au ground plane and the PMMA layer surfaces. The color map is in dB scale.

field intensity profiles in the PMMA layer, it can be seen that the Ag nanoprism is placed at the second antinode of the parabolic reflector at 840 nm wavelength, the same as in the planar reflector case; it is also at the focal point of the paraboloid. Therefore, the two effects, constructive interference and focusing, combine to give the enhanced Raman signal. Our parabolic reflector is able to collect more power from the incoming Gaussian wave to the Ag nanoprism feed element, indicating a better coupling between the far and the near field or, in a conventional antenna concept, a higher directivity.

In terms of Raman enhancement at the Ag nanoprism feed element, the relative Raman signal enhancement is proportional to the product of the excitation field intensity $|E_{\text{exc}}|^2$ and the emitted Raman field intensity $|E_{\text{raman}}|^2$. The Raman enhancement factor was computed at the near field of the Ag prism (within a rectangular box 10 nm away from the Ag prism). It was found from the local field enhancement

that the Raman enhancement near an Ag prism in a parabolic reflector arrangement is 40x larger than in a planar reflector arrangement. It is due to this high local field effect that the parabolic reflector nanoantenna results in a stronger Raman signal as compared to the circular waveguide nanoantenna (of Figure 2(c)), which produces only 1.2x enhancement of the local field by the introduction of the circular ring around the dipole over a ground plane.

5. Raman Scattering Experiments

Raman scattering experiments were carried out for the fabricated circular waveguide and parabolic antennas using Rhodamine 6 G as the Raman dye excited by a 785 nm laser. For this CW excitation, there is negligible two-photon fluorescence, which would show up as background in the Raman spectrum. The emitted wavelength at 1509 cm^{-1} Stokes line ($\lambda = 890 \text{ nm}$) was measured using a Renishaw inVia Raman microscope with a 100x objective and a spot size “ d ” of approximately $1.5 \mu\text{m}$ (as determined by mapping experiments). Raman dye, Rhodamine 6 G ($400 \mu\text{M}$ in ethanol), was drop-coated, and the sample was allowed to dry for 6 hours.

Figure 7(a) shows the measured Raman signal intensity as a function of Raman shift using the circular waveguide nanoantenna. The circular reflector with radius of 250 nm resulted in the strongest DERS signal as is predicted by the numerical results of Figure 4.

For comparison, detected intensities from dipole over ground and from the unmilled regions of the top gold surface (without any dipole antenna) are also shown. A dipole antenna of the same dimensions and on the same substrate was fabricated by removing a ring of diameter $10 \mu\text{m}$, to approximate the absence of the ring structure. This dipole over ground is used as the reference for the calculation of EF. The measured spot size of $1.5 \mu\text{m}$ results in illumination of an area of $1.76 (\mu\text{m})^2$, which is much larger than the area of the antenna gap. From the results of Figure 7(a), it can be seen that the contribution from the gold surface alone (i.e., without the antenna) is small when compared to that from the antenna. It should be noted that the Raman scattering intensity is boosted about 5.5x as compared to

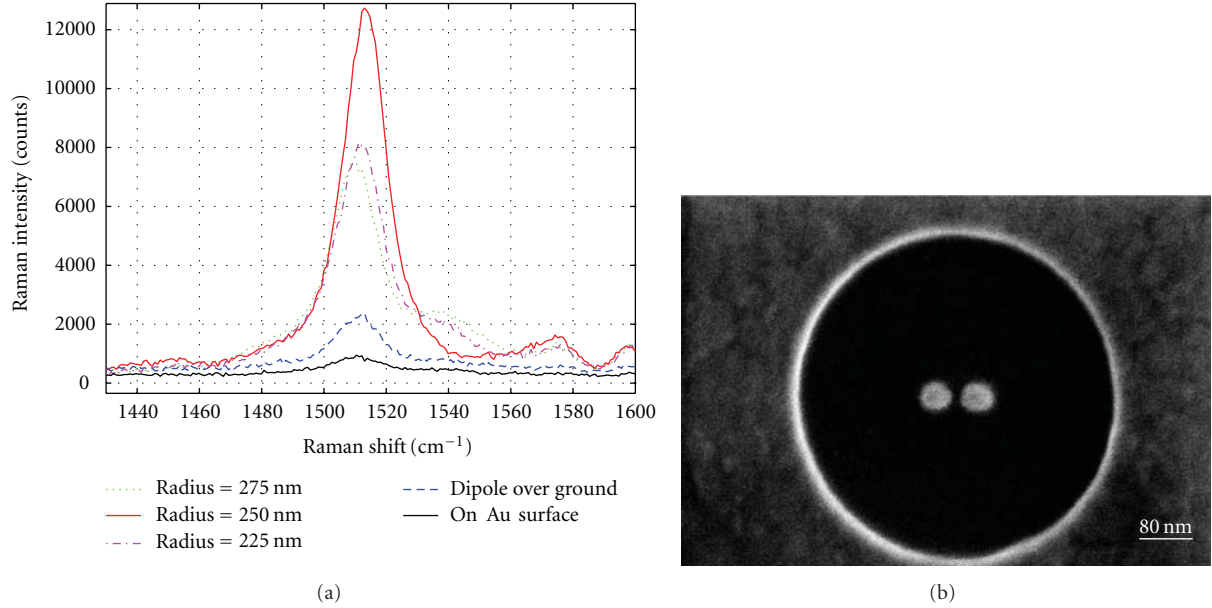


FIGURE 7: (a) Raman spectra from the nanoantenna structure for various radii of circular reflector, dipole over a ground plane, and the top unmilled Au surface. (b) Scanning electron microscopy image of the fabricated circular waveguide nanoantenna.

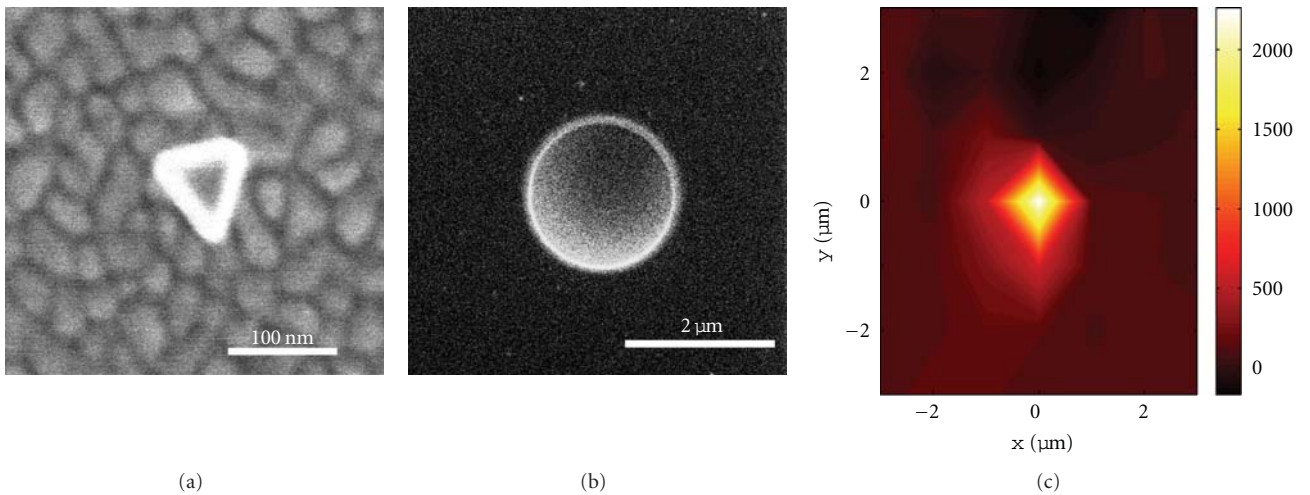


FIGURE 8: (a) Scanning electron microscopy image of Ag nanoprism. (b) A scanning ion microscope image of the paraboloid drilled on silicon taken directly from the FIB. (c) A $6 \times 6 \mu\text{m}^2$ map of the Raman signal around a parabolic reflector nanoantenna.

dipole over ground and about 13x with respect to the top Au surface. Note that this 5.5x increase is in addition to the 50x signal increase by use of the ground plane [37], and this additional enhancement is attributed to the improved directivity of the ring structure. Thus, the total enhancement from the circular waveguide nanoantenna can be estimated to be 275x as compared to nanoparticles on a glass substrate. Figure 7(b) shows an SEM image of the fabricated circular waveguide nanoantenna.

To demonstrate that the observed increase in Raman intensity is mainly from antenna directivity and with only a small contribution from local field enhancement, we calculated the enhancement factor arising from local electric

field (EF_{loc}) in the antenna feed gap. $EF_{\text{loc}} = |E_{\text{exc}}|^2 |E_{\text{scat}}|^2$, where $|E_{\text{exc}}|^2$ and $|E_{\text{scat}}|^2$ are the electric field intensities at the excitation wavelength of 785 nm and Stokes shifted scattered radiation at wavelength of 890 nm, respectively. We observe maximum $EF_{\text{loc}} = 1.2$. The measured 5.5x increase in Raman intensity is thus predominantly from improved directivity of the antenna. Numerically calculated EF using beam efficiency and radiation patterns of Figure 4 with cone angle of 30 degrees is in excellent agreement with the experimental results.

Figure 8(a) shows an SEM of an Ag nanoprism, the scanning ion microscope image of the fabricated structure (Figure 8(b)), and a $6 \times 6 \mu\text{m}^2$ map of the Raman signal

using the 1509 cm^{-1} Stokes line around a parabolic reflector nanoantenna (Figure 8(c)). A clear enhancement to the Raman signal is obtained from the parabolic reflector nanoantenna as compared to the surrounding area, where it is equivalent to a planar reflector nanoantenna. By comparing the maximum Raman signal from a parabolic reflector nanoantenna to the average surrounding signal, a 22x enhancement is obtained.

Our previous experiments on Ag nanoprism over planar reflector experiments have already shown a 50x Raman enhancement as compared to Ag nanoprisms on glass (without any reflector) [37]. Combining the result of this work and [37], we estimate that our designed parabolic reflector structure can enhance the SERS signal from metallic nanoprisms by 1100x. In other words, by directivity engineering, we have boosted the SERS signal from isolated metallic nanoprisms by 3 orders of magnitude.

We confirm that this high signal is not from an aggregation of nanoprisms by taking an SEM image of the antenna. We explain the Raman enhancement with respect to only nanoprisms on glass substrate by the high directivity from the parabolic antenna and enhanced local fields. In an SERS experiment where the nanoprisms are deposited directly onto glass, the light emission is in favor of the direction into the glass substrate due to higher refractive index of the glass. In comparison, the parabolic antenna gives an emission pattern with a tightly focused lobe into the air, with nearly all emitted light directed into the collecting microscope objective. In other words, we have improved the near- and far-field coupling from a poor efficiency to a nearly perfect efficiency by the parabolic antenna. Therefore, the 1100x enhancement between the two cases is not surprising.

The 22x SERS enhancement over the planar reflector from our experiment is very encouraging but is still an underestimate of the parabolic reflector nanoantenna DERS enhancement potential—still lower than our theoretical prediction of 40x enhancement. This may be due to the misalignment between the Ag nanoprism feed element and the Au parabolic reflector in the nanoantenna. The drop-coating technique is convenient to deposit the Ag nanoprisms; however, exactly controlling the nanoprism position is difficult. In future steps, we plan to build the metal feed element using lithographical methods such as FIB lithography. In that way, the position of the feed element can be precisely controlled, and an even higher SERS enhancement is hypothesized.

6. Conclusions

We have demonstrated directivity-enhanced Raman scattering (DERS) using directive nanoantennas including parasitic elements and parabolic and waveguide designs. The circular waveguide nanoantenna with a feed gap of 20 nm produces an enhancement factor of 275x as compared to nanoparticles over a glass substrate. This enhancement factor can be further increased by reducing the feed gap. Parabolic reflector results in an overall enhancement factor of 1100x as compared to nanoprisms over a glass substrate; however, as demonstrated in this work, the fabrication of the parabolic

structure is more challenging. The enhancement in these waveguide designs is specifically attributed to directivity effects, that is, beam-shaping the antenna cone to fall within the numerical aperture of the imaging optics. Therefore, DERS is separate from other near-field enhancements that arise, for example, from plasmonic effects. Considering the numerical aperture of our microscope Raman system, the nanoantenna presented has near-perfect excitation and collection of the electromagnetic energy. This work is also exciting for related applications, for example, photovoltaics, light-emitting applications, microscopy, sensing, and single-molecule detection [29, 31, 36].

Acknowledgment

The authors acknowledge support from NSERC Strategic Network for Bioplasmonic Systems (BiopSys), Canada.

References

- [1] P. Bharadwaj et al., "Optical antennas," *Advances in Optics and Photonics*, vol. 1, pp. 438–483, 2009.
- [2] H. Yagi, "Beam transmission of ultra short waves," *Proceedings of the IEEE*, vol. 16, pp. 715–741, 1928.
- [3] A. Hartschuh, H. Qian, C. Georgi, M. Böhmeler, and L. Novotny, "Tip-enhanced near-field optical microscopy of carbon nanotubes," *Analytical and Bioanalytical Chemistry*, vol. 394, no. 7, pp. 1787–1795, 2009.
- [4] S. Kawata and Y. Inouye, "Scanning probe optical microscopy using a metallic probe tip," *Ultramicroscopy*, vol. 57, no. 2-3, pp. 313–317, 1995.
- [5] C. Fumeaux, M. A. Gritz, I. Codreanu, W. L. Schaich, F. J. González, and G. D. Boreman, "Measurement of the resonant lengths of infrared dipole antennas," *Infrared Physics and Technology*, vol. 41, no. 5, pp. 271–281, 2000.
- [6] F. Neubrech, T. Kolb, R. Lovrincic et al., "Resonances of individual metal nanowires in the infrared," *Applied Physics Letters*, vol. 89, no. 25, Article ID 253104, 2006.
- [7] L. Novotny, "Effective wavelength scaling for optical antennas," *Physical Review Letters*, vol. 98, no. 26, Article ID 266802, 2007.
- [8] S. B. Hasan, R. Filter, A. Ahmed et al., "Relating localized nanoparticle resonances to an associated antenna problem," *Physical Review B*, vol. 84, no. 19, 2011.
- [9] J. N. Farahani, D. W. Pohl, H. J. Eisler, and B. Hecht, "Single quantum dot coupled to a scanning optical antenna: a tunable superemitter," *Physical Review Letters*, vol. 95, no. 1, Article ID 017402, pp. 1–4, 2005.
- [10] S. Kühn, U. Håkanson, L. Rogobete, and V. Sandoghdar, "Enhancement of single-molecule fluorescence using a gold nanoparticle as an optical nanoantenna," *Physical Review Letters*, vol. 97, no. 1, Article ID 017402, 2006.
- [11] T. H. Taminiau, F. D. Stefani, F. B. Segerink, and N. F. Van Hulst, "Optical antennas direct single-molecule emission," *Nature Photonics*, vol. 2, no. 4, pp. 234–237, 2008.
- [12] A. Sundaramurthy, P. J. Schuck, N. R. Conley, D. P. Fromm, G. S. Kino, and W. E. Moerner, "Toward nanometer-scale optical photolithography: utilizing the near-field of bowtie optical nanoantennas," *Nano Letters*, vol. 6, no. 3, pp. 355–360, 2006.
- [13] A. G. Curto, G. Volpe, T. H. Taminiau, M. P. Kreuzer, R. Quidant, and N. F. Van Hulst, "Unidirectional emission of a

- quantum dot coupled to a nanoantenna," *Science*, vol. 329, no. 5994, pp. 930–933, 2010.
- [14] H. Wang, D. W. Brandl, F. Le, P. Nordlander, and N. J. Halas, "Nanorice: a hybrid plasmonic nanostructure," *Nano Letters*, vol. 6, no. 4, pp. 827–832, 2006.
- [15] D. Dregely, R. Taubert, J. Dorfmueller, R. Vogelgesang, K. Kern, and H. Giessen, "3D optical Yagi-Uda nanoantenna array," *Nature Communications*, vol. 2, no. 1, 2011.
- [16] P. Mühlischlegel, H. J. Eisler, O. J. F. Martin, B. Hecht, and D. W. Pohl, "Applied physics: resonant optical antennas," *Science*, vol. 308, no. 5728, pp. 1607–1609, 2005.
- [17] P. J. Schuck, D. P. Fromm, A. Sundaramurthy, G. S. Kino, and W. E. Moerner, "Improving the mismatch between light and nanoscale objects with gold bowtie nanoantennas," *Physical Review Letters*, vol. 94, no. 1, Article ID 017402, 2005.
- [18] P. Anger, P. Bharadwaj, and L. Novotny, "Enhancement and quenching of single-molecule fluorescence," *Physical Review Letters*, vol. 96, no. 11, Article ID 113002, pp. 1–4, 2006.
- [19] T. Kosako, Y. Kadoya, and H. F. Hofmann, "Directional control of light by a nano-optical Yagi-Uda antenna," *Nature Photonics*, vol. 4, no. 5, pp. 312–315, 2010.
- [20] S. Graells, S. Aćimović, G. Volpe, and R. Quidant, "Direct growth of optical antennas using e-beam-induced gold deposition," *Plasmonics*, vol. 5, no. 2, pp. 135–139, 2010.
- [21] E. Ozbay, "Plasmonics: merging photonics and electronics at nanoscale dimensions," *Science*, vol. 311, no. 5758, pp. 189–193, 2006.
- [22] S. Wedge, J. A. E. Wasey, W. L. Barnes, and I. Sage, "Coupled surface plasmon-polariton mediated photoluminescence from a top-emitting organic light-emitting structure," *Applied Physics Letters*, vol. 85, no. 2, pp. 182–184, 2004.
- [23] R. Corkish, M. A. Green, and T. Puzzer, "Solar energy collection by antennas," *Solar Energy*, vol. 73, no. 6, pp. 395–401, 2002.
- [24] S. Pillai, K. R. Catchpole, T. Trupke, and M. A. Green, "Surface plasmon enhanced silicon solar cells," *Journal of Applied Physics*, vol. 101, no. 9, Article ID 093105, 2007.
- [25] H. R. Stuart and D. G. Hall, "Absorption enhancement in silicon-on-insulator waveguides using metal island films," *Applied Physics Letters*, vol. 69, no. 16, pp. 2327–2329, 1996.
- [26] L. Tang, S. E. Kocabas, S. Latif et al., "Nanometre-scale germanium photodetector enhanced by a near-infrared dipole antenna," *Nature Photonics*, vol. 2, no. 4, pp. 226–229, 2008.
- [27] A. M. Marks, "Device for conversion of light to electric power," U.S. Patent 4,445,050, 1984.
- [28] C. C. Neacsu, J. Dreyer, N. Behr, and M. B. Raschke, "Scanning-probe Raman spectroscopy with single-molecule sensitivity," *Physical Review B*, vol. 73, no. 19, Article ID 193406, 2006.
- [29] N. Liu, M. L. Tang, M. Hentschel, H. Giessen, and A. P. Alivisatos, "Nanoantenna-enhanced gas sensing in a single tailored nanofocus," *Nature Materials*, vol. 10, no. 8, pp. 631–636, 2011.
- [30] S. A. Maier, "Plasmonic field enhancement and SERS in the effective mode volume picture," *Optics Express*, vol. 14, no. 5, pp. 1957–1964, 2006.
- [31] S. Nie and S. R. Emory, "Probing single molecules and single nanoparticles by surface-enhanced Raman scattering," *Science*, vol. 275, no. 5303, pp. 1102–1106, 1997.
- [32] H. Xu, E. J. Bjerneld, M. Käll, and L. Börjesson, "Spectroscopy of single hemoglobin molecules by surface enhanced Raman scattering," *Physical Review Letters*, vol. 83, no. 21, pp. 4357–4360, 1999.
- [33] J. Kim, O. Benson, H. Kan, and Y. Yamamoto, "A single-photon turnstile device," *Nature*, vol. 397, no. 6719, pp. 500–503, 1999.
- [34] B. Lounis and W. E. Moerner, "Single photons on demand from a single molecule at room temperature," *Nature*, vol. 407, no. 6803, pp. 491–493, 2000.
- [35] T. Kalkbrenner, U. Håkanson, A. Schädle, S. Burger, C. Henkel, and V. Sandoghdar, "Optical microscopy via spectral modifications of a nanoantenna," *Physical Review Letters*, vol. 95, no. 20, Article ID 200801, pp. 1–4, 2005.
- [36] C. Höppener and L. Novotny, "Antenna-based optical imaging of single Ca²⁺ transmembrane proteins in liquids," *Nano Letters*, vol. 8, no. 2, pp. 642–646, 2008.
- [37] Q. Min, Y. Pang, D. J. Collins et al., "Substrate-based platform for boosting the surface-enhanced Raman of plasmonic nanoparticles," *Optics Express*, vol. 19, no. 2, pp. 1648–1655, 2011.
- [38] A. Ahmed and R. Gordon, "Directivity enhanced raman spectroscopy using nanoantennas," *Nano Letters*, vol. 11, no. 4, pp. 1800–1803, 2011.
- [39] C. A. Balanis, *Antenna Theory Analysis and Design*, John Wiley and Sons, NJ, USA, 3rd edition, 2005.
- [40] T. Pakizeh and M. Käll, "Unidirectional ultracompact optical nanoantennas," *Nano Letters*, vol. 9, no. 6, pp. 2343–2349, 2009.
- [41] A. Alù and S. Maslovski, "Power relations and a consistent analytical model for receiving wire antennas," *IEEE Transactions on Antennas and Propagation*, vol. 58, no. 5, Article ID 5422725, pp. 1436–1448, 2010.
- [42] A. Al and N. Engheta, "Tuning the scattering response of optical nanoantennas with nanocircuit loads," *Nature Photonics*, vol. 2, no. 5, pp. 307–310, 2008.
- [43] T. J. Seok, A. Jamshidi, M. Kim et al., "Radiation engineering of optical antennas for maximum field enhancement," *Nano Letters*, vol. 11, no. 7, pp. 2606–2610, 2011.
- [44] R. Jin, Y. Cao, C. A. Mirkin, K. L. Kelly, G. C. Schatz, and J. G. Zheng, "Photoinduced conversion of silver nanospheres to nanoprisms," *Science*, vol. 294, no. 5548, pp. 1901–1903, 2001.
- [45] D. M. Pozar, *Microwave Engineering*, John Wiley and Sons, New York, NY, USA, 1998.
- [46] D. R. Ward, N. K. Grady, C. S. Levin et al., "Electromigrated nanoscale gaps for surface-enhanced Raman spectroscopy," *Nano Letters*, vol. 7, no. 5, pp. 1396–1400, 2007.
- [47] J. Theiss, P. Pavaskar, P. M. Echternach, R. E. Muller, and S. B. Cronin, "Plasmonic nanoparticle arrays with nanometer separation for high-performance SERS substrates," *Nano Letters*, vol. 10, no. 8, pp. 2749–2754, 2010.

Research Article

Absorption by an Optical Dipole Antenna in a Structured Environment

E. Castanié, R. Vincent, R. Pierrat, and R. Carminati

Institut Langevin, ESPCI ParisTech, CNRS, 10 Rue Vauquelin, 75231 Paris Cedex 05, France

Correspondence should be addressed to R. Pierrat, romain.pierrat@espci.fr

Received 31 October 2011; Accepted 13 December 2011

Academic Editor: Nicolas Bonod

Copyright © 2012 E. Castanié et al. This is an open access article distributed under the Creative Commons Attribution License, which permits unrestricted use, distribution, and reproduction in any medium, provided the original work is properly cited.

We compute generalized absorption and extinction cross-sections of an optical dipole nanoantenna in a structured environment. The expressions explicitly show the influence of radiation reaction and the local density of states on the intrinsic absorption properties of the antenna. Engineering the environment could allow to modify the overall absorption as well as the frequency and the linewidth of a resonant antenna. Conversely, a dipole antenna can be used to probe the photonic environment, in a similar way as a quantum emitter.

1. Introduction

It is well known that the emission frequency and linewidth of a dipole quantum emitter is modified by its local environment [1–4]. The linewidth directly depends on the photonic local density of states (LDOS) which accounts for the number of radiative and nonradiative channels available for the emitter to relax in the ground state. The change in the emission frequency and linewidth induced by the environment can be described by considering the transition dipole as a classical dipole oscillator [2, 4]. Therefore, similar behaviors are expected for a dipole antenna (or a nanoparticle) interacting with its environment, the involved dipole being in this case the *induced* dipole that is responsible for scattering and absorption. Indeed, changes in the induced dipole dynamics in optical antennas have already been observed [5, 6], and the parallel with spontaneous emission dynamics has been mentioned on a qualitative phenomenological ground. Energy shifts and linewidths of plasmonic nanoparticles have also been discussed recently, based on general properties of damped harmonic oscillators [7]. A connection between LDOS maps and the scattering pattern of plasmonic structures has been established in a specific imaging configuration [8]. In this context, it seems that a general discussion of the influence of the environment on the absorption of an optical dipole antenna or nanoparticle would be useful. The purpose of this paper is to address

this question, using a rigorous framework based on scattering theory, and to illustrate the conclusions on a simple example.

In this paper, we investigate the role of the environment on the absorption cross-section of an optical dipole antenna using a rigorous theoretical framework. We show that it is possible to modify the overall absorption and its spectral properties by engineering the environment, and in particular the photonic LDOS. Conversely, it is possible to probe the environment using a resonant nanoantenna, specific measurements being able to produce LDOS maps. In Sections 2 and 3, we derive the exact expressions of the dressed electric polarizability of a dipole antenna in an arbitrary environment and deduce the expression of the generalized absorption and extinction cross-sections. In Section 4, we discuss qualitatively the physical mechanisms affecting both the resonance frequency and the linewidth of a resonant antenna, using a simplified model. In Section 5 we study numerically a simple but realistic example, based on the rigorous expression derived in Section 2. This allows us to illustrate the general trends and to give orders of magnitude. In Section 6, we summarize the main conclusions.

2. Dressed Polarizability

This section is devoted to the computation of the dressed polarizability of an optical dipole antenna or nanoparticle

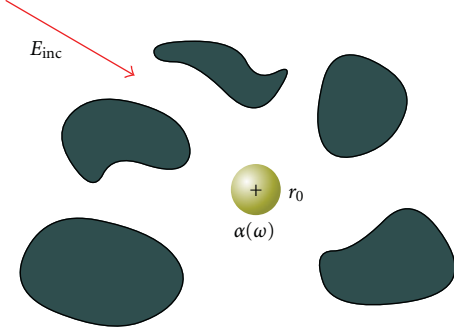


FIGURE 1: Optical dipole antenna of arbitrary shape in a structured environment. A point \mathbf{r}_0 inside the antenna is used to define its position.

(i.e., the polarizability that accounts for the interaction with the environment). To proceed, we follow the same procedure that has been used previously to compute the polarizability in vacuum [9–11]. We consider an electrically small particle (the generic term particle will be used to denote either a subwavelength optical antenna or a nanoparticle) of volume V and of permittivity $\epsilon(\omega)$ embedded in an arbitrary environment, the particle lying at position \mathbf{r}_0 (see Figure 1). We assume that position \mathbf{r}_0 lies in vacuum (the local refractive index at \mathbf{r}_0 is assumed to be unity). To describe light propagation in the environment, we use the electric dyadic Green function \mathbf{G} which connects the electric field at position \mathbf{r} to an electric dipole source at point \mathbf{r}' through the relation $\mathbf{E}(\mathbf{r}, \omega) = \mu_0 \omega^2 \mathbf{G}(\mathbf{r}, \mathbf{r}', \omega) \mathbf{p}(\mathbf{r}')$. We denote by \mathbf{E}_{ext} the field in the environment in the absence of the particle (exciting field). The total electric field \mathbf{E} at point \mathbf{r} and at frequency ω reads

$$\mathbf{E}(\mathbf{r}, \omega) = \mathbf{E}_{\text{ext}}(\mathbf{r}, \omega) + k_0^2 \int_V \mathbf{G}(\mathbf{r}, \mathbf{r}', \omega) [\epsilon(\omega) - 1] \times \mathbf{E}(\mathbf{r}', \omega) d^3 \mathbf{r}', \quad (1)$$

where $k_0 = \omega/c$, c being the speed of light in vacuum. The approximation of electrically small particle amounts to considering that the electric field is uniform inside the particle. Under this condition, the expression of the total electric field *inside* the particle (at point \mathbf{r}_0) becomes

$$\mathbf{E}(\mathbf{r}_0, \omega) = \mathbf{E}_{\text{ext}}(\mathbf{r}_0, \omega) + k_0^2 [\epsilon(\omega) - 1] \mathbf{E}(\mathbf{r}_0, \omega) \times \int_V \mathbf{G}(\mathbf{r}_0, \mathbf{r}', \omega) d^3 \mathbf{r}'. \quad (2)$$

We now split the integral of the Green dyadic into its singular part $-\mathbf{L}/k_0^2$ and its nonsingular part $V\mathbf{G}_{\text{reg}}(\mathbf{r}_0, \mathbf{r}_0, \omega)$ where we have assumed that $\mathbf{G}_{\text{reg}}(\mathbf{r}_0, \mathbf{r}', \omega)$ is constant over the volume of the nanoparticle. Note that \mathbf{L} is real since it corresponds to the singularity of the Green tensor at a point

that lies in vacuum (the Green tensor is computed in the absence of the particle) [12–14]. Equation (2) becomes

$$\mathbf{E}(\mathbf{r}_0, \omega) = \left\{ \mathbf{I} + [\epsilon(\omega) - 1] \mathbf{L} - k_0^2 V [\epsilon(\omega) - 1] \mathbf{G}_{\text{reg}}(\mathbf{r}_0, \mathbf{r}_0, \omega) \right\}^{-1} \mathbf{E}_{\text{ext}}(\mathbf{r}_0, \omega). \quad (3)$$

The expression of the polarizability follows by writing the induced electric dipole moment of the particle in the form

$$\mathbf{p}(\mathbf{r}_0, \omega) = \int_V \mathbf{P}(\mathbf{r}', \omega) d^3 \mathbf{r}' = V \epsilon_0 [\epsilon(\omega) - 1] \mathbf{E}(\mathbf{r}_0, \omega) = \epsilon_0 \boldsymbol{\alpha}(\omega) \mathbf{E}_{\text{ext}}(\mathbf{r}_0, \omega). \quad (4)$$

The last line defines the dressed polarizability $\boldsymbol{\alpha}(\omega)$, that in the most general situation is a tensor. Inserting (3) into (4), one obtains

$$\boldsymbol{\alpha}(\omega) = V [\epsilon(\omega) - 1] \times \left\{ \mathbf{I} + [\epsilon(\omega) - 1] \mathbf{L} - k_0^2 V [\epsilon(\omega) - 1] \mathbf{G}_{\text{reg}}(\mathbf{r}_0, \mathbf{r}_0, \omega) \right\}^{-1}. \quad (5)$$

A more useful expression of the dressed polarizability is obtained by defining a reference polarizability $\boldsymbol{\alpha}_0(\omega)$. A usual choice for this reference is the quasi-static polarizability of the particle in vacuum [11], that reads

$$\boldsymbol{\alpha}_0(\omega) = V [\epsilon(\omega) - 1] \left\{ \mathbf{I} + [\epsilon(\omega) - 1] \mathbf{L} \right\}^{-1}. \quad (6)$$

Note that in the case of a spherical particle, the singularity (or depolarization) dyadic is $\mathbf{L} = \mathbf{I}/3$ so that $\boldsymbol{\alpha}_0(\omega)$ would simplify into the well-known (scalar) quasi-static expression $\alpha_0 = 3V(\epsilon - 1)/(\epsilon + 2)$. Using (5) and (6), the dressed polarizability has the final form:

$$\boldsymbol{\alpha}(\omega) = \boldsymbol{\alpha}_0(\omega) \left\{ \mathbf{I} - k_0^2 \mathbf{G}_{\text{reg}}(\mathbf{r}_0, \mathbf{r}_0, \omega) \boldsymbol{\alpha}_0(\omega) \right\}^{-1}. \quad (7)$$

This expression is the main result of this section. It shows that the dressed polarizability of a particle depends on the environment, the influence of the environment being fully described by the non-singular part of the dyadic Green function $V\mathbf{G}_{\text{reg}}(\mathbf{r}_0, \mathbf{r}_0, \omega)$. Note that (7) is the explicit expression of the effective polarizability discussed in [4].

For a resonant antenna or nanoparticle (e.g., supporting a plasmon resonance), it is instructive to rewrite (7) in the form:

$$\boldsymbol{\alpha}(\omega)^{-1} = \boldsymbol{\alpha}_0(\omega)^{-1} - k_0^2 \mathbf{G}_{\text{reg}}(\mathbf{r}_0, \mathbf{r}_0, \omega). \quad (8)$$

The resonance frequency of the dressed polarizability is solution of the equation $\text{Re}[\boldsymbol{\alpha}_0^{-1}(\omega) - k_0^2 \mathbf{G}_{\text{reg}}(\mathbf{r}_0, \mathbf{r}_0, \omega)] = 0$, while the linewidth is given by $\text{Im}[\boldsymbol{\alpha}_0^{-1}(\omega) - k_0^2 \mathbf{G}_{\text{reg}}(\mathbf{r}_0, \mathbf{r}_0, \omega)]$. The influence of the environment on the resonance lineshape is made explicit by this simple analysis.

3. Generalized Absorption and Extinction Cross-Sections

The expression of the dressed polarizability is the starting point to compute generalized absorption and extinction cross-sections in an arbitrary environment. To carry out this derivation, we start with the expression of the time-averaged power absorbed inside the particle, given by

$$P_a = \frac{1}{2} \int_V \text{Re}[\mathbf{j}(\mathbf{r}', \omega) \cdot \mathbf{E}^*(\mathbf{r}', \omega)] d^3\mathbf{r}', \quad (9)$$

where $\mathbf{j}(\mathbf{r}', \omega) = -i\omega\epsilon_0[\epsilon(\omega) - 1]\mathbf{E}(\mathbf{r}', \omega)$ is the current density induced in the particle. As the electric field is assumed to be uniform inside the particle, the absorbed power becomes

$$P_a = \frac{\omega V \epsilon_0 \text{Im} \epsilon(\omega)}{2} |\mathbf{E}(\mathbf{r}_0, \omega)|^2. \quad (10)$$

Using (4), it can be rewritten as

$$P_a = \frac{\omega \epsilon_0 \text{Im} \epsilon(\omega)}{2V|\epsilon(\omega) - 1|^2} |\boldsymbol{\alpha}(\omega) \mathbf{E}_{\text{ext}}(\mathbf{r}_0, \omega)|^2. \quad (11)$$

To define a generalized absorption cross-section, we have to introduce an incident local energy flux ϕ_{ext} . Since the exciting field at the position of the particle is $\mathbf{E}_{\text{ext}}(\mathbf{r}_0, \omega)$, we define the incident local energy flux using the expression for a plane wave $\phi_{\text{ext}} = |\mathbf{E}_{\text{ext}}(\mathbf{r}_0, \omega)|^2 / (2\mu_0 c)$. This definition is arbitrary, but has the advantage to coincide with the standard one when the particle lies in a homogeneous medium. The generalized absorption cross-section is then given by the ratio P_a / ϕ_{ext} . Using the relation $\text{Im}[\boldsymbol{\alpha}_0][\boldsymbol{\alpha}_0 \boldsymbol{\alpha}_0^*]^{-1} = \text{Im} \epsilon(\omega) / [V|\epsilon(\omega) - 1|^2] \mathbf{I}$ (see Appendix A for a proof), we obtain the final expression of the generalized absorption cross-section:

$$\sigma_a(\omega) \mathbf{I} = k_0 \text{Im}[\boldsymbol{\alpha}_0(\omega)] [\boldsymbol{\alpha}_0(\omega) \boldsymbol{\alpha}_0^*(\omega)]^{-1} \frac{|\boldsymbol{\alpha}(\omega) \mathbf{E}_{\text{ext}}(\mathbf{r}_0, \omega)|^2}{|\mathbf{E}_{\text{ext}}(\mathbf{r}_0, \omega)|^2}. \quad (12)$$

Equation (12) is a central result of this paper. It deserves some remarks before we analyze its consequences. Although (12) involves tensor notations, the absorption cross-section $\sigma_a(\omega)$ is a scalar quantity. Expression (12) is exact and has been obtained under the only assumption that the electric field is uniform inside the particle (approximation of electrically small particle). It can be used, together with (7), to discuss the influence of the environment on the optical properties of any particle (or antenna) satisfying this condition. For a nonabsorbing material, the imaginary part of the permittivity $\epsilon(\omega)$ vanishes, and the quasi-static polarizability $\boldsymbol{\alpha}_0$ is real. The term $\text{Im}[\boldsymbol{\alpha}_0(\omega)]$ in (12) implies $\sigma_a(\omega) = 0$, as it should be. Finally, let us emphasize that the generalized absorption cross-section that we have defined really describes the change of the intrinsic absorption of the particle induced by the environment (or in other word of the absorption probability given a local incident power). Its proper normalization by the local incident energy flux clearly distinguishes this effect on the absorbed power from that

due to a mere change of the local incident power. It is also important to stress that although the generalized absorption cross-section that we have defined is a scalar, it depends on the orientation of the local exciting electric field, that encodes the anisotropy of the environment.

Following the same procedure, it is also possible to compute the extinction cross-section, starting from the expression of the power extracted from the external field by the nanoparticle. The latter can be written in the form [11]:

$$P_e = \frac{1}{2} \int_V \text{Re}[\mathbf{j}(\mathbf{r}', \omega) \cdot \mathbf{E}_{\text{ext}}^*(\mathbf{r}', \omega)] d^3\mathbf{r}'. \quad (13)$$

One obtains

$$\sigma_e = k_0 \frac{\text{Im}[\boldsymbol{\alpha}(\omega) \mathbf{E}_{\text{ext}}(\mathbf{r}_0, \omega) \cdot \mathbf{E}_{\text{ext}}^*(\mathbf{r}_0, \omega)]}{|\mathbf{E}_{\text{ext}}(\mathbf{r}_0, \omega)|^2}. \quad (14)$$

As for the generalized absorption cross-section, this expression is exact under the assumption of an electrically small particle. In the following, we will focus our attention on the absorption cross-section, but the analyses and the general trends can be translated to the extinction situation, that can be relevant to specific experimental configurations and type of measurements.

4. Qualitative Discussion

Equation (12) can be used to compute the absorption cross-sections in a given environment. For realistic geometries, the computation can only be performed numerically (we will study a simple example in Section 5). For example, it is possible to use an iteration scheme to solve numerically the Dyson equation which is the closed form of the equation governing the Green function similar to (1) [15]. Nevertheless, in order to get some insight based on simple analytical formulas, we will study an oversimplified situation. First, we consider a spherical nanoparticle of volume V , small enough to be consistent with the electric dipole approximation that we use throughout this paper. For such a shape, the singular part of the Green tensor is simply given by $\mathbf{L} = \mathbf{I}/3$ [12, 13]. Second, we assume that the nanosphere is embedded in an environment that preserves for $\mathbf{G}_{\text{reg}}(\mathbf{r}_0, \mathbf{r}_0, \omega)$ the same symmetry as that of free space (i.e., $\mathbf{G}_{\text{reg}}(\mathbf{r}_0, \mathbf{r}_0, \omega) = G_{\text{reg}}(\mathbf{r}_0, \mathbf{r}_0, \omega) \mathbf{I}$). This is an unrealistic hypothesis (it would be strictly valid only for a homogeneous medium or a medium with cubic symmetry), but we shall use it only to discuss qualitatively general trends. Under these hypotheses, the quasi-static polarizability reduces to $\alpha_0(\omega) = 3V[\epsilon(\omega) - 1]/[\epsilon(\omega) + 2]$, and the dressed polarizability takes the form:

$$\boldsymbol{\alpha}(\omega) = \frac{\alpha_0(\omega)}{1 - k_0^2 G_{\text{reg}}(\mathbf{r}_0, \mathbf{r}_0, \omega) \alpha_0(\omega)}. \quad (15)$$

The absorption cross-section becomes

$$\sigma_a(\omega) = k_0 \text{Im}[\alpha_0(\omega)] \frac{|\alpha(\omega)|^2}{|\alpha_0(\omega)|^2}. \quad (16)$$

It is clear in this expression that in absence of polarization anisotropy induced by the environment, the absorption

cross-section does not depend on the exciting field (this is not the case in (12)).

In order to get a simple model of a resonant optical dipole antenna, we consider a metallic nanoparticle described by Drude permittivity $\epsilon(\omega) = 1 - \omega_p^2/(\omega^2 + i\omega\gamma)$, where ω_p is the plasma frequency, and γ is the intrinsic collision rate that describes absorption losses in the bulk material. The real and imaginary parts of the Green tensor, that both influence the absorption cross-section, have a well-defined meaning. In order to make this more explicit, we introduce the photonic LDOS $\rho(\mathbf{r}_0, \omega)$, connected to the imaginary part of the Green tensor by

$$\rho(\mathbf{r}_0, \omega) = \frac{6\omega}{\pi c^2} \text{Im} [G_{\text{reg}}(\mathbf{r}_0, \mathbf{r}_0, \omega)]. \quad (17)$$

We also introduce $\phi(\mathbf{r}_0, \omega)$ that describes the influence of the real part of the non-singular Green tensor in a similar way:

$$\phi(\mathbf{r}_0, \omega) = \frac{6\omega}{\pi c^2} \text{Re} [G_{\text{reg}}(\mathbf{r}_0, \mathbf{r}_0, \omega)]. \quad (18)$$

Using these definitions, the dressed polarizability of the metallic nanoparticle reads

$$\alpha(\omega) = 3V\omega_0^2 \left[\omega_0^2 \left\{ 1 - \frac{\pi}{2} V\omega\phi(\mathbf{r}_0, \omega) \right\} - \omega^2 - i\omega \left\{ \gamma + \frac{\pi}{2} V\omega_0^2\rho(\mathbf{r}_0, \omega) \right\} \right]^{-1}, \quad (19)$$

where $\omega_0 = \omega_p/\sqrt{3}$ is the plasmon resonance frequency of the bare nanoparticle in the quasi-static limit. This expression naturally leads to the introduction of an effective frequency $\Omega_{\text{eff}}^2(\omega) = \omega_0^2 \{1 - \pi V\omega\phi(\mathbf{r}_0, \omega)/2\}$ such that the resonant frequency of the particle in the environment is solution of the equation $\Omega_{\text{eff}}^2(\omega) - \omega^2 = 0$. Similarly, an effective linewidth $\gamma_{\text{eff}}(\omega) = \gamma + \pi V\omega_0^2\rho(\mathbf{r}_0, \omega)/2$ can be introduced.

From (12) and (19), we can obtain the expression of the absorption cross-section in the simplified scalar model:

$$\sigma_a(\omega) = \frac{3V\omega_0^2}{c} \frac{\omega^2\gamma}{[\Omega_{\text{eff}}^2(\omega) - \omega^2]^2 + \omega^2\gamma_{\text{eff}}^2(\omega)}. \quad (20)$$

Equation (20), together with the expressions of $\Omega_{\text{eff}}(\omega)$ and $\gamma_{\text{eff}}(\omega)$, shows that the real part of the Green function contributes to a change of the resonance frequency, while the imaginary part (the LDOS) changes the linewidth. This is the same behavior as that known for a dipole emitter (either quantum or classical), although in the present situation we deal with the dipole induced inside the particle by the external field. It is interesting to note that the effective linewidth $\gamma_{\text{eff}}(\omega)$ can only be larger than the intrinsic linewidth γ because of its dependence on the LDOS which is a positive quantity.

The resonant behavior of $\sigma_a(\omega)$ and the influence of the LDOS (through $\gamma_{\text{eff}}(\omega)$) deserve to be analyzed more precisely. Due to the frequency dependence of both $\Omega_{\text{eff}}(\omega)$

and $\gamma_{\text{eff}}(\omega)$, the resonance lineshape is in general not a Lorentzian profile. Moreover, $\Omega_{\text{eff}}(\omega)$ and $\gamma_{\text{eff}}(\omega)$ are not independent, since the real and imaginary parts of the Green function are connected by Kramers-Kronig relations. It is nevertheless possible to derive the expression of the generalized absorption cross-section at resonance. The resonance frequency ω_a satisfies $d\sigma_a(\omega_a)/d\omega = 0$. As described in Appendix B, using this implicit equation, it is possible to express $\sigma_a(\omega_a)$ in the form:

$$\sigma_a(\omega_a) = \frac{3\gamma V\omega_0^2}{c} \times \left[\gamma_{\text{eff}}^2(\omega_a) \left\{ 1 + \frac{\omega_a^4}{[\Omega_{\text{eff}}^2(\omega_a) - 2\omega_a\Omega'_{\text{eff}}(\omega_a)\Omega_{\text{eff}}(\omega_a) + \omega_a^2]^2} \times \gamma_{\text{eff}}'^2(\omega_a) \right\} \right]^{-1}, \quad (21)$$

where the superscript ' denotes a first-order derivative. This expression shows that both the LDOS and its first-order derivative influence the amplitude of the generalized absorption cross-section, through $\gamma_{\text{eff}}^2(\omega_a)$ and $\gamma_{\text{eff}}'^2(\omega_a)$, respectively. An increase of both quantities tends to decrease the absorption cross-section. In the particular case of an environment for which the spectral dependence of the LDOS can be neglected [$\gamma_{\text{eff}}'(\omega) = 0$], we end up with $\sigma_a(\omega_a) \propto 1/\gamma_{\text{eff}}^2(\omega_a)$. This result can be qualitatively explained in simple terms. The first step in the absorption process by a metallic nanoparticle is the excitation of the conduction electron gas. Then, relaxation can occur either by radiative (emission of scattered light) or nonradiative channels (absorption due to electron-phonon collisions). Increasing the photonic LDOS increases the weight of radiative channels and therefore reduces absorption. The role of the LDOS in this process is essentially the same as that in the spontaneous decay rate of a quantum emitter by coupling to radiation.

5. Metallic Nanoparticle Interacting with a Perfect Mirror

In order to illustrate the effects discussed above on a real example and to get orders of magnitudes (i.e., to establish the possibility of experiments), we study quantitatively in this section the generalized absorption cross-section of a silver nanosphere, with radius $R = 15$ nm, interacting with a flat perfectly conducting surface (perfect mirror). The geometry of the system is shown in Figure 2. To describe the silver nanoparticle, we use the tabulated values of the bulk permittivity $\epsilon(\omega)$ taken from [16].

To compute the generalized absorption cross-section of the nanosphere, we use the exact expression equation (12). In

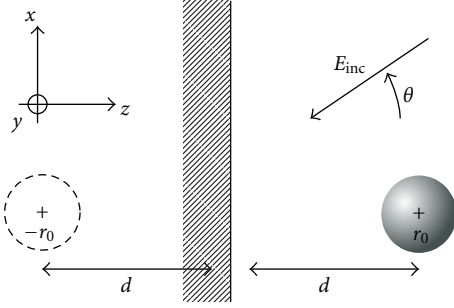


FIGURE 2: Geometry of the system: A spherical dipole nanoparticle interacts with a perfect mirror. The dashed sphere corresponds to the image dipole.

order to compute relative changes, we define the normalized cross-section $\sigma_a^n(\omega) = \sigma_a(\omega)/\sigma_a^{\text{vac}}(\omega)$, where $\sigma_a^{\text{vac}}(\omega)$ is the absorption cross-section of the bare nanosphere in vacuum:

$$\sigma_a^{\text{vac}}(\omega) = k_0 \text{Im}[\alpha_0(\omega)] \left| \frac{\alpha_{\text{vac}}(\omega)}{\alpha_0(\omega)} \right|^2. \quad (22)$$

The vacuum polarizability $\alpha_{\text{vac}}(\omega)$ is given by

$$\alpha_{\text{vac}} = \alpha_0(\omega) \left\{ 1 - i \frac{k_0^3}{6\pi} \alpha_0(\omega) \right\}^{-1}, \quad (23)$$

with $\alpha_0(\omega) = 3V[\epsilon(\omega) - 1]/[\epsilon(\omega) + 2]$ [10, 11]. The calculation of $\sigma_a^n(\omega)$ requires the calculation of the exciting field \mathbf{E}_{ext} and of the Green function $G_{\text{reg}}(\mathbf{r}_0, \mathbf{r}_0, \omega)$ in the geometry in Figure 2. This is a straightforward application of the image method, given in Appendix C for completeness.

We show in Figure 3(a) the variations of normalized LDOS (ratio between the full LDOS and the LDOS in vacuum) versus both the wavelength and the distance d between the mirror and the center of the nanoparticle. Figure 3(b) (red solid line) displays a section corresponding to $\lambda = 400$ nm in Figure 3(a). We observe the well-known oscillations due to interferences between incident and reflected waves on the mirror [2]. In the near-field regime corresponding to $d \ll \lambda$, the relative variations of the LDOS are on the order of 10%. These plots of the LDOS will be helpful in the qualitative analysis of the variations of the generalized absorption cross-section.

To study the influence of the mirror on $\sigma_a(\omega)$, we first consider an s -polarized illumination (the incident plane wave has an electric field linearly polarized along the direction y). In this case, the induced electric dipole in the nanosphere is oriented along y . As a consequence, $\sigma_a(\omega)$ is independent of the direction of incidence (angle θ in Figure 2). In Figure 4(a), we represent the variations of the normalized absorption cross-section $\sigma_a^n(\omega)$ (generalized absorption cross-section divided by free-space cross-section) versus both the wavelength λ and the distance d between the mirror and the center of the nanoparticle. The plasmon resonance, corresponding to $\lambda \approx 360$ nm, is visible for $d < 100$ nm. Figure 4(b) displays a section view of Figure 4(a) at $\lambda = 361$ nm. We observe oscillations of the absorption

cross-section, as a clear signature of the influence of the mirror. The relative variations are on the order of 5% for distances d between 50 and 250 nm. The behavior of $\sigma_a^n(\omega)$ can be compared to that of the partial LDOS $\rho_{yy}(\mathbf{r}_0, \omega)$ in Figure 3(b). The oscillations are in opposition, in agreement with the qualitative analysis presented in Section 4: An increase of the LDOS tends to decrease the absorption cross-section.

The case of an illumination with a p -polarized plane wave (i.e., with an electric field in the x - z plane) can be analyzed in a similar manner. In this case, the electric dipole induced in the nanosphere depends on the direction of incidence θ . We have chosen $\theta = 45^\circ$ for the sake of illustration (note that $\theta = 0$ would lead to the same behavior as that observed with s -polarized illumination). Figures 5(a) and 5(b) are the same as Figures 4(a) and 4(b), but for p -polarized illumination. We observe a similar behavior of σ_a^n , with oscillations corresponding to relative variations of a few percent. Close to resonance, and for $d = 30$ nm (which corresponds to strong nanoparticle mirror interaction in this simple system), the relative variation of the absorption cross-section is of the order of 20%. Finally, let us note that significant changes are observed in the near-field regime only. For $d > \lambda/2$, the influence of interactions with the environment remains weak.

6. Conclusion

We have described the influence of the environment on the absorption cross-section of an optical dipole antenna or a nanoparticle, based on a rigorous framework. We have derived a generalized form of the absorption cross-section, based on the only assumption that the electric field is uniform inside the antenna (electric dipole approximation). In the case of a resonant nanoparticle (plasmon resonance), we have analyzed qualitatively the role of the environment on the resonance frequency and on the linewidth. In particular, we have identified the role of the photonic LDOS and shown that an increase of the LDOS results in a reduction of the generalized absorption cross-section. These effects have been illustrated on the simple example of a metallic nanoparticle interacting with a perfect mirror. In the field of optical nanoantennas, these results could be exploited along two directions. First, engineering the LDOS around an optical nanoantenna could allow some control of both the resonance frequency, and more interestingly on the level of absorption. Since high absorption remains a serious drawback of metallic nanoantenna, it might be possible to reduce absorption by an appropriate structuration of the environment. Second, measuring changes in the resonance lineshape of a metallic nanoparticle, as performed, for example, in [18], should allow a direct mapping of the LDOS, without using fluorescent emitters. Finally, let us comment on the possibility of measuring σ_a *in situ*. A potential method could be based on photothermal detection, in which a probe beam probes the temperature increase of the nanoparticle due to absorption. Such methods already offer the possibility of sensitive detection of nanoparticles in complex environments [19–22].

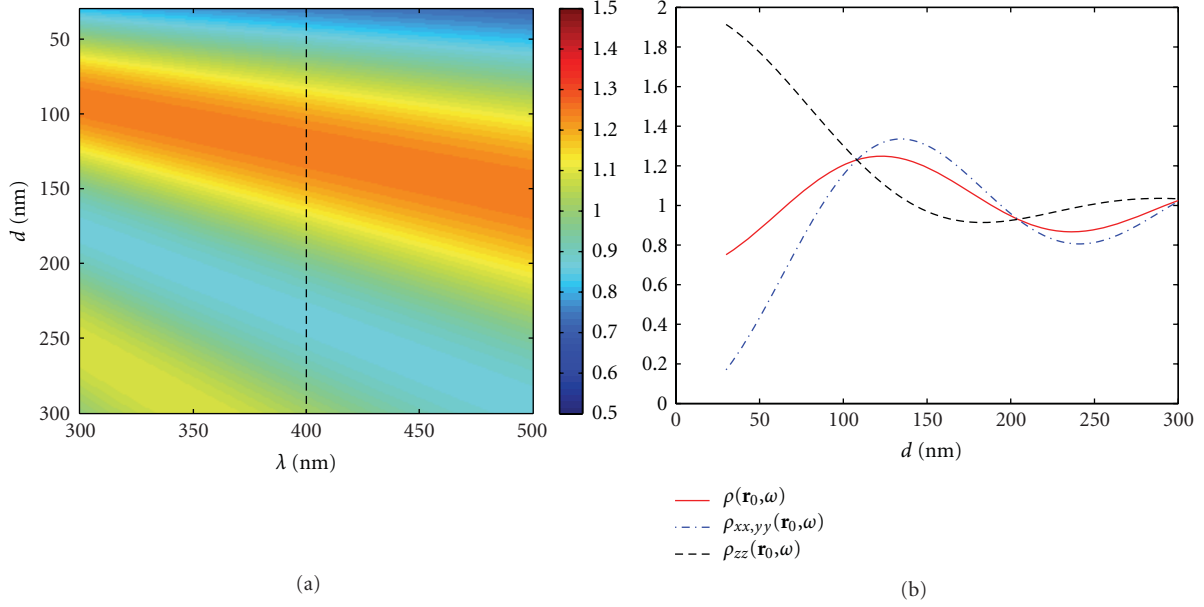


FIGURE 3: (a) map of the normalized LDOS $\rho(\mathbf{r}_0, \omega)/\rho_{\text{vac}}(\omega)$, with $\rho(\mathbf{r}_0, \omega) = 2\omega/(\pi c^2) \text{Im}[\text{Tr} \mathbf{G}_{\text{reg}}(\mathbf{r}_0, \mathbf{r}_0, \omega)]$ and $\rho_{\text{vac}}(\omega)$ the LDOS in vacuum, versus both the wavelength λ and the distance d between the mirror and the center of the nanoparticle. The vertical dashed line is a guide to precise the wavelength at which panel (b) has been plotted. (b) distance dependence of the LDOS (red solid line) and of the partial LDOS (blue and black dashed lines) defined by $\rho_{ii}(\mathbf{r}_0, \omega) = 2\omega/(\pi c^2) \text{Im}[G_{\text{reg},ii}(\mathbf{r}_0, \mathbf{r}_0, \omega)]$ with $i = x, y, z$ for $\lambda = 400$ nm. The partial LDOS $\rho_{ii}(\mathbf{r}_0, \omega)$ drives the dynamics of a dipole oriented along direction i , while the LDOS sums up the contributions of the three orientations. Due to symmetry in the geometry in Figure 2, the partial LDOS along x and y is equal. In all calculations, the minimum distance $d \simeq 2R$ has been chosen at the limit of validity of the dipole approximation [17].

Appendix

A. Proof of the Relation $\text{Im}[\alpha_0][\alpha_0 \alpha_0^*]^{-1} = \text{Im} \epsilon(\omega)/[V|\epsilon(\omega) - 1|^2] \mathbf{I}$

In this appendix, we give a proof of the relation $\text{Im}[\alpha_0][\alpha_0 \alpha_0^*]^{-1} = \text{Im} \epsilon(\omega)/[V|\epsilon(\omega) - 1|^2] \mathbf{I}$. The quasi-static polarizability is given by (6):

$$\alpha_0(\omega) = V[\epsilon(\omega) - 1] \{ \mathbf{I} + [\epsilon(\omega) - 1] \mathbf{L} \}^{-1}. \quad (\text{A.1})$$

Multiplying the previous expression on the left by $\{ \mathbf{I} + [\epsilon^*(\omega) - 1] \mathbf{L} \} \{ \mathbf{I} + [\epsilon(\omega) - 1] \mathbf{L} \}^{-1}$, we end up with:

$$\begin{aligned} \text{Im} \alpha_0(\omega) &= V \text{Im} \epsilon(\omega) \\ &\times \left\{ \mathbf{I} + 2 \text{Re}[\epsilon(\omega) - 1] \mathbf{L} + |\epsilon(\omega) - 1|^2 \mathbf{L}^2 \right\}^{-1}. \end{aligned} \quad (\text{A.2})$$

However, we also have

$$\begin{aligned} \alpha_0 \alpha_0^* &= V^2 |\epsilon(\omega) - 1|^2 \\ &\times \left\{ \mathbf{I} + 2 \text{Re}[\epsilon(\omega) - 1] \mathbf{L} + |\epsilon(\omega) - 1|^2 \mathbf{L}^2 \right\}^{-1}. \end{aligned} \quad (\text{A.3})$$

Using (A.2) and (A.3), we obtain the following relationship:

$$\text{Im}[\alpha_0][\alpha_0 \alpha_0^*]^{-1} = \frac{\text{Im} \epsilon(\omega)}{V|\epsilon(\omega) - 1|^2} \mathbf{I}, \quad (\text{A.4})$$

which concludes the proof.

B. Derivation of the Scalar Form of the Absorption Cross-Section at Resonance

To derive (21), we first compute the derivative of (20) with respect to ω :

$$\begin{aligned} \frac{d\sigma_a}{d\omega}(\omega) &= \frac{6V\gamma\omega\omega_0^2}{c} \left[\{ \Omega_{\text{eff}}^2(\omega) - \omega^2 \}^2 \right. \\ &\quad - 2\omega \{ \Omega'_{\text{eff}}(\omega) \Omega_{\text{eff}}(\omega) - \omega \} \\ &\quad \times \{ \Omega_{\text{eff}}^2(\omega) - \omega^2 \} - \omega^3 \gamma_{\text{eff}}(\omega)' \gamma_{\text{eff}}(\omega) \left. \right] \\ &\quad / \left\{ [\Omega_{\text{eff}}^2(\omega) - \omega^2]^2 + \omega^2 \gamma_{\text{eff}}^2(\omega) \right\}^2. \end{aligned} \quad (\text{B.1})$$

The resonance frequency ω_a is defined by $d\sigma_a(\omega_a)/d\omega = 0$. This gives us a relation satisfied by ω_a . By factorizing by $\Omega_{\text{eff}}^2(\omega_a) - \omega_a^2$, and by putting this relation into (20), we end up with:

$$\begin{aligned} \sigma_a(\omega_a) &= \frac{3\gamma V \omega_0^2}{c} \\ &\times \left[\gamma_{\text{eff}}^2(\omega_a) \left\{ 1 \right. \right. \\ &\quad \left. \left. + \frac{\omega_a^4}{[\Omega_{\text{eff}}^2(\omega_a) - 2\omega_a \Omega'_{\text{eff}}(\omega_a) \Omega_{\text{eff}}(\omega_a) + \omega_a^2]^2} \right. \right. \\ &\quad \left. \left. \times \gamma_{\text{eff}}^2(\omega_a) \right\} \right]^{-1}, \end{aligned} \quad (\text{B.2})$$

which concludes the derivation of (21).

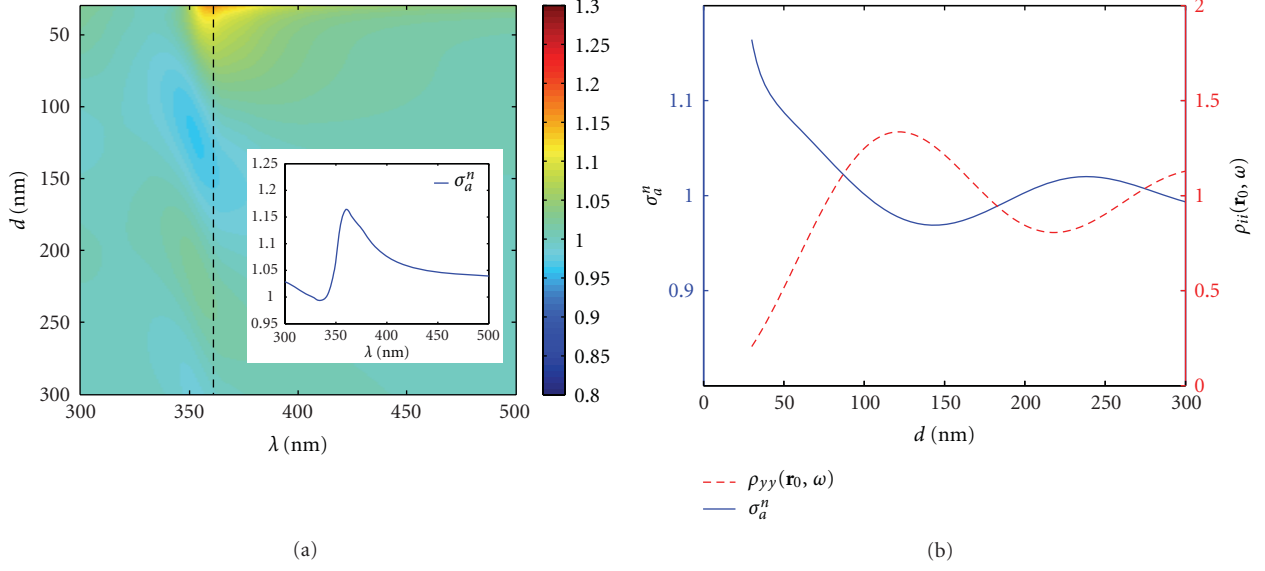


FIGURE 4: (a) map of the normalized absorption cross-section σ_a^n versus both the wavelength λ and the distance d between the mirror and the nanosphere. The vertical dashed line is a guide to precise the wavelength at which panel (b) has been plotted. Inset: plot of the absorption cross-section as a function of the wavelength for $d = 30$ nm. (b) plot of σ_a^n and of the partial LDOS $\rho_{yy}(\mathbf{r}_0, \omega)$ versus the distance d for $\lambda = 361$ nm, s -polarized illumination.

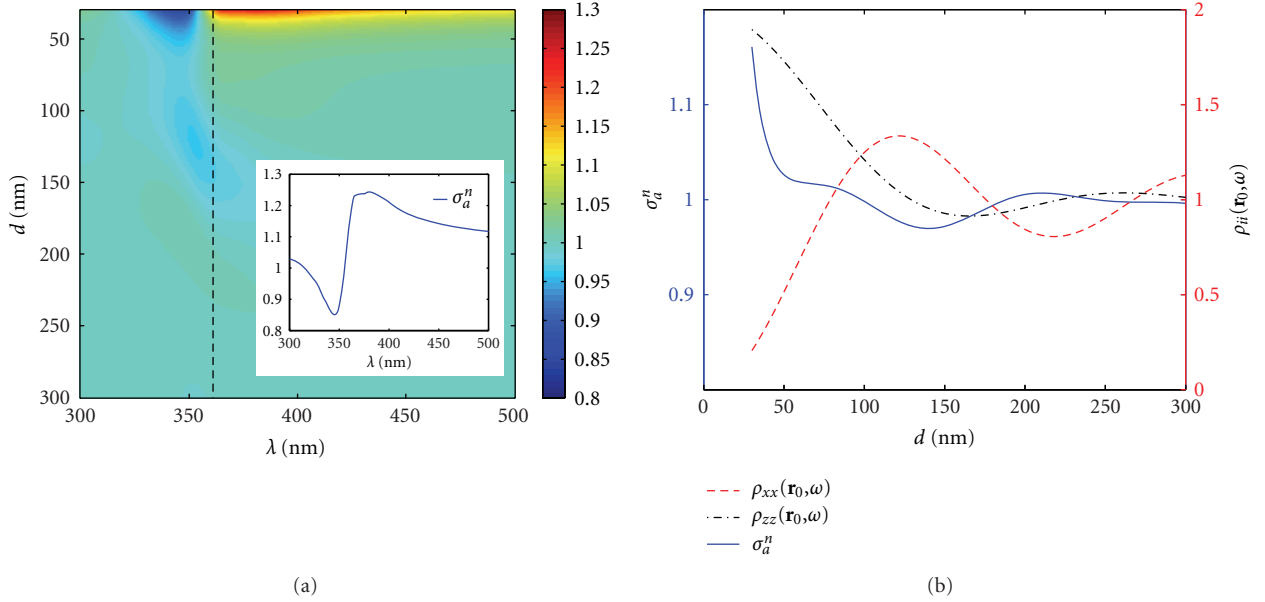


FIGURE 5: (a) same as Figure 4 for an illumination with a p -polarized plane wave, at an angle of incidence $\theta = 45^\circ$. Both the partial LDOS $\rho_{xx}(\mathbf{r}_0, \omega)$ and $\rho_{zz}(\mathbf{r}_0, \omega)$ are displayed in (b) since both influence the generalized cross-section in this situation.

C. Computation of the Exciting Field and of the Green Function of the Perfect Mirror System

The computation of the modified absorption cross-section for a metallic nanosphere close to a perfect mirror requires the computation of the exciting field and of the Green tensor of the system composed by the mirror only. In the case of a s -polarised incident field given by

$$\mathbf{E}_{\text{inc}}^s(\mathbf{r}, \omega) = E_0 \exp [ik_x x + ik_z z] \mathbf{e}_y, \quad (\text{C.1})$$

where the incident wave vector is $\mathbf{k} = k_0(-\sin \theta, 0, -\cos \theta)$, the exciting field at the position \mathbf{r}_0 of the nanosphere is simply given by the superposition of the incident and reflected fields:

$$\mathbf{E}_{\text{ext}}^s(\mathbf{r}_0, \omega) = -2iE_0 \sin [k_0 \cos \theta d] \mathbf{e}_y. \quad (\text{C.2})$$

In the same way, in the case of a p -polarised incident field given by

$$\mathbf{E}_{\text{inc}}^p(\mathbf{r}, \omega) = E_0 \exp [ik_x x + ik_z z] \{ \cos \theta \mathbf{e}_x + \sin \theta \mathbf{e}_z \}, \quad (\text{C.3})$$

the exciting field reads

$$\begin{aligned} \mathbf{E}_{\text{ext}}^p(\mathbf{r}_0, \omega) = & -2iE_0 \cos \theta \sin [k_0 \cos \theta d] \mathbf{e}_x \\ & + 2E_0 \sin \theta \cos [k_0 \cos \theta d] \mathbf{e}_z. \end{aligned} \quad (\text{C.4})$$

In order to express the Green function, we use the dipole image method. If the system consisting of the perfect mirror at $z = 0$ is illuminated by a source dipole $\mathbf{p} = (p_x, p_y, p_z)$ at position $\mathbf{r}_0 = (0, 0, z_0)$, the effect of the mirror can be replaced by the radiation of an image dipole $\mathbf{p}' = (-p_x, -p_y, p_z)$ placed at position $\mathbf{r}'_0 = (0, 0, -z_0)$. This allows us to compute the Green function of the system in a simple manner:

$$\mathbf{G}(\mathbf{r}, \mathbf{r}_0, \omega) \mathbf{p} = \mathbf{G}_0(\mathbf{r}, \mathbf{r}_0, \omega) \mathbf{p} + \mathbf{G}_0(\mathbf{r}, \mathbf{r}'_0, \omega) \mathbf{p}'. \quad (\text{C.5})$$

In this expression, \mathbf{G}_0 is the Green tensor in vacuum given by

$$\begin{aligned} \mathbf{G}_0(\mathbf{r}, \mathbf{r}_0, \omega) = \text{PV} \left\{ \left[\mathbf{I} - \mathbf{u} \otimes \mathbf{u} + \frac{ik_0 R - 1}{k_0^2 R^2} (\mathbf{I} - 3\mathbf{u} \otimes \mathbf{u}) \right] \right. \\ \left. \times \frac{\exp[ik_0 R]}{4\pi R} \right\} - \frac{\delta(\mathbf{R})}{3k_0^2} \mathbf{I}, \end{aligned} \quad (\text{C.6})$$

with $\mathbf{R} = \mathbf{r} - \mathbf{r}_0$ and $\mathbf{u} = \mathbf{R}/R$, PV denoting the principal value operator. At the position of the nanosphere (i.e., $\mathbf{r} = \mathbf{r}_0$), the singularity part of the Green tensor (needed to compute the quasi-static polarisability α_0 given by (6)) is simply $\mathbf{L} = \mathbf{I}/3$. The regular part (needed to compute the polarisability α given by (7)) is given by

$$\mathbf{G}_{\text{reg}}(\mathbf{r}_0, \mathbf{r}_0, \omega) \mathbf{p} = \mathbf{G}_{0,\text{reg}}(\mathbf{r}_0, \mathbf{r}_0, \omega) \mathbf{p} + \mathbf{G}_0(\mathbf{r}_0, \mathbf{r}'_0, \omega) \mathbf{p}'. \quad (\text{C.7})$$

Acknowledgments

This paper was supported by the EU Project *Nanomagma* under Contract no. NMP3-SL-2008-214107. E. Castanié acknowledges a doctoral grant from the French DGA.

References

- [1] E. M. Purcell, "Spontaneous emission probabilities at radio frequencies," *Physical Review*, vol. 69, p. 681, 1946.
- [2] R. R. Chance, A. Prock, and R. Silbey, *Molecular Fluorescence and Energy Transfer Near Interfaces*, vol. 37 of *Advances in Chemical Physics*, John Wiley & Sons, New York, NY, USA, 1978.
- [3] W. L. Barnes, "Fluorescence near interfaces: the role of photonic mode density," *Journal of Modern Optics*, vol. 45, no. 4, pp. 661–699, 1998.
- [4] L. Novotny and B. Hecht, *Principle of Nano-Optics*, Cambridge University Press, Cambridge, UK, 2006.
- [5] W. R. Holland and D. G. Hall, "Frequency shifts of an electric-dipole resonance near a conducting surface," *Physical Review Letters*, vol. 52, no. 12, pp. 1041–1044, 1984.
- [6] B. C. Buchler, T. Kalkbrenner, C. Hettich, and V. Sandoghdar, "Measuring the quantum efficiency of the optical emission of single radiating dipoles using a scanning mirror," *Physical Review Letters*, vol. 95, no. 6, Article ID 063003, 2005.
- [7] J. Zuloaga and P. Nordlander, "On the energy shift between near-field and far-field peak intensities in localized plasmon systems," *Nano Letters*, vol. 11, no. 3, pp. 1280–1283, 2011.
- [8] C. Huang, A. Bouhelier, G. Colas Des Francs, G. Legay, J. C. Weeber, and A. Dereux, "Far-field imaging of the electromagnetic local density of optical states," *Optics Letters*, vol. 33, no. 4, pp. 300–302, 2008.
- [9] A. Lakhtakia, "Strong and weak forms of the method of moments and the coupled dipole method for scattering of time-harmonic electromagnetic fields," *International Journal of Modern Physics C*, vol. 3, no. 3, pp. 583–603, 1992.
- [10] R. Carminati, J. J. Greffet, C. Henkel, and J. M. Vigoureux, "Radiative and non-radiative decay of a single molecule close to a metallic nanoparticle," *Optics Communications*, vol. 261, no. 2, pp. 368–375, 2006.
- [11] S. Albaladejo, R. Gómez-Medina, L. S. Froufe-Pérez et al., "Radiative corrections to the polarizability tensor of an electrically small anisotropic dielectric particle," *Optics Express*, vol. 18, no. 4, pp. 3556–3567, 2010.
- [12] J. van Bladel, *Singular Electromagnetic Fields and Sources*, Oxford University Press, Oxford, UK, 1991.
- [13] A. D. Yaghjian, "Electric dyadic Green's functions in the source region," *Proceedings of the IEEE*, vol. 68, no. 2, pp. 248–263, 1980.
- [14] C.-A. Guérin, B. Gralak, and A. Tip, "Singularity of the dyadic Green's function for heterogeneous dielectrics," *Physical Review E*, vol. 75, no. 5, Article ID 056601, 2007.
- [15] O. J. F. Martin, C. Girard, and A. Dereux, "Generalized field propagator for electromagnetic scattering and light confinement," *Physical Review Letters*, vol. 74, no. 4, pp. 526–529, 1995.
- [16] E. D. Palik, *Handbook of Optical Constants of Solids*, Academic Press, New York, NY, USA, 1985.
- [17] P. C. Chaumet, A. Rahmani, F. De Fornel, and J. P. Dufour, "Evanescent light scattering: the validity of the dipole approximation," *Physical Review B*, vol. 58, no. 4, pp. 2310–2315, 1998.
- [18] T. Kalkbrenner, U. Håkanson, A. Schädle, S. Burger, C. Henkel, and V. Sandoghdar, "Optical microscopy via spectral modifications of a nanoantenna," *Physical Review Letters*, vol. 95, no. 20, Article ID 200801, 2005.
- [19] D. Boyer, P. Tamarat, A. Maali, B. Lounis, and M. Orrit, "Photothermal imaging of nanometer-sized metal particles among scatterers," *Science*, vol. 297, no. 5584, pp. 1160–1163, 2002.
- [20] S. Berciaud, L. Cognet, G. A. Blab, and B. Lounis, "Photothermal heterodyne imaging of individual nonfluorescent nanoclusters and nanocrystals," *Physical Review Letters*, vol. 93, no. 25, Article ID 257402, 2004.
- [21] S. Berciaud, D. Lasne, G. A. Blab, L. Cognet, and B. Lounis, "Photothermal heterodyne imaging of individual metallic nanoparticles: theory versus experiment," *Physical Review B*, vol. 73, no. 4, Article ID 045424, 2006.
- [22] E. Absil, G. Tessier, M. Gross et al., "Photothermal heterodyne holography of gold nanoparticles," *Optics Express*, vol. 18, no. 2, pp. 780–786, 2010.

Research Article

Digital Heterodyne Holography Reveals the Non-Quasi-Static Scattering Behaviour of Transversally Coupled Nanodisk Pairs

Sarah Y. Suck,^{1,2} Sébastien Bidault,¹ Nicolas Bonod,³ Stéphane Collin,⁴
Nathalie Bardou,⁴ Yannick De Wilde,¹ and Gilles Tessier¹

¹Institut Langevin, ESPCI ParisTech, CNRS UMR 7587, 10 rue Vauquelin, 75231 Paris Cedex 05, France

²Fondation Pierre-Gilles de Gennes pour la Recherche, 29 rue d'Ulm, 75005 Paris, France

³Institut Fresnel, CNRS UMR 7249, Aix-Marseille Université, Ecole Centrale Marseille, Domaine Universitaire de Saint Jérôme, 13397 Marseille, France

⁴Laboratoire de Photonique et de Nanostructures (LPN-CNRS UPR 20), route de Nozay, 91460 Marcoussis, France

Correspondence should be addressed to Gilles Tessier, gilles.tessier@espci.fr

Received 27 October 2011; Accepted 9 December 2011

Academic Editor: Alexandre Bouhelier

Copyright © 2012 Sarah Y. Suck et al. This is an open access article distributed under the Creative Commons Attribution License, which permits unrestricted use, distribution, and reproduction in any medium, provided the original work is properly cited.

We reconstruct the full three-dimensional scattering pattern of longitudinal and transverse modes in pairs of coupled gold nanodisks using digital heterodyne holography. Near-field simulations prove that, in our experimental conditions, the induced dipoles in the longitudinal mode are in phase while they are nearly in opposite phase for the transverse mode. The scattering efficiency of the two modes is of the same order of magnitude, which goes against the common belief that antisymmetric transverse modes are “dark.” The analysis of the reconstructed hologram in the Fourier plane allows us to estimate the angular scattering pattern for both excited modes. In particular, the antisymmetric transverse mode scatters light mostly into one half-plane, demonstrating that the quasi-static approximation breaks down in nanodisk pairs even for an interparticle distance lower than $\lambda/4$.

1. Introduction

The coupling of two nanoparticles plays an important role in the context of plasmonics because of the increased near-field enhancement and confinement that occurs in the gap between particles. Pairs of coupled nanoparticles represent the simplest and most fundamental structure for studying the plasmon coupling phenomena which give rise to numerous applications like surface-enhanced Raman spectroscopy (SERS) [1, 2], nanosensing [3–5], and optical trapping [6, 7].

The resonances and optical properties of a two-particle antenna are often described in terms of the hybridization model which states that the coupling of individual particle dipole modes induces an energy splitting into bonding and antibonding modes [8]. This quasi-static model entails that the red-shifted bonding longitudinal mode and the blue-shifted antibonding transverse mode are the only ones that couple efficiently to far-field radiation. These modes are generally called “bright” modes while the antibonding

longitudinal and bonding transverse modes are described as nonscattering “dark” modes and are, thus, not observed in the far field.

With the increasing development in nanofabrication technology during the last decade, control over the design of two-particle antennas has been steadily improving. Since then, the coupling phenomena involved in the optical properties of a two-disk nanostructure have been studied extensively using experimental and numerical approaches [9–12]. In all these cases, the phase of the excitation is homogeneous on the particle dimers; thus, the spectral responses are consistent with the quasi-static hybridization model.

However, the study of chains of nanoparticles that span distances much greater than the vacuum wavelength has consistently shown that quasi-static approximations break down rapidly in nanofabricated samples [13, 14]. The retardation effects, which cannot be neglected at these length scales, have promising applications in the design of directional antennas

(in particular in Yagi-Uda geometries) for the control of single quantum emitters [15–19]. Recently, the directivity of Yagi-Uda nanoantennas has been studied by eigenmode imaging of amplitude and phase using apertureless scanning near-field optical microscopy [20].

In order to reveal the near-field phase effects that drive the performance of optical antennas, we investigate experimentally the optical properties of one of the simplest plasmon coupled systems: a gold nanodisk pair with an interparticle distance much smaller than the vacuum wavelength. Theoretical and experimental reports have shown that at large interparticle distances, retardation effects induce a periodic modulation of the scattering cross-section for both longitudinal and transversely coupled particles [21]. Furthermore, experimental results obtained recently on particle pairs using an excitation in total internal reflection geometry showed that two efficiently scattering transverse modes can be observed [22] which is inconsistent with the hybridization model. In 2011, Rolly et al. studied analytically the optical properties of silver nanogap antennas [23] and have shown that, even at short interparticle distances, phase effects in the induced dipoles have to be taken into account when illuminating the dimer in a direction parallel to its axis. This is not only due to retardation but also to an interparticle scattering term that arises from distance-dependent dipole coupling. In particular, they showed that the maximum scattering efficiency for nearly touching spheres occurs when exciting the antisymmetric (bonding) transverse mode. This mode which is “dark” in the quasi-static approximation is rendered “bright” by the interparticle scattering term. As demonstrated in bimetallic particle pairs, near-field phase effects strongly modify the angular pattern of the scattered light [24]. Three-dimensional (3D) analysis of the scattering pattern of gold dimers should directly discriminate cases where the hybridization model holds.

Digital heterodyne holography, a sensitive technique that relies on interferometry, has the ability to measure the optical amplitude and phase of light scattered by nanoobjects [25, 26]. Therefore, one hologram which can be recorded in less than 1 second contains the whole 3D information of the recorded scattered light. Furthermore, holography also allows the access to the angular scattering pattern of a nanostructure since the angular spectrum of the hologram can be obtained by computing the scattered field in the Fourier plane. To correlate measured optical data to the relative phases of the induced dipoles in the particle pair, we performed finite element method (FEM) simulations (based on the commercial software package “Comsol Multiphysics”). This allows us to compute the near-field intensity and phase maps of gold nanodisk pairs in the presence of a glass-air interface.

2. Simulated Near-Field Maps

We have developed a three-dimensional simulation model taking into account the presence of the glass-air interface, which is in many cases neglected or simplified in simulations due to its additional complexity when regarding scattering. In our model, we chose to describe the incident wave field

in the whole volume, using the analytical expressions of the Fresnel equations describing the diffraction at an interface. The incident light comes from the glass substrate under an incident angle of 45° , which corresponds to the total internal reflection (TIR) configuration used in the experiment.

We were interested in examining the scattered near field of a pair of gold nanodisks in the presence of a glass-air interface under two different excitations using s-polarized light: (a) incident k -vector perpendicular to the principal axis (i.e., along the x -axis) of the nanostructure with an electric field E_x along its axis and (b) incident k -vector parallel to its principal axis where the field E_y is perpendicular to the structure. Both configurations are schematically depicted on the left of Figure 1. In case (a), the two disks interact by means of near-field coupling, and the in-phase longitudinal mode is excited, giving rise to a strong field enhancement in the gap. In case (b), in contrast, the near-field coupling of the two particles is weak, as the regions of high near fields are away from the gap between the disks. A transverse mode is excited.

Figure 1 plots the near-field intensity maps in the x - y plane, $|E_x^{sc}|^2 + |E_y^{sc}|^2$ (left images) and the phase maps of the corresponding dominant near-field component, that is, $\Phi(E_x^{sc})$ for case (a) and $\Phi(E_y^{sc})$ for case (b) (right images). The near-field is calculated 10 nm above the disks surface to avoid field discontinuities on the gold interfaces and to better correspond to scanning near-field measurements.

The near-field intensity image corresponding to case (a) confirms the excitation of a longitudinal mode. There is a strong field confinement in the gap, which corresponds to an intensity near-field enhancement of 140. The phase image clearly shows that both disks are in phase. In case (b), we observe no field confinement in the gap, which confirms the excitation of a transverse mode. The near-field intensity image reveals a slight asymmetry close to the surface of the disks’ sides: the near field close to the right disk is higher than that close to the left disk. This feature is due to the incoming field impinging on the right particle from the positive x direction. A possible mode is sketched in the left-handed scheme in Figure 1(b). Regarding the corresponding phase image, both disks are nearly at opposite phase ($\Delta\Phi = 1.28\pi$) which proves that the disk pair exhibits an antisymmetric transverse mode. Using an illumination in total internal reflection, it will therefore be possible to excite an in-phase longitudinal mode and an opposite-phase transverse mode in the pair of coupled disks and compare their scattering behaviours using digital heterodyne holography. Isotropic gold particles should allow the investigation of the opposite-phase transverse mode as shown in the literature [22]. However, for p-polarized incident light, the strong component of the evanescent field normal to the sample plane forbids the excitation of the symmetric transverse and antisymmetric longitudinal modes in gold disk pairs.

3. Experimental Setup

The experimental holographic setup is based on a Mach-Zehnder interferometer. It is schematically depicted in

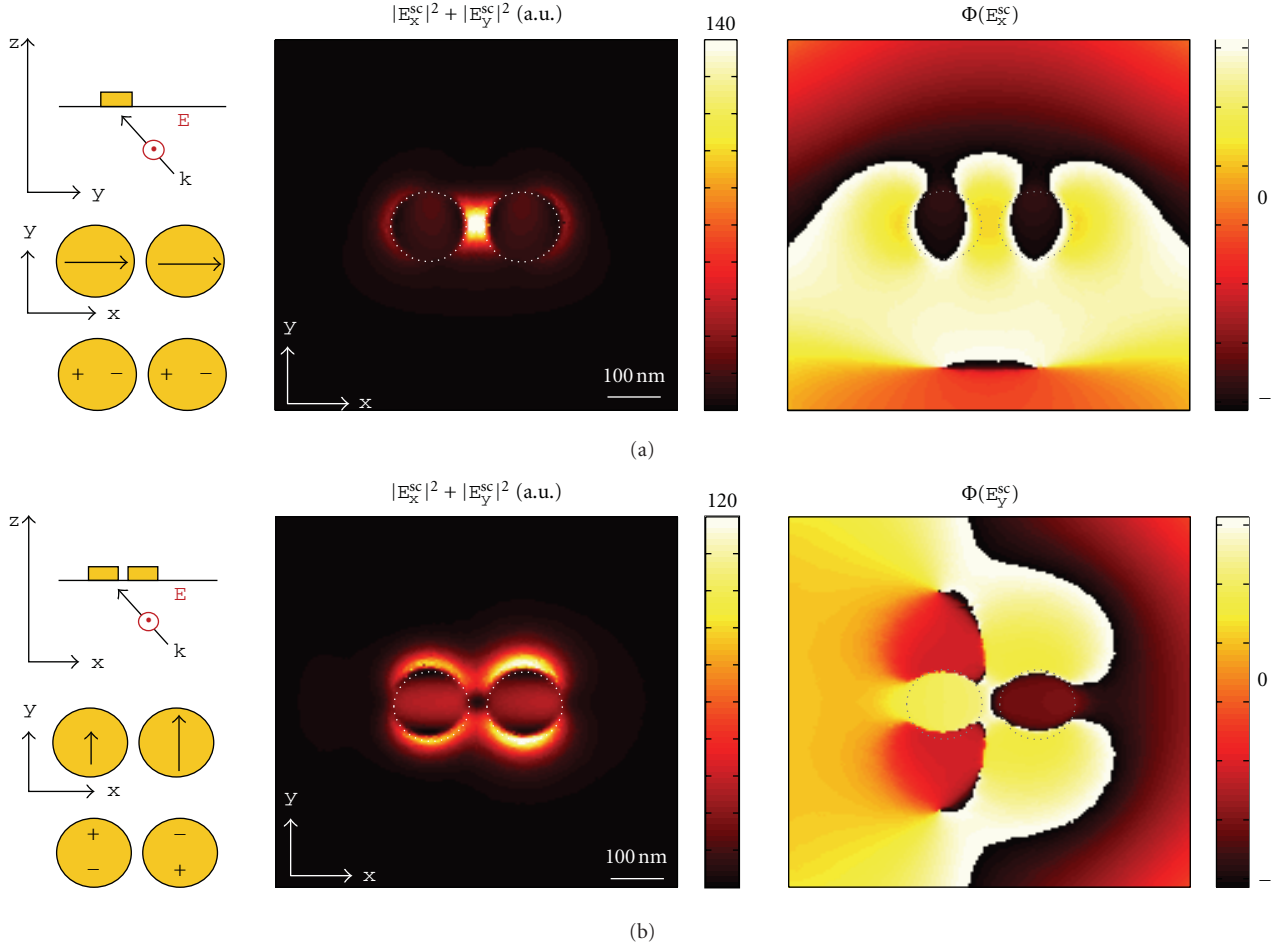


FIGURE 1: Simulation of the near-field of two coupled disks ($d = 150$ nm, gap = 40 nm) for 2 different illumination configurations using s-polarized light: (a) wave vector \perp to dimer axis, (b) wave vector \parallel to dimer axis. Note that only the in-plane components are plotted, that is, the x - and y -components. Left: near-field intensity $|E^{\text{sc}}|^2 = |E_x^{\text{sc}}|^2 + |E_y^{\text{sc}}|^2$ in the x - y plane plotted 10 nm above the surface of the disks. Right: corresponding phase images. The position of the disks is indicated by dotted circles.

Figure 2. A single mode laser diode ($\lambda = 785$ nm, Power = 80 mW, Sanyo DL7140-201S) beam is separated with a polarizing beam splitter (PBS) in reference (E_R) and object arms (E_O) which are frequency shifted by two acousto-optical modulators (AOM1, AOM2) at frequencies f_{AOM1} and f_{AOM2} creating an accurate phase shift. Half wave plates ($\lambda/2$) and neutral density filters (ND1, ND2) allow the control of the optical power in each arm. Two lens systems are introduced in the setup ($L1, L2$). An expanded reference beam fully illuminates the CCD camera (Roper Cascade 512F EMCCD, frame transfer $512 \times 512, 16 \times 16 \mu\text{m}$ pixel matrix, triggered at a frame rate $f_{\text{CCD}} = 16$ Hz, integration time $t_{\text{int}} = 50$ ms). The glass substrate of the sample is coupled to a prism using an index matching liquid and illuminated in TIR configuration to achieve dark field illumination. The scattered field is collected by a microscope objective (MO, 100x magnification, NA = 0.95 in air) and reaches the CCD camera where it interferes with the reference beam in an off-axis manner. The resulting interference pattern is modulated at a beat frequency $\Delta f = f_{\text{AOM1}} - f_{\text{AOM2}}$, and the hologram is recorded by the camera

at a rate $f_{\text{CCD}} = 4\Delta f$. The holograms presented here are obtained with an acquisition time of 2 seconds. The reconstruction of the hologram is achieved numerically after k -space filtering using a method inspired by Cuche et al. [27]. The off-axis configuration, combined with heterodyne modulation, allows spatial and temporal filtering, yielding excellent signal-to-noise ratios and sensitivities [25, 28].

The gold nanostructures under study have been fabricated by electron beam lithography onto a glass substrate. The two gold nanodisks have a thickness of 30 nm with an additional 2 nm thick chromium (Cr) wetting layer, a diameter d of 150 nm and are separated by an interdisk spacing of 40 nm. Since we use 785 nm excitation, the nanodisk pairs feature strongly subwavelength dimensions with a $\lambda/4$ center-to-center spacing.

We investigated the far-field spectral response of the nanostructures using a white light source in dark field illumination and an imaging spectrometer, as described in Suck et al. [26]. Figure 3 plots the normalized scattering intensity spectrum of the longitudinal mode of a pair of coupled disks in comparison with the spectrum of a single

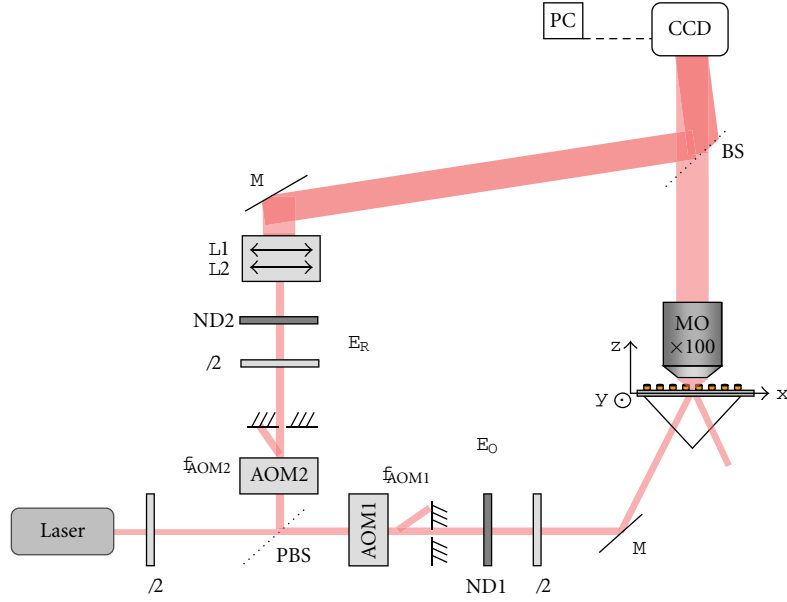


FIGURE 2: Experimental setup based on heterodyne off-axis holography. See text for details and abbreviations.

disk. The longitudinal mode is excited using an incoming polarization parallel to the dimer axis. The resonance wavelength at 760 nm is close to the excitation wavelength used in the holographic setup. The symmetric transverse mode resonance is expected to be close to the single disk resonance [9, 10].

4. Far-Field Scattering Maps of Two Coupled Disks

In order to excite two different modes in the coupled disks system, we used the two different illumination configurations as described above. Figure 4 presents cross sections along the three main reconstruction planes (x - y , y - z , and x - z planes) of far-field scattering images obtained by digital heterodyne holography on two coupled disks. The position of the nanostructure with respect to two different planes of incidence (y - z for case (a) and x - z for case (b)) is schematically shown on top of each image. Note that the planes containing the z -axis are plotted using a logarithmic scale. When analysing the holographic images, cross sections along the z -axis should be interpreted with care for negative z -values: the holographic signal only collects forward scattered light, and the intensity shown in the glass substrate ($z < 0$) only corresponds to backpropagation of this light without a direct physical meaning.

Analysing the scattering characteristics in the three reconstruction planes, it is seen that in both cases the scattering maps in the x - y plane show a bright dot with a size of around 500 nm. Cross-sections containing the z -axis indicate that most of the scattered light is distributed along the z -axis in the half space of air. The measured scattered intensities in both excitation geometries are of the same order of magnitude, indicating that both induced modes couple to the far-field with comparable efficiencies. The in-phase

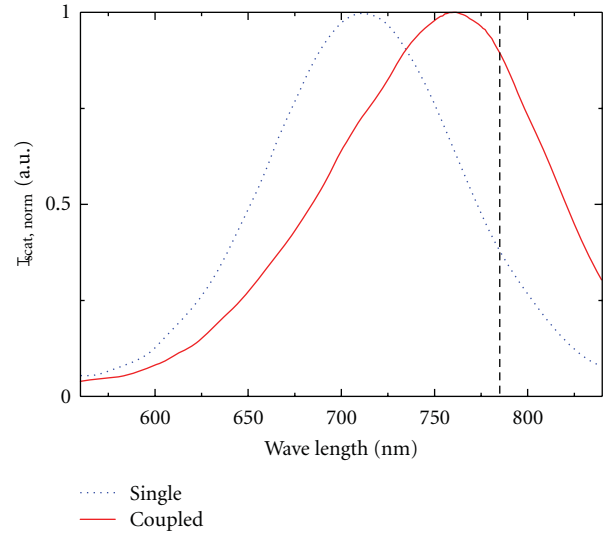


FIGURE 3: Normalized scattered intensity $I_{\text{scat}, \text{norm}}$ spectra of a single disk, $d = 150$ nm (dotted spectrum), and a pair of coupled disks, $d = 150$ nm, gap = 40 nm (continuous spectrum). The straight dashed line denotes the position of the exciting wavelength, $\lambda_{\text{exc}} = 785$ nm.

longitudinal mode has only a scattering efficiency between 2 and 3 times larger than the antisymmetric transverse mode, even though the excitation wavelength is close to the resonance of the longitudinal mode. According to analytical calculations, it should be possible to render the transverse mode brighter than the longitudinal mode by reducing the interparticle spacing and tuning the excitation wavelength [23].

Furthermore, we observe that the far-field scattering pattern of the transverse mode differs slightly from the

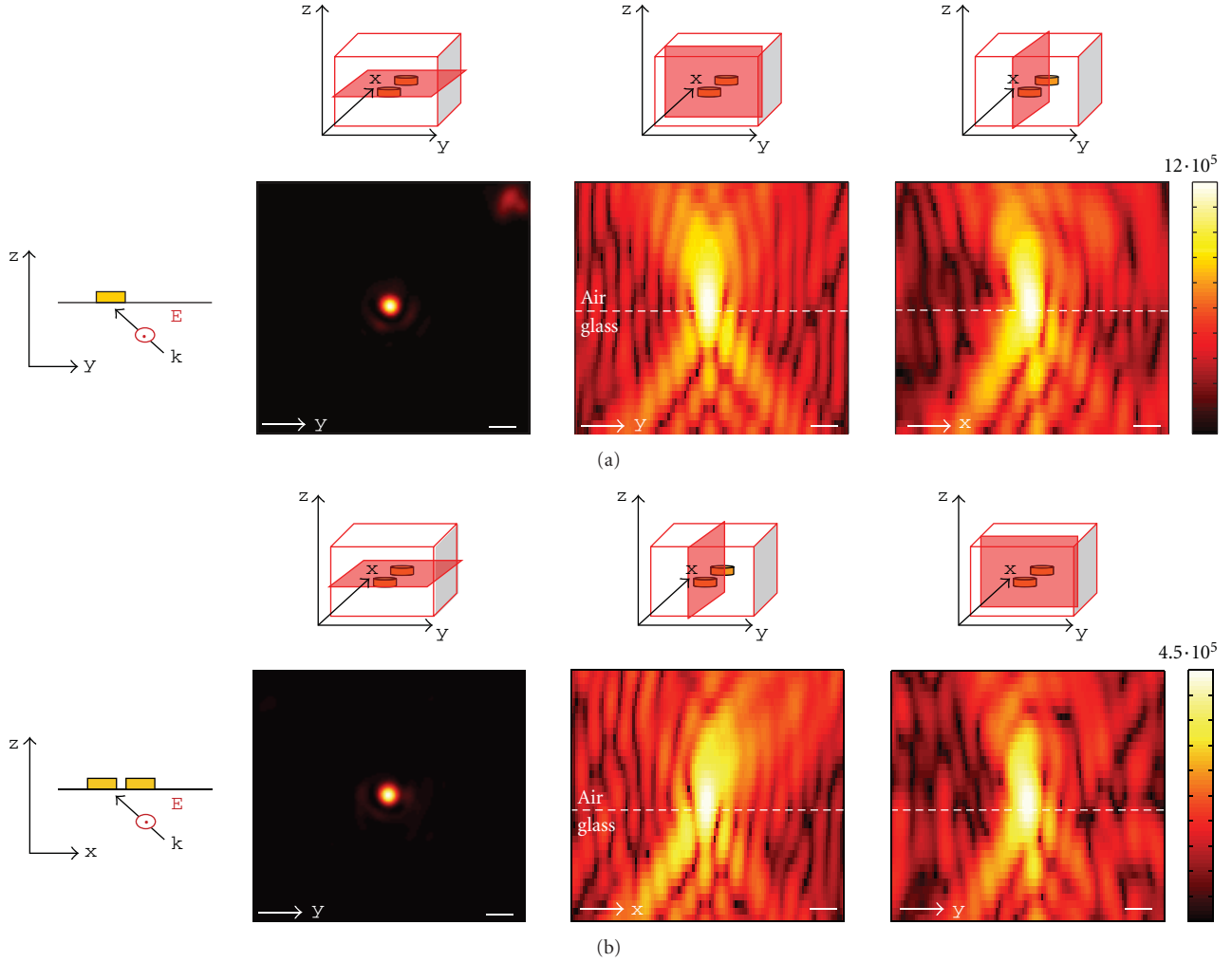


FIGURE 4: Intensity (arb. unit) of the scattered field reconstructed from a single hologram at $\lambda_{\text{exc}} = 785 \text{ nm}$ for two disks, illuminated under 2 configurations (see schemes on the left): s-polarized excitation with the dimer axis (a) perpendicular to the plane of incidence and (b) in the plane of incidence. The color scale of the x - y cross section (1st column) is linear while that of the y - z and x - z sections is logarithmic. The length of the scale bar is $1 \mu\text{m}$.

pattern observed with the longitudinal mode. While the scattering pattern of the longitudinal mode (case (a)) extends directionally along the z -axis in the incident plane (y - z plane), the scattering pattern of the transverse mode (case (b)) is slightly inclined towards positive y -values. In order to reveal finer differences between the two modes, we analyse the Fourier space of the hologram which contains information about the angular scattered intensity.

5. Angular Scattering Pattern of Two Coupled Disks

The emission pattern of an object can be recorded by collecting the emitted photons with an objective lens and imaging the intensity distribution in the back focal plane of the objective. These images, that display the Fourier plane, contain the angular distribution of the emitted light [29]. The intensity and the coordinates of the Fourier space are

related to the angular radiation pattern as demonstrated in the literature [17]. In contrast, in digital holography, which records the amplitude and the phase of the scattered light, the Fourier plane can be obtained via Fourier transformation of the reconstructed hologram. The angular intensity distribution of the scattered light can thus be accessed in the hologram. Since the setup collects forward scattered light, the Fourier space only contains information on the angular scattering pattern in air.

Figures 5(a) and 5(b) display the Fourier planes, calculated from measurements of Figure 4, that is, the angular scattering pattern of the recorded holograms. A circular scattering pattern is observed with coordinates directly linked to the two angles θ and φ . Its radius corresponds to the maximum collection angle of $\theta_{\text{NA}} = 72^\circ$, limited by the $\text{NA} = 0.95$ objective.

Whereas cross-sections of the scattering pattern revealed minor differences, it is evident that the two induced modes

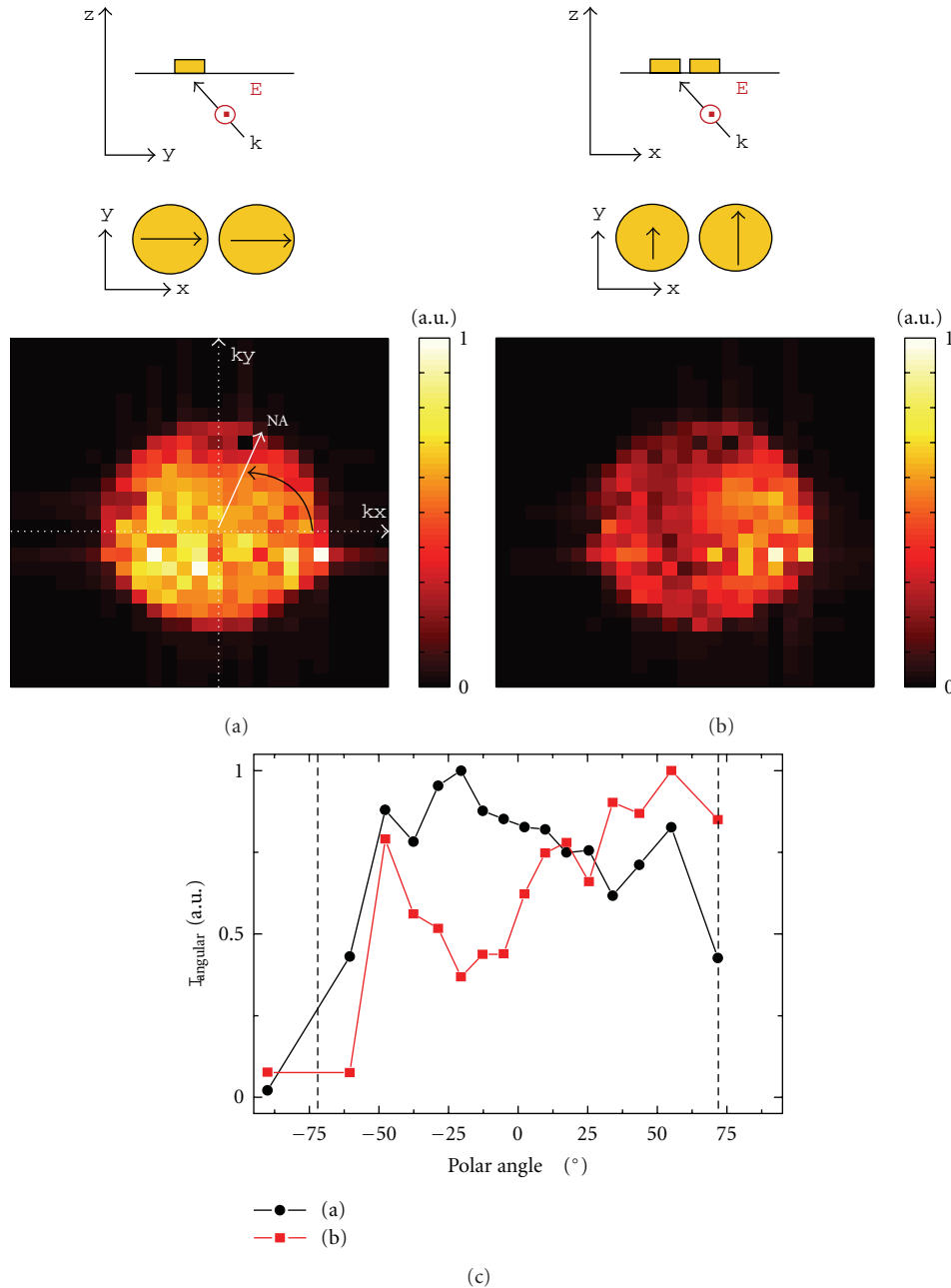


FIGURE 5: (a, b) Fourier planes of the recorded holograms of two coupled disks, corresponding to Figure 4. The two axes k_x and k_y are indicated by dotted lines in image (a). (c) Angular normalized intensity distribution I_{angular} as a function of the polar angle θ (corresponding to the k_x -axis, resp.) for the two different illumination configurations for $\varphi = 0^\circ$, averaged over 3 lines of pixels.

differ strongly in their angular distribution. In configuration (a), the intensity is distributed homogeneously in the k -space, whereas in configuration (b), most of the intensity is distributed along the $+k_x$ -axis. The graph in Figure 5(c) plots the normalized angular scattering intensity I_{angular} as a function of the polar angle θ , which is in fact a line plot along the k_x -axis. Due to the pixelation in the k -space, we obtain an angle resolution of around 8° . This plot confirms the images of Figures 5(a) and 5(b) with preferential light scattering in configuration (b) towards positive θ values.

We have seen that the two holograms, although very similar in the real space, reveal a profound difference in the Fourier space. This indicates different phase behaviour of the two excited modes in the nanodisk pair as expected from the near-field simulations. The symmetry of the scattering behaviour of the longitudinal mode is consistent with in-phase induced dipoles. On the other hand, strong directionality in the angular scattering pattern of the transverse mode reveals the influence of phase differences between induced dipoles separated by $\lambda/4$.

6. Conclusion

We have presented a study of the spatial scattering behaviour of sub-wavelength coupled nanodisks, excited in an in-phase longitudinal or an antisymmetric transverse mode. The nature of the induced modes was estimated using near-field three-dimensional calculations which account for the total internal reflection excitation geometry used in our experimental setup. Three-dimensional far-field measurements revealed that both modes scatter light with comparable efficiencies which contradicts quasi-static approximations such as the hybridization model. The analysis of the reconstructed hologram in the Fourier plane demonstrates that the two investigated modes display strikingly different scattering patterns. In particular, the transverse mode scatters light preferentially into one half-plane, indicating that phase effects must occur in the two induced dipoles. Our study proves that the quasi-static approximation breaks down in a simple particle dimer even for center-to-center spacings smaller than $\lambda/4$. The thorough analysis of the near-field phase effects that occur in coupled induced dipoles is necessary to fully comprehend and optimize the control offered by optical antennas on the directionality of single quantum emitters.

Acknowledgments

The authors are grateful to C. Dupuis from the LPN where the nanofabrication has been performed. They would like to acknowledge financial support from the Fondation Pierre-Gilles de Gennes and Agence Nationale de la Recherche Grants 3D BROM (ANR 11 BS10 015 01) and TWINS (ANR 11 BS10 002 02).

References

- [1] S. Nie and S. R. Emory, "Probing single molecules and single nanoparticles by surface-enhanced Raman scattering," *Science*, vol. 275, no. 5303, pp. 1102–1106, 1997.
- [2] J. P. Camden, J. A. Dieringer, Y. Wang et al., "Probing the structure of single-molecule surface-enhanced Raman scattering hot spots," *Journal of the American Chemical Society*, vol. 130, no. 38, pp. 12616–12617, 2008.
- [3] N. Liu, M. L. Tang, M. Hentschel, H. Giessen, and A. P. Alivisatos, "Nanoantenna-enhanced gas sensing in a single tailored focus," *Nature Materials*, vol. 10, pp. 631–636, 2011.
- [4] P. Bharadwaj, R. Beams, and L. Novotny, "Nanoscale spectroscopy with optical antennas," *Chemical Science*, vol. 2, no. 1, pp. 136–140, 2011.
- [5] S. S. Ćimović, M. P. Kreuzer, M. U. González, and R. Quidant, "Plasmon near-field coupling in metal dimers as a step toward single-molecule sensing," *ACS Nano*, vol. 3, no. 5, pp. 1231–1237, 2009.
- [6] A. N. Grigorenko, N. W. Roberts, M. R. Dickinson, and Y. Zhang, "Nanometric optical tweezers based on nanostructured substrates," *Nature Photonics*, vol. 2, no. 6, pp. 365–370, 2008.
- [7] W. Zhang, L. Huang, C. Santschi, and O. J. F. Martin, "Trapping and sensing 10 nm metal nanoparticles using plasmonic dipole antennas," *Nano Letters*, vol. 10, no. 3, pp. 1006–1011, 2010.
- [8] P. Nordlander, C. Oubre, E. Prodan, K. Li, and M. I. Stockman, "Plasmon hybridization in nanoparticle dimers," *Nano Letters*, vol. 4, no. 5, pp. 899–903, 2004.
- [9] W. Rechberger, A. Hohenau, A. Leitner, J. R. Krenn, B. Lamprecht, and F. R. Aussenegg, "Optical properties of two interacting gold nanoparticles," *Optics Communications*, vol. 220, no. 1–3, pp. 137–141, 2003.
- [10] K.-H. Su, Q.-H. Wei, X. Zhang, J. J. Mock, D. R. Smith, and S. Schultz, "Interparticle coupling effects on plasmon resonances of nanogold particles," *Nano Letters*, vol. 3, no. 8, pp. 1087–1090, 2003.
- [11] T. Atay, J.-H. Song, and A. V. Nurmikko, "Strongly interacting plasmon nanoparticle pairs: from dipole-dipole interaction to conductively coupled regime," *Nano Letters*, vol. 4, no. 9, pp. 1627–1631, 2004.
- [12] P. K. Jain, W. Huang, and M. A. El-Sayed, "On the universal scaling behavior of the distance decay of plasmon coupling in metal nanoparticle pairs: a plasmon ruler equation," *Nano Letters*, vol. 7, no. 7, pp. 2080–2088, 2007.
- [13] A. F. Koenderink, R. de Waele, J. C. Prangsma, and A. Polman, "Experimental evidence for large dynamic effects on the plasmon dispersion of subwavelength metal nanoparticle waveguides," *Physical Review B*, vol. 76, no. 20, Article ID 201403, 4 pages, 2007.
- [14] R. de Waele, A. F. Koenderink, and A. Polman, "Tunable nanoscale localization of energy on plasmon particle arrays," *Nano Letters*, vol. 7, no. 7, pp. 2004–2008, 2007.
- [15] J. N. Farahani, D. W. Pohl, H.-J. Eisler, and B. Hecht, "Single quantum dot coupled to a scanning optical antenna: a tunable superemitter," *Physical Review Letters*, vol. 95, no. 1, pp. 1–4, 2005.
- [16] T. Kosako, Y. Kadoya, and H. F. Hofmann, "Directional control of light by a nano-optical Yagi-Uda antenna," *Nature Photonics*, vol. 4, no. 5, pp. 312–315, 2010.
- [17] A. G. Curto, G. Volpe, T. H. Taminiau, M. P. Kreuzer, R. Quidant, and N. F. van Hulst, "Unidirectional emission of a quantum dot coupled to a nanoantenna," *Science*, vol. 329, no. 5994, pp. 930–933, 2010.
- [18] N. Bonod, A. Devilez, B. Rolly, S. Bidault, and B. Stout, "Ultra-compact and unidirectional metallic antennas," *Physical Review B*, vol. 82, no. 11, Article ID 115429, 6 pages, 2010.
- [19] B. Rolly, B. Stout, S. Bidault, and N. Bonod, "Crucial role of the emitter-particle distance on the directivity of optical antennas," *Optics Letters*, vol. 36, no. 17, pp. 3368–3370, 2011.
- [20] J. Dorfmueller, D. Dregely, M. Esslinger et al., "Near-field dynamics of optical Yagi-Uda nanoantennas," *Nano Letters*, vol. 11, no. 7, pp. 2819–2824, 2011.
- [21] P. Olk, J. Renger, M. T. Wenzel, and L. M. Eng, "Distance dependent spectral tuning of two coupled metal nanoparticles," *Nano Letters*, vol. 8, no. 4, pp. 1174–1178, 2008.
- [22] S.-C. Yang, H. Kobori, C.-L. He et al., "Plasmon hybridization in individual gold nanocrystal dimers: direct observation of bright and dark modes," *Nano Letters*, vol. 10, no. 2, pp. 632–637, 2010.
- [23] B. Rolly, B. Stout, and N. Bonod, "Metallic dimers: when bonding transverse modes shine light," *Physical Review B*, vol. 84, no. 12, article 125420, 8 pages, 2011.
- [24] T. Shegai, S. Chen, V. D. Miljković, G. Zengin, P. Johansson, and M. Käll, "A bimetallic nanoantenna for directional colour routing," *Nature Communications*, vol. 2, no. 1, article 481, 2011.
- [25] M. Atlan, M. Gross, P. Desbiolles, E. Absil, G. Tessier, and M. Coppey-Moisan, "Heterodyne holographic microscopy of gold particles," *Optics Letters*, vol. 33, no. 5, pp. 500–502, 2008.

- [26] S. Y. Suck, S. Collin, N. Bardou, Y. de Wilde, and G. Tessier, "Imaging the three-dimensional scattering pattern of plasmonic nanodisk chains by digital heterodyne holography," *Optics Letters*, vol. 36, no. 6, pp. 849–851, 2011.
- [27] E. Cuhe, P. Marquet, and C. Depeursinge, "Spatial filtering for zero-order and twin-image elimination in digital off-axis holography," *Applied Optics*, vol. 39, no. 23, pp. 4070–4075, 2000.
- [28] E. Absil, G. Tessier, M. Gross et al., "Photothermal heterodyne holography of gold nanoparticles," *Optics Express*, vol. 18, no. 2, pp. 780–786, 2010.
- [29] M. A. Lieb, J. M. Zavislan, and L. Novotny, "Single-molecule orientations determined by direct emission pattern imaging," *Journal of the Optical Society of America B*, vol. 21, no. 6, pp. 1210–1215, 2004.

Research Article

Gold Nanoparticles as Probes for Nano-Raman Spectroscopy: Preliminary Experimental Results and Modeling

V. Le Nader,¹ J.-Y. Mevellec,¹ T. Minea,² and G. Louarn¹

¹*Institut des Matériaux Jean Rouxel (IMN)-UMR 6502, 2 rue de la Houssinière, BP 32229, 44322 Nantes Cédex 3, France*

²*Laboratoire de Physique des Gaz et des Plasmas, UMR 8578 CNRS-Université Paris-Sud, Bat. 210, Campus d'Orsay, 91405 Orsay, France*

Correspondence should be addressed to V. Le Nader, victor.lenader@cnrs-imn.fr

Received 28 July 2011; Revised 14 December 2011; Accepted 29 December 2011

Academic Editor: Ali Passian

Copyright © 2012 V. Le Nader et al. This is an open access article distributed under the Creative Commons Attribution License, which permits unrestricted use, distribution, and reproduction in any medium, provided the original work is properly cited.

This paper presents an effective Tip-Enhanced Raman Spectrometer (TERS) in backscattering reflection configuration. It combines a tip-probe nanopositioning system with Raman spectroscopy. Specific tips were processed by anchoring gold nanoparticles on the apex of tapered optical fibers, prepared by an improved chemical etching method. Hence, it is possible to expose a very small area of the sample ($\sim 20 \text{ nm}^2$) to the very strong local electromagnetic field generated by the lightning rod effect. This experimental configuration was modelled and optimised using the finite element method, which takes into account electromagnetic effects as well as the plasmon resonance. Finally, TERS measurements on single-wall carbon nanotubes were successfully performed. These results confirm the high Raman scattering enhancement predicted by the modelling, induced by our new nano-Raman device.

1. Introduction

The Raman effect is a well-known phenomenon of the inelastic diffusion of light, with change in the frequency of the incident radiation passing through materials or molecules. In the spectrum of the scattered light, new bands can be observed, and their energies are characteristic of the chemical nature of the investigated object. Raman spectroscopy is a useful tool, which is widely used in academic and industrial laboratories. This nondestructive spectroscopy provides structural information about various materials and can be exploited to build sensors that operate in different areas such as gas detection or bio- and chemical sensing. Generally, these equipments were built from an optical system that analyzes the diffusion of the light and transfers this information to spectroscopic detectors and finally to the electronic system for data processing. Nevertheless, the weakness of the signal does not allow the investigation of single molecules or individual nanoobjects.

However, in the 70s, it was observed and proved [1–3] that Raman intensity can be strongly enhanced using

a specific surface-sensitive technique based on the optical properties of noble metals, such as silver or gold. Nowadays, this phenomenon is well known and commonly called Surface Enhanced Raman Scattering (SERS) effect. This enhancement occurs for molecules adsorbed on rough metal surfaces or on metal nanoparticles. The main Raman enhancement contribution is attributed to the excitation of surface plasmons-polaritons resonances (collective oscillations of the electrons localised near the surface of metals) occurring near metallic nanostructures. The interaction of light with metallic nanoparticles is dominated by strong optical resonances due to the excitation of localized surface plasmons. One of the main consequences of this surface plasmon resonance is the high electromagnetic field created at the surface of the nanoparticle, which significantly enhanced the Raman scattering. The scattering signal can be enhanced by 10 orders of magnitude meaning that this technique may detect single molecules and that the characterization of individual nanoobjects becomes possible [4–7]. This possibility of using colloidal dispersions of silver (Ag) or gold (Au) nanoparticles in aqueous solutions as a method

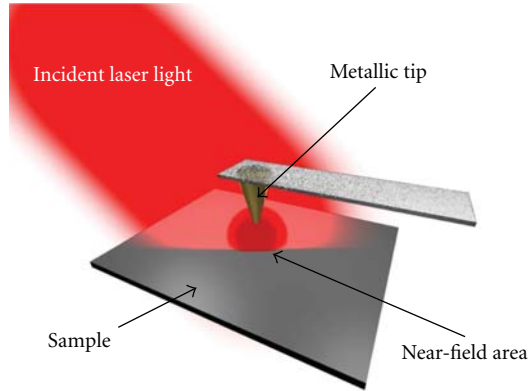


FIGURE 1: Schematic representation of Tip-Enhanced Raman Spectroscopy in the side-illumination mode.

for enhancing Raman scattering was first demonstrated by Creighton et al. [8]. Note that the intensity of the electromagnetic field strongly depends on the nanoparticle size, shape, and interparticle distance. Such high enhancement factors are also obtained from well-defined nanostructures, like nanoparticles [9–11], nanoholes [12] or nanotips [13]. Hence, Tip-Enhanced Raman Spectroscopy (TERS) [14–19] exploits this effect induced by a nanotip, derived from the local probe microscopy techniques, among the Atomic Force Microscopy (AFM) is the most notorious example.

TERS principle consists in the illumination of a sharp metallic tip by a monochromatic light in order to benefit from plasmons resonance and antenna effects. Theoretical studies show that a strongly localized electric field can be created near the tip apex. The strong field is very localized showing strong gradients and thus ensuring both the very good nanometer scale spatial resolution and the enhancement of the optical scattering signal for detection. Finding optimal conditions for achieving a maximal localized field thus becomes one of the most critical issues in tip-enhanced spectroscopies. The field confinement is readily achieved if the polarization vector of the excitation light is orientated along the direction of the tip and if the tip-surface distance is very low. In these conditions, the surface charge density oscillates and very high electromagnetic field amplitudes arise at the tip apex, as a function of the induced-dipole strength. As schematized in Figure 1, a strong confinement and enhancement of the electromagnetic field at the vicinity of the tip apex can occur.

Conventional Raman scattering is known as a very weak light-matter interaction phenomenon, whose cross section is usually 10^{-8} , much weaker than the cross section of infrared absorption [20]. Additionally, the spatial resolution of Raman spectroscopy is limited by the Rayleigh criterion (theoretical diffraction limit $\sim \lambda/2$). TERS spectroscopy is a way to overcome these limits, and the success of such devices depends on the ability to focus the laser beam on the apex of a sharp metallic probe, located in the nanoscale vicinity (1 to 10 nanometers) of a nanoobject or a surface. Since the first

experimental published results, worldwide research groups have implemented several TERS configurations. Two types of setups can be distinguished based on light reflection or light transmission.

In the transmission configuration, the scattered light is collected from the opposite side of the sample, which is illuminated by a monochromatic source [21–26]. Generally, the incident beam is focused under the tip apex through the sample. This configuration uses microscope objectives with high Numerical Aperture (NA), including oil-immersion objectives, improving thus the collection efficiency and minimizing the far-field contribution. However, this configuration is limited to optically transparent samples or very thin substrates.

In the backscattering mode, the incident beam does not cross the sample [27–31]. This configuration requires the use of objectives with a numerical aperture ranging from 0.25 to 0.6. Consequently, in backscattering configuration, the background signal due to the far-field is higher than in transmission mode. This problem can be partially solved by using suitable light polarization [32, 33]. In spite of this drawback, the backscattering configuration is very interesting due to its versatility. On the contrary to the transmission operation mode, the backscattering one is efficient for the investigation of all types of samples (transparent or not), in particular metallic substrates where plasmonic tip-sample coupling can highly improve the Raman scattering by the local enhancement of the signal.

In this work, we introduce an experimental confocal TERS device in reflection configuration (side illumination) developed in our laboratory and dedicated to nanoobjects investigation. The presented TERS device is based on a commercial Raman spectrometer coupled with a tip-probe nanopositioning system. As plasmon resonance of gold metals occurs in the visible range, special tips improved by gold nanoparticles grafted on the silica tips were designed. Finally, experimental results recorded on single-wall carbon nanotubes (SWCNT) are presented and compared with finite elements analysis.

2. Experimental Setup

2.1. Tip-Probe Preparation. The tip accounts as central element in our device. The lateral resolution depends on the tip dimensions (aperture angle, apex diameter). As underlined above, particular optical properties of noble metals can significantly increase Raman scattering. There is a large variety of technical possibilities to elaborate metallic probes and several report efficient probes for TERS spectroscopy [19, 34–37]. The most frequently used are the electrochemical etching of solid metal rods and the thermal evaporation technique to deposit metal on sharp tips.

Here, we describe an alternative method based on the physical anchoring (electrostatic) of gold nanoparticles on a sharp silica tip. In the first step of the process, multimode fibers (125 μm core diameter) are etched using the substitute-sheath etching method [38]. After removing

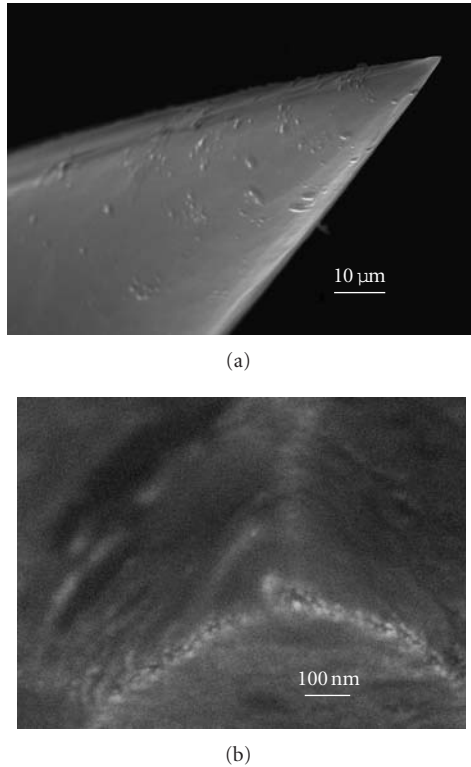


FIGURE 2: SEM images of tips coated with 15 nm gold nanoparticles: (a) 1300x magnification. (b) 85000x magnification. At this magnification, nanoparticles on the tip apex can be observed.

the jacket (around 2.5 cm length from the free extremity of the fiber) by mechanical stripping, a substitution sheath is obtained using a liquid wax. Then optical fibers are immersed for 4 h in aqueous HF solution at room temperature, leading to the fiber etching following a conical shape. Afterwards the wax coating is simply removed mechanically (Figure 2(a)).

The second step consists of the grafting of gold nanoparticles on the tapered optical fiber. A colloidal solution is obtained from a mixture of chloroauric acid solution (HAuCl_4) and a trisodium citrate solution ($\text{Na}_3\text{C}_6\text{H}_5\text{O}_7$) [11]. A Dynamic Light Scattering (DLS) experiment revealed that the diameter of the nanoparticles was about 15 nm. Finally, the Au nanoparticles are immobilized at the apex of the sharp silica tip by way of a chemical agent. The extremities of the optical fibers are immersed in an APTMS (3-aminopropyltrimethoxysilane) solution in order to functionalize the silica surface of the tip. The electrostatic interactions between the positive charges of amines functional groups of the APTMS and the negative charges provided by the citrate embedding the nanoparticles are here exploited to graft the gold colloids.

Figure 2 shows a typical nanotip obtained using this process. After the etching step, one can observe that the extremity of the tip is faceted and the tip apex dimensions are around 50 nm. As detailed in Figure 2(b), the face edges

of the probe extremity constitute the preferential sites to graft gold nanoparticles. In particular, gold nanoparticles are caught by the tip apex. Sometimes, just one or a small group of gold nanoparticles emerges from the silica tip apex. Therefore, this tip preparation method is very interesting to reduce the probe dimensions.

2.2. Tip-Probe Nanopositioning System. The approach of such prepared tip to the sample is performed by a nanomechanic system providing accuracy higher than 1 nm. The used piezoelectric system (Solver SNOM, NT-MDT) was managed by a controller (NT-MDT, BL022MT). The piezoelectric head can move the tip-probe position in each X, Y and Z direction, over $40 \mu\text{m} \times 40 \mu\text{m} \times 5 \mu\text{m}$. The lateral resolution given by the manufacturer is lower than 20 nm, while the resolution in Z direction is in the order of 0.1 nm, guaranteeing a reliable tip/sample distance. A feedback control loop, based on the amplitude of the tip oscillation, checks and maintains a constant tip/sample distance.

This mode is called “shear-force” because the tip oscillations are forced to be parallel to the surface of the sample [39, 40]. Near the surface, the shear-force damps the oscillations of the tip. From the resulting electric signal, proportional to the strength of the shear-force applied to the tip, the nanopositioning device adjusts the tip position regarding a setpoint value to keep constant the tip-sample distance. In this work, tips were glued on one prong of a quartz tuning fork (Farnell quartz 32.768 kHz). Figure 3(a) shows the tip stuck (arrows). The tuning fork is excited by the piezodriver with a frequency close to its own resonance.

2.3. Coupling of the Optical Setup to the Nanopositioning System. The last point of the nanoRaman concerns the coupling, in time and space, of the tip with the incident laser beam and the Raman spectrometer. The Raman spectrometer used in this work is a commercial T64000 model from HORIBA Jobin-Yvon. The optical detector is a CCD camera cooled by liquid nitrogen. An optical microscope (BH2-UMA) outfitted with a $\times 100$ magnification objective (NA: 0.6, WD: 7.6 mm) allows to survey the tip and the sample motions. These movements are managed by an XY table. Experimental results presented in this work were performed using a monochromatic red light (645 nm) excitation provided by a coherent Krypton ion laser (Figure 4). The incident laser beam was focused in the vicinity of the tip apex by the objective and the scattered signal was collected by the same objective (backscattering configuration). The scattered light passes then through a simple monochromator, with a diffraction grating of 1800 traces/mm, allowing thus the best compromise between signal intensity and spectral resolution. Let us remember that the orientation of the electric field with respect to the tip axis plays an important role [41–44].

Numerical simulations made by Sun and Shen reveal that the optimal angle between the incident electric field and the axis of a silver tip is in the $30\text{--}35^\circ$ range, which corresponds to 55° between direction of the propagating

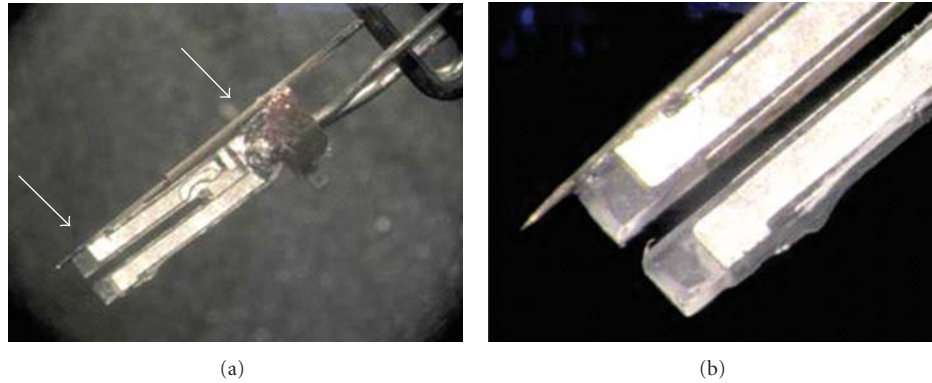


FIGURE 3: Optical images of the tips glued on a quartz tuning fork. (a) Points of glue are indicated by arrows. (b) Zoom of the quartz fork with the tip.

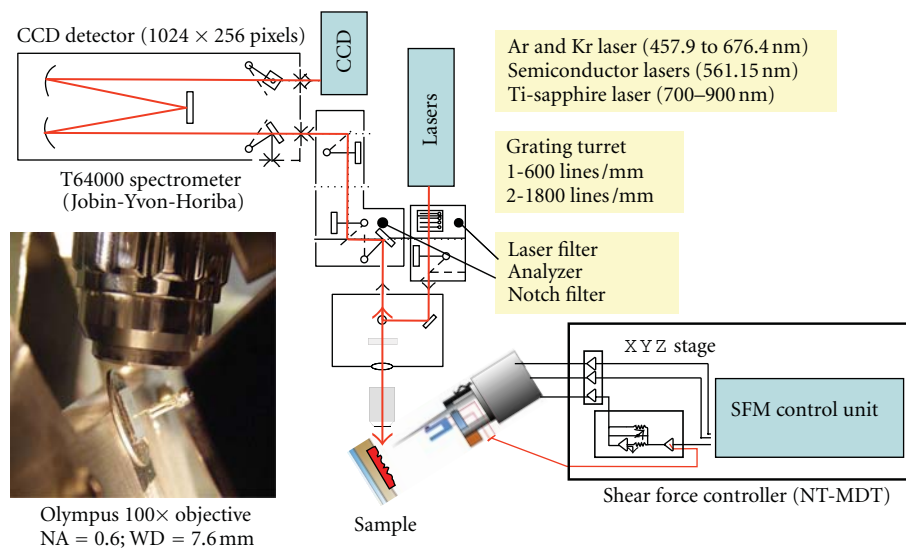


FIGURE 4: A schematic of the tip-enhanced Raman setup with an image of the tip-surface area (inset). The sharp gold tip is scanned through a strongly focused laser beam. The optical signal is detected by combining a spectrometer and a CCD detector. The axis of the illuminating/collecting optics is positioned at 55° with respect to the tip axis.

wave (p-polarisation) and the tip axis [45]. In agreement with these published results, a specific piezoscanner holder was designed (Inset Figure 4).

2.4. Numerical Modeling. In order to model the experiments, we coupled Finite Element Analysis (FEM) of the electromagnetic field at the vicinity of the surface with the dispersion effects of metals. The equations used to solve the electromagnetic field derive from the Maxwell equations following the simplifying assumptions, particularly about the geometry of the tip. For the resolution of the partial derivative equations (PDEs) and for the space discretization, the software Comsol Multiphysics 3.5 was used [46, 47]. The coupling with the optical properties of gold was implemented under Matlab 7. In this way, the optical effects induced by the plasmon resonance of gold nanoparticles and the partial derivative equations representing the electromagnetic field around the tip were calculated simultaneously

as a function of the wavelength taking into account the geometry of the tip.

3. Results and Discussion

We designed a spherical gold colloid anchored on the apex of a silica tip close to a smooth golden surface. In this modelling, the angle between the axis of the tip and the direction of the propagating wave was fixed at 55° .

Figure 5(a) shows the enhancement factor G , defined as the square of the normalized local electric field amplitude. This map shows the extreme enhancement of the electromagnetic field in a very small area surrounding the tip. In order to determine the wavelength of the incident light which is the most relevant for our system, we calculated the enhancement factor G between the tip and the golden surface as a function of the incident wavelength. Thereby, the FEM calculations predict that the best enhancement is in the range of 550 to

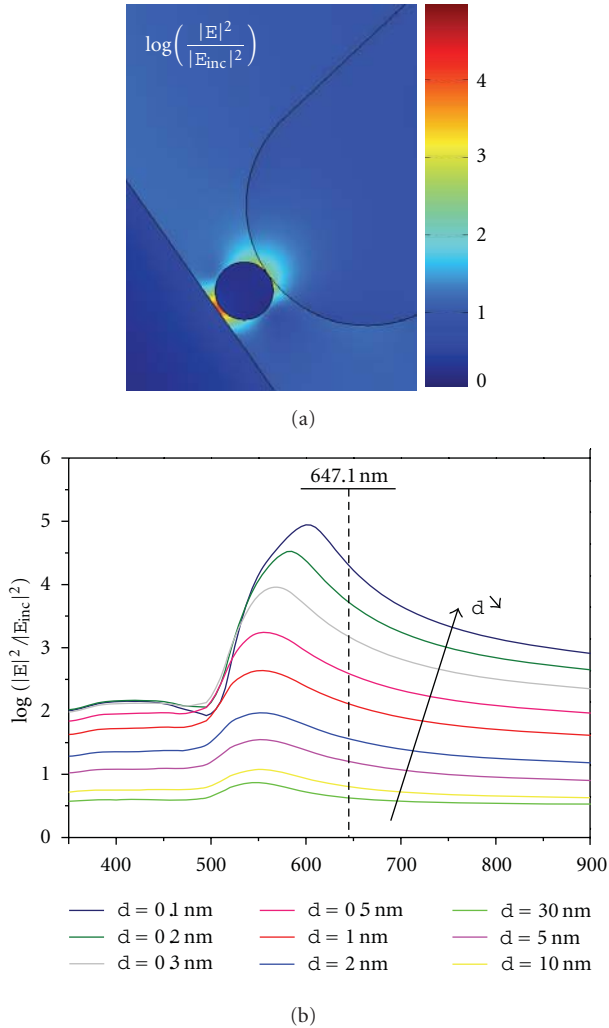


FIGURE 5: (a) map of the Raman enhancement factor in the vicinity of the surface. For modeling this 2D structure, only 1 nanoparticle is considered. The diameter of the NPs was fixed to 15 nm, and the distance between tip-surface was taken 1 nm. The wavelength of the Raman excitation was fixed at 650 nm. (b) Finite Elements Analysis (FEA) of the near-field profile of the gold tip under Plasmon resonance excitation, as a function of the wavelength (400–900 nm) and of the tip-surface distance (0.1 to 10 nm).

650 nm, depending on the distance between the probe and the surface of interest.

In the light of these numerical predictions, we performed TERS experiments on single-wall carbon nanotubes (SWCNT) placed on a smooth gold surface and illuminated by a red monochromatic light (excitation wavelength = 647 nm).

Before discussing in detail the results, let us underline that only carbon nanotubes being in resonance or near-resonance conditions can be detected by Raman spectroscopy. These conditions are reached when the excitation energy corresponds to the energy difference between two Van Hove electronic states. By considering the G-bands profile of the spectrum, presented in Figure 6, and the excitation

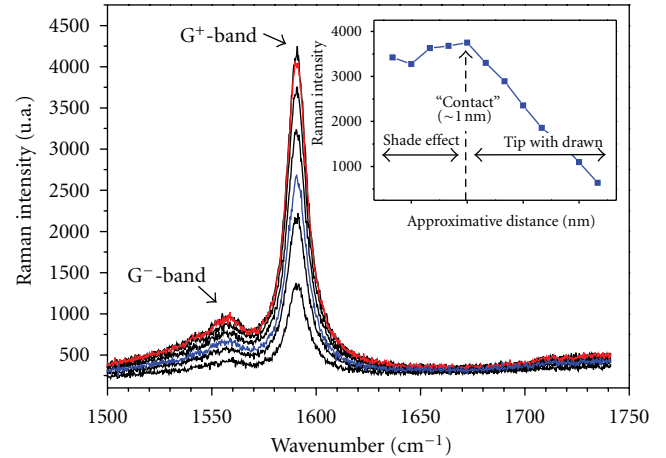


FIGURE 6: TERS signal recorded on an individual SWCNT placed on the surface. Raman spectra are recorded for different tip-SWCNT distance (excitation line: 647.1 nm; laser power: 10 mW/ μm^2 exposure time: 30 seconds). The inset indicate the intensity of the experimental Raman as a function of the estimated tip-SWCNT distance.

wavelength, we assume that metallic carbon nanotubes are mainly detected. The G^+ (1586 cm^{-1}) band profile is Lorentzian. It is accompanied by the G^- band at 1566 cm^{-1} and the D band at 1320 cm^{-1} and RBM (not shown). The dispersive (D) band indicates the presence of defects such as undesirable sp^3 carbon including disordered carbon. Information about nanotubes diameter can be obtained from the radial breathing mode (RBM) at low wavenumbers (usually between 120 cm^{-1} and 350 cm^{-1}).

We focus here on the G-bands, which are attributed to atomic displacements along the tube axis (G^- band) and atomic vibrations along the circumferential direction (G^+ band) [48–52]. To quantify the experimental enhancement effect under the tip, Raman spectra were recorded by varying the distance between the nanoprobe and the SWCNT (Figure 6).

One can distinguish two phases during the approach of the tip. During the first phase, the gold nanotip is first roughly approached to the sample by means of a micrometer screw, then during the second phase, a finer approach with the piezoscanner is performed. According to the nanopositioning system, we estimated that the tip-sample distance can vary in the range of $2\text{ }\mu\text{m}$ to 2 nm. The spectra show the enhancement of the Raman signal (G^+ -band). By reducing the sample-tip distance from around $2\text{ }\mu\text{m}$ to 2 nm, the Raman intensity is 6 times enhanced (contrast). In order to estimate the enhancement factor yielding under the tip, the far-field signal must be separated from the near-field signal. We estimated the average diameter of the focus incident beam at $1.5\text{ }\mu\text{m}$, which is generally assumed for the used objective ($\times 100$, NA: 0.6, WD: 7.6 mm). From the modelling, it is possible to assess the area that contains the largest near-field contribution. Hence, for a diameter of 20 nm the best signal is expected for a tip-sample distance of 2 nm and an excitation wavelength of 645 nm. The equation (1) gives us

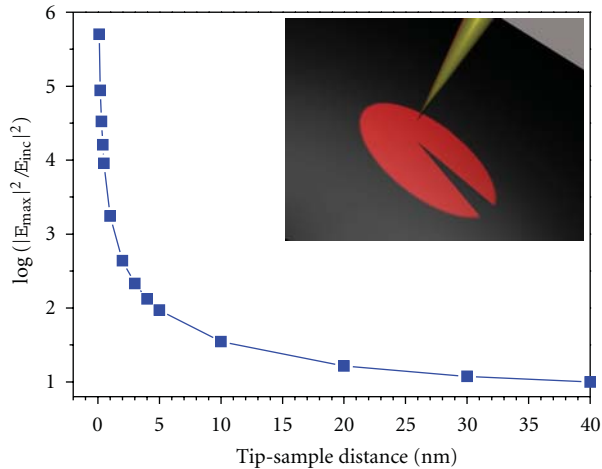


FIGURE 7: Raman enhancement factor estimated by Finite Elements Analysis (FEA) in the vicinity of the surface of interest, as a function of the tip-surface distance (0.1 to 40 nm). The inset shows the tip approach from the incident beam and the shadowing of the incident beam during the approach process.

an estimation of the observed Raman enhancement factor (G) below the tip apex. The contrast is defined as the ratio between the intensities of near-field and far-field signals [53, 54]

$$G = \frac{I_{\text{NF}}}{I_{\text{FF}}} = \text{contrast} \times \frac{\sigma_{\text{tot}}}{\sigma_{\text{NF}}} - 1. \quad (1)$$

where σ_{tot} , σ_{NF} , I_{FF} , and I_{NF} are respectively, the total section of analysis, the area of the near-field contribution (below the tip), the Raman intensity without any tip (far-field signal resulting from an area equal to σ_{NF} and the Raman intensity due to the tip (near-field signal resulting from an area equal to σ_{NF}).

Applying this equation, the Raman enhancement factor below the tip apex is around 3.2×10^4 . The quantitative estimation is in good agreement with already published papers [28, 29, 54].

The second phase of these experiments starts when the tip is brought very close to the sample, less than 2 nm. In this phase, tip displacements are controlled by the nanopositioning system. In order to manage the distance between the tip and the sample, the operator adjusts the setpoint value in which a feedback control is assigned. The contact between the tip and the sample occurs when the setpoint is equal to 0. Contrarily to FEM prediction (Figure 7), the Raman intensity enhancement slowly decreased when the tip is very close to SWNTC.

Comparison with modelling predicts that the peak will be between 0.3 and 0.5 nm from the surface. Let us remark that FEM calculations do not take into account the area of the sample hidden by the tip itself. An illustration of this possible phenomenon is showed in the inset of Figure 7. Regarding TERS experiments, we are assuming that this shadowing effect must be taken in consideration when the tip-sample

distance is very small. This effect could probably be limited by reducing the dimensions of the silica tip apex and its aperture angle.

4. Conclusion

A side-illumination TERS device created by combining a nanopositioning system of a tip with a Raman spectrometer was described. The Raman signal is enhanced by the interaction of a nanoscale gold nanoparticle grafted onto sharp silica tips. This area was estimated to be 20 nm^2 using finite element analysis. Even if a shadowing effect was clearly shown very close to the sample ($<2 \text{ nm}$), our TERS experiments lead to an enhancement factor of about 3.2×10^4 of the Raman scattering intensity. The precision of the nanopositioning system and the high spatial resolution provided by the sharp tip are sufficient to scan and characterize non-transparent nanoobjects with nanometric spatial resolution. These preliminary experiments reveal the potential of the TERS device. Indeed, the benefits of a triple confocal Raman spectrometer, such as polarization control, choice of excitation wavelength (argon, krypton ionized, and solid semiconducting crystal lasers covering all the visible range), and high resolution are preserved by our setup. The possibility to explore low frequency bands of SWCNT by Tip-Enhanced Raman Spectroscopy opens up very interesting and promising developments of this technique.

References

- [1] M. G. Albrecht and J. A. Creighton, "Anomalous intense Raman spectra of pyridine at a silver electrode," *Journal of the American Chemical Society*, vol. 99, no. 15, pp. 5215–5217, 1977.
- [2] M. Fleischmann, P. J. Hendra, and A. J. McQuillan, "Raman spectra of pyridine adsorbed at a silver electrode," *Chemical Physics Letters*, vol. 26, no. 2, pp. 163–166, 1974.
- [3] D. L. Jeanmaire and R. P. Van Duyne, "Surface Raman spectroelectrochemistry—part I. Heterocyclic, aromatic, and aliphatic amines adsorbed on the anodized silver electrode," *Journal of Electroanalytical Chemistry*, vol. 84, no. 1, pp. 1–20, 1977.
- [4] K. Kneipp, Y. Wang, H. Kneipp et al., "Single molecule detection using surface-enhanced Raman scattering (SERS)," *Physical Review Letters*, vol. 78, no. 9, pp. 1667–1670, 1997.
- [5] S. Nie and S. R. Emory, "Probing single molecules and single nanoparticles by surface-enhanced Raman scattering," *Science*, vol. 275, no. 5303, pp. 1102–1106, 1997.
- [6] Z.-Y. Li and Y. Xia, "Metal nanoparticles with gain toward single-molecule detection by surface-enhanced Raman scattering," *Nano Letters*, vol. 10, no. 1, pp. 243–249, 2010.
- [7] S. Rao, S. Raj, S. Balint et al., "Single DNA molecule detection in an optical trap using surface-enhanced Raman scattering," *Applied Physics Letters*, vol. 96, no. 21, Article ID 213701, 2010.
- [8] J. A. Creighton, C. G. Blatchford, and M. G. Albrecht, "Plasma resonance enhancement of Raman scattering by pyridine adsorbed on silver or gold sol particles of size comparable to the excitation wavelength," *Journal of the Chemical Society, Faraday Transactions 2*, vol. 75, pp. 790–798, 1979.
- [9] C. J. Orendorff, L. Gearheart, N. R. Jana, and C. J. Murphy, "Aspect ratio dependence on surface enhanced Raman

- scattering using silver and gold nanorod substrates,” *Physical Chemistry Chemical Physics*, vol. 8, no. 1, pp. 165–170, 2006.
- [10] K. Faulds, R. E. Littleford, D. Graham, G. Dent, and W. E. Smith, “Comparison of surface-enhanced resonance Raman scattering from unaggregated and aggregated nanoparticles,” *Analytical Chemistry*, vol. 76, no. 3, pp. 592–598, 2004.
- [11] T. Makiabadi, A. Bouvrée, V. Le Nader, H. Terrisse, and G. Louarn, “Preparation, optimization, and characterization of SERS sensor substrates based on two-dimensional structures of gold colloid,” *Plasmonics*, vol. 5, no. 1, pp. 21–29, 2010.
- [12] J. T. Bahns, F. Yan, D. Qiu, R. Wang, and L. Chen, “Hole-enhanced raman scattering,” *Applied Spectroscopy*, vol. 60, no. 9, pp. 989–993, 2006.
- [13] L. Novotny and B. Hecht, *Principles of Nano-Optics*, Cambridge University Press, Cambridge, UK, 2006.
- [14] J. Wessel, “Surface-enhanced optical microscopy,” *The Journal of the Optical Society of America*, vol. 2, pp. 1538–1541, 1985.
- [15] S. L. Sharp, R. J. Warmack, J. P. Goudonnet, I. Lee, and T. L. Ferrell, “Spectroscopy and imaging using the photon scanning-tunneling microscope,” *Accounts of Chemical Research*, vol. 26, no. 7, pp. 377–382, 1993.
- [16] A. Hartschuh, M. R. Beversluis, A. Bouhelier, and L. Novotny, “Tip-enhanced optical spectroscopy,” *Philosophical Transactions of the Royal Society A*, vol. 362, no. 1817, pp. 807–819, 2004.
- [17] B. Pettinger, “Tip-Enhanced Raman Spectroscopy (TERS),” *Topics in Applied Physics*, vol. 103, pp. 217–240, 2006.
- [18] E. Bailo and V. Deckert, “Tip-enhanced Raman scattering,” *Chemical Society Reviews*, vol. 37, no. 5, pp. 921–930, 2008.
- [19] B. S. Yeo, J. Stadler, T. Schmid, R. Zenobi, and W. Zhang, “Tip-enhanced Raman spectroscopy—its status, challenges and future directions,” *Chemical Physics Letters*, vol. 472, no. 1–3, pp. 1–13, 2009.
- [20] R. Aroca, *Surface-Enhanced Vibrational Spectroscopy*, John Wiley and Sons, Chichester, UK, 2007.
- [21] C. Vannier, B. S. Yeo, J. Melanson, and R. Zenobi, “Multi-functional microscope for far-field and tip-enhanced Raman spectroscopy,” *Review of Scientific Instruments*, vol. 77, no. 2, article 023104, 2006.
- [22] W. Zhang, B. S. Yeo, T. Schmid, and R. Zenobi, “Single molecule tip-enhanced Raman spectroscopy with silver tips,” *Journal of Physical Chemistry C*, vol. 111, no. 4, pp. 1733–1738, 2007.
- [23] E. Bailo and V. Deckert, “Tip-enhanced Raman spectroscopy of single RNA strands: towards a novel direct-sequencing method,” *Angewandte Chemie*, vol. 47, no. 9, pp. 1658–1661, 2008.
- [24] Y. Saito, P. Verma, K. Masui, Y. Inouye, and S. Kawata, “Nanoscale analysis of graphene layers by tip-enhanced near-field Raman spectroscopy,” *Journal of Raman Spectroscopy*, vol. 40, no. 10, pp. 1434–1440, 2009.
- [25] B. S. Yeo, E. Amstad, T. Schmid, J. Stadler, and R. Zenobi, “Nanoscale probing of a polymer-blend thin film with Tip-enhanced Raman spectroscopy,” *Small*, vol. 5, no. 8, pp. 952–960, 2009.
- [26] L. G. Cançado, A. Hartschuh, and L. Novotny, “Tip-enhanced Raman spectroscopy of carbon nanotubes,” *Journal of Raman Spectroscopy*, vol. 40, no. 10, pp. 1420–1426, 2009.
- [27] D. Mehtani, N. Lee, R. D. Hartschuh et al., “Nano-Raman spectroscopy with side-illumination optics,” *Journal of Raman Spectroscopy*, vol. 36, no. 11, pp. 1068–1075, 2005.
- [28] Y. Saito, M. Motohashi, N. Hayazawa, M. Iyoki, and S. Kawata, “Nanoscale characterization of strained silicon by tip-enhanced Raman spectroscopy in reflection mode,” *Applied Physics Letters*, vol. 88, no. 14, Article ID 143109, 2006.
- [29] N. Lee, R. D. Hartschuh, D. Mehtani et al., “High contrast scanning nano-Raman spectroscopy of silicon,” *Journal of Raman Spectroscopy*, vol. 38, no. 6, Article ID 143109, pp. 789–796, 2007.
- [30] G. Picardi, Q. Nguyen, J. Schreiber, and R. Ossikovski, “Comparative study of atomic force mode and tunneling mode tip-enhanced Raman spectroscopy,” *The European Physical Journal*, vol. 40, no. 2, pp. 197–201, 2007.
- [31] P. G. Gucciardi, M. Lopes, R. Déturche, C. Julien, D. Barchiesi, and M. Lamy De La Chapelle, “Light depolarization induced by metallic tips in apertureless near-field optical microscopy and tip-enhanced Raman spectroscopy,” *Nanotechnology*, vol. 19, no. 21, Article ID 215702, 2008.
- [32] M. Motohashi, N. Hayazawa, A. Tarun, and S. Kawata, “Depolarization effect in reflection-mode tip-enhanced Raman scattering for Raman active crystals,” *Journal of Applied Physics*, vol. 103, no. 3, Article ID 034309, 2008.
- [33] A. Merlen, J. C. Valmalette, P. G. Gucciardi, M. Lamy de la Chapelle, A. Frigout, and R. Ossikovski, “Depolarization effects in tip-enhanced raman spectroscopy,” *Journal of Raman Spectroscopy*, vol. 40, no. 10, pp. 1361–1370, 2009.
- [34] B. Ren, G. Picardi, and B. Pettinger, “Preparation of gold tips suitable for tip-enhanced Raman spectroscopy and light emission by electrochemical etching,” *Review of Scientific Instruments*, vol. 75, no. 4, pp. 837–841, 2004.
- [35] C. C. Neacsu, S. Berweger, and M. B. Raschke, “Tip-enhanced raman imaging and nanospectroscopy: Sensitivity, symmetry, and selection rules,” *Nanobiotechnology*, vol. 3, no. 3-4, pp. 172–196, 2007.
- [36] C. Williams and D. Roy, “Fabrication of gold tips suitable for tip-enhanced Raman spectroscopy,” *Journal of Vacuum Science and Technology B: Microelectronics and Nanometer Structures*, vol. 26, no. 5, pp. 1761–1764, 2008.
- [37] R. M. Stöckle, Y. D. Suh, V. Deckert, and R. Zenobi, “Nanoscale chemical analysis by tip-enhanced Raman spectroscopy,” *Chemical Physics Letters*, vol. 318, no. 1-3, pp. 131–136, 2000.
- [38] M. Chaigneau, G. Ollivier, T. Minea, and G. Louarn, “Nanoprobes for near-field optical microscopy manufactured by substitute-sheath etching and hollow cathode sputtering,” *Review of Scientific Instruments*, vol. 77, no. 10, Article ID 103702, 2006.
- [39] R. M. Stöckle, Y. D. Suh, V. Deckert, and R. Zenobi, “Nanoscale chemical analysis by tip-enhanced Raman spectroscopy,” *Chemical Physics Letters*, vol. 318, no. 1–3, pp. 131–136, 2000.
- [40] S. S. Kharintsev, G. G. Hoffmann, P. S. Dorozhkin, G. De With, and J. Loos, “Atomic force and shear force based tip-enhanced Raman spectroscopy and imaging,” *Nanotechnology*, vol. 18, no. 31, Article ID 315502, 2007.
- [41] N. Anderson, A. Hartschuh, and L. Novotny, “Near-field Raman microscopy,” *Materials Today*, vol. 8, no. 5, pp. 50–54, 2005.
- [42] A. L. Demming, F. Festy, and D. Richards, “Plasmon resonances on metal tips: Understanding tip-enhanced Raman scattering,” *Journal of Chemical Physics*, vol. 122, no. 18, Article ID 184716, pp. 1–7, 2005.
- [43] N. Hayazawa, Y. Saito, and S. Kawata, “Detection and characterization of longitudinal field for tip-enhanced Raman spectroscopy,” *Applied Physics Letters*, vol. 85, no. 25, pp. 6239–6241, 2004.

- [44] K. F. Domke and B. Pettinger, "Tip-enhanced Raman spectroscopy of 6H-SiC with graphene adlayers: selective suppression of E1 modes," *Journal of Raman Spectroscopy*, vol. 40, no. 10, pp. 1427–1433, 2009.
- [45] W. X. Sun and Z. X. Shen, "Apertureless near-field scanning Raman microscopy using reflection scattering geometry," *Ultramicroscopy*, vol. 94, no. 3-4, pp. 237–244, 2003.
- [46] D. Roy, J. Wang, and M. E. Welland, "Nanoscale imaging of carbon nanotubes using tip enhanced Raman spectroscopy in reflection mode," *Faraday Discussions*, vol. 132, pp. 215–225, 2006.
- [47] R. J. C. Brown, J. Wang, R. Tantra, R. E. Yardley, and M. J. T. Milton, "Electromagnetic modelling of Raman enhancement from nanoscale substrates: A route to estimation of the magnitude of the chemical enhancement mechanism in SERS," *Faraday Discussions*, vol. 132, pp. 201–213, 2006.
- [48] A. Jorio, M. A. Pimenta, A. G. Souza Filho, R. Saito, G. Dresselhaus, and M. S. Dresselhaus, "Characterizing carbon nanotube samples with resonance Raman scattering," *New Journal of Physics*, vol. 5, pp. 139.1–139.17, 2003.
- [49] N. Anderson, A. Hartschuh, S. Cronin, and L. Novotny, "Nanoscale vibrational analysis of single-walled carbon nanotubes," *Journal of the American Chemical Society*, vol. 127, no. 8, pp. 2533–2537, 2005.
- [50] A. Hartschuh, H. Qian, A. J. Meixner, N. Anderson, and L. Novotny, "Nanoscale optical imaging of excitons in single-walled carbon nanotubes," *Nano Letters*, vol. 5, no. 11, pp. 2310–2313, 2005.
- [51] N. Anderson, A. Hartschuh, and L. Novotny, "Chirality changes in carbon nanotubes studied with near-field Raman spectroscopy," *Nano Letters*, vol. 7, no. 3, pp. 577–582, 2007.
- [52] T. A. Yano, T. Ichimura, A. Taguchi et al., "Confinement of enhanced field investigated by tip-sample gap regulation in tapping-mode tip-enhanced Raman microscopy," *Applied Physics Letters*, vol. 91, no. 12, Article ID 121101, 2007.
- [53] T. Schmid, A. Messmer, B. S. Yeo, W. Zhang, and R. Zenobi, "Towards chemical analysis of nanostructures in biofilms II: tip-enhanced Raman spectroscopy of alginates," *Analytical and Bioanalytical Chemistry*, vol. 391, no. 5, pp. 1907–1916, 2008.
- [54] A. Tarun, N. Hayazawa, M. Motohashi, and S. Kawata, "Highly efficient tip-enhanced Raman spectroscopy and microscopy of strained silicon," *Review of Scientific Instruments*, vol. 79, no. 1, Article ID 013706, 2008.

Research Article

Mie Plasmons: Modes Volumes, Quality Factors, and Coupling Strengths (Purcell Factor) to a Dipolar Emitter

G. Colas des Francs, S. Derom, R. Vincent, A. Bouhelier, and A. Dereux

Laboratoire Interdisciplinaire Carnot de Bourgogne, UMR 6303, CNRS-Université de Bourgogne, 9 Avenue A. Savary, BP 47 870, 21078 Dijon, France

Correspondence should be addressed to G. Colas des Francs, gerard.colas-des-francs@u-bourgogne.fr

Received 27 October 2011; Accepted 22 November 2011

Academic Editor: Nicolas Bonod

Copyright © 2012 G. Colas des Francs et al. This is an open access article distributed under the Creative Commons Attribution License, which permits unrestricted use, distribution, and reproduction in any medium, provided the original work is properly cited.

Using either quasistatic approximation or exact Mie expansion, we characterize the localized surface plasmons supported by a metallic spherical nanoparticle. We estimate the quality factor Q_n and define the effective volume V_n of the n th mode in such a way that coupling strength with a neighbouring dipolar emitter is proportional to the ratio Q_n/V_n (Purcell factor). The role of Joule losses, far-field scattering, and mode confinement in the coupling mechanism is introduced and discussed with simple physical understanding, with particular attention paid to energy conservation.

1. Introduction

Metallic nanoparticles support localized surface plasmon-polaritons (SPP) strongly confined at the metal surface ensuring efficient electromagnetic coupling with neighbouring materials, offering a variety of applications such as surface-enhanced spectroscopies [1, 2], photochemistry [3], or optical nanoantennas [4]. This also opens the way towards control of light emission at the nanoscale [5–10]. The ratio Q/V_{eff} is generally used to quantify the coupling strength between a dipolar emitter and a cavity mode (polariton). Q and V_{eff} refers to the mode quality factor and effective volume, respectively. High ratio Q/V_{eff} may lead to strong coupling regime with characteristic Rabi oscillations revealing cycles of energy exchange between the emitter and the cavity. In the weak coupling regime, the emitter energy dissipation into the cavity mode is nonreversible and follows the Purcell factor:

$$\frac{\gamma}{n_B \gamma_0} = \frac{3}{4\pi^2} \left(\frac{\lambda}{n_B} \right)^3 \frac{Q}{V_{\text{eff}}}, \quad (1)$$

where γ is the emitter spontaneous decay rate into the cavity compared to its free-space value γ_0 , n_B is the optical index

inside the cavity, and λ is the emission wavelength. Spontaneous emission rate in complex systems follows the more general Fermi's golden rule that expresses γ as a function of the density of electromagnetic mode [11]. However, for describing the coupling to a cavity mode, the Purcell factor is usually preferred since it clearly introduces the cavity resonance quality factor Q and the mode extension V_{eff} on which coupling remains efficient, bringing therefore a clear physical understanding of the coupling process.

In this context, we propose to determine the quality factors and effective volumes of localized SPPs supported by a metallic nanosphere. Indeed, these quantities are useful parameters to understand and evaluate the coupling mechanisms between dipolar emitters and plasmonic nanostructures [12, 13]. This would help for achieving strong coupling regime [14, 15] or for designing plasmonic nanolasers [16–18]. We have chosen a spherical particle, a highly symmetrical system, since it is fully analytical and simple expressions can be derived with clear physical meaning [19–23]. Moreover, our results could be extended to more complex structures [24, 25].

In Section 2, we focus on the dipolar mode and present in details the derivation of its quality factor and effective

volume. We extend our approach to each mode of the particle in Section 3. Finally, we discuss the coupling efficiency to one of the particle modes in the last section. For the sake of simplicity, all the analytical expressions are derived assuming a particle in air and dipolar emitter perpendicular to the particle surface. The generalisation to arbitrary emitter orientation and a background medium of optical index n_B is provided in the appendix. Exact calculations presented in the main text using Mie expansion correctly include both the background medium and dipolar orientation.

2. Dipolar Mode

We first characterize the dipolar mode of a spherical particle. For sphere radius R small compared to the excitation wavelength $\lambda = 2\pi c/\omega$, the electric field is considered uniform over the metallic particle. The metallic particle is polarized by the incident electric field \mathbf{E}_0 and behaves as a dipole

$$\mathbf{p}^{(1)}(\omega) = 4\pi\epsilon_0\alpha_1(\omega)\mathbf{E}_0, \quad (2)$$

$$\alpha_1(\omega) = \frac{\epsilon_m(\omega) - 1}{\epsilon_m(\omega) + 2} R^3, \quad (3)$$

where α_1 is the nanoparticle quasistatic (dipolar) polarisability and ϵ_m is the metal dielectric constant. The dipole plasmon resonance appears at ω_1 such that $\epsilon_m(\omega_1) + 2 = 0$. In case of Drude metal, the dipolar resonance is $\omega_1 = \omega_p/\sqrt{3}$ with ω_p the bulk metal plasma angular frequency. However, expression (3) does not satisfy the optical theorem (energy conservation). It is wellknown that this apparent paradox is easily overcome by taking into account the finite size of the particle and leads to define the effective polarisability [26]:

$$\alpha_1^{\text{eff}} = \left[1 - i\frac{2k^3}{3}\alpha_1 \right]^{-1} \alpha_1, \quad \left(k = \frac{2\pi}{\lambda} \right). \quad (4)$$

The corrective term ($2k^3\alpha_1/3$) is the so-called radiative reaction correction and microscopically originates from the radiation emitted by the charges oscillations induced inside the nanoparticle by the excitation field [27].

The dipolar polarisability presents a simple shape near the resonance if the metallic dielectric constant follows Drude model [20] (ω_p and Γ_{abs} refers to metal plasma frequency an Ohmic loss rate, resp.) (for the sake of clarity, we use lowercase notation γ for the emitter decay rates and uppercase Γ for the quantities associated with the metallic particle);

$$\epsilon_m = 1 - \frac{\omega_p^2}{\omega^2 + i\Gamma_{\text{abs}}\omega}; \quad (5)$$

$$\alpha_1^{\text{eff}}(\omega) \sim \frac{\omega_1}{\omega_1} \frac{1}{2(\omega_1 - \omega) - i\Gamma_1} R^3, \quad (6)$$

$$\Gamma_1 = \Gamma_{\text{abs}} + \frac{2(k_1 R)^3 \omega_1}{3}, \quad \left(k_1 = \frac{\omega_1}{c} \right). \quad (7)$$

where Γ_1 is the decay rate of the particle dipolar mode and includes both the Joule (Γ_{abs}) and radiative [$\Gamma_1^{\text{rad}} = 2(k_1 R)^3 \omega_1/3$] losses rates.

2.1. Quality Factor. The dipolar response can be described by either the extinction efficiency Q_{ext} , proportional to $\text{Im}(\alpha_1)$, or scattering efficiency Q_{scatt} , proportional to $|\alpha_1|^2$, and therefore follows a Lorentzian profile centered at ω_1 and with a full width at half maximum (FWHM) $\Delta\omega_1 = \Gamma_1$:

$$Q_{\text{ext}}(\omega) = \frac{4k}{R^2} \text{Im}[\alpha_1^{\text{eff}}(\omega)] \propto \frac{1}{(\omega - \omega_1)^2 + (\Gamma_1/2)^2}, \quad (8)$$

$$Q_{\text{scatt}}(\omega) = \frac{8}{3R^2} k^4 |\alpha_1^{\text{eff}}(\omega)|^2 \propto \frac{1}{(\omega - \omega_1)^2 + (\Gamma_1/2)^2}.$$

The quality factor of this resonance is therefore

$$Q_1 = \frac{\omega_1}{\Gamma_1}. \quad (9)$$

As an example, we consider a $R = 25$ nm silver sphere in air. The Drude model parameters are $\hbar\omega_p = 9.1$ eV and $\hbar\Gamma_{\text{abs}} = 18$ meV that lead to a resonance peak at $\hbar\omega_1 = 5.2$ eV ($\omega_1 = 7.98 \times 10^{15}$ Hz) and radiative energy $\hbar\Gamma_1^{\text{rad}} = 1$ eV. The quality factor is then $Q_1 = 5$. Note that the metal optical properties are better described when including the bound electrons in the Drude model: $\epsilon_m = \epsilon_\infty - \omega_p^2/(\omega^2 + i\Gamma_{\text{abs}}\omega)$, ($\epsilon_\infty = 3.7$ for silver, see also the appendix). In that case, we obtain $\hbar\omega_1 = 3.74$ eV ($\omega_1 = 5.7 \times 10^{15}$ Hz), $\hbar\Gamma_1^{\text{rad}} = 0.13$ eV, and $Q_1 = 24$.

Although Drude model qualitatively explains the shape of the resonance, a more representative value of the quality factor can only be determined using tabulated data for the dielectric constant of the metal [28]. The extinction efficiencies associated with the dipolar resonance are represented in Figure 1. For silver particle (Figure 1(a)), the extinction efficiency closely follows a Lorentzian shape, as expected, with a quality factor $Q_1 = 21$, in good agreement with the value obtained using Drude model (with the contribution of the bound electrons included). In case of gold, the resonance profile is not well defined due to interband transitions for $\omega > 4 \cdot 10^{15}$ Hz but a quality factor of 7 can be estimated (Figure 1(b)). Figure 1(c) represents the extinction efficiency for a gold particle embedded in polymethylmethacrylate (PMMA) into which metallic particles are routinely dispersed. This leads to a small redshift of a resonance, avoiding therefore the resonance disturbance by interband absorption, and we recover partly the Lorentzian profile [29].

2.2. Effective Volume. Coupling rate of a dipolar emitter to a dipolar particle expresses for very short emitter-particle distances d ($z_0 = R + d$ is the distance to the particle center) as [19–21]

$$\frac{\gamma_1^\perp}{\gamma_0} \sim \frac{6}{k^3 z_0^6} \text{Im}(\alpha_1), \quad (10)$$

for a dipole emitter orientation perpendicular to the nanoparticle surface. Using (6), we obtain, in case of a dipolar

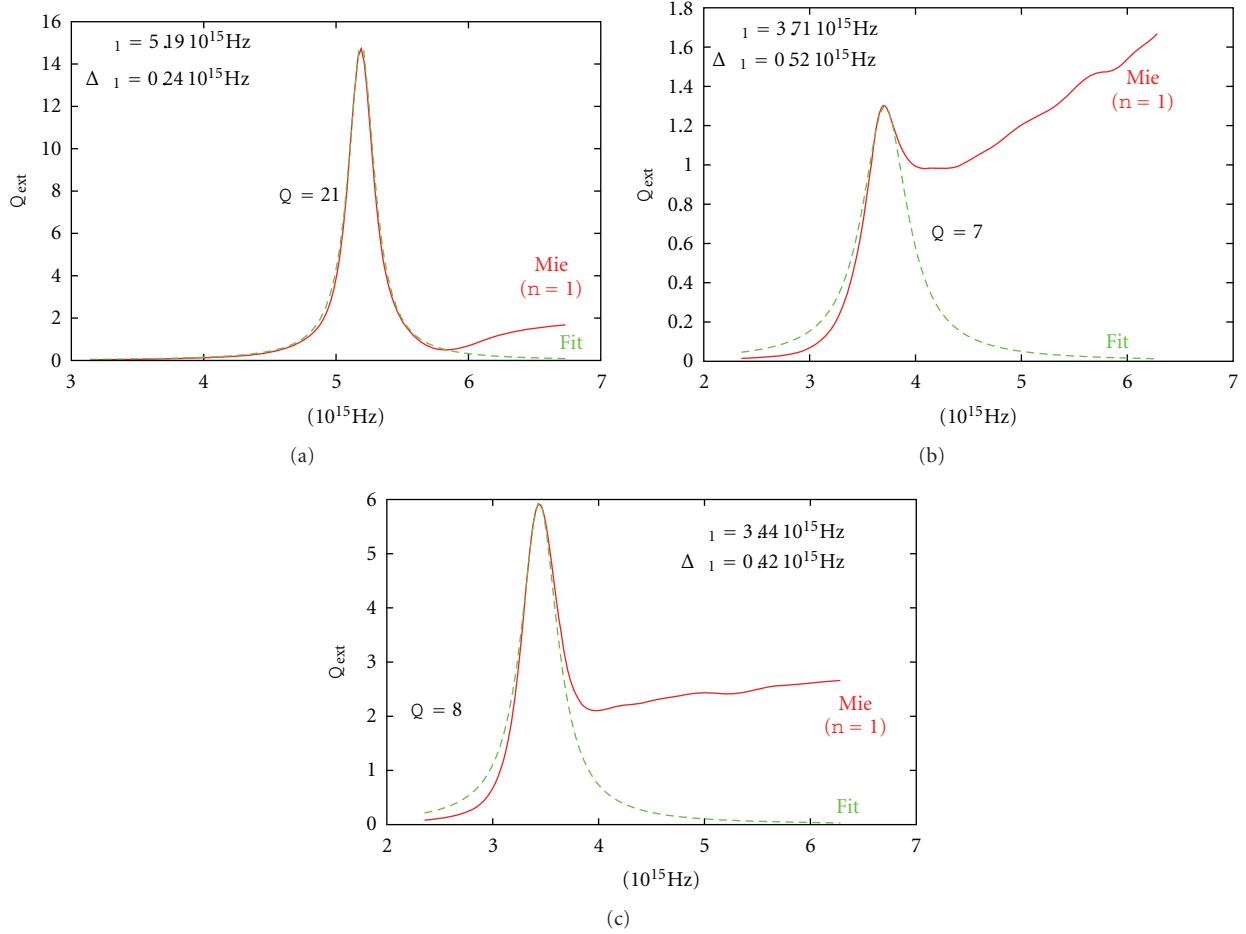


FIGURE 1: Extinction efficiency for the dipolar resonance calculated keeping only the dipolar mode ($n = 1$) in the Mie expansion and using experimental value for the metal dielectric constant [28]. (a) Silver particle in air. (b) Gold particle in air. (c) Gold particle in PMMA (optical index $n_B = 1.5$). The particle radius is $R = 25$ nm for each case. Fit refers to a Lorentzian fit using parameters indicated on the figure.

emitter emission tuned to the dipolar particle resonance ($\lambda = \lambda_1 = 2\pi c/\omega_1$)

$$\frac{\gamma_1^\perp}{\gamma_0} \sim \frac{6\omega_1 R^3}{k_1^3 z_0^6 \Gamma_1} \sim \frac{3}{4\pi^2} \lambda_1^3 \frac{R^3}{\pi z_0^6} Q_1. \quad (11)$$

In order to determine the dipolar mode effective volume, we now identify the coupling rate γ/γ_0 to the Purcell factor ((1), assuming $n_B = 1$), so that we obtain

$$V_1^\perp = \frac{\pi z_0^6}{R^3}, \quad (12)$$

in full agreement with expression recently derived by Greffet et al. by defining the optical impedance of the nanoparticle antenna [30]. For a $R = 25$ nm radius sphere in air, we estimate the mode effective volume $V_1^\perp = 3.7 \times 10^{-4} \mu\text{m}^3 = (72 \text{ nm})^3$ for an emitter 10 nm away from the particle surface ($z_0 = 35$ nm).

Unlike here, usual definition of the mode effective volume does not include the emitter position. For instance, in case of cavity quantum electrodynamics (cQED)

applications, it can be expressed as $V_{\text{eff}} = \int \epsilon |\mathbf{E}(\mathbf{r})|^2 d\mathbf{r} / \max(\epsilon |\mathbf{E}(\mathbf{r})|^2)$, so that it directly characterizes the mode extension. However, in that case, Purcell factor expression (1) is only valid for an emitter located at the cavity center where the mode-emitter coupling is maximum (mode antinode). In close analogy with the definition used in cQED, we derive later another expression for the SPP effective volume, independent of the emitter position (see (22), and the discussion below).

3. Multipolar Modes

If the excitation field is generated by a dipolar emitter (fluorescent molecules, quantum dots, ...), it cannot be considered uniform anymore and the dipolar approximation fails. One needs therefore to consider the coupling strength to high-order modes (Figure 2). Here again, we discuss the mode quality factors and volume first using quasistatic approximation and then discuss their quantitative behaviour using exact Mie theory.

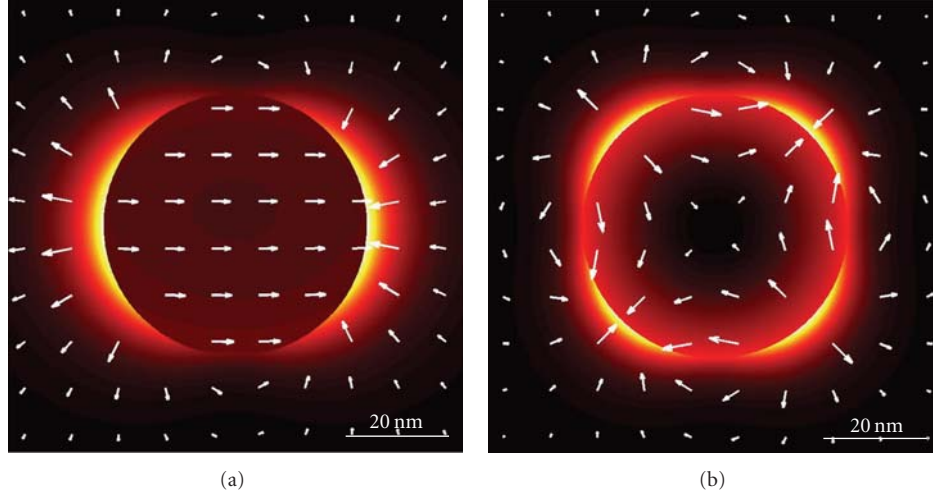


FIGURE 2: (a) Dipolar and (b) quadrupolar mode profiles of a $R = 25$ nm silver sphere, embedded in PMMA calculated using exact Mie expansion. Silver dielectric constant is taken from [28]. Color and arrows refer to electric field intensity and vector respectively.

The n th multipole tensor moment of the metallic particle is given by

$$\mathbf{p}^{(n)} = \frac{4\pi\epsilon_0}{(2n-1)!!} \alpha_n \nabla^{n-1} \mathbf{E}_0, \quad (13)$$

$$\alpha_n = \frac{n(\epsilon_m - 1)}{n\epsilon_m + (n+1)} R^{(2n+1)}, \quad (14)$$

with $(2n+1)!! = 1 \times 3 \times 5 \times \dots \times (2n+1)$ and ∇ is the vector differential operator. As discussed above, the dipole moment $\mathbf{p}^{(1)} = 4\pi\epsilon_0\alpha_1\mathbf{E}_0$ is the unique mode excited in a uniform field. However, the dipolar emitter near field behaves as $1/r^3$ and strongly varies spatially so that higher modes can be excited in the particle.

For a Drude metal, the n th resonance appears at $\omega_n = \omega_p \sqrt{n/(2n+1)}$. Therefore, higher-order modes accumulate near $\omega_\infty = \omega_p/\sqrt{2}$. Moreover, as discussed for the dipolar case, quasistatic expression of the n th mode polarisability (14) does not obey energy conservation. Applying the optical theorem, we recently extend the radiative correction to all the spherical particles modes [22]. This leads to

$$\alpha_n^{\text{eff}} = \left[1 - i \frac{(n+1)k_n^{2n+1}}{n(2n-1)!!(2n+1)!!} \alpha_n \right]^{-1} \alpha_n. \quad (15)$$

3.1. Quality Factors. It is now a simple matter to generalize the dipolar mode analysis reported in the previous section to all the particle modes. The n th mode polarisability can be approximated near resonance. A simple expression for the polarisability is achieved considering a Drude metal:

$$\begin{aligned} \alpha_n^{\text{eff}} &\sim \frac{\omega_n}{\omega_n} \frac{\omega_n}{2(\omega_n - \omega) - i\Gamma_n} R^{2n+1}, \\ \Gamma_n &= \Gamma_{\text{abs}} + \Gamma_n^{\text{rad}}, \\ \Gamma_n^{\text{rad}} &= \omega_n \frac{(n+1)(k_n R)^{2n+1}}{n(2n-1)!!(2n+1)!!}, \quad \left(k_n = \frac{\omega_n}{c} \right), \end{aligned} \quad (16)$$

where Γ_n is the total decay rate of the n th mode, that includes both ohmic losses and radiative scattering. As expected, for a given mode n , the radiative scattering rate $\Gamma_n^{\text{rad}} \propto R^{2n+1}$ increases with the particle size since it couples more efficiently to the far field. For instance, we obtain $\hbar\Gamma_2^{\text{rad}} = 39$ meV ($\hbar\Gamma_2^{\text{rad}} = 1.8$ meV with $\epsilon_\infty = 3.7$) for the quadrupolar mode of a $R = 25$ nm silver particle in air. As expected, the radiative rate of the quadrupolar is strongly reduced compared to the dipolar mode.

The quality factor associated with the n th mode is therefore

$$Q_n = \frac{\omega_n}{\Gamma_n} = \frac{\omega_n}{\Gamma_{\text{abs}} + \Gamma_n^{\text{rad}}}. \quad (17)$$

Figure 3 details the quality factor of the two first modes of a silver sphere in PMMA using tabulated value for ϵ_m . The quadrupolar mode presents a quality factor almost 5 times higher than the dipolar mode since it has limited radiative losses. Indeed, quadrupolar mode poorly couples to the far field. Finally, similar Q values ($Q_n \approx 50$) are obtained for all the higher modes ($n \geq 3$). Here again, assuming a Drude metal and in the quasistatic approximation, we qualitatively explain this result. Actually, Q factors of high-order modes are absorption loss limited ($\Gamma_n^{\text{rad}} \ll \Gamma_{\text{abs}}$, so called dark modes) and tend to $Q_\infty = \omega_\infty/\Gamma_{\text{abs}}$. However this overestimates the mode quality factor ($Q_\infty \approx 207$) as compared to the value deduced using tabulated value for ϵ_m and exact Mie expansion.

3.2. Effective Volumes. Last, we express the *total* coupling strength of a dipolar emitter to the spherical metallic particle for very short separation distances ($kz_0 \ll 1$) [21, 22]:

$$\frac{\gamma_{\text{tot}}^\perp}{\gamma_0} \approx \frac{3}{2} \frac{1}{(kz_0)^3} \sum_{n=1}^{\infty} \frac{(n+1)^2}{z_0^{(2n+1)}} \text{Im}(\alpha_n^{\text{eff}}), \quad (18)$$

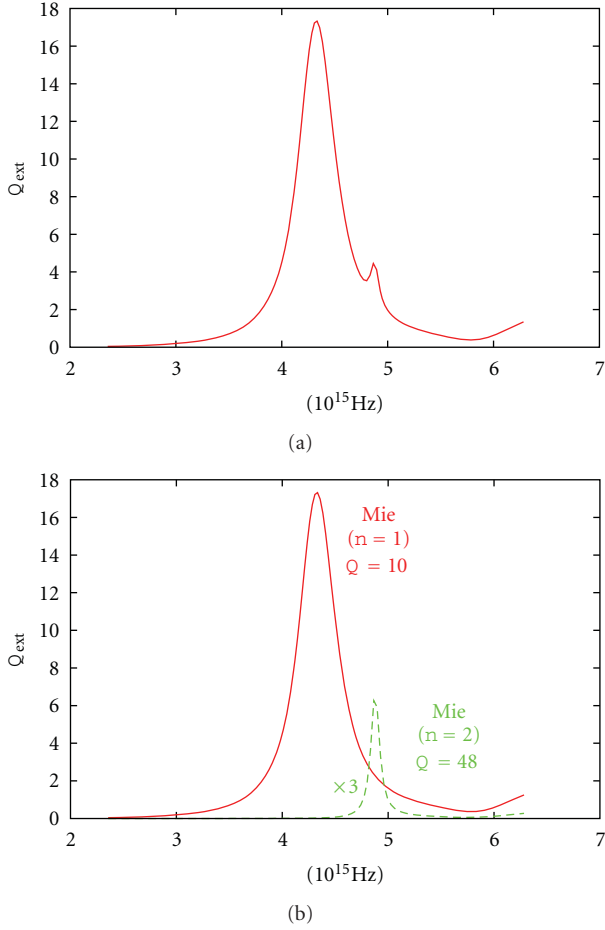


FIGURE 3: (a) Extinction efficiency of a $R = 25$ nm silver sphere embedded in PMMA, calculated using full Mie expansion. (b) Contribution of the dipolar ($n = 1$) and quadrupolar ($n = 2$) mode to the full extinction efficiency. The quality factor is indicated for each mode. Dielectric constant for silver is taken from [28].

so that the coupling strength to the n th mode is easily deduced as

$$\frac{\gamma_n^\perp}{\gamma_0} \approx \frac{3}{2} \frac{1}{(kz_0)^3} \frac{(n+1)^2}{z_0^{2n+1}} \text{Im}(\alpha_n^{\text{eff}}), \quad (19)$$

$$\sim \frac{3}{\omega_n} \frac{R^{2n+1}}{(k_n z_0)^3} \frac{(n+1)^2}{z_0^{2n+1}} Q_n,$$

where we have used approximated expression (16) for the n th polarisability. The mode effective volume is then straightforwardly deduced from comparison to the Purcell factor (1)

$$V_n^\perp = \frac{4\pi z_0^{2n+4}}{(n+1)^2 R^{2n+1}}. \quad (20)$$

We obtain for instance quadrupole effective volume $V_2^\perp = 4\pi z_0^8 / (9R^5) = 3.2 \times 10^{-4} \mu\text{m}^3 = (68 \text{ nm})^3$ for an emitter 10 nm away from a 25 nm radius metallic particle in air. The calculated effective volumes of the three first modes are

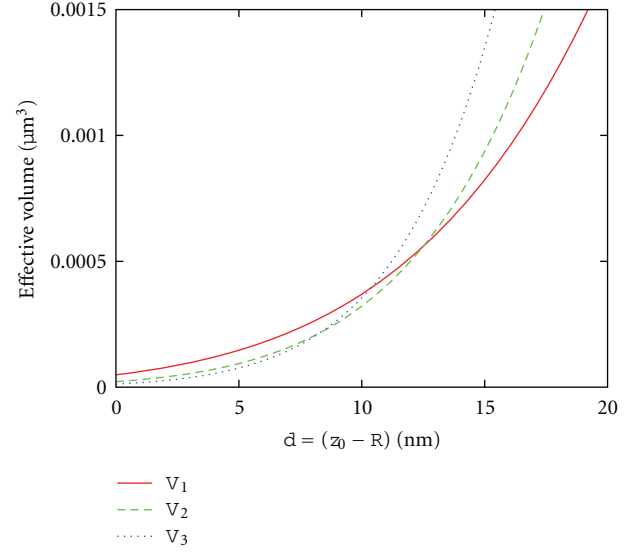


FIGURE 4: Effective volume of the dipole (V_1), quadrupole (V_2) and hexapole (V_3) modes of a $R = 25$ nm sphere as a function of the emitter-particle distance. The emitter is perpendicular to the particle surface.

shown on Figure 4. At long distance, the smaller effective volume (most efficient coupling to an emitter) is associated with the dipole mode since it presents the largest extension. When the emitter-particle distance decreases the coupling strength to the quadrupolar ($d \leq 12$ nm), then hexapolar ($d \leq 10$ nm) mode becomes stronger as revealed by their lower effective volume. Most efficient coupling between an emitter and one of the particle modes obviously occurs at contact since plasmons modes are confined near the particle surface.

Finally, it is worthwhile to note that mode effective volume is generally defined independently on the particle-emitter distance so that it gives an estimation of the mode extension. This is done by evaluating the maximum effective volume available and for a random emitter orientation. In case of localized SPP, this is achieved for contact ($z_0 = R$). Since the decay rate of a randomly oriented emitter expresses $\gamma = (\gamma^\perp + 2\gamma^\parallel)/3$, it comes

$$\frac{1}{V_n} = \frac{1}{3V_n^\perp(R)} + \frac{2}{3V_n^\parallel(R)}, \quad (21)$$

$$V_n = \frac{9}{(2n+1)(n+1)} V_0, \quad (22)$$

where $V_0 = 4\pi R^3/3$ is the metallic sphere volume and V_n^\parallel refers to a dipole parallel to the sphere surface (see (B.4) in Appendix B, with $\epsilon_B = 1$). Dipolar and quadrupolar mode volumes are $V_1 = 3/2V_0$ and $V_2 = 3/5V_0$, respectively. The expression (22), derived for a Drude metal, *quantifies an extremely important property of localized SPPs; their effective volume does not depend on the wavelength and is of the order of the particle volume*. Metallic nanoparticles therefore support localized modes of strongly subwavelength extension. Highest-order modes have negligible extension ($V_n \rightarrow 0$ for $n \rightarrow \infty$, see Figure 5). As a comparison, photonics cavity

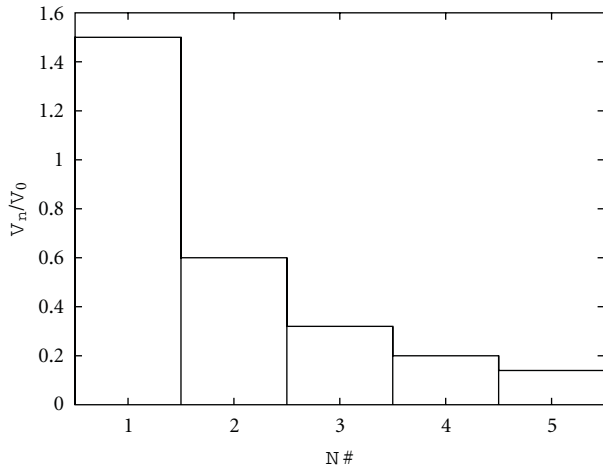


FIGURE 5: Normalized effective volume V_n/V_0 as a function of mode order.

modes are generally limited by the diffraction limit so that their effective volume is at best of the order of $(\lambda/n_B)^3$ (see [31]). Nevertheless, the extremely reduced SPP volume is achieved at the expense of the mode quality factor. It should be noticed that a low-quality factor indicates a large cavity resonance FWHM so that emitter-SPP coupling can occur on a large spectrum range.

Note that mode effective volume is generally defined by its energy confinement $V_{\text{eff}} = \int \epsilon |\mathbf{E}(\mathbf{r})|^2 d\mathbf{r} / \max(\epsilon |\mathbf{E}(\mathbf{r})|^2)$ [12]. Khurgin and Sun used this definition and obtained [32] $V_n = 6V_0/(n+1)^2$ that is in agreement with our expression for the dipolar mode volume ($V_1 = 1.5V_0$) but leads to slightly different values for other modes (e.g., $V_2 \approx 0.67V_0$ instead of $V_2 = 0.60V_0$). Recently, Koenderink showed that defining the mode volume on the basis of energy density could lead to underestimating the Purcell factor near plasmonic nanostructures [33] (however, he defined the coupling rate to the whole system rather than considering the coupling into a single mode). Oppositely, we adopt here a phenomenological approach where the mode volume is defined so that Purcell factor remains valid. Nevertheless, both methods lead to very similar results for the effective volumes of localized SPPs supported by a nanosphere. Since mode volume is generally a simple way to qualitatively characterize the mode extension, expressions derived here or by Sun et al. could be used.

4. β -Factor

Purcell factor quantifies the coupling strength between a quantum emitter and a (plasmon) mode but lacks information on the coupling efficiency as compared to all the other emitter relaxation channels. For the sake of clarity, it has to be mentioned that coupling strength to one SPP mode corresponds to the total emission decay rate induced by this coupling. It does not permit to distinguish radiative (γ_{rad}) and nonradiative (γ_{NR}) coupling into a single mode. This could be done by numerically cancelling the imaginary part of the

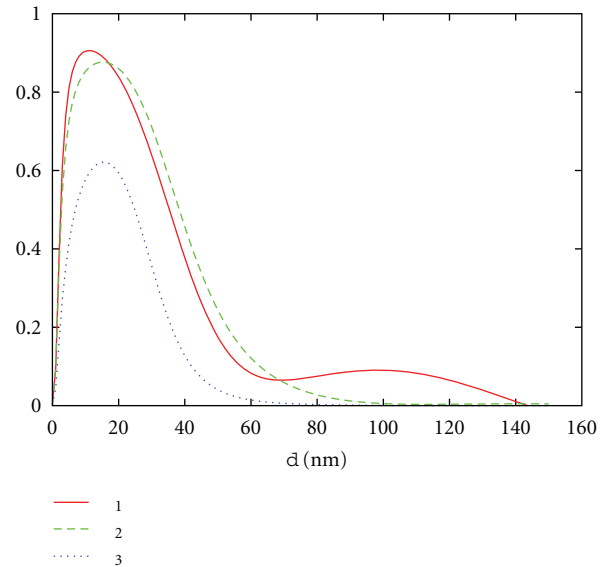


FIGURE 6: Coupling efficiency into the dipolar (β_1), quadrupolar (β_2) and hexapolar (β_3) mode of a $R = 25$ nm silver sphere in PMMA, calculated using exact Mie expansion. The emitter wavelength is assumed to match the considered mode. Therefore β_1 , β_2 and β_3 are calculated at $\lambda_1 = 435$ nm (dipolar resonance), $\lambda_2 = 387$ nm (quadrupolar resonance), and $\lambda_3 = 375$ nm (hexapolar resonance), respectively.

metal dielectric function (see also [34] for similar discussion in case of coupling to delocalized SPPs). However, one can determine the coupling efficiency into a single mode as compared to all other modes. This coupling efficiency, or the so-called β -factor, is easily estimated in case of a spherical metallic particle since all the available channels are taken into account in the Mie expansion. Coupling efficiency into n th mode writes

$$\beta_n = \frac{\langle \gamma_n \rangle}{\langle \gamma_{\text{tot}} \rangle}, \quad (23)$$

where $\langle \gamma \rangle = (\gamma^\perp + 2\gamma^\parallel)/3$ is the decay rate of a randomly oriented molecule. β -factor is represented on Figure 6 for the first three modes. A maximum efficiency of 90% can be achieved in the dipolar mode ($d \sim 10$ nm) and 87% into quadrupolar mode ($d \sim 15$ nm). The coupling efficiency into the hexapolar mode is lower ($\sim 60\%$ around $d \sim 15$ nm) since it has a very low extension, as indicated in Figure 5. For very short distances, all the coupling efficiencies drop down to zero since all the higher-order modes accumulate in this region, opening numerous alternative decay channels. Moreover, it is possible to efficiently couple the emitter to either the dipolar or quadrupolar mode, by matching the emitter and mode wavelengths. This is of strong importance when designing a SPASER (or plasmon laser) [5] so that the active mode can be tuned on the dipolar or quadrupolar mode. This last *spacing* mode would consist of an extremely localized and ultrafast nanosource [18].

5. Conclusion

We explicitly determined the effective volumes for all the SPP modes supported by a metallic nanosphere. Their quality factor is also approximated in the quasistatic case or calculated using exact Mie expansion. Rather low-quality factors ranging from 10 to 100 can be achieved, associated with extremely confined effective volume of nanometric dimensions. This results in high Q/V_{eff} ratios indicating efficient coupling strength with a quantum emitter. At the opposite to cavity quantum electrodynamics where the coupling strength is obtained on diffraction limited volumes thanks to ultra-high Q factors, plasmonics structures allow efficient coupling on nanometric scales with reasonable Q factors, defining therefore high-bandwidth interaction. Finally, high coupling efficiencies (80%–90%) to dipolar or quadrupolar mode can be achieved and are of great interest for nanolasers realization.

Appendices

In this appendix, we derive the expression of mode quality factor and effective volume for a spherical particle embedded in homogeneous background of optical index $n_B = \sqrt{\epsilon_B}$. For a better description of the metal optical properties, we include the contributions of the bound electrons into the metal dielectric constant $\epsilon_m = \epsilon_\infty - \omega_p^2/(\omega^2 + i\Gamma_{\text{abs}}\omega)$.

A. Effective Polarisability Associated to n th SPP Mode

The n th multipole tensor moment of the metallic particle is given by

$$\begin{aligned} \mathbf{p}^{(n)} &= \frac{4\pi\epsilon_0\epsilon_B}{(2n-1)!!} \alpha_n \nabla^{n-1} \mathbf{E}_0, \\ \alpha_n &= \frac{n(\epsilon_m - \epsilon_B)}{n\epsilon_m + (n+1)\epsilon_B} R^{2n+1}. \end{aligned} \quad (\text{A.1})$$

The resonance angular frequency is then $\omega_n = \omega_p \sqrt{n/[n\epsilon_\infty + (n+1)\epsilon_B]}$ ($\omega_\infty = \omega_p/\sqrt{\epsilon_\infty + \epsilon_B}$). Finally, the effective polarisability, including finite size effects writes [22]

$$\alpha_n^{\text{eff}} = \left[1 - i \frac{(n+1)k_B^{2n+1}}{n(2n-1)!!(2n+1)!!} \alpha_n \right]^{-1} \alpha_n \quad (\text{A.2})$$

with $k_B = n_B k$ the wavenumber in the background medium.

Considering a Drude metal, we achieve a simple approximated expression for α_n^{eff} near a resonance

$$\begin{aligned} \alpha_n^{\text{eff}} &\sim \frac{(2n+1)\epsilon_B}{\omega_n n\epsilon_\infty + (n+1)\epsilon_B} \frac{\omega_n}{2(\omega_n - \omega) - i\Gamma_n} R^{2n+1}, \\ \Gamma_n &= \Gamma_{\text{abs}} + \Gamma_n^{\text{rad}}, \end{aligned} \quad (\text{A.3})$$

$$\Gamma_n^{\text{rad}} = \frac{(2n+1)\epsilon_B}{n\epsilon_\infty + (n+1)\epsilon_B} \omega_n \frac{(n+1)(k_B R)^{2n+1}}{n(2n-1)!!(2n+1)!!},$$

so that the quality factor expression $Q_n = \omega_n/\Gamma_n$ remains valid but with the corrected expressions for resonance frequency ω_n and total dissipation rate Γ_n .

B. Effective Volumes

The total coupling strength of a dipolar emitter to the spherical metallic particle, embedded in n_B medium, expresses [21, 22]

$$\frac{\gamma_{\text{tot}}^\perp}{n_B \gamma_0} \approx \frac{3}{2} \frac{1}{(k_B z_0)^3} \sum_{n=1}^{\infty} \frac{(n+1)^2}{z_0^{(2n+1)}} \text{Im}(\alpha_n^{\text{eff}}), \quad (\text{B.1})$$

$$\frac{\gamma_{\text{tot}}^\parallel}{n_B \gamma_0} \approx \frac{3}{4} \frac{1}{(k_B z_0)^3} \sum_{n=1}^{\infty} \frac{n(n+1)}{z_0^{(2n+1)}} \text{Im}(\alpha_n^{\text{eff}}).$$

The coupling strength to the n th mode is

$$\begin{aligned} \frac{\gamma_n^\perp}{n_B \gamma_0} &\approx \frac{3}{2} \frac{1}{(k_B z_0)^3} \frac{(n+1)^2}{z_0^{(2n+1)}} \text{Im}(\alpha_n^{\text{eff}}) \\ &\sim \frac{3}{4\pi^2} \left(\frac{\lambda}{n_B} \right)^3 \frac{R^{2n+1}}{4\pi z_0^3} \frac{(2n+1)\epsilon_B}{n\epsilon_\infty + (n+1)\epsilon_B} \frac{(n+1)^2}{z_0^{(2n+1)}} Q_n, \\ \frac{\gamma_n^\parallel}{n_B \gamma_0} &\approx \frac{3}{4} \frac{1}{(k_B z_0)^3} \frac{n(n+1)}{z_0^{(2n+1)}} \text{Im}(\alpha_n^{\text{eff}}) \\ &\sim \frac{3}{4\pi^2} \left(\frac{\lambda}{n_B} \right)^3 \frac{R^{2n+1}}{8\pi z_0^3} \frac{(2n+1)\epsilon_B}{n\epsilon_\infty + (n+1)\epsilon_B} \frac{n(n+1)}{z_0^{(2n+1)}} Q_n, \end{aligned} \quad (\text{B.2})$$

and the mode effective volume is deduced from comparison to the Purcell factor (1)

$$V_n^\perp = \frac{n\epsilon_\infty + (n+1)\epsilon_B}{(2n+1)\epsilon_B} \frac{4\pi z_0^{2n+4}}{(n+1)^2 R^{2n+1}}, \quad (\text{B.3})$$

$$V_n^\parallel = \frac{n\epsilon_\infty + (n+1)\epsilon_B}{(2n+1)\epsilon_B} \frac{8\pi z_0^{2n+4}}{n(n+1)R^{2n+1}}. \quad (\text{B.4})$$

Finally, we define the mode volume as

$$\frac{1}{V_n} = \frac{1}{3V_n^\perp(R)} + \frac{2}{3V_n^\parallel(R)}, \quad (\text{B.5})$$

$$V_n = \frac{n\epsilon_\infty + (n+1)\epsilon_B}{(2n+1)\epsilon_B} \frac{9}{(2n+1)(n+1)} V_0.$$

All the expressions obtained in this appendix reduce to the simple analytical case discussed in the main text for $\epsilon_\infty = 1$ (bound electrons contribution neglected) and $\epsilon_B = 1$ (background medium is air).

Acknowledgments

This work is supported by the Agence Nationale de la Recherche (ANR) under Grants Plastips (ANR-09-BLAN-0049-01), Fenoptixs (ANR-09-NANO-23), and HYNNA (ANR-10-BLAN-1016). This paper was also motivated by the preparation of a lecture for the 2nd Summer School On Plasmonics organized by Nicolas Bonod in October 2011.

References

- [1] M. Moskovits, "Surface-enhanced spectroscopy," *Reviews of Modern Physics*, vol. 57, no. 3, pp. 783–826, 1985.
- [2] V. Giannini, A. I. Fernández-Domínguez, S. C. Heck, and S. A. Maier, "Plasmonic nanoantennas: fundamentals and their use in controlling the radiative properties of nanoemitters," *Chemical Reviews*, vol. 111, no. 6, pp. 3888–3912, 2011.
- [3] C. Deeb, R. Bachelot, J. Plain et al., "Quantitative analysis of localized surface plasmons based on molecular probing," *ACS Nano*, vol. 4, no. 8, pp. 4579–4586, 2010.
- [4] P. Bharadwaj, B. Deutsch, and L. Novotny, "Optical antennas," *Advances in Optics and Photonics*, vol. 1, no. 3, pp. 438–483, 2009.
- [5] D. J. Bergman and M. I. Stockman, "Surface plasmon amplification by stimulated emission of radiation: quantum generation of coherent surface plasmons in nanosystems," *Physical Review Letters*, vol. 90, no. 2, Article ID 027402, 2003.
- [6] S. Schietinger, M. Barth, T. Aichele, and O. Benson, "Plasmon-enhanced single photon emission from a nanoassembled metal—diamond hybrid structure at room temperature," *Nano Letters*, vol. 9, no. 4, pp. 1694–1698, 2009.
- [7] C. Huang, A. Bouhelier, J. Berthelot et al., "External control of the scattering properties of a single optical nanoantenna," *Applied Physics Letters*, vol. 96, no. 14, Article ID 143116, 2010.
- [8] R. Marty, A. Arbouet, V. Paillard, C. Girard, and G. Colas Des Francs, "Photon antibunching in the optical near field," *Physical Review B*, vol. 82, no. 8, Article ID 081403, 2010.
- [9] R. Vincent and R. Carminati, "Magneto-optical control of Förster energy transfer," *Physical Review B*, vol. 83, no. 16, Article ID 165426, 2011.
- [10] J.-H. Kang, Y.-S. No, S.-H. Kwon, and H.-G. Park, "Ultrasubwavelength nanorod plasmonic cavity," *Optics Letters*, vol. 36, no. 11, pp. 2011–2013, 2011.
- [11] C. Girard, O. J. F. Martin, G. Lévêque, G. C. Des Francs, and A. Dereux, "Generalized Bloch equations for optical interactions in confined geometries," *Chemical Physics Letters*, vol. 404, no. 1–3, pp. 44–48, 2005.
- [12] S. A. Maier, "Plasmonic field enhancement and SERS in the effective mode volume picture," *Optics Express*, vol. 14, no. 5, pp. 1957–1964, 2006.
- [13] V. V. Datsyuk, "Ultimate enhancement of the local density of electromagnetic states outside an absorbing sphere," *Physical Review A*, vol. 75, no. 4, Article ID 043820, 2007.
- [14] A. Trügler and U. Hohenester, "Strong coupling between a metallic nanoparticle and a single molecule," *Physical Review B*, vol. 77, no. 11, Article ID 115403, 2008.
- [15] S. Savasta, R. Saija, A. Ridolfo, O. Di Stefano, P. Denti, and F. Borghese, "Nanopolaritons: vacuum Rabi splitting with a single quantum dot in the center of a dimer nanoantenna," *ACS Nano*, vol. 4, no. 11, pp. 6369–6376, 2010.
- [16] I. E. Protsenko, A. V. Uskov, O. A. Zaimidoroga, V. N. Samoilov, and E. P. O'Reilly, "Dipole nanolaser," *Physical Review A*, vol. 71, no. 6, Article ID 063812, 7 pages, 2005.
- [17] M. A. Noginov, G. Zhu, A. M. Belgrave et al., "Demonstration of a spaser-based nanolaser," *Nature*, vol. 460, no. 7259, pp. 1110–1112, 2009.
- [18] M. I. Stockman, "The spaser as a nanoscale quantum generator and ultrafast amplifier," *Journal of Optics A*, vol. 12, no. 2, Article ID 024004, 13 pages, 2010.
- [19] G. Colas Des Francs, C. Girard, M. Juan, and A. Dereux, "Energy transfer in near-field optics," *Journal of Chemical Physics*, vol. 123, no. 17, Article ID 174709, 7 pages, 2005.
- [20] R. Carminati, J. J. Greffet, C. Henkel, and J. M. Vigoureux, "Radiative and non-radiative decay of a single molecule close to a metallic nanoparticle," *Optics Communications*, vol. 261, no. 2, pp. 368–375, 2006.
- [21] G. Colas Des Francs, A. Bouhelier, E. Finot et al., "Fluorescence relaxation in the near-field of a mesoscopic metallic particle: distance dependence and role of plasmon modes," *Optics Express*, vol. 16, no. 22, pp. 17654–17666, 2008.
- [22] G. C. Des Francs, "Molecule non-radiative coupling to a metallic nanosphere: an optical theorem treatment," *International Journal of Molecular Sciences*, vol. 10, no. 9, pp. 3931–3936, 2009.
- [23] B. Rolly, B. Stout, S. Bidault, and N. Bonod, "Crucial role of the emitter-particle distance on the directivity of optical antennas," *Optics Letters*, vol. 36, no. 17, pp. 3368–3370, 2011.
- [24] N. Bonod, A. Devilez, B. Rolly, S. Bidault, and B. Stout, "Ultracompact and unidirectional metallic antennas," *Physical Review B*, vol. 82, no. 11, Article ID 115429, 2010.
- [25] G. Sun and J. B. Khurgin, "Theory of optical emission enhancement by coupled metal nanoparticles: an analytical approach," *Applied Physics Letters*, vol. 98, no. 11, 2011.
- [26] A. Wokaun, J. P. Gordon, and P. F. Liao, "Radiation damping in surface-enhanced Raman scattering," *Physical Review Letters*, vol. 48, no. 14, pp. 957–960, 1982.
- [27] J. Jackson, *Classical Electrodynamics*, John Wiley & Sons, Hoboken, NJ, USA, 3rd edition, 1998.
- [28] P. B. Johnson and R. W. Christy, "Optical constants of the noble metals," *Physical Review B*, vol. 6, no. 12, pp. 4370–4379, 1972.
- [29] C. Sönnichsen, T. Franzl, T. Wilk et al., "Drastic reduction of plasmon damping in gold nanorods," *Physical Review Letters*, vol. 88, no. 7, Article ID 077402, 4 pages, 2002.
- [30] J. J. Greffet, M. Laroche, and F. Marquier, "Impedance of a nanoantenna and a single quantum emitter," *Physical Review Letters*, vol. 105, no. 11, Article ID 117701, 2010.
- [31] K. J. Vahala, "Optical microcavities," *Nature*, vol. 424, no. 6950, pp. 839–846, 2003.
- [32] J. B. Khurgin and G. Sun, "Enhancement of optical properties of nanoscaled objects by metal nanoparticles," *Journal of the Optical Society of America B*, vol. 26, no. 12, pp. B83–B95, 2009.
- [33] A. F. Koenderink, "On the use of Purcell factors for plasmon antennas," *Optics Letters*, vol. 35, no. 24, pp. 4208–4210, 2010.
- [34] J. Barthes, G. Colas Des Francs, A. Bouhelier, J.-C. Weeber, and A. Dereux, "Purcell factor for a point-like dipolar emitter coupled to a two-dimensional plasmonic waveguide," *Physical Review B*, vol. 84, no. 7, Article ID 073403, 2011.

Research Article

Nanocrosses with Highly Tunable Double Resonances for Near-Infrared Surface-Enhanced Raman Scattering

Ye Jian^{1,2} and VanDorpe Pol¹

¹IMEC vzw, Kapeldreef 75, 3001 Leuven, Belgium

²Chemistry Department, KU Leuven, 3001 Leuven, Belgium

Correspondence should be addressed to Ye Jian, jian.ye@imec.be

Received 14 October 2011; Accepted 2 December 2011

Academic Editor: A. Femius Koenderink

Copyright © 2012 Y. Jian and V. Pol. This is an open access article distributed under the Creative Commons Attribution License, which permits unrestricted use, distribution, and reproduction in any medium, provided the original work is properly cited.

We present asymmetric gold nanocrosses with highly tunable double resonances for the near-infrared (NIR) surface-enhanced Raman scattering (SERS), optimizing electric field enhancement at both the excitation and Stokes Raman wavelengths. The calculated largest SERS enhancement factor can reach a value as large as 1.0×10^{10} . We have found that the peak separation, the resonance position, and peak intensity ratio of the double-resonance gold nanocrosses can be tuned by changing the structural dimensions or the light polarization.

Surface-enhanced Raman scattering (SERS) effect boosts the Raman signals of adsorbates on the surfaces of metallic nanostructures when their plasmon resonances and consequently an enhanced near field are excited at the wavelength of the stimulating laser beam. The enhancement factor (EF) of SERS may reach a level of single-molecule resolution [1, 2]. The SERS technique has demonstrated its use in many applications such as a pH meter, biosensing, and bioimaging [3–5]. Recently, because of the usage of SERS for *in vivo* bioapplications, there is increased interest of SERS in the near-infrared (NIR) region (700–1400 nm) in the optical spectrum, where blood and tissue are most transparent and light can penetrate tissue over a deepest distance [6, 7].

There are two mechanisms behind SERS, electromagnetic (EM) and charge transfer (CT) effect, which are extensively mentioned in the literature. It is, however, generally accepted that the EM effect is the dominant one. In the EM mechanism, the EF of each adsorbate is proportional to the product of the field intensity at the laser excitation wavelength and that at the Stokes-shifted Raman scattering wavelength, namely, $EF = |EF_{\text{ex}}|^2 |EF_{\text{scat}}|^2$. As plasmon resonances, which are usually responsible for the EM enhancement mechanism, are spectrally relatively broad, usually it is assumed that $|EF_{\text{ex}}|^2$ and $|EF_{\text{scat}}|^2$ are equal if the center of the resonance is chosen in between the two wavelength

positions. For NIR SERS, however, the Raman scattering wavelength and the excitation wavelength can be separated by over 100 nm, limiting the efficiency of a single resonance. Very recently, SERS substrates with double plasmon resonances at the laser excitation and Raman scattering wavelengths have been demonstrated by Crozier's group by showing higher enhancement compared to similar structures with single resonances [8, 9]. In addition, it is well known that a strong plasmonic coupling in the structures (e.g., bow-tie and disk dimer) will generate the near-field hot spots in the tiny gap, which may amplify the Raman signal significantly [10–13]. In this paper, we report on a different type of double-resonance plasmonic substrate consisting of gold (Au) nanocrosses potentially useful for the NIR SERS application. Strong near field enhancement is achieved by the plasmonic coupling between two opposite tips of the cross-bars. The achievement of the double resonances can be realized by breaking the symmetry of the Au nanocross. We have found that the peak separation (namely, the distance between the excitation and scattering wavelength), the resonance position, and peak intensity ratio of the double-resonance Au nanocrosses are highly tunable in the NIR range by changing the light polarization or the structural dimensions. We have also numerically demonstrated that the SERS EF of the Au nanocross can reach a value as large as 1.0×10^{10} .

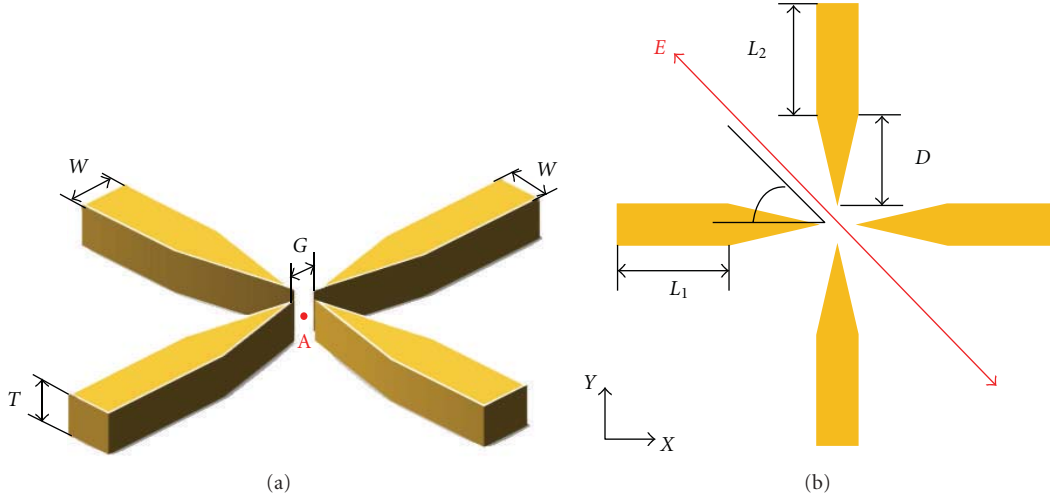


FIGURE 1: Schematic and dimensional parameters of an Au nanocross. The symmetry of the Au nanocrosses can be broken by tuning the different arm lengths of L_1 and L_2 .

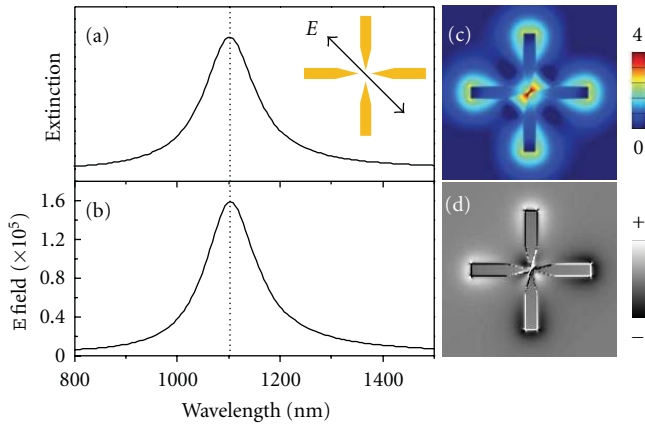


FIGURE 2: (a) Extinction spectrum, (b) electric field intensity ($|E^2|$) spectrum at the point A (see Figure 1), (c) the on-resonance electric field distribution ($\text{Log}|E^2|$), and (d) surface charge distribution for a symmetric Au nanocross (120, 120) normally illuminated by a $\theta = 45^\circ$ polarized plane wave.

We employed the three-dimensional finite different time domain (FDTD) calculation method to investigate the optical properties of Au nanocrosses in this work. Figures 1(a) and 1(b) display the schematic illustration and dimensional parameters of the Au nanocross used in the simulation with a width (W), thickness (T), gap size (G), tip length (D), arm length along X axis (L_1), and arm length along Y axis (L_2). Herein, an Au nanocross with L_1 and L_2 can be denoted (L_1, L_2) because the other dimensional parameters are constant ($W = 40$ nm, $T = 40$ nm, $G = 4$ nm, and $D = 78$ nm). L_1 and L_2 are varied to achieve the double resonances at different wavelengths and with different peak separations. The light is propagating normal to the XY plane and is polarized along the direction of $\theta = 45^\circ$ (see Figure 1(b)). The simulations were performed by using the FDTD software from Lumerical Solutions, Inc. The empirical dielectric function of Au has been described in our previous work [14]. We have placed

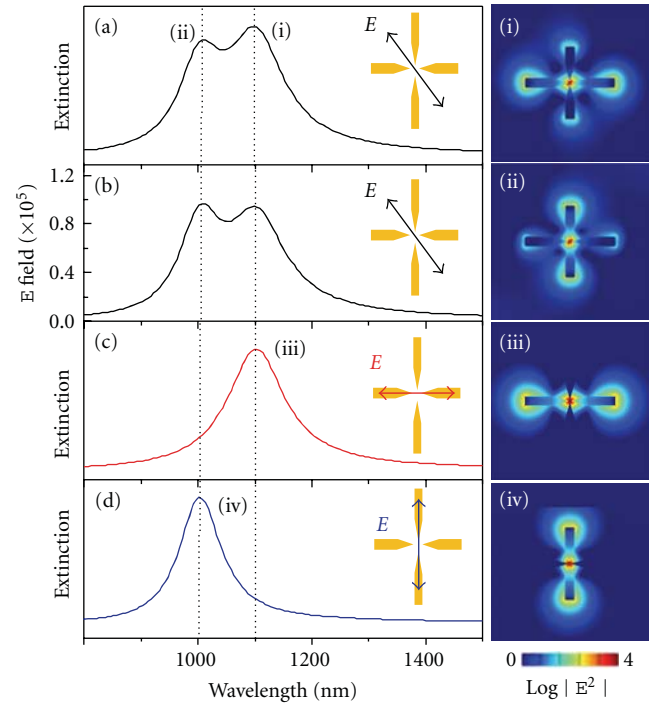


FIGURE 3: (a) Extinction spectrum and (b) electric field intensity ($|E^2|$) spectrum at the point A (see Figure 1) for an asymmetric Au nanocross (120, 80) normally illuminated by a $\theta = 45^\circ$ polarized plane wave. (c, d) Extinction spectra of the Au nanocross (120, 80) with a polarization along the (c) x - and (d) y -axis. The electric field distributions ($\text{Log}|E^2|$) of the plasmon resonance modes (i–iv) are shown on the right.

a point monitor (point A) in the middle of the structure gap, whose position is indicated in Figure 1(a). All extinction spectra, electric field intensity spectra at the point A, electric field distribution, and surface charge distribution images were obtained from the simulations. The amplitude of the electric field of the incident light is set to 1.

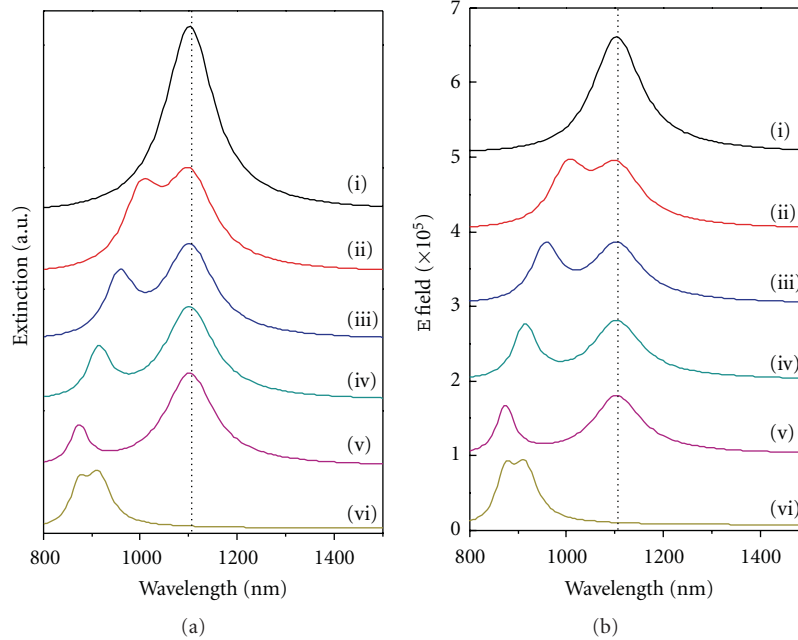


FIGURE 4: (a) Extinction and (b) electric field intensity ($|E|^2$) spectra at the point A (see Figure 1) for different dimensional Au nanocrosses: (i) 120, 120; (ii) 120, 80; (iii) 120, 60; (iv) 120, 40; (v) 120, 20; and (vi) 40, 20.

Au nanocrosses may strongly couple to the incident radiation by the dipolar mode and higher order modes, but the higher order modes are dark for the normal incidence [15]. For a symmetric Au nanocross (120, 120) normally illuminated by $\theta = 45^\circ$ polarized light, we can only observe a bright resonance mode at 1103 nm in the NIR range (Figure 2(a)). In order to fully understand its mode feature, we plot its electric field distribution image in Figure 2(c). It is clearly shown that each arm of the Au nanocross displays a strong dipolar resonant character and couples to each other, consequently producing a rather enhanced electric field in the gap. The electric field intensity spectrum at the point A shows that the maximum electric field ($|E|^2$) can reach a value as large as 1.6×10^5 . The calculated charge distribution image shown in Figure 2(d) further confirms the dipolar nature of the modes and their strong coupling for the arms of the Au nanocross.

To achieve the double resonances for SERS, we break the symmetry of the Au nanocross by changing the arm length L_2 . Figure 3(a) shows an extinction spectrum of an asymmetric Au nanocross (120, 80) with a decreased value of L_2 . We can observe two resonance at 1103 (i) and 1007 nm (ii). Interestingly, the corresponding electric field intensity spectrum at the point A shows two maximum values at the same two resonance positions, which can be used for the SERS excitation and the scattering enhancement. More importantly, the electric field intensity spectrum shows that the field enhancements of these two resonances both reach a value of around 1.0×10^5 (Figure 3(b)). Therefore, the total SERS EF may reach a value of 1.0×10^{10} . We simulated the excitation spectra of the Au nanocross (120, 80) with a light polarization along the long arm (x -axis) and the

short arm (y -axis) in Figures 3(c) and 3(d) in order to determine the origin of the prescribed two resonances' (i) and (ii) formation. It is shown that the resonance (i) and (ii) are actually from the resonance (iii) and (iv), formed by the light polarization along the long and short arms, respectively. The electric field distributions of the resonance mode in Figure 3 further show that the dominant modes of resonance (i) and (ii) are rather similar to that of (iii) and (iv), respectively, which indicates a weak coupling between two bright modes (iii) and (iv) resulting in the double-resonance feature. Figure 3 also implies that we can easily tune the resonance positions by controlling the arm lengths of the Au nanocrosses. This is very common to tune the resonance position by controlling the asymmetric geometry of the plasmonic structure, for example, asymmetric split ring resonators [16, 17].

In Figure 4(a), we show the excitation and the electric field intensity spectra of six different dimensional Au nanocrosses: (i) 120, 120; (ii) 120, 80; (iii) 120, 60; (iv) 120, 40; (v) 120, 20; and (vi) 40, 20. Some plasmonic resonant behaviors are observed: (1) two resonances are highly tunable in the NIR range; (2) the resonance at higher wavelength corresponds to the mode along the long arm of the nanocross, and the lower resonance to that of the short arm; (3) the more difference between the long and short arm, the larger the peak separation; (4) for different dimensional nanocrosses, the field enhancement for both resonances can reach a value in the range of 5.0×10^4 – 1.0×10^5 ; consequently, the total SERS EF remaining in the range of 1.0×10^9 – 1.0×10^{10} . For the structures of (ii), (iii), (iv) and (v), one resonance remains at 1103 nm and the other one can be tuned from 1007 to 872 nm by changing the short arm from

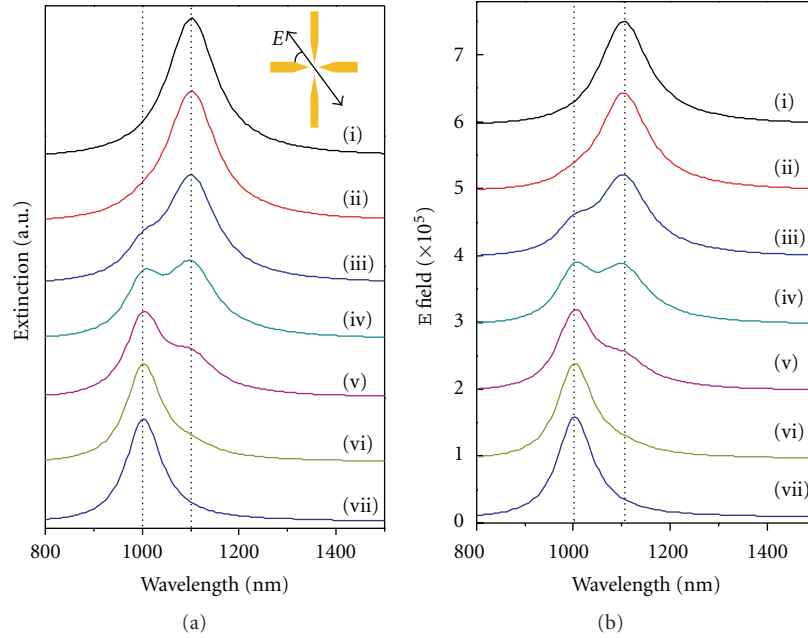


FIGURE 5: (a) Extinction and (b) electric field intensity ($|E^2|$) spectra at the point A (see Figure 1) for a Au nanocross (120, 80) illuminated by a plane wave with different polarizations. The angle (θ) between the light polarization and the x -axis is (i) 0, (ii) 15, (iii) 30, (iv) 45, (v) 60, (vi) 75, and (vii) 90 degree.

80 to 20 nm. The peak separation can be controlled from 30 to 231 nm (Figure 4(b)). The high tunability and flexibility of the double-resonance position and peak separation offer us a couple of advantages for SERS. First, we can easily match the double resonances of the Au nanocross to the laser line and the Stoke Raman band. Second, the large peak separation allows us to enhance the Raman band, for example, $\nu(=CH)$, having a Stoke Raman shift at a longer wavenumber at around 3000 cm^{-1} , which is 240 nm away from the NIR laser line (e.g., 785 nm). In addition, we believe that the double-resonance nanocross is potential useful for the surface-enhanced second harmonic generation [18]. The plasmon resonances of the asymmetric Au nanocrosses are not only arm length dependent but also incident light polarization dependent. Figures 5(a) and 5(b) show the extinction and electric field intensity spectra of the Au nanocross (120, 80) with different light polarizations. By changing the polarization angle (θ), we can control the peak intensity ratio between the two resonances of the Au nanocross at 1007 and 1103 nm, respectively. Moreover, we have simulated the double-resonance nanocross with rounded tips (with a 4 nm curvature radius) in order to have a more realistic estimation for the experimental samples. We have found that the maximum SERS EF drops to 2.0×10^9 for the Au nanocross (120, 80), one order of magnitude smaller than that with sharp tips, which is still a rather large EF for the molecular detection.

In conclusion, we have numerically demonstrated asymmetric Au nanocrosses as double-resonance SERS substrates. Strong field enhancements at the excitation and scattering wavelengths lead to a total SRS EF of around 1.0×10^{10} . Moreover, we have shown that the resonance position, the

peak separation, and the peak intensity ratio of the Au nanocrosses can be tuned by changing their arm lengths and the light polarization. Strong near field and large peak separation are particularly important to the enhancement of the Raman band at high wavenumbers. We anticipate that this work will offer an aid for the design and the fabrication of new SERS substrates with a large EF.

Acknowledgment

J. Ye and P. V. Dorpe acknowledge financial support from the FWO of Flanders.

References

- [1] K. Kneipp, Y. Wang, H. Kneipp et al., "Single molecule detection using surface-enhanced Raman scattering (SERS)," *Physical Review Letters*, vol. 78, no. 9, pp. 1667–1670, 1997.
- [2] S. Nie and S. R. Emory, "Probing single molecules and single nanoparticles by surface-enhanced Raman scattering," *Science*, vol. 275, no. 5303, pp. 1102–1106, 1997.
- [3] S. W. Bishnoi, C. J. Rozell, C. S. Levin et al., "All-optical nanoscale pH meter," *Nano Letters*, vol. 6, no. 8, pp. 1687–1692, 2006.
- [4] D. Graham, K. Faulds, and W. E. Smith, "Biosensing using silver nanoparticles and surface enhanced resonance Raman scattering," *Chemical Communications*, no. 42, pp. 4363–4371, 2006.
- [5] Y. Huang, V. P. Swarup, and S. W. Bishnoi, "Rapid raman imaging of stable, functionalized nanoshells in mammalian cell cultures," *Nano Letters*, vol. 9, no. 8, pp. 2914–2920, 2009.
- [6] R. Weissleder, "A clearer vision for in vivo imaging," *Nature Biotechnology*, vol. 19, no. 4, pp. 316–317, 2001.

- [7] A. M. Smith, M. C. Mancini, and S. Nie, "Bioimaging: second window for *in vivo* imaging," *Nature Nanotechnology*, vol. 4, no. 11, pp. 710–711, 2009.
- [8] Y. Chu, M. G. Banaee, and K. B. Crozier, "Double-resonance plasmon substrates for surface-enhanced raman scattering with enhancement at excitation and stokes frequencies," *ACS Nano*, vol. 4, no. 5, pp. 2804–2810, 2010.
- [9] M. G. Banaee and K. B. Crozier, "Mixed dimer double-resonance substrates for surface-enhanced Raman spectroscopy," *ACS Nano*, vol. 5, no. 1, pp. 307–314, 2011.
- [10] Z. Zhang, A. Weber-Bargioni, S. W. Wu, S. Dhuey, S. Cabrini, and P. J. Schuck, "Manipulating nanoscale light fields with the asymmetric bowtie nano-colorsorter," *Nano Letters*, vol. 9, no. 12, pp. 4505–4509, 2009.
- [11] I. Romero, J. Aizpurua, G. W. Bryant, and F. J. García De Abajo, "Plasmons in nearly touching metallic nanoparticles: singular response in the limit of touching dimers," *Optics Express*, vol. 14, no. 21, pp. 9988–9999, 2006.
- [12] M. I. Stockman, L. N. Pandey, L. S. Muratov, and T. F. George, "Comment on "photon scanning tunneling microscopy images of optical excitations of fractal metal colloid clusters"" *Physical Review Letters*, vol. 75, no. 12, p. 2450, 1995.
- [13] N. J. Halas, S. Lal, W.-S. Chang, S. Link, and P. Nordlander, "Plasmons in strongly coupled metallic nanostructures," *Chemical Reviews*, vol. 111, no. 6, pp. 3913–3961, 2011.
- [14] J. Ye, N. Verellen, W. Van Roy et al., "Plasmonic modes of metallic semishells in a polymer film," *ACS Nano*, vol. 4, no. 3, pp. 1457–1464, 2010.
- [15] N. Verellen, P. Van Dorpe, C. Huang et al., "Plasmon line shaping using nanocrosses for high sensitivity localized surface plasmon resonance sensing," *Nano Letters*, vol. 11, no. 2, pp. 391–397, 2011.
- [16] B. Lahiri, A. Z. Khokhar, R. M. De La Rue, S. G. Mcmeekin, and N. P. Johnson, "Asymmetric split ring resonators for optical sensing of organic materials," *Optics Express*, vol. 17, no. 2, pp. 1107–1115, 2009.
- [17] V. A. Fedotov, M. Rose, S. L. Prosvirnin, N. Papasimakis, and N. I. Zheludev, "Sharp trapped-mode resonances in planar metamaterials with a broken structural symmetry," *Physical Review Letters*, vol. 99, no. 14, Article ID 147401, 2007.
- [18] N. J. Borys, M. J. Walter, and J. M. Lupton, "Intermittency in second-harmonic radiation from plasmonic hot spots on rough silver films," *Physical Review B*, vol. 80, no. 16, Article ID 161407, 2009.

Research Article

Optimization of *s*-Polarization Sensitivity in Apertureless Near-Field Optical Microscopy

Yuika Saito, Yoshiro Ohashi, and Prabhat Verma

Department of Applied Physics, Osaka University, 2-1 Yamadaoka, Suita, Osaka 565-0871, Japan

Correspondence should be addressed to Yuika Saito, yuika@ap.eng.osaka-u.ac.jp

Received 31 August 2011; Revised 27 October 2011; Accepted 14 November 2011

Academic Editor: Alexandre Bouhelier

Copyright © 2012 Yuika Saito et al. This is an open access article distributed under the Creative Commons Attribution License, which permits unrestricted use, distribution, and reproduction in any medium, provided the original work is properly cited.

It is a general belief in apertureless near-field microscopy that the so-called *p*-polarization configuration, where the incident light is polarized parallel to the axis of the probe, is advantageous to its counterpart, the *s*-polarization configuration, where the incident light is polarized perpendicular to the probe axis. While this is true for most samples under common near-field experimental conditions, there are samples which respond better to the *s*-polarization configuration due to their orientations. Indeed, there have been several reports that have discussed such samples. This leads us to an important requirement that the near-field experimental setup should be equipped with proper sensitivity for measurements with *s*-polarization configuration. This requires not only creation of effective *s*-polarized illumination at the near-field probe, but also proper enhancement of *s*-polarized light by the probe. In this paper, we have examined the *s*-polarization enhancement sensitivity of near-field probes by measuring and evaluating the near-field Rayleigh scattering images constructed by a variety of probes. We found that the *s*-polarization enhancement sensitivity strongly depends on the sharpness of the apex of near-field probes. We have discussed the efficient value of probe sharpness by considering a balance between the enhancement and the spatial resolution, both of which are essential requirements of apertureless near-field microscopy.

1. Introduction

Apertureless near-field scanning optical microscopy (ANSOM) is becoming more and more popular for its application to a variety of nanoscale samples, where one can do microscopic as well as spectroscopic analysis at nanoscale [1, 2]. The key feature of ANSOM is enormous enhancement and confinement of light field at the apex of the near-field probe, which is a sharp metallic nanotip. The enhancement of scattered light from a sample can be more effective under proper polarization. Thus near-field imaging through ANSOM combined with proper control of polarization provides even more information about the sample, such as molecule and crystal symmetry, orientation, intermolecular interaction, optical transition, and so forth. In fact, many researchers have occasionally employed polarization-controlled ANSOM to enhance the contrast of measurements [3–7]. Under a reflection-type (or side-illumination-type) near-field setup where the incident and scattered lights are in opposite directions, the optical

configuration makes it easy to conveniently control the polarization of incident light at the tip apex. For this reason, the method of polarization control has been widely used for the analysis of nanoscale anisotropy, such as the crystalline structure, for reflection-type systems [8–13]. On the other hand, in a more commonly used transmission-type ANSOM configuration, where the incident and scattered lights are in the same direction, it is not easy to control the polarization, and hence one can find very few experimental reports on the polarization measurement in this type of experimental setup [14–16]. Even when a polarization control is employed in ANSOM setup, it is mostly to study the *p*-polarization configuration. One reason is that the *p*-polarization of excitation can form a strongly enhanced light source under the sharp apex of the near-field probe [17, 18], which also gives strong enhancement to the scattering from the sample in most of the cases. However, if one is studying the optical mode of a sample that has a dipole transition perpendicular to the probe axis, the *p*-polarization is no longer suitable. In this case, one needs to arrange the

s-polarization enhancement by the near-field probe. Indeed several experimental reports suggested that ANSOM probes show *s*-polarization sensitivity [19, 20], though none of them discussed it clearly.

In this study, we will provide an experimental evidence of the *s*-polarization sensitivity in apertureless near-field probes. Our near-field probes are fabricated by coating a thin layer of metal on a sharp dielectric nanotip. The sharpness of the tip apex depends on the thickness of the metallic layer. We prepared near-field probes with varying metal thickness and employed them to measure near-field Rayleigh scattering images under *s*-polarized illumination by scanning the tip over the focused laser spot. The method has been employed to evaluate the surface plasmon behavior [21], and such scattering images also are indicators of the polarization sensitivity of the enhancement by the near-field probes. We have discussed the *s*-polarization sensitivity of various probes through the contrast in the corresponding scattering images. In addition, we have also performed some calculations and computer simulations to obtain supportive information for checking the tendency polarization sensitivity on the sharpness of the near-field probe. We make a note that even though the simulation indicates that less sharpened probes with larger apex tend to give better enhancement for the *s*-polarized light, they are not ideal probes for near-field imaging because they lose the spatial confinement of the light. Thus one can find an optimum value of probe sharpness by evaluating the system sensitivity and the requirement of spatial resolution.

2. Experimental

The apertureless near-field probes were prepared by coating thin layers of silver on commercially available atomic force microscopy (AFM) cantilevers made of silicon (CSG01 tips purchased from NT-MDT co.). Silver coating was performed by the method of vacuum evaporation under a high vacuum of 2×10^{-6} Torr. By controlling the evaporation parameters, the probes were prepared with silver coating of 20, 40, and 60 nm. Since it was difficult to prepare thicker layers of silver under the same condition, we utilized simultaneous annealing at 400°C during the evaporation, to achieve the silver layer thickness of about 150 nm. The apex sharpness for all the silver-coated probes was checked by scanning electron microscope (SEM).

The optical setup for our near-field measurement is illustrated in Figure 1, which shows a system based on inverted microscope [22, 23]. The incident laser (CW, $\lambda = 488$ nm) is expanded 20 times in diameter and is introduced via various optical components to the inverted microscope. In order to achieve an *s*-polarized incident light at the near-field probe, we first prepared azimuthal polarization of the propagating laser by using a spatially patterned $\lambda/2$ waveplate (*z*-pol from Nanophoton). This waveplate can realize a perfect *x*-*y*-polarization as shown in the inset in Figure 1. The detailed explanation of how the waveplate works was shown in [23]. The experiment was done by utilizing a high-NA objective lens ($\times 60$, NA = 1.4, oil emersion) to focus

the light on the probe and by inserting an optical mask on the beam path that rejects the low-NA component (NA < 1) of the incident light. The near-field probe was set on an AFM stage and was scanned over the tightly focused laser spot. Rayleigh scattered signal was collected by the same objective lens in low-NA (NA < 1) configuration, which was detected by a photodiode. In the case of *s*-polarization excitation the scattering signal from the tip apex is efficiently collected in the low NA region because of the emission pattern of the dipole [24]. Moreover, the incident light that was introduced in an evanescent illumination configuration can be effectively reduced by the detection aperture, which results in the reduction of background signal in detection. The probe was scanned at the steps 30 nm to cover a scanning area of about $1 \mu\text{m}$ in square.

The simulation for a 2D finite difference time domain (FDTD) calculation was performed by using R-soft with nonuniform mesh. Since this is a rough estimation just to check the trend, we have employed 2D simulation instead of 3D. The quantitative difference between 2D and 3D is not an issue in this estimation. The probe apex was assumed to be a single silver sphere with different diameters, which was placed 2 nm above a glass substrate (index 1.5). The *s*-polarized incident light was launched at an angle of 45° from the substrate to achieve an evanescent illumination under the condition of total internal reflection. The field intensity was monitored $10 \mu\text{m}$ downward from the particle to anticipate the far field intensity.

3. FDTD Simulations

In order to understand the effect of polarization on the near-field enhancement in the proximity of a probe, we first made a rough estimation through FDTD simulation. Although a silver nanoparticle considered in simulation can never represent the real near-field probe prepared by silver evaporation, it still gives correct information about the trend that a real probe would follow on enhancement. For simplicity, we considered an ellipsoid-shaped nanoparticle with an aspect ratio of 1 : 4. Figure 2 shows the enhancement in the proximity of the nanoparticle for both *p*- and *s*-polarizations, which was calculated following the method of Moon and Spencer [17]. The horizontal dashed line represents the sample plane. As one can see, the light field is greatly enhanced near the apex (between the nanoparticle and the sample plane) for *p*-polarized illumination, whereas it is significantly enhanced at the middle area of the nanoparticle for the *s*-polarized illumination. As one goes away from the middle area towards the apex, the enhancement decreases and becomes very weak near the apex area. This result confirms that the enhancement near the sample is very weak for *s*-polarization, and hence *p*-polarization is a preferred configuration for most near-field experiments. However, if we consider scattering in the far field (when the detector is placed far from the probe apex), there are rooms for the *s*-polarization to be scattered back within the cone angle of the objective lens. To see if this happens, we performed numerical simulations by keeping the detector far from the

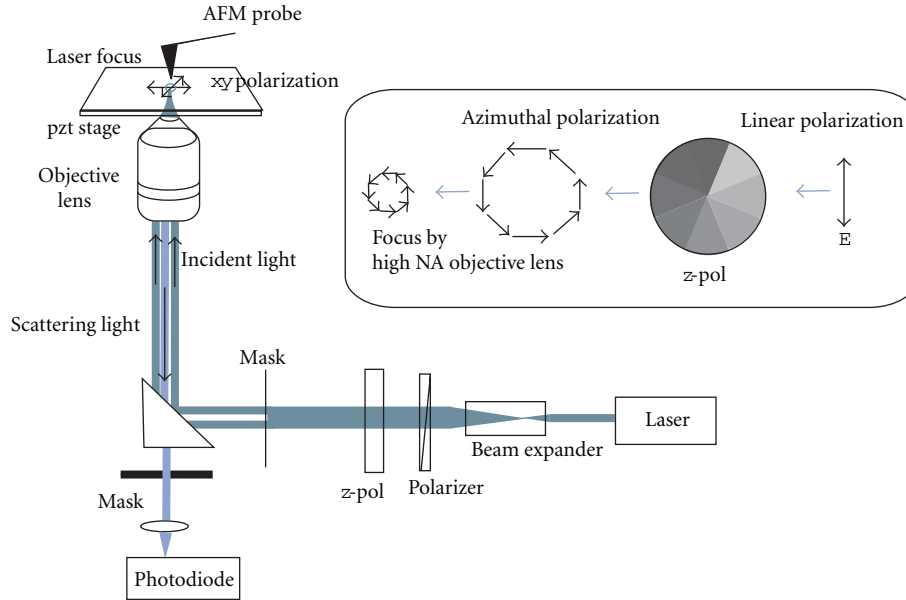


FIGURE 1: Experimental setup of near-field probe scanning over the laser focus in s -polarization condition. The inset illustrates a schematic of s -polarization formation by using z -pol.

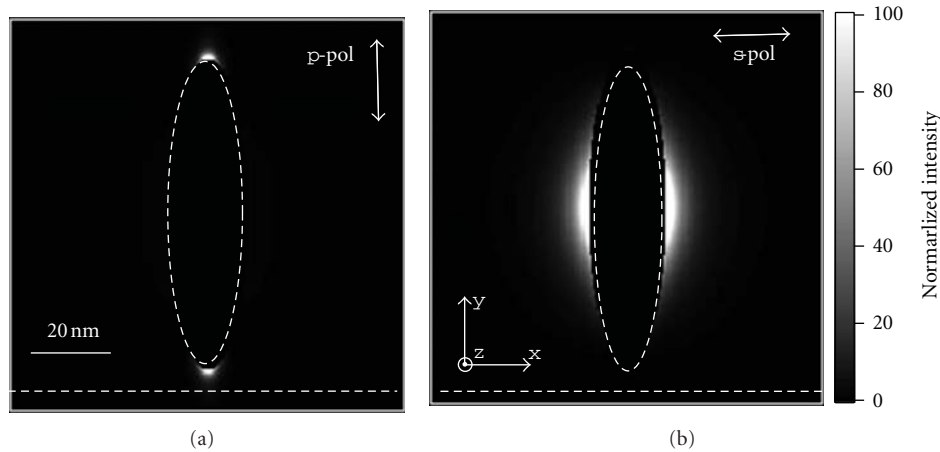


FIGURE 2: Theoretical calculation of electric field distributions near an ellipsoidal metallic nanoparticle under (a) p -polarization and (b) s -polarization excitations. The horizontal dotted lines indicate the sample surface. Strong field confinement can be seen near the apex between the sample and the probe in p -polarization, which is almost negligible in s -polarization.

probe. We also considered the effect of sharpness of the probe apex on the far-field enhancement, for which we approximated the probe apex by a single spherical silver particle and varied the diameter of that particle. Figure 3 shows some FDTD simulation results for far-field scattering under evanescent illumination employing s -polarization excitations for varying apex size. The simulation conditions are illustrated in the inset. As one can see in Figure 3, the far-field enhancement under s -polarized illumination has a significant dependence on the apex size. The scattering intensity shows relatively small rise for the apex diameter varying from 0 to ~ 20 nm, then it monotonically increases with the apex diameter. This brings us to a conclusion that the scattering efficiency for s -polarization illumination

increase, as the particle size increases, or as the apex sharpness decreases. The signal intensity becomes almost double for a probe with the diameter of 50 nm as compared to 30 nm. This is a reasonable figure for the net enhancement that is in accordance with our experimental statistics.

4. Results and Discussions

We anticipate from the calculation that the s -polarization sensitivity of a near-field probe increases as the sharpness of the probe apex decreases. As discussed before, the near-field probes used in this study were prepared by coating a thin silver layer on silicon nanotips. The apex of the silicon tip

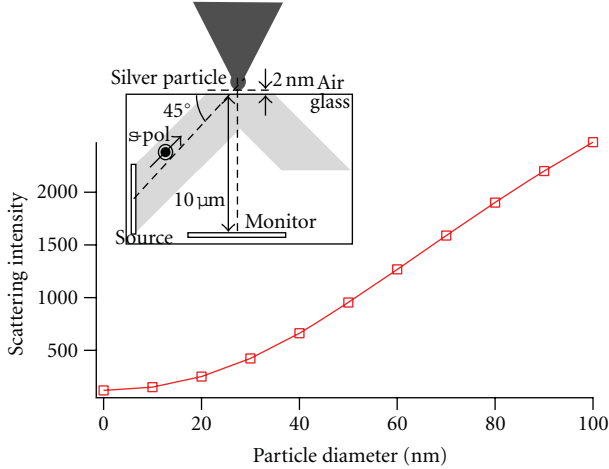


FIGURE 3: FDTD simulation of s -polarization scattering intensity from silver particle with respect to the apex diameter. Inset illustrates the simulation conditions.

is quite sharp; however the sharpness of the probe decreases as the thickness of the silver layer coated on the silicon tip increases. Even though the entire shape of the real probe is different from the probes used in FDTD simulation, we expect a similar trend of enhancement as the thickness of the silver layer on the probe increases. That means we expect the s -polarization sensitivity of the probes with thicker silver layers to be higher than that for the probes with thinner silver layers. Figures 4(a)–4(d) show SEM images of probes that have silver layers with thickness 0, 20, 40, and 60 nm, respectively. A closer look at the probe apex in these SEM images reveals that the apex diameter of the probe increases gradually as the coating thickness increases. Figures 5(a)–5(d) show Rayleigh scattering images of s -polarized laser spot measured by employing the probes shown in Figures 4(a)–4(d), respectively. Doughnut-shaped patterns could be seen in these Rayleigh scattering images, which is an evidence of s -polarization condition. The contrast variation in these images corresponds to the scattering efficiency for excitation light. Since we created s -polarized illumination at the probe apex by introducing the high-NA component of an azimuthally polarized laser beam, a comparison of image contrast in Figure 5 can be considered as the comparison of s -polarization sensitivity of the probes [25]. We also calculated the quantitative values of contrast by a simple relation

$$\text{contrast} = \frac{(I_S - I_{Bg})}{(I_S + I_{Bg})}, \quad (1)$$

where I_S indicates the signal intensity corresponding to the signal area (laser spot) and I_{Bg} denotes the background intensity corresponding to the background area. The net intensities were the summations over the measured areas. Table 1 shows the contrast values obtained from (1) for different probes. As seen in Figure 5(a), we could not get any image pattern under s -polarization for the noncoated probe in Figure 4(a), because this bare silicon probe did not have an s -polarization sensitivity. The contrast is still

TABLE 1: Contrast of the probes shown in Figure 5, as calculated from (1).

Tip	Diameter/nm	Contrast
a	5	0
b	20	0.023
c	40	0.037
d	60	0.061

weak in Figure 5(b) for the probe with silver thickness of 20 nm; however, it becomes stronger in Figure 5(c) when the silver layer on the probe is as thick as 60 nm. This result is consistent with the simulation results in Figure 3, where the tip apex is approximated as a single silver particle. It is not appropriate to make a quantitative comparison however, it is clear that the scattering intensity monotonously increases as the particle size increases.

One may expect from the simulation results that a broader probe would scatter more light under s -polarization, thus further increasing the probe size may result in an enormous enhancement. However, experimentally this was not true. The Rayleigh scattering image contrast decreased for the broader probe ~ 150 nm in apex diameter. This may come from the surface plasmon resonance wavelength of the coated silver, which is shifted to longer wavelength for larger structure; however the reason is still unclear. Apart from this decrease in scattering efficiency, a probe with larger apex diameter also degrades the spatial resolution in the measurement. Thus a probe with larger apex diameter is not suitable for near-field studies. This leads us to the conclusion that the s -polarization efficiency of a near-field probe can be increased by increasing the apex diameter of the probe, however, up to a certain limit where the spatial resolution is still acceptable.

The optimum value of probe apex diameter that can give best results for both s -polarization sensitivity and spatial resolution in near-field measurement would depend on the experimental system and requirement. In general, a near-field probe that can provide contrast of about 0.03 is acceptable for a good-quality imaging. In our case, the probes shown in Figures 4(c) and 4(d) provide acceptable contrast, and hence they qualify for s -polarization ANSOM experiments. We can thus conclude that a 30–60 nm-thick silver coating can result in reasonably good near-field probe for enhancement of s -polarization. The lower limit can still be changed by optimizing the collection efficiency of the optical setup, and the upper limit can be determined by the requirement of spatial resolution. For tips with more efficient s -polarization sensitivity, the on-gap mode tips could provide good results [26]. However, fabrication of a gap as small as ~ 1 nm at the tip apex is difficult with current technology, and hence it is still not in practical use. Therefore, the best way to achieve the s -polarization sensitivity at this moment is to carefully control the size of the probe apex by optimizing evaporation parameters.

Finally, we would also like to make a small note on the p -polarization sensitivity of these probes. Instead of the azimuthal polarization, using radial polarization of incidence

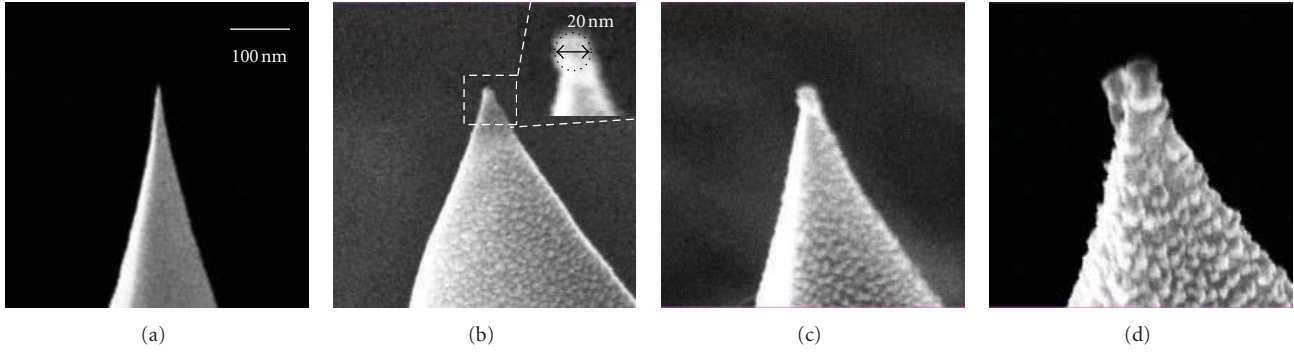


FIGURE 4: SEM images of several ANSOM probes with varying thickness of silver coating. (a) Bare silicon probe with no silver coating, (b) probe with 20 nm silver coating, (c) probe with 40 nm silver coating, and (d) probe with 60 nm silver coating. The zoomed inset shows how we estimate the apex size.

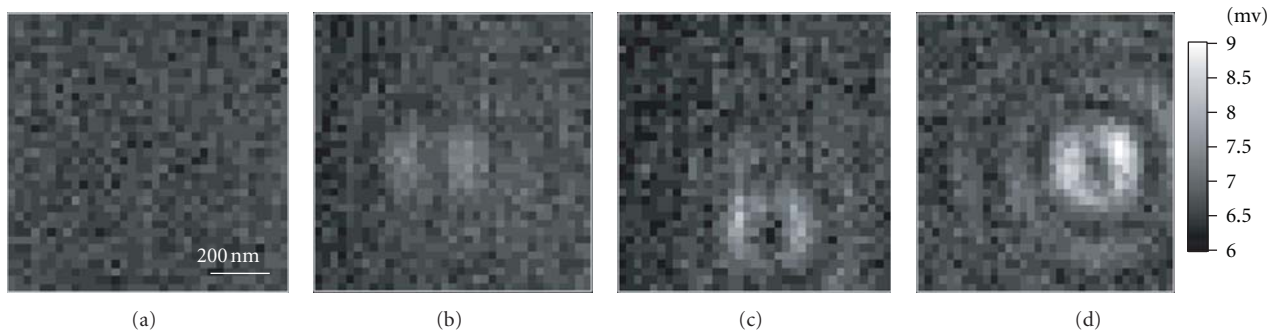


FIGURE 5: Scattering images of the s -polarization laser focus measured by the probes with different silver coatings. The images (a)–(d) correspond to the probes shown in Figures 4(a)–4(d), respectively. The contrasts in the images correspond to the s -polarization sensitivities of these probes.

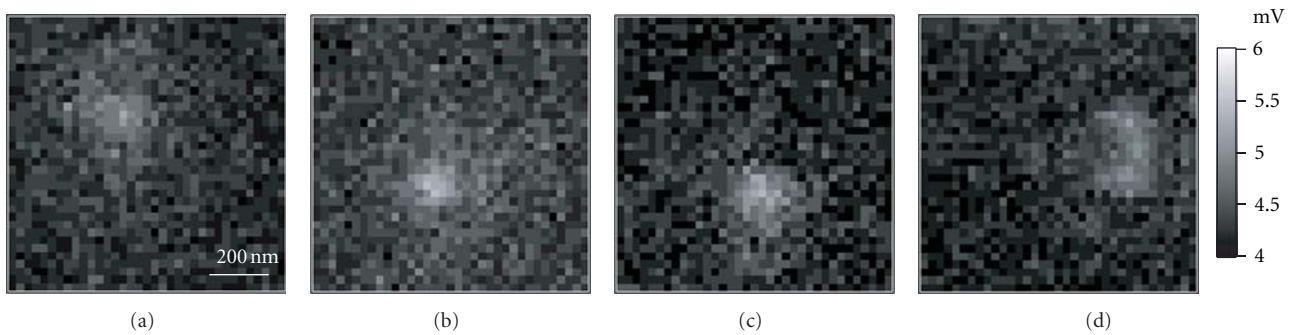


FIGURE 6: Scattering images of the p -polarization laser focus measured by the probes with different silver coatings. The images (a)–(d) correspond to the probes shown in Figures 4(a)–4(d), respectively.

laser beam can result in the dominant generation of p -polarization at probe apex. By utilizing radial polarization, we measured the Rayleigh scattering images for the same probes that were discussed earlier in Figure 4. The results are shown in Figures 6(a)–6(d), which corresponds to the p -polarization sensitivity. Since the p -polarization dipole was not efficiently collected in this experimental configuration, the image did not show a strong contrast. Nevertheless, every probe shows certain amount of p -polarization sensitivity

even if they did not have s -polarization sensitivity such as the uncoated probe shown in Figure 4(a).

5. Conclusions

In conclusion, we have examined the enhancement phenomena of ANSOM probes for their s -polarization sensitivities, which could be extremely important for those samples,

which have optical response in the direction perpendicular to the probe axis. A supporting FDTD simulation as well as experimental results showed that the probes with larger apex diameter yield stronger scattering when illuminated with *s*-polarized light. However, the experimental results also indicated that the contrast could not be improved only by increasing the diameter of the apex. We conclude that the metal coating thicker than 30 nm is necessary for *s*-polarization sensitivity in our system. For further improvement of *s*-polarization sensitivity in ANSOM measurements, there could still be some scope for optimizing the probe design, including the possibility of estimations through calculations and simulations [27, 28].

References

- [1] Y. Saito and P. Verma, "Imaging and spectroscopy through plasmonic nano-probe," *EPJ Applied Physics*, vol. 46, no. 2, Article ID 20101, 2009.
- [2] P. Verma, T. Ichimura, T. A. Yano, Y. Saito, and S. Kawata, "Nano-imaging through tip-enhanced Raman spectroscopy: stepping beyond the classical limits," *Laser and Photonics Reviews*, vol. 4, no. 4, pp. 548–561, 2010.
- [3] N. Lee, R. D. Hartschuh, D. Mehtani et al., "High contrast scanning nano-Raman spectroscopy of silicon," *Journal of Raman Spectroscopy*, vol. 38, no. 6, pp. 789–796, 2007.
- [4] M. Motohashi, N. Hayazawa, A. Tarun, and S. Kawata, "Depolarization effect in reflection-mode tip-enhanced Raman scattering for Raman active crystals," *Journal of Applied Physics*, vol. 103, no. 3, Article ID 034309, 2008.
- [5] P. G. Gucciardi, M. Lopes, R. D eturche, C. Julien, D. Barchiesi, and M. Lamy De La Chapelle, "Light depolarization induced by metallic tips in apertureless near-field optical microscopy and tip-enhanced Raman spectroscopy," *Nanotechnology*, vol. 19, no. 21, article 215702, 2008.
- [6] A. Merlen, J. C. Valmalette, P. G. Gucciardi, M. Lamy de la Chapelle, A. Frigout, and R. Ossikovski, "Depolarization effects in tip-enhanced Raman spectroscopy," *Journal of Raman Spectroscopy*, vol. 40, no. 10, pp. 1361–1370, 2009.
- [7] M. P. Nikiforov, S. C. Kehr, T. H. Park et al., "Probing polarization and dielectric function of molecules with higher order harmonics in scattering-near-field scanning optical microscopy," *Journal of Applied Physics*, vol. 106, no. 11, Article ID 114307, 2009.
- [8] D. A. Higgins, D. A. Vanden Bout, J. Kerimo, and P. F. Barbara, "Polarization-modulation near-field scanning optical microscopy of mesostructured materials," *Journal of Physical Chemistry*, vol. 100, no. 32, pp. 13794–13803, 1996.
- [9] S. C. Schneider, S. Grafstr om, and L. M. Eng, "Scattering near-field optical microscopy of optically anisotropic systems," *Physical Review B*, vol. 71, no. 11, Article ID 115418, pp. 1–8, 2005.
- [10] G. Picardi, Q. Nguyen, R. Ossikovski, and J. Schreiber, "Polarization properties of oblique incidence scanning tunneling microscopy-tip-enhanced Raman spectroscopy," *Applied Spectroscopy*, vol. 61, no. 12, pp. 1301–1305, 2007.
- [11] Z. H. Kim and S. R. Leone, "Polarization-selective mapping of near-field intensity and phase around gold nanoparticles using apertureless near-field microscopy," *Optics Express*, vol. 16, no. 3, pp. 1733–1741, 2008.
- [12] S. Berweger and M. B. Raschke, "Polar phonon mode selection rules in tip-enhanced Raman scattering," *Journal of Raman Spectroscopy*, vol. 40, no. 10, pp. 1413–1419, 2009.
- [13] M. Chaigneau, G. Picardi, and R. Ossikovski, "Molecular arrangement in self-assembled azobenzene-containing thiol monolayers at the individual domain level studied through polarized near-field Raman spectroscopy," *International Journal of Molecular Sciences*, vol. 12, no. 2, pp. 1245–1258, 2011.
- [14] E. J. S anchez, L. Novotny, and X. S. Xie, "Near-field fluorescence microscopy based on two-photon excitation with metal tips," *Physical Review Letters*, vol. 82, no. 20, pp. 4014–4017, 1999.
- [15] Y. Saito, N. Hayazawa, H. Kataura et al., "Polarization measurements in tip-enhanced Raman spectroscopy applied to single-walled carbon nanotubes," *Chemical Physics Letters*, vol. 410, no. 1–3, pp. 136–141, 2005.
- [16] W. Chen and Q. Zhan, "Numerical study of an apertureless near field scanning optical microscope probe under radial polarization illumination," *Optics Express*, vol. 15, no. 7, pp. 4106–4111, 2007.
- [17] P. Moon and D. E. Spencer, *Field Theory for Engineers*, Van Nost. Reinhold, 1961.
- [18] S. Kawata, Y. Inouye, and T. Sugiura, "Near-field Scanning Optical Microscope with a laser trapped probe," *Japanese Journal of Applied Physics*, vol. 33, no. 12a, pp. L1725–L1727, 1994.
- [19] A. Hartschuh, E. J. S anchez, X. S. Xie, and L. Novotny, "High-resolution near-field Raman microscopy of single-walled carbon nanotubes," *Physical Review Letters*, vol. 90, no. 9, article 095503, pp. 1–4, 2003.
- [20] T. A. Yano, P. Verma, Y. Saito, T. Ichimura, and S. Kawata, "Pressure-assisted tip-enhanced Raman imaging at a resolution of a few nanometres," *Nature Photonics*, vol. 3, no. 8, pp. 473–477, 2009.
- [21] A. Bouhelier, F. Ignatovich, A. Bruyant et al., "Surface plasmon interference excited by tightly focused laser beams," *Optics Letters*, vol. 32, no. 17, pp. 2535–2537, 2007.
- [22] N. Hayazawa, Y. Saito, and S. Kawata, "Detection and characterization of longitudinal field for tip-enhanced Raman spectroscopy," *Applied Physics Letters*, vol. 85, no. 25, pp. 6239–6241, 2004.
- [23] Y. Saito, P. Verma, K. Masui, Y. Inouye, and S. Kawata, "Nano-scale analysis of graphene layers by tip-enhanced near-field Raman spectroscopy," *Journal of Raman Spectroscopy*, vol. 40, no. 10, pp. 1434–1440, 2009.
- [24] Y. Saito, M. Kobayashi, D. Hiraga et al., "Z-polarization sensitive detection in micro-Raman spectroscopy by radially polarized incident light," *Journal of Raman Spectroscopy*, vol. 39, no. 11, pp. 1643–1648, 2008.
- [25] Y. Saito, M. Honda, Y. Moriguchi, and P. Verma, "Temporally dynamic photopolymerization of C60 molecules encapsulated in single-walled carbon nanotubes," *Physical Review B*, vol. 81, no. 24, Article ID 245416, 2010.
- [26] J. N. Farahani, H. J. Eisler, D. W. Pohl et al., "Bow-tie optical antenna probes for single-emitter scanning near-field optical microscopy," *Nanotechnology*, vol. 18, no. 12, Article ID 125506, 2007.
- [27] R. Ossikovski, Q. Nguyen, and G. Picardi, "Simple model for the polarization effects in tip-enhanced Raman spectroscopy," *Physical Review B*, vol. 75, no. 4, Article ID 045412, 2007.
- [28] P. Biagioni, J. S. Huang, L. Du o, M. Finazzi, and B. Hecht, "Cross resonant optical antenna," *Physical Review Letters*, vol. 102, no. 25, Article ID 256801, 2009.

Research Article

Water-Based Assembly and Purification of Plasmon-Coupled Gold Nanoparticle Dimers and Trimers

Sébastien Bidault^{1,2} and Albert Polman¹

¹ Center for Nanophotonics, FOM Institute AMOLF, Science Park 104, 1098 XG Amsterdam, The Netherlands

² Institut Langevin, ESPCI ParisTech, CNRS UMR 7587, INSERM U979, 10 Rue Vauquelin, 75005 Paris, France

Correspondence should be addressed to Sébastien Bidault, bidault@gmail.com

Received 18 October 2011; Accepted 22 November 2011

Academic Editor: Nicolas Bonod

Copyright © 2012 S. Bidault and A. Polman. This is an open access article distributed under the Creative Commons Attribution License, which permits unrestricted use, distribution, and reproduction in any medium, provided the original work is properly cited.

We describe a simple one-pot water-based scheme to produce gold nanoparticle groupings with short interparticle spacings. This approach combines a cross-linking molecule and a hydrophilic passivation layer to control the level of induced aggregation. Suspensions of dimers and trimers are readily obtained using a single electrophoretic purification step. The final interparticle spacings allow efficient coupling of the particle plasmon modes as verified in extinction spectroscopy.

1. Introduction

The reproducible synthesis of well-defined metal nanoparticle groupings has been the subject of intense research during the last few years [1–6], driven largely by their use as substrates for surface-enhanced Raman scattering (SERS) [7–10]. The electromagnetic field impinging on pairs of silver or gold particles separated by a few nanometers is enhanced in the gap region by several orders of magnitude [11], allowing for single-molecule sensitivity of the SERS signal [12, 13]. For a 1 nm gap, the SERS enhancement factor is larger than 10^8 for gold particles larger than 30 nm in diameter [7], becoming sufficient to achieve single-molecule SERS sensitivity.

Several approaches have been described using organic linkers [1–4, 6] or salt-induced aggregation [5, 9] to produce shortly spaced nanoparticle assemblies. In general, particle groupings with controlled geometries and valencies are obtained after several purification and reaction steps. Furthermore, in order to separate dimers and trimers from single particles and larger aggregates, the particles need to be sufficiently stable to sustain electrophoresis [2] or differential centrifugation [5]. Since the colloidal stability of metal nanoparticles decreases for larger diameters, it is difficult to combine efficient purification and large enough particles for SERS.

Electrophoresis was used successfully to purify symmetric or asymmetric gold nanoparticle (AuNP) dimers and trimers linked by DNA strands [2]. Using this technique, we recently demonstrated the controlled assembly of gold nanoparticles smaller than 20 nm with a 1 nm gap using a DNA template [7]. Using DNA as a linker offers a large flexibility since a single oligonucleotide can be grafted on the surface of one particle [14]. However, controlled DNA functionalization is difficult to adapt to particles larger than 20 nm in diameter because of the intrinsic limitations of electrophoresis [15]. In particular, for particles larger than 30 nm in diameter, the gold surface needs to be passivated before electrophoresis using ethylene glycol oligomers [16]. Furthermore, the DNA single strand grafted on the AuNP must be lengthened during the purification process by hybridizing it to several long strands in order to separate particles conjugated to one biomolecule [17]. Another solution to produce DNA templated groupings with large particles is to increase their size after DNA functionalization by growing a silver shell. This recently allowed single-molecule SERS measurements in a DNA linked particle dimer [10]. In all cases, DNA templated dimers and trimers are obtained after numerous reaction steps carried out over at least 24 hours.

Chen and coworkers recently demonstrated another separation technique of AuNP particle groupings using differential centrifugation [5]. It was used to obtain controlled

particle nanoassemblies aggregated by salt [5] or organic linkers [6]. However, this approach requires a hydrophobic polymer shell to passivate the particles. Not only does the passivation process require several reaction steps and an organic solvent, the hydrophobic shell also shields the AuNP surface from Raman active molecules. Dye molecules need to be grafted on the gold surface before the passivation and purification steps to obtain a SERS signal [18].

In this paper, we combine fast aggregation and hydrophilic passivation to obtain AuNP dimers and trimers in a water-based one-pot scheme that only requires several minutes. The aggregation process is driven by salt and a dithiol molecule, dithiothreitol (DTT), which provides short interparticle distances. The final hydrophilic ethylene glycol oligomer (PEG) shell allows the electrophoretic purification of particles as large as 35 nm in diameter. Furthermore, thiolated PEG ligands introduce a negligible background SERS signal on gold particles and are compatible with Raman active molecules [19, 20]. The combination of large particle diameters and small interparticle spacings yields efficient coupling of the particle plasmon modes as verified in extinction spectroscopy.

2. Experimental

2.1. Synthesis of Gold Nanoparticle Dimers. Citrate-coated 35 nm diameter gold particles were purchased from BBInternational (UK). Bis(p-sulfonatophenyl)phenylphosphine (BSPP) was obtained from Strem Chemicals Europe (France). Thiolated, methyl terminated ethylene glycol oligomers ($n = 6$) were purchased from Polypure (Norway). All other chemicals were obtained from Sigma-Aldrich (USA) and used without further purifications.

A stock solution of AuNPs coated with BSPP is prepared following published procedures [14, 16] and is kept for up to 6 months. In brief, 50 mL of citrate-coated particles are left to incubate overnight with 10 mg BSPP. Particles are then centrifuged to remove the supernatant before being rinsed and finally resuspended in a 0.5 mM BSPP solution. The final AuNP concentration is of the order of $0.02 \mu\text{M}$, and these particles are kept at 8°C . A typical dimer synthesis is performed using 20 fmol AuNPs in a 50 mM NaCl solution with a varying dithiothreitol (DTT) concentration (from 1 mM to 40 mM) and a $10 \mu\text{L}$ reaction volume. The incubation time varies between 1 s and 10 min before adding an excess (100 pmol) of thiolated, methyl-terminated ethylene glycol oligomer (mPEG), which stops the cross-linking effect of DTT by passivating the AuNPs.

The resulting suspensions of single particles and cross-linked groupings are loaded in 1.5% agarose gels (0.5x Tris-Borate-EDTA as running buffer) after adding one volume of ficoll loading buffer for four volumes of loaded sample. The gels are run at 8 V/cm for 30 mins. The extraction procedure is done following published protocols [7, 14], and the sample is concentrated by centrifugation if needed.

2.2. Scanning Electron Microscopy. $2 \mu\text{L}$ of dimer and trimer suspensions obtained after electrophoresis are deposited on freshly cleaned silicon substrates and left to dry before rinsing

the sample with 18 M Ω water and drying it with nitrogen. The samples are imaged using a field emission scanning electron microscope (FEI XL30) operating at 30 keV.

2.3. Optical Characterization. Extinction spectra of purified suspensions of dimers and trimers were measured using a dual-beam Genesys 10 S UV-visible spectrometer (Thermo Fisher Scientific) and compared to a reference 20 pM single-particle sample.

3. Results and Discussion

Dithiothreitol (DTT) was chosen as the cross-linking agent to obtain short interparticle spacings since it features only 5 covalent single bonds (less than 1 nm long). However, gold nanoparticles coated with a negatively charged phosphine shell (BSPP) and mixed with DTT do not aggregate without charge screening cations. NaCl is thus required in the reaction buffer to allow a successful interaction. To produce small groupings of particles and not large three-dimensional networks, the assembly process is stopped by adding a thiolated ethylene glycol oligomer (mPEG) that passivates the particle surface and increases the colloidal stability in high salt concentrations. This ligand exchange scheme was used previously to produce DNA functionalized AuNPs with high NaCl stability [15, 16]. Our proposed model underlying the fabrication process is summarized in Figure 1. If NaCl is necessary to drive the particle aggregation process, DTT is necessary to produce stable hydrophilic groupings. Indeed, if the particles are aggregated in salt without DTT, the mPEG surface passivation separates the aggregates back to single particles. Furthermore, if the mPEG excess is left to incubate with the DTT cross-linked particles for several hours, the aggregates are also separated back to single particles. The efficient displacement of the BSPP ligand shell by the mPEG excess can be observed in a Raman spectrum of the AuNPs before and after purification (data not shown): the BSPP SERS response [21] disappears after the ligand exchange process since the mPEG/DTT shell does not produce a measurable Raman signal.

We visualize the formation of particle dimers and trimers by purifying the reaction mix in electrophoresis. In this technique, separation is driven by size and surface charge differences of the different groupings. Electrophoresis also removes unbound ligands and excess salt. We tuned two experimental parameters to optimize the dimer formation: the DTT concentration and the incubation time before adding the mPEG ligand. Figure 2(a) shows the effect of increasing the DTT concentration with a 1 s incubation time in a 50 mM NaCl solution. The left lane (lane 1) corresponds to a reference mPEG passivated 35 nm AuNP sample. Lanes 2 to 4 correspond to DTT concentrations of 1 mM, 10 mM, and 40 mM respectively. New bands are clearly visible in lanes 3 and 4 and correspond to the formation of cross-linked groupings. These bands are also visible using a 1 mM DTT concentration when the incubation time is increased (still with 50 mM NaCl) as seen in Figure 2(b) with 1 s, 1 min, 2 min, 5 min, and 10 min incubation times. DTT-driven cross-linking is compatible with smaller particles

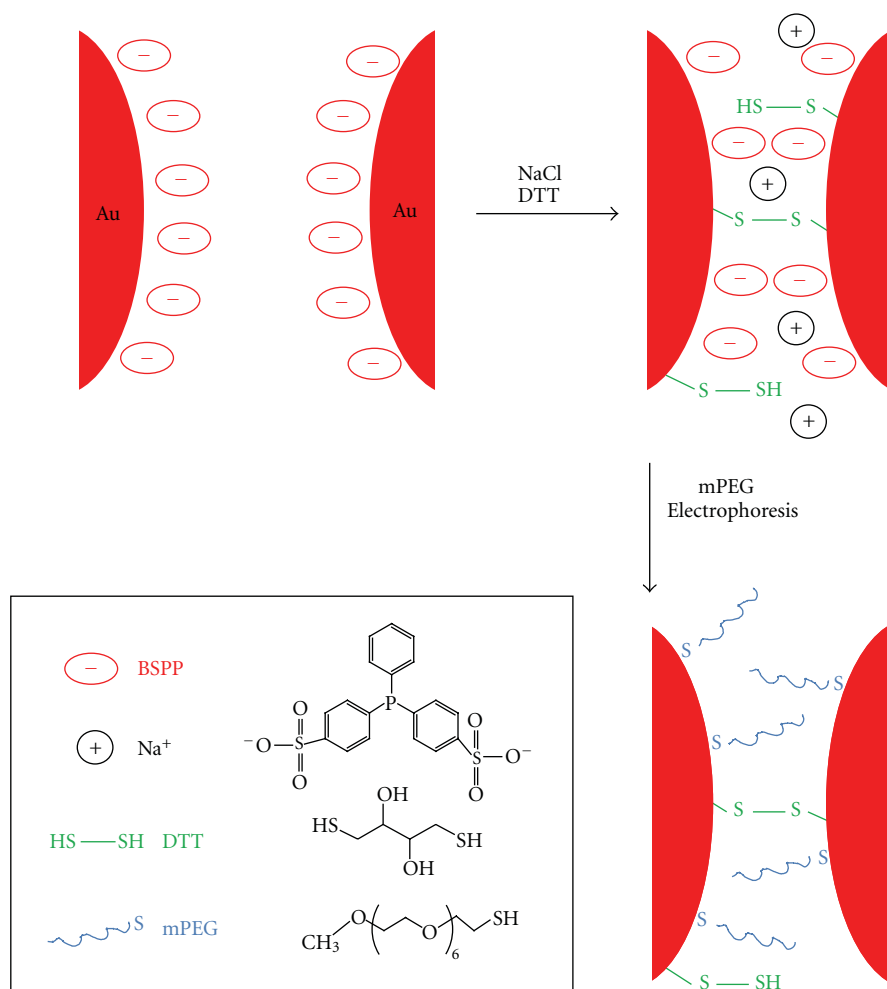


FIGURE 1: Cross-linking scheme. The single linking DTT molecule is only a schematic representation as several molecules can be involved in the dimer formation. The mPEG excess displaces DTT molecules from the gold surface and can thus break interparticle bonds.

by increasing the ionic strength during the aggregation process and adapting the density of agarose gels during electrophoretic purification (100 mM NaCl and 2% agarose gels for 18 nm diameter AuNPs). Controlled cross-linking of larger gold particles can probably be performed with similar experimental conditions but PEG-stabilized AuNPs larger than 60 nm do not provide well-defined bands in agarose gel electrophoresis. A different purification process would be necessary.

The first, second, and third fastest bands are recovered from the gel and studied using scanning electron microscopy (SEM). The fastest band, also found on reference samples, only exhibits single particles. The second and third bands correspond preferentially to dimers and trimers as shown in Figures 3(a) and 3(b). The sample purity is estimated by counting the number of particles involved in specific grouping geometries. For the second band, 77% of the AuNPs are observed in dimers and 23% as single particles. For the third band, 52% of the particles form trimers. The rest of the particles are found as dimers (30%), single particles (12%), or larger aggregates (6%). Since the dimer

and trimer suspensions are dried on a silicon substrate for the SEM analysis, the interparticle distances observed in electron microscopy can be modified by drying effects. Cryoelectron microscopy would be necessary to observe the particle groupings as they are in suspension [17]. However, the sample purities observed in cryoelectron microscopy and dry SEM are similar, indicating that, at low grouping concentrations, drying effects do not modify significantly the distribution of grouping geometries.

To verify that the short cross-linker allows efficient plasmon coupling necessary for high field enhancements, we measure the extinction spectra of the dimer and trimer suspensions compared to a single-particle sample (all measured in the electrophoresis buffer that does not contain NaCl). These extinction spectra are normalized outside of the plasmon resonance frequency (450 nm) as shown in Figure 4 to correct for the unknown particle concentration in the dimer and trimer samples. The single-particle sample exhibits a typical dipolar plasmon resonance at 525 nm. The dimer and trimer samples exhibit an additional strongly red-shifted side-band that peaks at 630 nm. This band

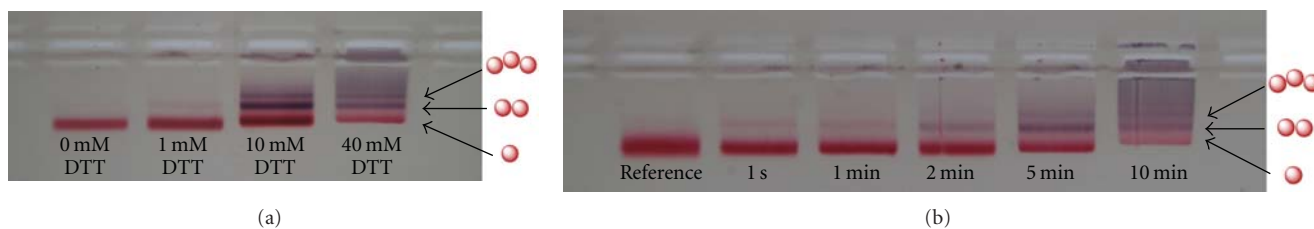


FIGURE 2: Agarose gels after electrophoretic purification of reaction mixes. (a) 1 s incubation time with a 50 mM NaCl and varying DTT concentrations: 0 mM (lane 1), 1 mM (lane 2), 10 mM (lane 3), and 40 mM (lane 4). (b) 50 mM NaCl and 1 mM DTT with different incubation times: reference single particles (lane 1), 1 s (lane 2), 1 min (lane 3), 2 min (lane 4), 5 min (lane 5), and 10 min (lane 6).

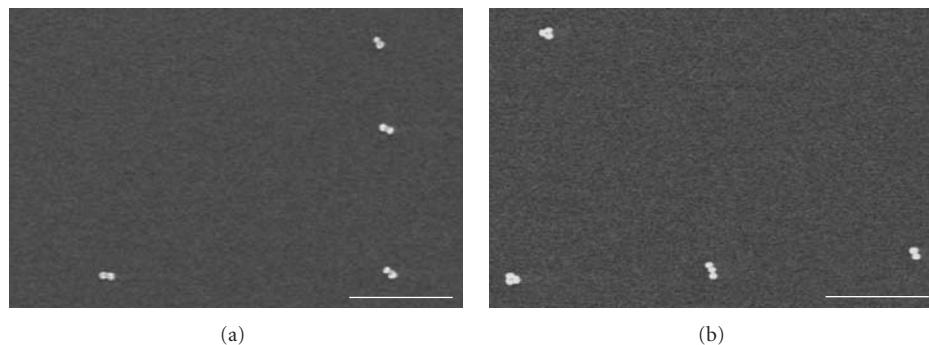


FIGURE 3: SEM images of dimer (a) and trimer (b) samples deposited on silicon substrates (30 keV electrons, scale bar = 500 nm).

corresponds to the longitudinally coupled dipole mode [22, 23]. According to the generalized Mie theory, a 630 nm longitudinal plasmon resonance for a 35 nm diameter AuNP dimer in a homogeneous dielectric environment with index 1.4 (intermediate between water and the organic ligand shell [17]) corresponds to an interparticle distance between 1 and 1.5 nm. This distance is consistent with the length of DTT when considering that electrostatic interactions can stretch the groupings in buffers with low ionic strengths [17]. The 630 nm resonance induces a strong color change in the particle suspension as is clearly visible in Figures 2(a) and 2(b): while the reference single-particle sample is red (lane 1), the slower bands corresponding to the larger AuNP groupings appear purple due to absorption and scattering of both green and red light.

The relative strength of the resonances at 525 nm and 630 nm decreases for trimers as they exhibit several longitudinally coupled modes with different phase relations [24]. Furthermore, these resonances are inhomogeneously broadened in the trimer sample since the angle between the particles varies from one grouping to the other (see Figure 3(b)). Similar results were observed in suspensions of 15 nm diameter AuNP clusters stabilized in block copolymer shells without a cross-linking agent [5]. Overall, these measurements demonstrate that the DTT assembled dimer and trimer suspensions exhibit efficient plasmon coupling and should provide large local field enhancements.

4. Conclusion

We have demonstrated that a cross-linking agent, several surface ligand exchange steps, and electrophoresis can be

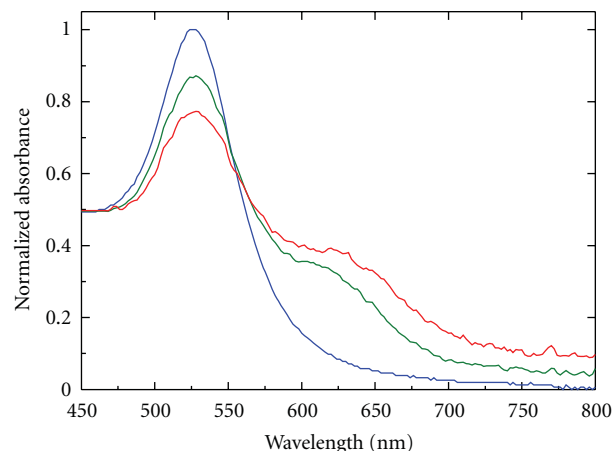


FIGURE 4: Normalized extinction spectra of mPEG stabilized single particles (blue solid line) and electrophoretically purified dimer (green solid line) and trimer (red solid line) suspensions.

used to produce high-purity suspensions of gold particle dimers and trimers with diameters as large as 35 nm and short interparticle spacings. The overall reaction process only takes a few minutes and the suspensions are obtained with a single purification step. Ensemble extinction measurements demonstrate efficient plasmon coupling in the cross-linked groupings which corresponds to high local field enhancements. By chemically modifying the cross-linking agent to exhibit a molecule with a high Raman cross-section or the binding site of a chosen analyte, it will be possible to produce

fast and sensitive SERS-based chemical sensors based on this assembly scheme.

Acknowledgments

Work at AMOLF is part of the research program of FOM which is financially supported by NWO and was also supported by NanoNed, a nanotechnology program of the Dutch Ministry of Economic Affairs.

References

- [1] A. P. Alivisatos, K. P. Johnsson, X. Peng et al., "Organization of 'nanocrystal molecules' using DNA," *Nature*, vol. 382, no. 6592, pp. 609–611, 1996.
- [2] D. Zanchet, C. M. Micheel, W. J. Parak, D. Gerion, S. C. Williams, and A. P. Alivisatos, "Electrophoretic and structural studies of DNA-directed Au nanoparticle groupings," *Journal of Physical Chemistry B*, vol. 106, no. 45, pp. 11758–11763, 2002.
- [3] R. Sardar, T. B. Heap, and J. S. Shumaker-Parry, "Versatile solid phase synthesis of gold nanoparticle dimers using an asymmetric functionalization approach," *Journal of the American Chemical Society*, vol. 129, no. 17, pp. 5356–5357, 2007.
- [4] M. M. Maye, D. Nykypanchuk, M. Cuisinier, D. Van Der Lelie, and O. Gang, "Stepwise surface encoding for high-throughput assembly of nanoclusters," *Nature Materials*, vol. 8, no. 5, pp. 388–391, 2009.
- [5] G. Chen, Y. Wang, L. H. Tan et al., "High-purity separation of gold nanoparticle dimers and trimers," *Journal of the American Chemical Society*, vol. 131, no. 12, pp. 4218–4219, 2009.
- [6] Y. Wang, G. Chen, M. X. Yang et al., "A systems approach towards the stoichiometry-controlled hetero-assembly of nanoparticles," *Nature Communications*, vol. 1, p. 87, 2010.
- [7] S. Bidault, F. J. García De Abajo, and A. Polman, "Plasmon-based nanolenses assembled on a well-defined DNA template," *Journal of the American Chemical Society*, vol. 130, no. 9, pp. 2750–2751, 2008.
- [8] J. Kneipp, X. Li, M. Sherwood et al., "Gold nanolenses generated by laser ablation-efficient enhancing structure for surface enhanced Raman scattering analytics and sensing," *Analytical Chemistry*, vol. 80, no. 11, pp. 4247–4251, 2008.
- [9] W. Li, P. H. C. Camargo, X. Lu, and Y. Xia, "Dimers of silver nanospheres: facile synthesis and their use as hot spots for surface-enhanced raman scattering," *Nano Letters*, vol. 9, no. 1, pp. 485–490, 2009.
- [10] D. K. Lim, K. S. Jeon, H. M. Kim, J. M. Nam, and Y. D. Suh, "Nanogap-engineerable Raman-active nanodumbbells for single-molecule detection," *Nature Materials*, vol. 9, pp. 60–67, 2010.
- [11] H. Xu, J. Aizpurua, M. Käll, and P. Apell, "Electromagnetic contributions to single-molecule sensitivity in surface-enhanced Raman scattering," *Physical Review E*, vol. 62, no. 3, pp. 4318–4324, 2000.
- [12] K. Kneipp, Y. Wang, H. Kneipp et al., "Single molecule detection using surface-enhanced Raman scattering (SERS)," *Physical Review Letters*, vol. 78, no. 9, pp. 1667–1670, 1997.
- [13] S. Nie and S. R. Emory, "Probing single molecules and single nanoparticles by surface-enhanced Raman scattering," *Science*, vol. 275, no. 5303, pp. 1102–1106, 1997.
- [14] D. Zanchet, C. M. Micheel, W. J. Parak, D. Gerion, and A. P. Alivisatos, "Electrophoretic isolation of discrete au nanocrystal/DNA conjugates," *Nano Letters*, vol. 1, no. 1, pp. 32–35, 2001.
- [15] S. A. Claridge, H. W. Liang, S. R. Basu, J. M. J. Fréchet, and A. P. Alivisatos, "Isolation of discrete nanoparticle–DNA conjugates for plasmonic applications," *Nano Letters*, vol. 8, no. 4, pp. 1202–1206, 2008.
- [16] B. M. Reinhard, S. Sheikholeslami, A. Mastroianni, A. P. Alivisatos, and J. Liphardt, "Use of plasmon coupling to reveal the dynamics of DNA bending and cleavage by single EcoRV restriction enzymes," *Proceedings of the National Academy of Sciences of the United States of America*, vol. 104, no. 8, pp. 2667–2672, 2007.
- [17] M. P. Busson, B. Rolly, B. Stout et al., "Optical and topological characterization of gold nanoparticle dimers linked by a single DNA double-strand," *Nano Letters*, vol. 11, pp. 5060–5065, 2011.
- [18] G. Chen, Y. Wang, M. Yang et al., "Measuring ensemble-averaged surface-enhanced Raman scattering in the hotspots of colloidal nanoparticle dimers and trimers," *Journal of the American Chemical Society*, vol. 132, no. 11, pp. 3644–3645, 2010.
- [19] X. M. Qian, X. H. Peng, D. O. Ansari et al., "In vivo tumor targeting and spectroscopic detection with surface-enhanced Raman nanoparticle tags," *Nature Biotechnology*, vol. 26, pp. 83–90, 2008.
- [20] S. C. Boca and S. Astilean, "Detoxification of gold nanorods by conjugation with thiolated poly(ethylene glycol) and their assessment as SERS-active carriers of Raman tags," *Nanotechnology*, vol. 21, no. 23, Article ID 235601, 2010.
- [21] M. L. Sauthier, R. Lloyd Carroll, C. B. Gorman, and S. Franzen, "Nanoparticle layers assembled through DNA hybridization: characterization and optimization," *Langmuir*, vol. 18, no. 5, pp. 1825–1830, 2002.
- [22] W. Rechberger, A. Hohenau, A. Leitner, J. R. Krenn, B. Lamprecht, and F. R. Aussenegg, "Optical properties of two interacting gold nanoparticles," *Optics Communications*, vol. 220, no. 1–3, pp. 137–141, 2003.
- [23] K. H. Su, Q. H. Wei, X. Zhang, J. J. Mock, D. R. Smith, and S. Schultz, "Interparticle coupling effects on plasmon resonances of nanogold particles," *Nano Letters*, vol. 3, no. 8, pp. 1087–1090, 2003.
- [24] A. Devilez, B. Stout, and N. Bonod, "Mode-balancing far-field control of light localization in nanoantennas," *Physical Review B*, vol. 81, no. 24, Article ID 245128, 2010.

Research Article

Plasmonic-Resonant Bowtie Antenna for Carbon Nanotube Photodetectors

Hongzhi Chen,¹ Ning Xi,¹ King Wai Chiu Lai,¹ Liangliang Chen,¹
Carmen Kar Man Fung,¹ and Jianyong Lou²

¹Department of Electrical and Computer, Engineering, Michigan State University, East Lansing, MI 48824, USA

²State Key Laboratory of Electrical Insulation and Power Equipment, Xi'an Jiaotong University, Xi'an 710049, China

Correspondence should be addressed to Hongzhi Chen, chenhon5@msu.edu

Received 12 September 2011; Accepted 17 November 2011

Academic Editor: A. Femius Koenderink

Copyright © 2012 Hongzhi Chen et al. This is an open access article distributed under the Creative Commons Attribution License, which permits unrestricted use, distribution, and reproduction in any medium, provided the original work is properly cited.

The design of bowtie antennas for carbon nanotube (CNT) photodetectors has been investigated. CNT photodetectors have shown outstanding performance by using CNT as sensing element. However, detection wavelength is much larger than the diameter of the CNT, resulting in small fill factor. Bowtie antenna can confine light into a subwavelength volume based on plasmonic resonance, thus integrating a bowtie antenna to CNT photodetectors can highly improve photoresponse of the detectors. The electric field enhancement of bowtie antennas was calculated using the device geometry by considering fabrication difficulties and photodetector structure. It is shown that the electric field intensity enhancement increased exponentially with distance reduction between the CNT photodetector to the antenna. A redshift of the peak resonance wavelength is predicted due to the increase of tip angles of the bowtie antennas. Experimental results showed that photocurrent enhancement agreed well with theoretical calculations. Bowtie antennas may find wide applications in nanoscale photonic sensors.

1. Introduction

With the development of nanotechnologies, one-dimensional (1D) materials, including nanowires and nanotubes, emerged as important components in photonics and optoelectronics [1]. Compared to bulk materials, 1D materials possess a number of unique properties arose from their geometries, making them potential candidates to outperform traditional optical devices. In particular, carbon nanotubes (CNTs) are of great interest for exploring as functional elements for 1D photodetectors due to their perfect nanohollow cylinder structure [2, 3]. However, a critical challenge for obtaining high-performance 1D photodetectors is the dimension incompatibility between photodetectors and optical wavelengths. The radial sizes of CNTs are much smaller than detection wavelengths, resulting in low fill factor and responsivity. Motivated by this challenge, optical antennas were designed to integrate with CNT photodetectors so as to bridge the gap between nanosize sensing elements and microsize wavelengths. Due to plasmonic resonance, optical antennas can confine strong optical near fields in a volume

far below a cubic wavelength of excitation light. This can greatly enhance photon absorption owing to the increase of coupling between CNT and vibrating electrical fields of photons. By integrating CNT photodetectors with optical antennas, the nanoscale photodetectors can be made with outstanding performance and photon absorption efficiency.

There are two main categories of photodetectors: thermal detectors and photonic detectors. Both thermal detectors and photonic detectors have their limitations: thermal detectors have slow response and low detectivity, while traditional photon detectors can only detect a narrow spectrum, which is limited by their bandgap energies. Some of the photon detectors need to operate with cryogenic cooling system, particularly middle-wave infrared (IR) or longer wavelength detectors. Photodetectors using nanomaterials as core materials were proposed to overcome these problems, since nanomaterials, especially CNTs, have a number of exceptional optoelectronic properties [4]. CNT-based photodetectors were extensively investigated. Multiexciton was observed in a CNT photodetector, showing the potential of making photodetectors with higher responsivity [5]. A photovoltaic

CNT detector was reported to detect middle-wave IR at room temperature [6]. A spectral tunable CNT photodetector could modulate its detection spectrum by electrically tailoring the diameters of CNTs [7], because the bandgap energies of the 1D materials are inversely proportional to their diameters [8]. All these promising properties stem from the 1D quantum confined geometry of CNTs, which, nevertheless, cause low fill factor and absorption. In order to fully employ the exceptional advantages of the CNTs in photosensors, the problem of low absorption needs to be addressed, and optical antennas are promising in solving this issue.

In our design, the optical antenna performs as a plasmonic lens that funnels light into the CNT photodetector. This is analogous to the microlenses on top of conventional charge coupled device (CCD) array to increase detector fill factor [9, 10]. If the CNT photodetector occupied the same area as the antenna/CNT photodetector, they have same fill factor. However, technical difficulties prevent the assembling of a large array of uniform CNTs. Assembling a CNT thin film has been demonstrated, but the interaction between CNTs in thin film resulted in the loss of their unique optical properties. Therefore, one single CNT is more favorable and easier to manipulate in order to fabricate high-performance photodetectors. But the challenge of one individual CNT as the core material for photodetectors is the small diameter of CNT. The optical antenna can strongly concentrate light into subwavelength volume that couples to the CNT in order to improve fill factor.

Optical antennas have invoked considerable interests, because of their ability to generate large and localized electromagnetic fields. The basic principle of optical antennas is based on the resonant behavior between excitation light and metal structure. When light interacts with optical antennas that have proper dimensions, surface plasmons are generated due to resonant coupling between the electromagnetic surface waves and oscillations of free electrons in the metal. Light irradiating on the optical antenna at frequencies below the resonant frequency is reflected, since it induces motion in the charge carriers that act to screen out the incident field; when the frequency of light is above the resonant frequency, light is transmitted because the charges are unable to respond quickly enough to screen out the incident field [11]; only at the resonant frequency, light is resonant coupling to free charges of metals, and the incident waves will be absorbed and reradiated. By properly orienting the reradiated waves, intensely localized near-fields can be generated. Confining or localizing light into a small volume has found plenty of applications in many research fields, including spectroscopy, microscopy, lithography, biosensing, chemical studies, and so on [12, 13]. In recent years, optical antennas used to improve the performance of planar photovoltaic devices became a hot field [14]. However, very little research was conducted to improve the performance of 1D photodetectors using optical antenna, although 1D materials become an emerging platform in photovoltaic devices [15].

There are a variety of novel shaped optical antennas, such as nanosphere, nanorod and nanotriangle monomers, nanosphere dimmers, dipole antennas, bowtie antennas,

Yagi-Uda antennas, cross-antennas, and so on [13]. Among all these optical antennas, dipole and bowtie antennas are particularly suitable for integrating with 1D photodetectors because of their geometries. Dipole antennas are nanorod dimmers, while bowtie antennas are nanotriangle dimmers, therefore, both dipole and bowtie antennas can be considered as two opposing tip-to-tip nanotriangles (nonzero apex width) with tip angles ranging from 0° (dipole antennas) to wider angles. The coupling between two pieces of metals in these antennas concentrates the incident light into a nanoscale gap, which locates above a CNT photodetector in order to enhance the interaction between the localized near-fields and CNTs.

There were a number of approaches to improve a photodetector's performance using plasmonic resonance: photocurrent enhancement was demonstrated in an Si photodiode via the excitation of plasmon resonances in spherical Au nanoparticles deposited on the Si surface [16]; a middle-wave IR photodetector, comprised of a metallic grating filled with HgCdTe, was proposed to improve the signal-to-noise ratio by plasmonic resonance [17]; an optical antenna was utilized as a metal electrode for a Si Schottky diode to boost photo-detection [18]. Optical antennas were embedded in these photodetectors, acting as part of the photodetectors. In our design, the bowtie antenna performs as a plasmonic lens, which can be easily integrated into all types of high performance 1D photodetectors [3, 19–22]. In particular, the bowtie antenna perfectly matches with the CNT photodetector due to the compatibility of the diameter of CNT and gap distance of the bowtie antenna, because the electric field (*E*-field) enhancement exponentially increases with decreasing gap distance [23].

The properties of free-standing optical bowtie antennas have been studied extensively [23, 24], and our group has demonstrated that dipole antenna can boost photoresponse of 1D IR detectors [25]. However, the design of bowtie antennas for 1D photodetectors was not systematically studied. In this paper, we will present the design of bowtie antennas that can be integrated with CNT photodetectors to highly improve the detection of IR signal with wavelength of 830 nm. *E*-field enhancement with bowtie antennas was calculated to seek the optimized tip angle and insulator thickness. Experimental results showed that the photocurrent enhancement was 12.67 times by adding a bowtie antenna with precise alignment and dimension control in fabrication. Calculation of relative energy difference on the CNT photodetector at absence and presence of the bowtie antenna quantitatively explained the photocurrent enhancement.

2. Design of Optical Antennas

Before the discussion of antenna design, an introduction of CNT photodetectors will be provided. The basic structure of a CNT photodetector is sketched in Figure 1(a), comprised of a single CNT connecting to two electrodes with high/low workfunctions (Ti and Au); the band diagram of the device is shown in Figure 1(b). On the left contact between Ti and CNT, Ti has a workfunction that is smaller than that of the CNT and forms a Schottky barrier; on the right contact,

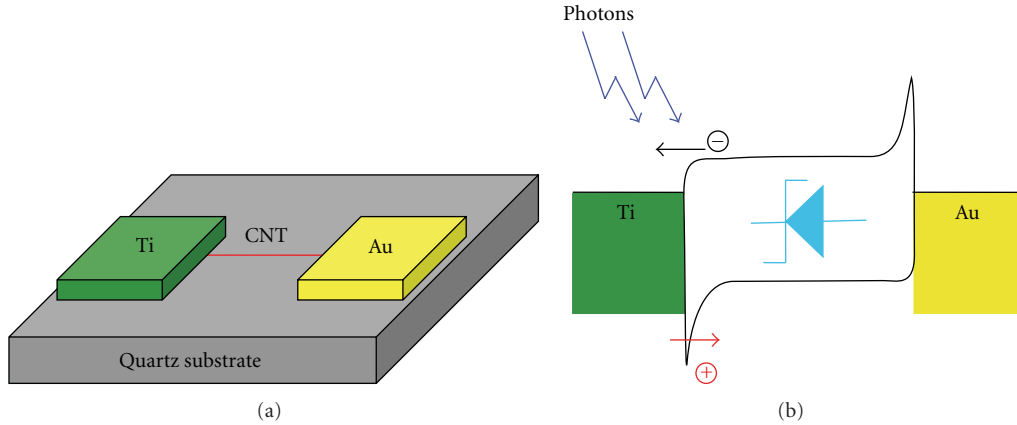


FIGURE 1: (a) The basic structure of a CNT photodetector, consisting of a CNT connecting to Ti and Au electrodes on top of a quartz substrate. (b) The band diagram of the CNT photodetector.

Au has a workfunction that is higher than (or similar with) that of the CNT and forms an ohmic contact (or quasi-ohmic contact) [22]. When the photons with energy higher than the CNT bandgap strike the CNT, electron and hole pairs will be generated, and be separated by the built-in potential of the Schottky barrier. We have demonstrated that CNT photodetectors exhibited outstanding performance to detect IR signals, and the sensitivity of photodetectors with asymmetric metal structure was much better than the ones with symmetric metal structures [22]. One thing should be noted is that the depletion region of the CNT photodetector may extend into the whole tube of the CNT, since the charge distribution of the 1D systems has a long-range tail [26], extending over the entire CNT [27]. In other words, the entire CNT can be considered as depletion region. Therefore, the optical antennas cannot only be located on the contacts, but they also can be placed on top of the CNT body.

The bowtie antenna consists of two tip-to-tip nanotriangles that can confine strong electromagnetic field between two triangles at resonance frequency. Light illuminating on the bowtie antennas will generate instantaneous current, which oscillates at the frequency along the polarization of the incident light. The instantaneous current is maximum near the center of the nanotriangle, and decreases toward the edges of the antenna. This leads to a high density of surface charge at the tip of the nanotriangles. Displacement current flows into the small air gap of the bowtie antennas, reradiating the absorbed energy. The strong coupling of these two opposing tip-to-tip triangles brings the center of the reradiating source to the center of the gap [28]. The maximum intensity enhancement can be obtained at resonance frequency, which is mainly determined by the dimension and materials of antennas.

The relative position of the CNT photodetector and bowtie antenna is shown in Figure 2. A thin insulator (Si_3N_4) is sandwiched between the bowtie antenna and the photodetector (Figure 2(c)), with the gap of bowtie antenna aligning to the center of CNT channel. The geometrical parameters are also denoted in Figure 2: where d is the gap distance, w is the apex width, L is the length of the bowtie

antenna, θ is the tip angle, and t is the thickness of the insulator between antenna and CNT.

This CNT photodetector is designed for detecting IR signal at 830 nm, thus the bowtie antenna should resonate at or close to this wavelength. Resonance wavelength is very sensitive to the dimensions of bowtie antennas, but several parameters are fixed in simulation considering the fabrication constraints, and some parameters have been extensively studied [28, 29]: the gap distance d is set to be 30 nm for easier alignment of the bowtie antenna to the photodetector; apex width is 30 nm to leave some tolerance for electron beam lithography (EBL); antenna length L is 400 nm because it is close to half-wavelength of the IR signal; the bowtie antenna is made of 3 nm Ti and 20 nm Au. The width of both Au and Ti electrodes is 400 nm, and the gap between two electrodes is 1000 nm. The following simulation was based on the geometry including both electrodes and bowtie antennas, as shown in Figure 2.

The E -field enhancement spectra of bowtie antennas will be simulated with varying insulator thickness t and tip angle θ , not only since these two parameters can be easily tuned in real device fabrication, but they also have significant impacts to the E -field intensity enhancement.

Figure 2(a) also shows the direction of incident light polarization and the coordinate system for all numerical simulations using ANSYS HFSS: a plane wave is normally incident on the structure from the top with the electric field being polarized along the x axis, which is parallel to the axis between two triangles, with electric field component amplitudes of $E_x = 1 \text{ V/m}$, $E_y = E_z = 0$.

2.1. Insulator-Thickness-Dependent E -Field Enhancement.

The plasmonic resonance of the bowtie antennas was first investigated by varying the insulator thickness t between the antenna to the CNT photodetector. This is a critical parameter, since the photodetector needs to be placed in close proximity to the optical antennas in order to fully take advantage of near fields [30]. The insulator-thickness-dependent E -field distribution at the substrate plane (the plane between Si_3N_4 and quartz substrate), where CNT

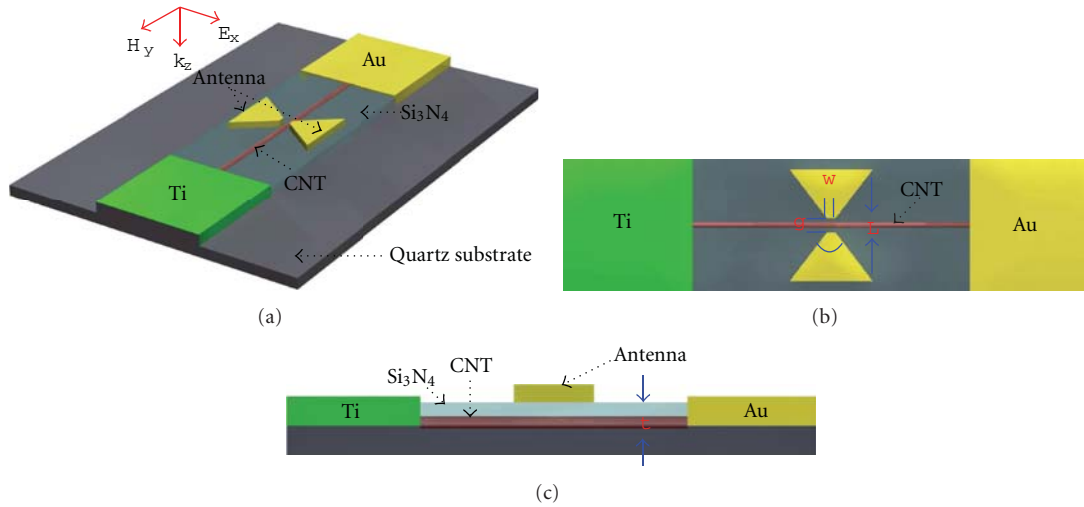


FIGURE 2: (a) A 3D geometry shows the relative position between the CNT photodetector and the bowtie antenna. The incident light with electric field polarized in the x direction propagates in the z direction. (b) Top view of the device, and parameters of the bowtie antenna: $L = 400$ nm is the length of the antenna, $g = 30$ nm is the gap of two pieces of the antenna, $w = 30$ nm is the apex width, and θ is the tip angle. (c) Side view of the device, showing the CNT photodetector and bowtie antenna sandwiching the Si₃N₄ layer that has a thickness of t .

located, was calculated based on equilateral Au triangles ($\theta = 60^\circ$) with $d = 30$ nm, $w = 30$ nm, $L = 400$ nm. The CNT photodetector and optical antenna are on the top of a quartz substrate, with a plane-wave light polarized in the x direction normally illuminating the device from the top.

The resonance wavelength for this antenna is at 845 nm with $t = 10$ nm. Figure 3(a) shows the E -field distribution between two electrodes at the substrate plane for the device with $t = 10$ nm at its resonance wavelength. The E -field is confined into the gap of the bowtie antenna with the maximum amplitude located at the center of the gap due to the strong coupling between two nanotriangles. The E -field distribution is in the shape of a horizontal bowtie, and the amplitude of the E -field decreases as the distance to the center of the gap increases in the horizontal direction. The illuminating light had $E = 1$ V/m, while the peak amplitude at substrate plane became $E = 14.608$ V/m at resonance after adding the bowtie antenna, with an enhancement of 14.608 fold.

The peak E -field intensity enhancement $\max(|E|^2)$ as a function of insulator thickness at resonance wavelength was shown in Figure 3(b). The E -field distributions with thickness of Si₃N₄ ranging from 10 nm to 50 nm were investigated. The blue curve shows the peak intensity enhancement at the substrate plane: the enhancement decreased from 213.1 to 26.7 when the thickness of the Si₃N₄ increased from 10 nm to 50 nm. The red curve in Figure 3(b) is the exponential fit of the data, which matches very well with the blue curve. The resonance wavelength of the antenna redshifted from 845 nm to 1034 nm with the thickness increasing of Si₃N₄ layer from $t = 10$ nm to $t = 50$ nm [31]. The inset of Figure 3(b) shows that the E -field enhancement at wavelength of 830 nm, which corresponds to the wavelength of our laser source, decreases dramatically by increasing the insulator thickness. The simulation results indicate that

the field intensity enhancement decreases significantly with the increasing thickness of the insulator, because evanescent waves decay exponentially from the antenna. Therefore, in order to fully use the power of the antenna, the photodetector needs to be fabricated close to the bowtie antenna.

2.2. Tip-Angle-Dependent E -Field Enhancement Spectra. Not only is the tip angle of the bowtie antennas easily modified in real device fabrication, but it also has critical impact on both resonance wavelength and E -field intensity enhancement. The E -field spectra as a function of the tip angle were calculated with $d = 30$ nm, $w = 30$ nm, $L = 400$ nm, and $t = 10$ nm. Figure 4 shows the E -field spectra of bowtie antenna with tip angles of 0 degrees (dipole antenna), 30 degrees, 60 degrees, 90 degrees, and 120 degrees.

The spectra vary significantly with different tip angles. It is shown that bowtie antennas cover wider spectrum with larger tip angles. Bowtie antennas can be considered as a two-dimensional analogue of biconical antenna, therefore, wider tip angles are expected to possess broader bandwidth. The bowtie antenna with tip angle of 120 degrees shows field intensity enhancement in a broadest spectrum. What is more, two resonance wavelengths was found with a fundamental resonance wavelength at $1.13 \mu\text{m}$ and a high-order resonance at $0.77 \mu\text{m}$. High-order resonance is easier to be excited for large angle Bowtie antennas, since larger angle bowtie antennas are prone to overcome the symmetry limitation of octupolar resonance, while octupolar resonance is forbidden in the 0 degree bowtie antenna under normal incidence [32].

The peak E -field intensity enhancement increases with wider tip angles when the tip angle is smaller than 60 degrees, while it reduces when the tip angle is larger than 90 degrees. In addition, the resonance wavelengths, where the peak intensity enhancements are obtained, redshift with

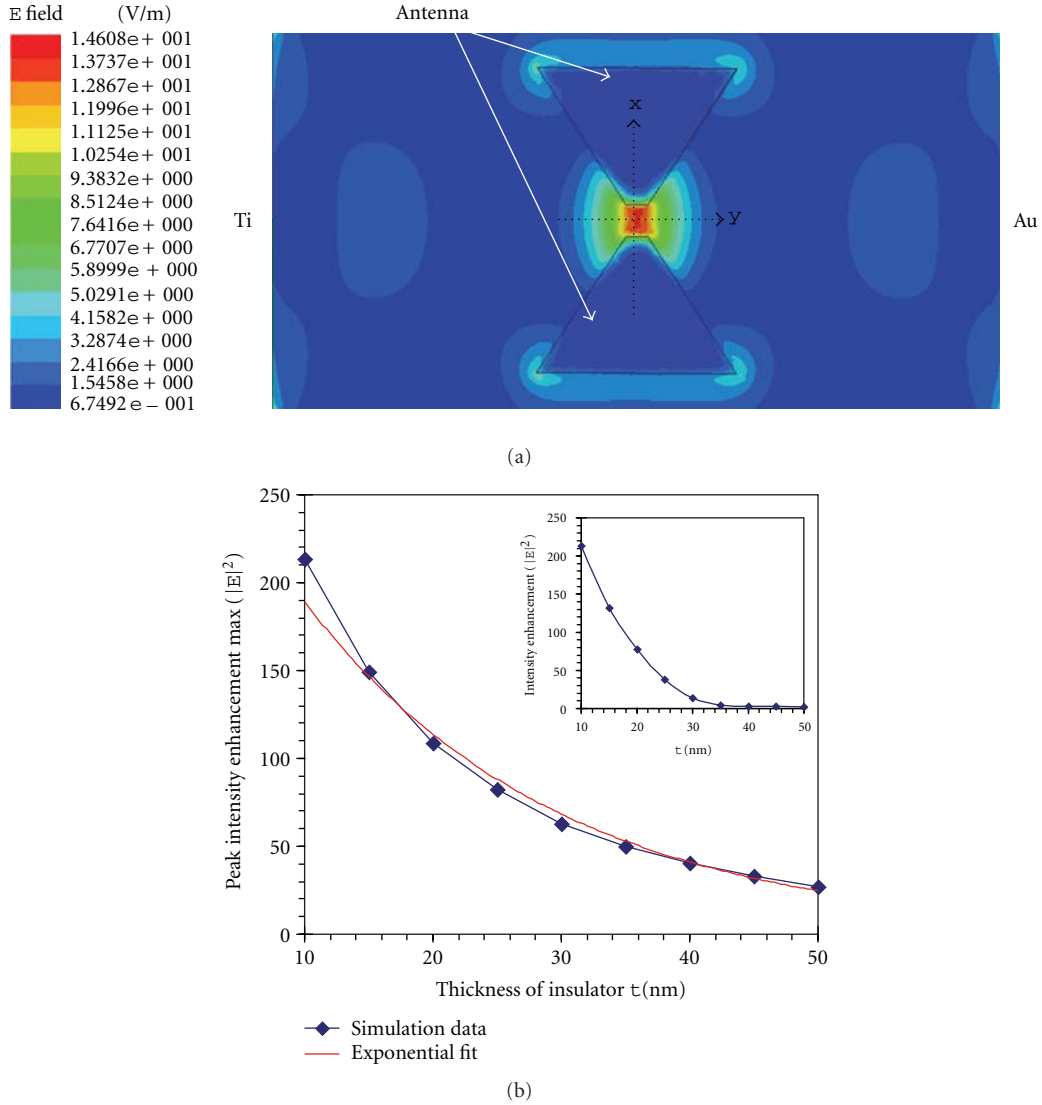


FIGURE 3: (a) The E -field distribution of the resonance frequency (845 nm) of the bowtie antenna with $\theta = 60^\circ$, and $t = 10$ nm. The $x - y$ axis show the coordinate for simulation. (b) The t dependent peak field intensity max ($|E|^2$), blue curve is the simulation values, and red curve is the exponential fit. The inset shows field intensity enhancement $|E|^2$ at wavelength of 830 nm.

increasing tip angles. Resonance wavelength is proportional to the length of the triangle edges of bowtie antennas, and thus resonance wavelength redshifts as tip angle increases [33]. This can be explained as follows: the two opposite Au/air interfaces in one cross-section vertical to the antenna axis are far away from each other in the y direction, thus the local surface plasmon polariton is confined at one Au/air interface and not affected by the opposite one, especially when the cross-section is close to the extremity edges. As a result, the bowtie antennas are dominated by isolated surface plasmon polaritons that propagate along the triangle edges; consequently, a standing wave along the triangle edges is generated, with resonance wavelength scales with the length of the triangle edges, therefore, redshifts as the tip angle increases [32]. The length of triangle edges of the bowties

increases from 185 nm to 272 nm when the tip angle is widened from 0 degrees to 90 degrees, with an increment of only 87 nm. As a result, the cross-section along y axis from the tip to extremity edges changes gradually, and thus resonance wavelength differs slightly. The length of triangle edge increases to 383 nm when the tip angle becomes 120 degrees. This major length change causes a rapid change of local cross-section, resulting in a big shift of the resonance wavelength.

The simulation results show that larger angle bowtie antennas can cover broader spectrum together with multiple resonances, which are suitable for photodetectors with wide-spectrum detection. In our experiment, we were detecting IR signals with single wavelength of 830 nm. Bowtie antennas with a 60-degree tip angle were fabricated to verify the field

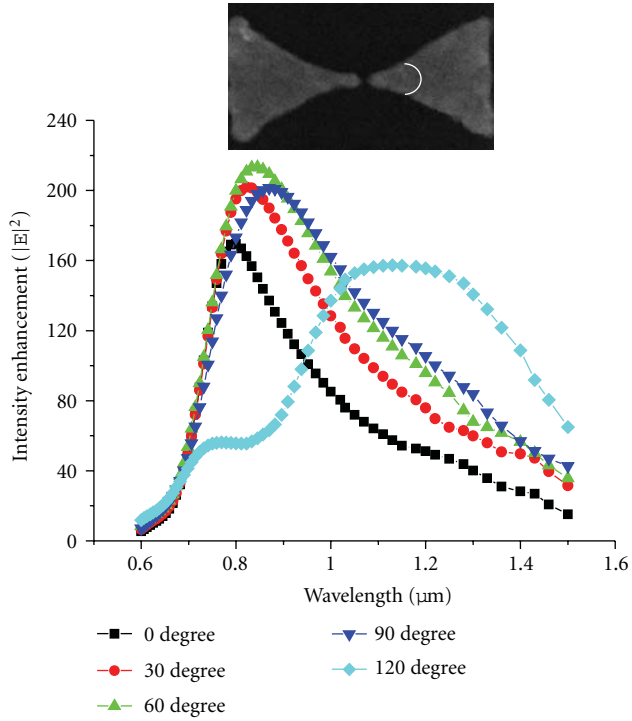


FIGURE 4: E -field intensity enhancement $|E|^2$ spectra of bowtie antennas with tip angles ranging from 0 degrees to 120 degrees. The inset shows a scanning electron microscopy (SEM) image of a bowtie antenna, denoting the tip angle.

intensity enhancement of the antennas, since the highest peak field intensity enhancement is obtained at this tip angle, and whose resonance wavelength is close to 830 nm.

3. Fabrication and Experimental Results

In order to investigate the performance of bowtie antennas, Au bowties were fabricated on top of a CNT photodetector as depicted in Figure 2(a). Photocurrent of CNT photodetector with absence and presence of bowtie antennas was compared so as to examine the field intensity enhancement of the antennas.

3.1. Fabrication Process. The fabrication process starts with EBL an Au electrode on top of a quartz substrate. Prior to EBL, the quartz substrate was cleaned in acetone and bombarded with oxygen plasma for 5 minutes to remove residues. A 360 nm thick layer of polymethyl-methacrylate copolymer resist (PMMA/MMA) (9% in Ethyl Lactate, from MicroChem Corp.) was spun at 4000 rpm on the substrate, and the sample was baked in a hot plate at 175°C for 5 minutes to harden the resist and remove solvent. It was followed by spinning a layer of polymethyl-methacrylate (PMMA) (2% in Chlorobenzene, from MicroChem Corp.) at 4000 rpm with a thickness of 130 nm to form a bilayer resist. After that, the sample was baked in a hot plate at 175°C for 30 minutes to remove solvent residue. A thin layer of Au with thickness of 10 nm was deposited on top

of the resist to avoid charging effect on the sample during EBL writing. The resist was exposed with the patterned of an Au electrode with width of 400 nm and some alignment mark at an acceleration voltage of 30 kV and an area dose of $290 \mu\text{C}/\text{cm}^2$. After exposure, the thin Au layer on the resist was stripped using gold etching for 10 seconds, and then the resist was developed using a 1 : 3 methyl-iso-butyl-ketone (MIBK) in isopropyl alcohol (IPA) solution for 29 seconds. Following development, the sample was rinsed with DI water, and bombarded by oxygen plasma for 90 seconds to remove residual resist. A 3 nm thick Ti adhesion layer and 40 nm thick Au layer were deposited using a thermal evaporator. The Au electrode and alignment mark were transferred to the substrate via a lift-off process using acetone (Figure 5(a)). Following the same processes with precise alignment, another electrode made by Ti was fabricated on the quartz substrate, with a gap of $1 \mu\text{m}$ to the Au electrode (Figure 5(b)). A droplet of CNT suspension in ethanol alcohol was dispersed at the vicinity to the gap of electrodes, and an AC voltage of $1 V_{pp}$ and 10 kHz frequency was applied between the electrodes through the dielectrophoresis (DEP) deposition system [34]. With the assistance of an atomic force microscope (AFM) manipulation system [35], an individual single wall CNT (SWCNT), with diameter of 1-2 nm, was assembled between the electrodes, as shown in the inset of Figure 5(c), which is the AFM image of the CNT photodetector. A detailed deposition process was introduced in [36]. After that, a layer of Si_3N_4 with thickness of 10 nm was deposited on top of the device using plasma-enhanced chemical vapor deposition (PECVD). The PECVD is a uniform deposition process, but Figure 5(d) shows the Si_3N_4 only in the region between two electrodes for making the schematic clearer. Eventually, a bowtie antenna with two tip-to-tip equilateral Au triangles was fabricated on top of the Si_3N_4 layer by aligning the gap of bowtie antenna to the SWCNT between two electrodes. The fabrication of the bowtie antenna started with spinning a 100 nm thick layer of PMMA at 6000 rpm on the device, and the sample was baked on a hot plate at 175°C for 30 minutes. After that, an Au layer of 10 nm was deposited on top of the device to prevent charging effect. In order to precisely align the antenna to the detector, AFM was used to record the position of the SWCNT for designing antenna layout. The bowtie antenna was layout using single pass lines to reduce proximity effects in order to increase resolution. During EBL, the resist was exposed with a line dose of $0.75 \mu\text{C}/\text{cm}$ to form the pattern of bowtie antenna. After EBL, the thin Au layer was stripped, and the resist was developed using a 1 : 3 MIBK in IPA solution for 29 seconds. Following development, a 2 nm thick Ti adhesion layer and 20 nm Au layer were then deposited using a thermal evaporator. The antenna pattern was transferred to the substrate via a lift-off process Figure 5(e).

Figure 5(f) shows a 3D AFM image of one of the devices integrating bowtie antenna to a CNT photodetector. The SWCNT was not located at the center of the axis of two electrodes, thus the position of bowtie antenna was adjusted according to the position of the CNT. AFM images cannot show accurate dimensions in $x - y$ plane due to the image broadening, which is caused by the large radius of

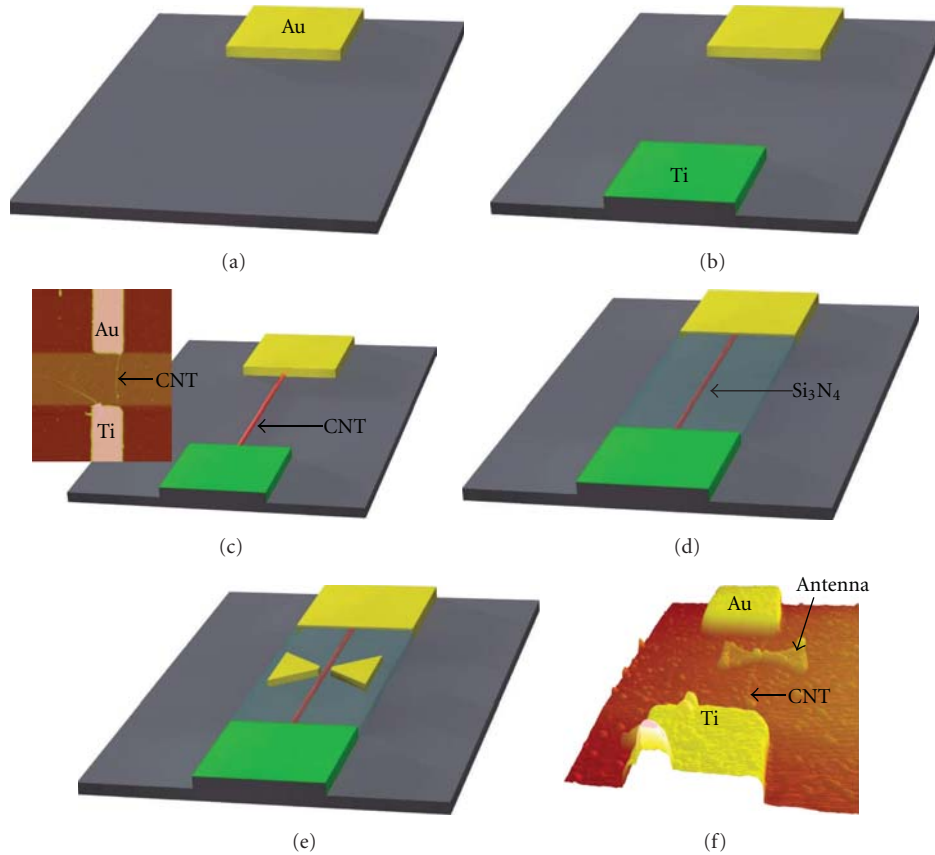


FIGURE 5: (a–e) Fabrication process of integrating a bowtie antenna to a CNT photodetector. The inset of (c) is an AFM image of an SWCNT bridging a Ti and an Au electrode. (f) A 3D AFM image of the device.

curvature of the apex of AFM tips, therefore, two triangles of the bowties in the AFM image seems connecting. SEM was utilized to measure the real dimensions of the bowtie antennas. The gap of bowtie antennas (g) was 30 ± 10 nm, the apex width (w) of the triangles was 30 ± 10 nm, length of the bowtie antenna (L) was 400 ± 30 nm.

3.2. Experimental Results. Photocurrent measurements were carried out on CNT photodetectors with absence and presence of bowtie antennas so as to investigate the field enhancement of the antennas. An IR laser, which had 830 nm wavelength and polarization in x direction (the axis of bowtie antenna), illuminated on the CNT photodetector that was housed in a testing chamber, and electrical signals were measured using Agilent semiconductor analyzer 4156C.

Photoresponse of the CNT photodetector without bowtie antenna was firstly recorded at room temperature by switching the IR laser on and off at 0.2 Hz for several cycles (blue curve of Figure 6). Photoresponse of the CNT photodetector was measured again after the fabrication of the bowtie antenna (red curve of Figure 6). The photocurrent is the current difference at presence and absence of IR illumination. The comparison of photoresponses was based

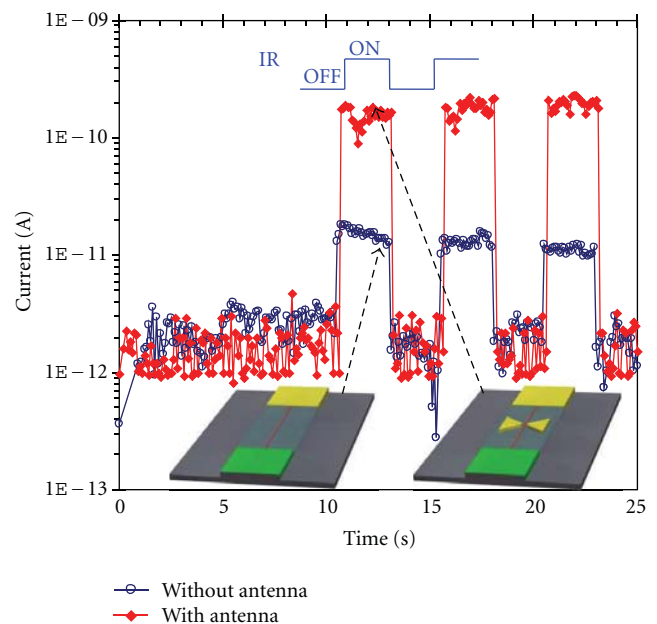


FIGURE 6: Photoresponses of the CNT photodetector without and with bowtie antenna by switching IR laser on and off at 0.2 Hz.

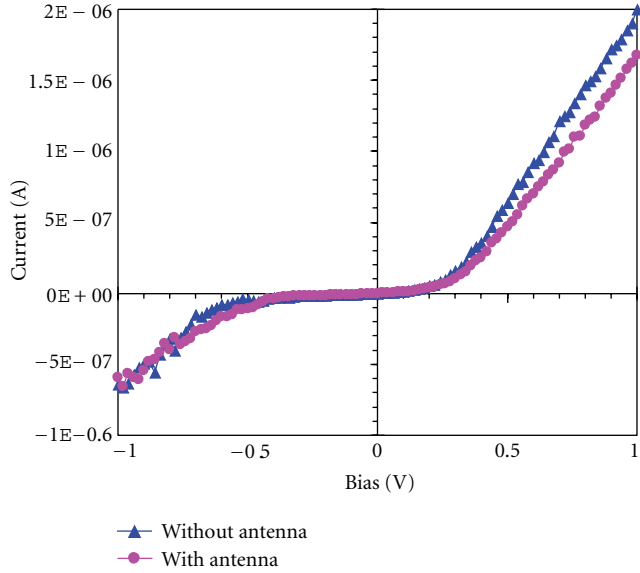


FIGURE 7: I-V characteristics of the CNT photodetector without and with the bowtie antenna.

on the amplitude change of photocurrent. Figure 6 shows that the dark current was $\sim 2 \times 10^{-12}$ A at the absence of IR illumination, and the current was increased significantly upon light illumination because of the photons generated electron and hole pairs within the CNT, which were separated in the Schottky barrier to produce photocurrent. The current dropped to the dark current when the IR laser was turned off. The reproducibility of the photoresponse was excellent. The photocurrent for CNT photodetector without antenna was $\sim 1.5 \times 10^{-11}$ A, and it was increased to $\sim 1.9 \times 10^{-10}$ A after the fabrication of the bowtie antenna, with a photocurrent enhancement of 12.67 times.

The bowtie antenna functions as a plasmonic lens to funnel light into the CNT, which has a size much smaller than the gap of bowtie antenna. Hence, the area of detector material (physical cross-section) and absorption probability did not change with the absence or presence of the antenna. With the presence of bowtie antenna, the photon energy density on the detector material was enhanced due to sub-wavelength near-field confinement. It has been defined that the absorption cross-section of the detector is the total light power absorbed by detector material normalized by the incident photon flux [17]. Therefore, calculation of relative energy intensity difference on the CNT body at absence and presence of antenna will directly reflect the photocurrent enhancement.

The field intensity increment on the CNT can be calculated by integrating the E -field intensity along the CNT by $I = \int |E(y)|^2 dy$ (Figure 3(a)), since the depletion region of the asymmetric CNT photodetector extended to the whole CNT. In other words, the photocurrent enhancement was caused by the E -field intensity increment on the CNT. Without the nanoantenna, the total field intensity on the CNT is equal to 10^{-6} V because $E_x(y) = 1$ V/m and $y = 1 \mu\text{m}$. The field intensity distribution with the antenna was

calculated by using the parameters that were the same as fabricated device and experimental setup ($d = 30$ nm, $w = 30$ nm, $L = 400$ nm, $t = 10$ nm, $\theta = 60^\circ$, and radiation wavelength = 830 nm). By integrating the field intensity along the y axis between two electrodes (where the CNT located in Figure 3(a)), the field intensity was enhanced to 14.87×10^{-6} V, with a field enhancement of 14.87 fold. Therefore, the photocurrent enhancement is in good agreement with the simulation. Differences are attributed to geometry differences between the actual antennas and the simulation model, and some losses were occurred in the antennas due to edge and surface roughness.

In order to validate that the photocurrent enhancement was caused by the light confinement of the nanoantenna, rather than the contact condition change during fabrication, I-V characteristics of the photodetector without and with antenna were measured and shown in Figure 7. The I-V characteristics showed current rectifying at low voltage, implying the existence of Schottky barriers. In addition, the bias-dependent currents of the CNT photodetector with absence and presence of nanoantenna were almost identical, which indicated that the contact condition did not change with the fabrication of the nanoantenna, since electrical signal was extremely sensitive to contact condition. This verifies that the photocurrent increment was caused by field intensity enhancement from the bowtie antenna.

4. Conclusion

The design of bowtie antennas integrating to the CNT photodetectors was studied. The E -field intensity enhancement of bowtie antennas with a small gap located on top of the asymmetric CNT photodetector was calculated. It was shown that the peak field intensity of the antenna was exponentially decreased with the distance between the antenna to the CNT photodetector. The resonance wavelength of the bowtie antenna redshifts with increasing tip angles. A fabrication process was developed to integrate the bowtie antenna with the CNT detector. It should be noted that the 1D CNT detector is perfectly matched with the bowtie antenna, since the diameter of CNTs is in the same scale as the gap of the bowtie antenna. The experimental results agreed well with the simulation by measuring photocurrent enhancement. The nanoantenna may become an important component to the nanoscale photonic devices.

Acknowledgement

This research work is partially supported under NSF grant IIS 0713346, ONR Grants N00014-07-1-0935, and ONR Grants N00014-04-1-0799.

References

- [1] R. Agarwal and C. M. Lieber, "Semiconductor nanowires: optics and optoelectronics," *Applied Physics A*, vol. 85, no. 3, pp. 209–215, 2006.

- [2] M. Freitag, Y. Martin, J. A. Misewich, R. Martel, and P. Avouris, "Photoconductivity of single carbon nanotubes," *Nano Letters*, vol. 3, no. 8, pp. 1067–1071, 2003.
- [3] J. B. Zhang et al., "Photovoltaic effect in single carbon nanotube-based Schottky diodes," *International Journal of Nanoparticles*, vol. 6, no. 8, p. 11, 2008.
- [4] P. Avouris, M. Freitag, and V. Perebeinos, "Carbon-nanotube photonics and optoelectronics," *Nature Photonics*, vol. 2, no. 6, pp. 341–350, 2008.
- [5] S. Wang, M. Khafizov, X. Tu, M. Zheng, and T. D. Krauss, "Multiple exciton generation in single-walled carbon nanotubes," *Nano Letters*, vol. 10, no. 7, pp. 2381–2386, 2010.
- [6] M. B. Tzolov, T. F. Kuo, D. A. Straus, A. Yin, and J. Xu, "Carbon nanotube-silicon heterojunction arrays and infrared photocurrent responses," *Journal of Physical Chemistry C*, vol. 111, no. 15, pp. 5800–5804, 2007.
- [7] K. W. C. Lai, N. Xi, C. K. M. Fung, H. Chen, and T. J. Tarn, "Engineering the band gap of carbon nanotube for infrared sensors," *Applied Physics Letters*, vol. 95, no. 22, Article ID 221107, 2009.
- [8] P. G. Collins, M. S. Arnold, and P. Avouris, "Engineering carbon nanotubes and nanotube circuits using electrical breakdown," *Science*, vol. 292, no. 5517, pp. 706–709, 2001.
- [9] E. R. Fossum, "CMOS image sensors: electronic camera-on-a-chip," *IEEE Transactions on Electron Devices*, vol. 44, no. 10, pp. 1689–1698, 1997.
- [10] Y. Ishihara and K. Tanigaki, "A high sensitivity IL-CCD image sensor with monolithic resin lens array," in *Proceedings of the IEEE International Electron Devices Meeting Technical Digests*, pp. 497–500, 1983.
- [11] W. A. Murray and W. L. Barnes, "Plasmonic materials," *Advanced Materials*, vol. 19, no. 22, pp. 3771–3782, 2007.
- [12] J. A. Schuller, E. S. Barnard, W. Cai, Y. C. Jun, J. S. White, and M. L. Brongersma, "Plasmonics for extreme light concentration and manipulation," *Nature Materials*, vol. 9, no. 3, pp. 193–204, 2010.
- [13] P. Bharadwaj, B. Deutsch, and L. Novotny, "Optical antennas," *Advances in Optics and Photonics*, vol. 1, no. 3, pp. 438–483, 2009.
- [14] H. A. Atwater and A. Polman, "Plasmonics for improved photovoltaic devices," *Nature Materials*, vol. 9, no. 3, pp. 205–213, 2010.
- [15] Z. Fan, D. J. Ruebusch, A. A. Rathore et al., "Challenges and prospects of nanopillar-based solar cells," *Nano Research*, vol. 2, no. 11, pp. 829–843, 2009.
- [16] D. M. Schaadt, B. Feng, and E. T. Yu, "Enhanced semiconductor optical absorption via surface plasmon excitation in metal nanoparticles," *Applied Physics Letters*, vol. 86, no. 6, Article ID 063106, pp. 1–3, 2005.
- [17] Z. Yu, G. Veronis, S. Fan, and M. L. Brongersma, "Design of midinfrared photodetectors enhanced by surface plasmons on grating structures," *Applied Physics Letters*, vol. 89, no. 15, Article ID 151116, 2006.
- [18] M. W. Knight, H. Sobhani, P. Nordlander, and N. J. Halas, "Photodetection with active optical antennas," *Science*, vol. 332, no. 6030, pp. 702–704, 2011.
- [19] N. M. Gabor, Z. Zhong, K. Bosnick, J. Park, and P. L. McEuen, "Extremely efficient multiple electron-hole pair generation in carbon nanotube photodiodes," *Science*, vol. 325, no. 5946, pp. 1367–1371, 2009.
- [20] O. Hayden, R. Agarwal, and C. M. Lieber, "Nanoscale avalanche photodiodes for highly sensitive and spatially resolved photon detection," *Nature Materials*, vol. 5, no. 5, pp. 352–356, 2006.
- [21] C. Soci, A. Zhang, B. Xiang et al., "ZnO nanowire UV photodetectors with high internal gain," *Nano Letters*, vol. 7, no. 4, pp. 1003–1009, 2007.
- [22] H. Chen, N. Xi, K. W. C. Lai, C. K. M. Fung, and R. Yans, "Development of infrared detectors using single carbon-nanotube-based field-effect transistors," *IEEE Transactions on Nanotechnology*, vol. 9, no. 5, pp. 582–589, 2010.
- [23] P. J. Schuck, D. P. Fromm, A. Sundaramurthy, G. S. Kino, and W. E. Moerner, "Improving the mismatch between light and nanoscale objects with gold bowtie nanoantennas," *Physical Review Letters*, vol. 94, no. 1, Article ID 017402, 2005.
- [24] D. P. Fromm, A. Sundaramurthy, P. James Schuck, G. Kino, and W. E. Moerner, "Gap-dependent optical coupling of single "bowtie" nanoantennas resonant in the visible," *Nano Letters*, vol. 4, no. 5, pp. 957–961, 2004.
- [25] C. K. M. Fung, N. Xi, B. Shanker, and K. W. C. Lai, "Nanoresonant signal boosters for carbon nanotube based infrared detectors," *Nanotechnology*, vol. 20, no. 18, Article ID 185201, 2009.
- [26] F. Léonard and J. Tersoff, "Novel length scales in nanotube devices," *Physical Review Letters*, vol. 83, no. 24, pp. 5174–5177, 1999.
- [27] H. Chen, N. Xi, K. W. Lai, C. K. Fung, L. Chen, and J. Lou, "Analysis and design of carbon nanotube based field effect transistors for nano infrared sensors," in *Proceedings of the IEEE Nanotechnology Materials and Devices Conference (NMDC '10)*, pp. 164–168, 2010.
- [28] A. Sundaramurthy, K. B. Crozier, G. S. Kino, D. P. Fromm, P. J. Schuck, and W. E. Moerner, "Field enhancement and gap-dependent resonance in a system of two opposing tip-to-tip Au nanotriangles," *Physical Review B*, vol. 72, no. 16, pp. 1–6, 2005.
- [29] K. B. Crozier, A. Sundaramurthy, G. S. Kino, and C. F. Quate, "Optical antennas: resonators for local field enhancement," *Journal of Applied Physics*, vol. 94, no. 7, pp. 4632–4642, 2003.
- [30] E. Betzig, J. K. Trautman, T. D. Harris, J. S. Weiner, and R. L. Kostelak, "Breaking the diffraction barrier: optical microscopy on a nanometric scale," *Science*, vol. 251, no. 5000, pp. 1468–1470, 1991.
- [31] R. A. Pala, J. White, E. Barnard, J. Liu, and M. L. Brongersma, "Design of plasmonic thin-film solar cells with broadband absorption enhancements," *Advanced Materials*, vol. 21, no. 34, pp. 3504–3509, 2009.
- [32] W. Ding, R. Bachelot, S. Kostcheev, P. Royer, and R. Espiau De Lamaestre, "Surface plasmon resonances in silver Bowtie nanoantennas with varied bow angles," *Journal of Applied Physics*, vol. 108, no. 12, Article ID 124314, 2010.
- [33] K. L. Shuford, M. A. Ratner, and G. C. Schatz, "Multipolar excitation in triangular nanoprisms," *Journal of Chemical Physics*, vol. 123, no. 11, pp. 1–9, 2005.
- [34] K. W. C. Lai, N. Xi, C. K. M. Fung et al., "Automated nanomanufacturing system to assemble carbon nanotube based devices," *International Journal of Robotics Research*, vol. 28, no. 4, pp. 523–536, 2009.
- [35] J. Zhang, N. Xi, L. Liu, H. Chen, K. W. C. Lai, and G. Li, "Atomic force yields a master nanomanipulator," *IEEE Nanotechnology Magazine*, vol. 2, no. 2, pp. 12–17, 2008.
- [36] J. Zhang, N. Xi, H. Chen, K. W. C. Lai, G. Li, and U. C. Wejinya, "Design, manufacturing, and testing of single-carbon-nanotube-based infrared sensors," *IEEE Transactions on Nanotechnology*, vol. 8, no. 2, Article ID 4663874, pp. 245–251, 2009.

Research Article

Ultrafast Plasmonic Nanoantenna-ITO Hybrid Switches

Martina Abb and Otto L. Muskens

SEPnet and the Department of Physics and Astronomy, University of Southampton, Highfield, Southampton SO17 1BJ, UK

Correspondence should be addressed to Otto L. Muskens, o.muskens@soton.ac.uk

Received 31 August 2011; Revised 13 October 2011; Accepted 14 October 2011

Academic Editor: Alexandre Bouhelier

Copyright © 2012 M. Abb and O. L. Muskens. This is an open access article distributed under the Creative Commons Attribution License, which permits unrestricted use, distribution, and reproduction in any medium, provided the original work is properly cited.

We present here a new type of device using nonlinear hybrid antenna-semiconductor (ITO) interaction. We observe a picosecond transient response from the antenna that cannot be explained by either pure ITO or antenna nonlinearities independently. We study the dependence of the hybrid interaction on several experimental parameters, including the polarization of excitation and detection.

Nanoscale plasmonic components such as nanoantennas [1, 2] are of enormous interest for their capabilities of locally enhancing electromagnetic fields and controlling emission. Active control of such components will enable a new generation of tunable devices. We recently introduced a new concept of antenna switches relying on photoconductive loading of the gap between the arms of a dimer antenna [3]. Experimentally, modulation of localized plasmon modes has been achieved using the refractive index of liquid crystals [4]. Active tuning of the antenna gap has also been demonstrated using mechanical means, such as using stretchable elastomeric films [5] to reversibly engineer the distance between particle dimers. The temporal response of these changes is limited by the gap loading mechanisms that are used.

As a potentially ultrafast implementation of our concept [3], we demonstrated experimentally picosecond all-optical control of a plasmonic nanoantenna on ITO, referred to as a nanoantenna-ITO hybrid [6]. For ITO, unity-order changes of the refractive index have been achieved [7] by applying an electric field. We have shown that optical pumping of ITO leads to a local reduction of the free-carrier density in the substrate. The transient nonlinear response of the antenna-ITO hybrid shows a redshift of the plasmon resonance, as opposed to transient bleaching on SiO₂.

Here, we present a detailed study of the response of antennas on 20 nm thick ITO film (low cond.), both with and without ITO cover layer. We find an effect for both

perpendicular and parallel modes of the antenna, although the parallel mode shift is more pronounced, as well as a polarization dependence of the pump beam. Additionally, we look at the interaction of a larger cylindrical goldpad with the ITO surrounding it to further investigate the injection mechanism of fast electrons from the gold into the ITO.

Nanoantennas were fabricated with e-beam lithography on low-conductivity (70–100 Ω/sq, 20 nm thick) and high-conductivity (8–12 Ω/sq, 120 nm thick) ITO substrates from Sigma-Aldrich using a bilayer of photoresist. After exposure and development, 25 nm of gold was deposited, followed by liftoff. To stay in focus when moving away from the edge of the sample, pads were burned along the way, which turned out useful as a test area later. The nanostructures were covered by sputtering a matching ITO layer of 25 nm on either top or left without cover. This did not produce a measurable difference, as we shall see.

For ultrafast spectroscopy, pulses of 4 ps length with a repetition rate of 40 MHz from an ytterbium fiber laser amplifier (Fianium, Ltd.) were used. The linear antenna response was spectrally characterized using the spatial modulation technique [8, 9], selecting wavelengths between 500–1800 nm using a subtractive mode double prism monochromator. The tunable probe beam was focused onto the sample from the front with a Mitutoyo 100x NIR objective with 0.5 NA, giving a spot size of 0.7 μm FWHM for 900 nm wavelength. As pump beam, we split off part of the original 1064 nm beam and frequency-double it with a 5 mm KTP

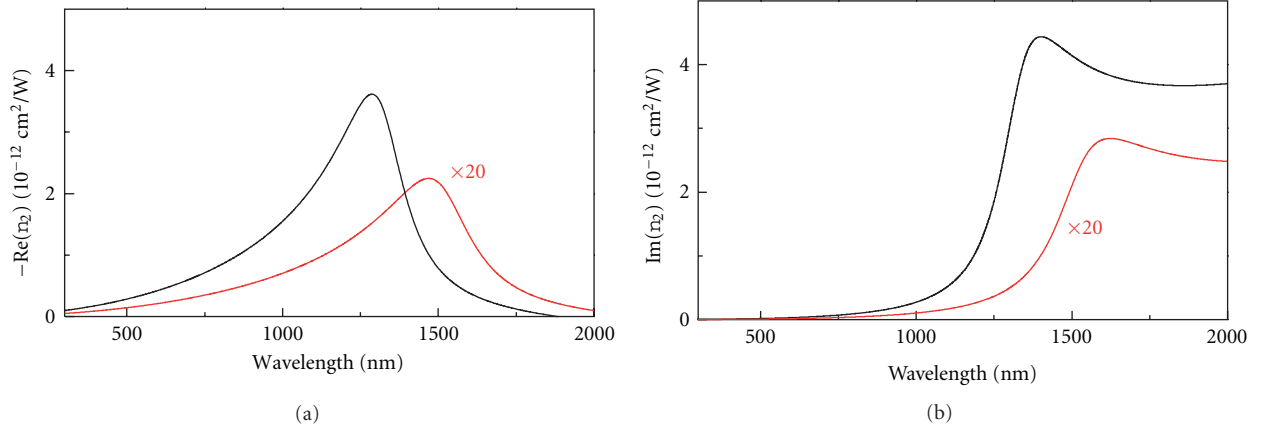


FIGURE 1: Free-carrier nonlinearity described by the nonlinear coefficient for 20 nm low-conductivity (red) and 120 nm high-conductivity (black) ITO.

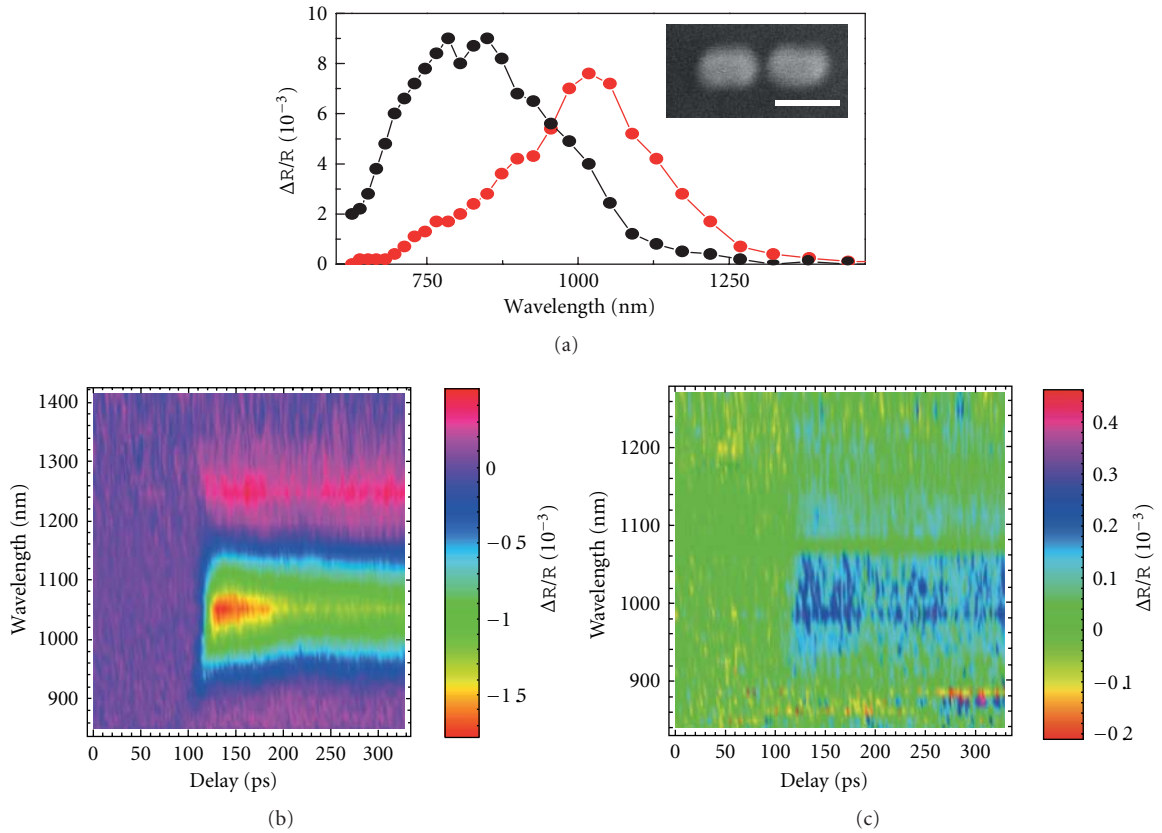


FIGURE 2: (a) Plasmonic resonances along the long (red circles) and the short (black circles) axis of our dimer antenna on low-conductivity ITO, covered with a 20 nm layer of low-conductivity ITO. The inset shows a SEM picture of the antenna, with the scale bar being for 200 nm. (b) and (c) depict the time traces of the pump probe nonlinear response, (b) for the longitudinal and (c) for the transversal mode.

crystal to obtain a 532 nm beam which was focused on the backside of the sample by a 0.6 NA aspheric lens, yielding a spot of $2\ \mu\text{m}$ FWHM. To characterize the nonlinearity of the ITO and the antenna-ITO hybrids, we took time-resolved scans for different wavelengths to give a clear picture of the dynamics.

The nonlinearity of ITO is governed by the free-carrier density, as shown in [6]. This third-order nonlinearity can be expressed by a nonlinear coefficient n_2 , representing the resulting refractive index modulation normalized to the optical peak intensity of the excitation beam: $n_2 = \Delta n/I$.

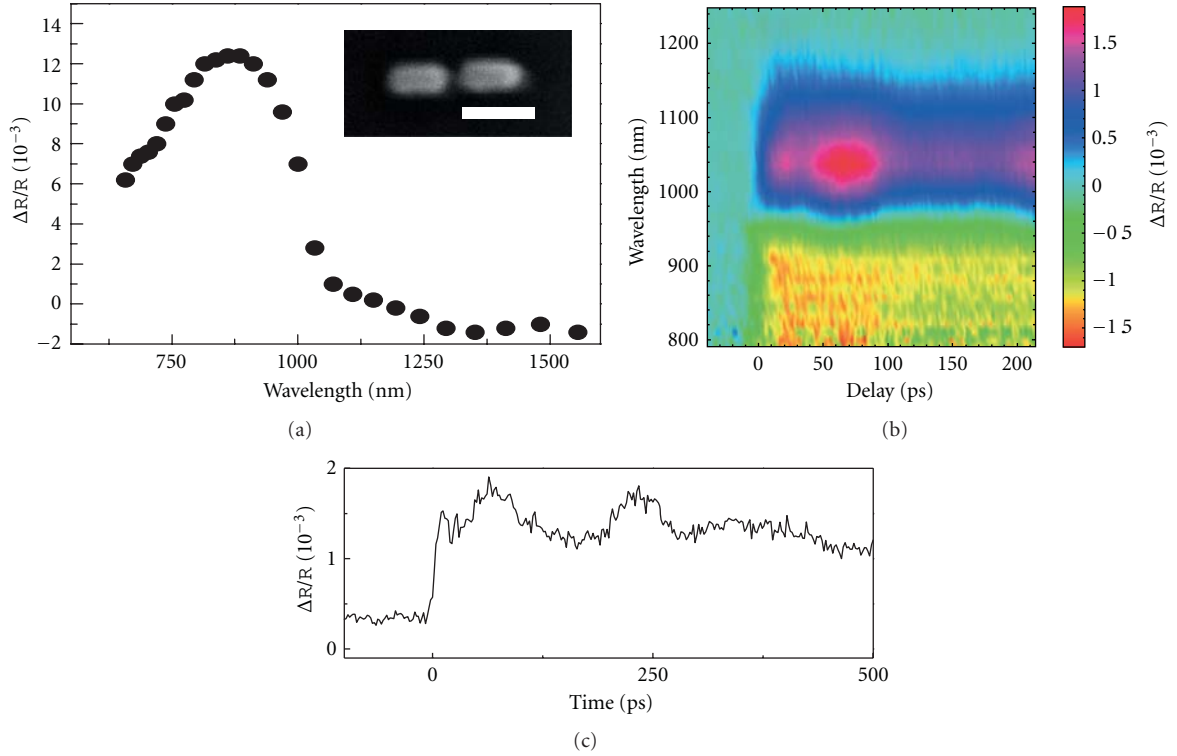


FIGURE 3: Spectral resonance of an antenna with a gap of 40 nm on low-conductivity ITO without cover. Optical pumping leads to a redshift of the original resonance. To the left of the plasmonic resonance and on the maximum of the pump probe signal, we observe an acoustic mode.

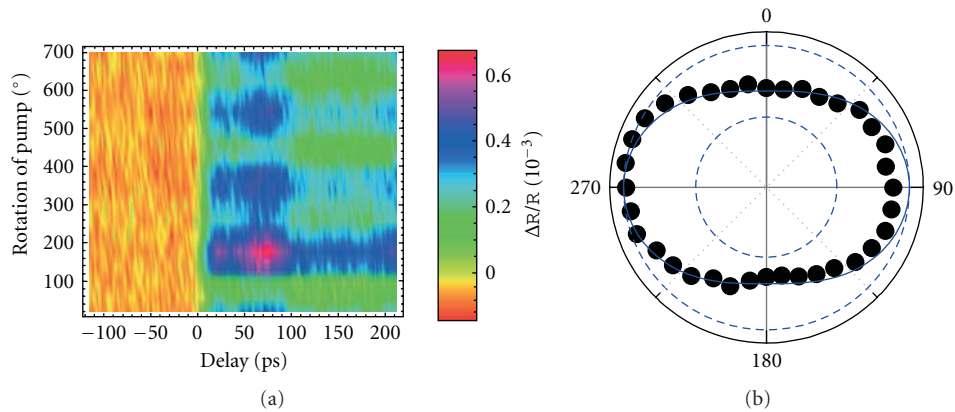


FIGURE 4: Dependence of the pump probe signal from Figure 3 on the polarization of the pump.

Resulting values of n_2 for both the real and the imaginary part of this nonlinear refractive index coefficient over the spectral range are shown in Figure 1 for 20 nm of low-conductivity and 120 nm of high-conductivity ITO. These are obtained from fits to the experimental reflectivity data shown in [6], where we found initial carrier concentrations of $N = 9.2 \times 10^{20} \text{ cm}^{-3}$ for the high-conductivity ITO and $N = 7.3 \times 10^{20} \text{ cm}^{-3}$ for the low-conductivity ITO. Optical pumping with 532 nm and 180 pJ pump energy was shown to deplete the ITO, and we observed changes in carrier concentration of $\Delta N = (2.1 \pm 0.1) \times 10^{18} \text{ cm}^{-3}$

for the high-conductivity ITO and $\Delta N = (5.4 \pm 0.2) \times 10^{16} \text{ cm}^{-3}$ for the low-conductivity ITO. We find a much larger nonlinearity (more than a factor 20) for the high-conductivity ITO, as can be expected. Our values for the Kerr nonlinearity are in excellent agreement with literature values of similar ITO films [10], taken at a single wavelength around 720 nm.

On the antennas, we measure the extinction spectra of an antenna with a gap of 40 nm on low-conductivity ITO, covered with a matching layer of ITO. We find a resonance at around 800 nm for the perpendicular mode

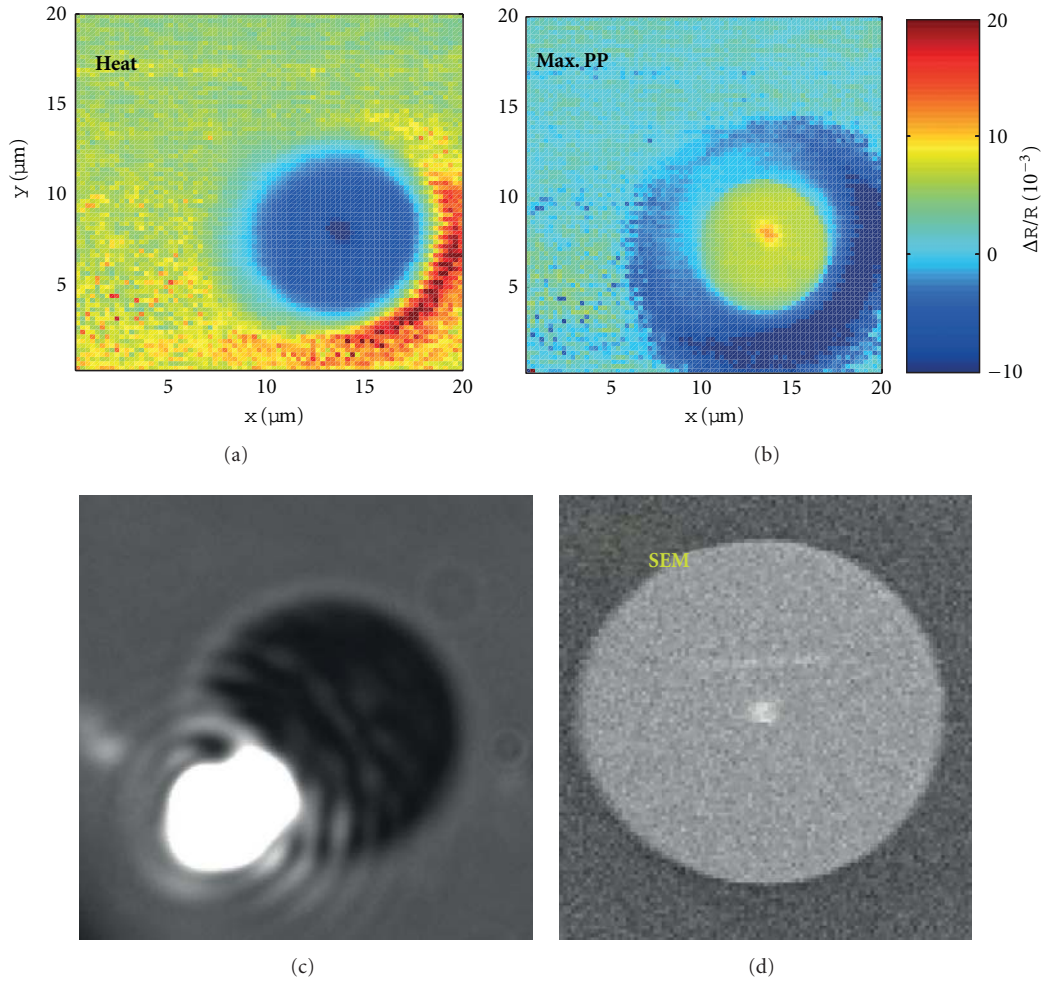


FIGURE 5: Pump probe signal around a gold pad at 985 nm probe wavelength and a pump energy of 180 pJ, for the heat background (a) and the maximum pump probe signal with the heat background subtracted (b). Below are a microscope image with the beam on the edge of the contamination dot (c) and a SEM image of the dot (d).

and another at around 1000 nm for the parallel antenna mode, see Figure 2(a). The corresponding that spectrally resolved nonlinear time trace is shown in Figures 2(b) and 2(c), with the heat background already subtracted. The spectral bipolar form is different from the well-known transient bleaching found for all kinds of nanoparticles [11, 12], which corresponds to a decrease and broadening of the plasmonic resonance due to fast electron generation in the particle which leads to a change in the refractive index of the gold itself. Instead, we observe a bipolar transient response for both polarizations, although the effect is more pronounced for polarization parallel to the antenna. The negative pump probe signal can be identified with the spatial modulation extinction spectra, with a new redshifted resonance appearing next to it.

When modelling single antenna extinction spectra with FEM simulations (Comsol v3.5), the refractive index change and the concomitant resonance shift predicted for changes in carrier density of the order of our measured value for

just the ITO film, $\Delta N = (2.1 \pm 0.1) \times 10^{18} \text{ cm}^{-3}$ cannot account for the large shift. This leads us to deduce that this must be an effect of the hybrid ITO-antenna system, as described in [6]. We propose that the shift is caused by hot electron injection from the gold into the surrounding ITO. This proposed energy transfer mechanism consists of two parts: first, hot electrons are injected from the antennas into the ITO substrate, leading to a temperature increase in the close vicinity. Apart from the heating effect, the hot electrons are not accountable for changes in the refractive index, since they are swiftly replaced by cold electrons transferring back to the antenna. But the heating effect is big enough to give way to a secondary effect, that of migration of free carriers from the heated region to the surrounding ITO, thus effectively depleting the ITO. This depletion changes the local refractive index of the ITO and therefore shifts the plasmon resonance of the antenna. The nonlinear coefficients needed to describe the Kerr ITO-antenna hybrid nonlinearity is a factor 37 larger than the pure substrate in the case of high-conductivity ITO and as large as a factor of 1475

in the case of low-conductivity ITO (see [6]), which makes the results for low-conductivity ITO-antenna hybrids even more remarkable.

Another notable difference between antennas on low- and high-conductivity ITO that supports our proposition is the fact that we observe acoustic modes in the fast nonlinear response of hybrids on low-conductivity ITO, as shown in Figure 3, but not for hybrids on high-conductivity ITO [6]. This was the case for 11 out of 17 antennas on low-conductivity ITO, for 15 out of 24 antennas on SiO₂, and for none of the 19 antennas on high-conductivity ITO that we have studied. These vibrations are present only on the maximum signal of the new redshifted mode and have oscillation periods of 100–300 ps for our antennas, depending on size. The reason for this position of the acoustic modes is still unclear. Their occurrence, however, indicates that the fast electrons that are excited by the pump beam transfer their energy to the lattice which starts the vibrations in the nanostructure. On high-conductivity ITO, on the other hand, we did not observe these lattice vibrations [6], which leads us to believe that the energy is not transferred to the lattice, but instead is dissipated into heat after the hot electrons are injected into the surrounding semiconductor.

In Figure 4, we show measurements of the excitation anisotropy for an antenna on low-conductivity ITO obtained by rotating a half-wave plate in the pump beam. We find an excitation anisotropy $(\Delta R_{\parallel} - \Delta R_{\perp})/(\Delta R_{\parallel} + \Delta R_{\perp})$ of 0.19 ± 0.02 , which indicates that absorption takes place partly through the nanoantenna [13].

To further investigate the hybrid interaction at the gold-ITO interface, we take advantage of one of the gold pads that was written into the photoresist to optimize the focus before exposure. Such a gold pad is shown in Figure 5, as a SEM picture as well as a picture taken in the home-built microscope. We performed pump probe scans on an area of $20 \mu\text{m} \times 20 \mu\text{m}$, both for the slow signal typical for heating of the sample (Figure 5(a)) as well as for the fast pump probe signal. Interestingly, for the heat scan, we observe a clear minimum on the gold pad itself, corresponding to a local heating of the gold surface. For the fast scan (Figure 5(b)), however, the gold pad itself has a clearly positive signal unlike its immediate surroundings. We observe a corona of negative signal up to $2 \mu\text{m}$ around the contamination dot, which is even further than the 126 nm hot electron diffusion length that we suggest in [6]. This is partly due to the size of the pump beam (around $2 \mu\text{m}$ FWHM), which generates heat and hot electrons in areas around the smaller probe spot.

In conclusion, we have shown ultrafast all-optical control of ITO-nanoantenna hybrids. We identify a picosecond nonlinear response that can be described by an enormous corresponding Kerr-nonlinearity that is a factor of 1475 bigger than for the pure ITO. This huge nonlinearity originates in free carriers being injected from the antenna whose energy generates substantial heat in the surrounding substrate. This is very promising indeed for exploitation in creating nanophotonic switches in other designs and warrants further investigations. Hybrid plasmonic components are of great interest for active control of optical fields and integration

of photonic and electronic functionalities. Our antenna-ITO hybrid in particular holds great promise for this since electrically controlled refractive index changes for ITO have already been demonstrated [7].

Acknowledgments

The authors thank Z. Webber and M. A. Bampton for their technical support. O. L. Muskens thanks support from EPSRC through Grant EP/H019669/1.

References

- [1] W. L. Barnes, A. Dereux, and T. W. Ebbesen, "Surface plasmon subwavelength optics," *Nature*, vol. 424, no. 6950, pp. 824–830, 2003.
- [2] O. L. Muskens, V. Giannini, J. A. Sánchez-Gil, and J. G. Rivas, "Optical scattering resonances of single and coupled dimer plasmonic nanoantennas," *Optics Express*, vol. 15, no. 26, pp. 17736–17746, 2007.
- [3] N. Large, M. Abb, J. Aizpurua, and O. L. Muskens, "Photoconductively loaded plasmonic nanoantenna as building block for ultracompact optical switches," *Nano Letters*, vol. 10, no. 5, pp. 1741–1746, 2010.
- [4] J. Berthelot, A. Bouhelier, C. Huang et al., "Tuning of an optical dimer nanoantenna by electrically controlling its load impedance," *Nano Letters*, vol. 9, no. 11, pp. 3914–3921, 2009.
- [5] F. Huang and J. J. Baumberg, "Actively tuned plasmons on elastomerically driven Au nanoparticle dimers," *Nano Letters*, vol. 10, no. 5, pp. 1787–1792, 2010.
- [6] M. Abb, P. Albella, J. Aizpurua, and O. L. Muskens, "All-optical control of a single plasmonic nanoantenna-ITO hybrid," *Nano Letters*, vol. 11, no. 6, pp. 2457–2463, 2011.
- [7] E. Feigenbaum, K. Diest, and H. A. Atwater, "Unity-order index change in transparent conducting oxides at visible frequencies," *Nano Letters*, vol. 10, no. 6, pp. 2111–2116, 2010.
- [8] A. Arbouet, D. Christofilos, N. del Fatti, F. Vallée, J. R. Huntzinger, and M. Broyer, "Direct measurement of the single-metal-cluster optical absorption," *Physical Review Letters*, vol. 93, Article ID 127401, 2004.
- [9] O. L. Muskens, N. del Fatti, F. Vallée, J. R. Huntzinger, and M. Broyer, "Single metal nanoparticle absorption spectroscopy and optical characterization," *Applied Physics Letters*, vol. 88, Article ID 063109, 3 pages, 2006.
- [10] H. I. Elim, W. Ji, and F. Zhu, "Carrier concentration dependence of optical Kerr nonlinearity in indium tin oxide films," *Applied Physics B: Lasers and Optics*, vol. 82, no. 3, pp. 439–442, 2006.
- [11] S. Link and M. A. El-Sayed, "Spectral properties and relaxation dynamics of surface plasmon electronic oscillations in gold and silver nanodots and nanorods," *Journal of Physical Chemistry B*, vol. 103, no. 40, pp. 8410–8426, 1999.
- [12] C. Voisin, D. Christofilos, P. A. Loukakos et al., "Ultrafast electron-electron scattering and energy exchanges in noble-metal nanoparticles," *Physical Review B*, vol. 69, no. 19, Article ID 195416, 2004.
- [13] O. L. Muskens, G. Bachelier, N. del Fatti et al., "Quantitative absorption spectroscopy of a single gold nanorod," *Journal of Physical Chemistry C*, vol. 112, no. 24, pp. 8917–8921, 2008.

Review Article

Fluorescence Enhancement Factors on Optical Antennas: Enlarging the Experimental Values without Changing the Antenna Design

Jérôme Wenger

Institut Fresnel, CNRS, Aix Marseille Université, Ecole Centrale Marseille, Campus St. Jérôme, 13013 Marseille, France

Correspondence should be addressed to Jérôme Wenger, jerome.wenger@fresnel.fr

Received 13 July 2011; Accepted 3 October 2011

Academic Editor: A. Femius Koenderink

Copyright © 2012 Jérôme Wenger. This is an open access article distributed under the Creative Commons Attribution License, which permits unrestricted use, distribution, and reproduction in any medium, provided the original work is properly cited.

Plasmonic antennas offer promising opportunities to control the emission of quantum objects. As a consequence, the fluorescence enhancement factor is widely used as a figure of merit for a practical antenna realization. However, the fluorescence enhancement factor is not an intrinsic property of the antenna. It critically depends on several parameters, some of which are often disregarded. In this contribution, I explore the influence of the setup collection efficiency, emitter's quantum yield, and excitation intensity. Improperly setting these parameters may significantly alter the enhancement values, leading to potential misinterpretations. The discussion is illustrated by an antenna example of a nanoaperture surrounded by plasmonic corrugations.

1. Introduction

Plasmonic antennas are receiving a large interest to interface light with nanoscale quantum emitters on dimensions much beyond the optical wavelength [1, 2]. Recent developments involve squeezing light into nanoscale volumes [3], enhancing the excitation and emission rate of individual emitters [4–8], tuning the luminescence spectrum [9, 10], polarization [11], and directivity properties [12–16]. Several plasmonic systems are being investigated to enhance the luminescence emission of fluorescent molecules or quantum dots, such as metallic nanoparticles [4, 5, 17–20], core-shell particles [21], thin films [22, 23], nanoantennas [6, 7, 15, 24], nanowires [16], nanoporous gold [25], nanopockets [26], metallic gratings [27], nanoaperture arrays [28], and single nanoapertures [29, 30]. A general review on surface-enhanced fluorescence can be found in [31].

A natural question while performing experiments on nanoantenna-enhanced luminescence deals with the quantification of the luminescence enhancement factor η_F , which is commonly defined as the ratio of the detected radiation power per emitter with the antenna to the reference radiation power per emitter without the antenna. η_F determines how many extra photons are detected for each emitter thanks to

the use of the optical antenna. It is well known that this factor critically depends on several parameters: the antenna material and geometry, its spectral resonance, and overlap with the emitter's absorption and luminescence spectra, as well as the emitter's orientation and location relative to the antenna [32]. These many parameters often hide the influence of other parameters: the collection efficiency used in the experiments, the emitter's quantum yield in the absence of the antenna, and the excitation intensity relative to the saturation process. These last three parameters are more technically oriented and depend on the specific experimental implementation. Therefore, they have received less attention from theoretical investigations. However, as I will show below, these parameters have a major influence on the measured values of the luminescence enhancement factor. Improperly setting these parameters may significantly alter the value found for the luminescence enhancement factor, leading to potential experimental pitfalls.

In this contribution, I explore the influence of the collection efficiency, molecular quantum yield, and excitation intensity on the fluorescence enhancement factor. Several rules are derived to maximize the enhancement factor by tuning the experimental conditions without affecting the antenna's design. Using the fluorescence enhancement factor

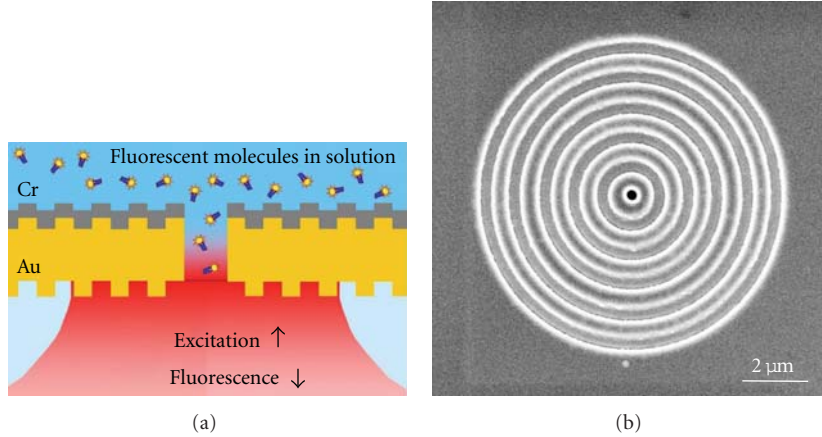


FIGURE 1: Corrugated aperture antenna used here to illustrate the influence of experimental parameters on the measured fluorescence enhancement factor. (a) Experimental configuration to probe molecules randomly diffusing in aqueous solution. (b) Scanning electron microscope image of the antenna with five corrugations. Adapted with permission from [33]. Copyright 2011 American Chemical Society.

as a figure of merit to compare between different antenna designs has to be done with caution. Analytical formulas are illustrated by a practical antenna example made of a single nanoaperture surrounded by five shallow grooves in a gold film (Figure 1). This optical antenna can significantly enhance the fluorescence count rates per molecule and control the emission directivity, as demonstrated recently [33]. Very much in the spirit of the review in [34] about the comparison between experiments and numerical simulations, I hope that this paper may initiate some reflection and avoid any misleading interpretation.

2. Designing the Experiment to Maximize the Fluorescence Enhancement Factor

A loophole in any measurement of the luminescence enhancement factor deals with the normalization of the detected signal *per emitter*. This can be done by performing experiments on single molecules directly [4, 5, 7], by surface normalization [25, 28], or by calibrating the number of emitters with fluorescence correlation spectroscopy [29, 30]. Hereafter, I consider that this normalization issue is resolved and that a reliable value for the detected radiated power per emitter can be obtained. I also assume that the signal per emitter has been averaged over several positions and dipole orientations. The aim of this paper is to focus on the influence of experimental parameters on the measured values for the fluorescence enhancement factor η_F .

2.1. Theoretical Background: Fluorescence Count Rate per Molecule. Throughout this paper, the quantum emitter is modelled by a two energy levels system. k_r and k_{nr} are the rate constants for radiative and nonradiative transitions from the excited singlet state to the ground state. The total deexcitation rate from the excited singlet state is noted as $k_{\text{tot}} = k_r + k_{nr}$, which is the inverse of the excited state lifetime τ . $\phi = k_r/k_{\text{tot}} = k_r/(k_r + k_{nr})$ is the quantum yield. σI_e is the excitation rate, where σ denotes the excitation cross-section

and I_e the excitation intensity. Under steady-state conditions, the fluorescence count rate per molecule CRM is given by [35]

$$\text{CRM} = \kappa\phi \frac{\sigma I_e}{1 + I_e/I_s}. \quad (1)$$

We note κ the light collection efficiency and $I_s = k_{\text{tot}}/\sigma$ the saturation intensity.

Equation (1) takes two limits for the extreme regimes of weak excitation ($I_e \ll I_s$) and fluorescence saturation ($I_e \gg I_s$). In the weak excitation regime, the CRM reduces to

$$\text{CRM} = \kappa\phi\sigma I_e \quad (I_e \ll I_s) \quad (2)$$

which indicates that the fluorescence rate per molecule is proportional to the collection efficiency, the quantum yield, and the excitation intensity. This expression appears to be the one commonly used in fluorescence spectroscopy and microscopy applied to the life sciences [36].

In the saturation regime $I_e \gg I_s$, (1) reduces to

$$\text{CRM} = \kappa\phi\sigma I_s = \kappa\kappa_r \quad (I_e \gg I_s) \quad (3)$$

which indicates that the fluorescence rate per molecule at saturation is determined only by the radiative rate and the collection efficiency and is of course independent on the excitation rate. This expression is generally used for single-photon sources used for quantum communication purposes, such as quantum cryptography [37, 38].

2.2. Excitation Intensity. From (1), it is apparent that the detected fluorescence rate per emitter—hence the fluorescence enhancement factor—bears a complex dependence upon the excitation intensity I_e . In the weak excitation regime (below the transition to saturation), the CRM is linearly proportional with I_e , and the fluorescence enhancement factor η_F can therefore be expressed as

$$\eta_F = \frac{\text{CRM}^*}{\text{CRM}} = \frac{\kappa^* \phi^* I_e^*}{\kappa \phi I_e} \quad (I_e \ll I_s). \quad (4)$$

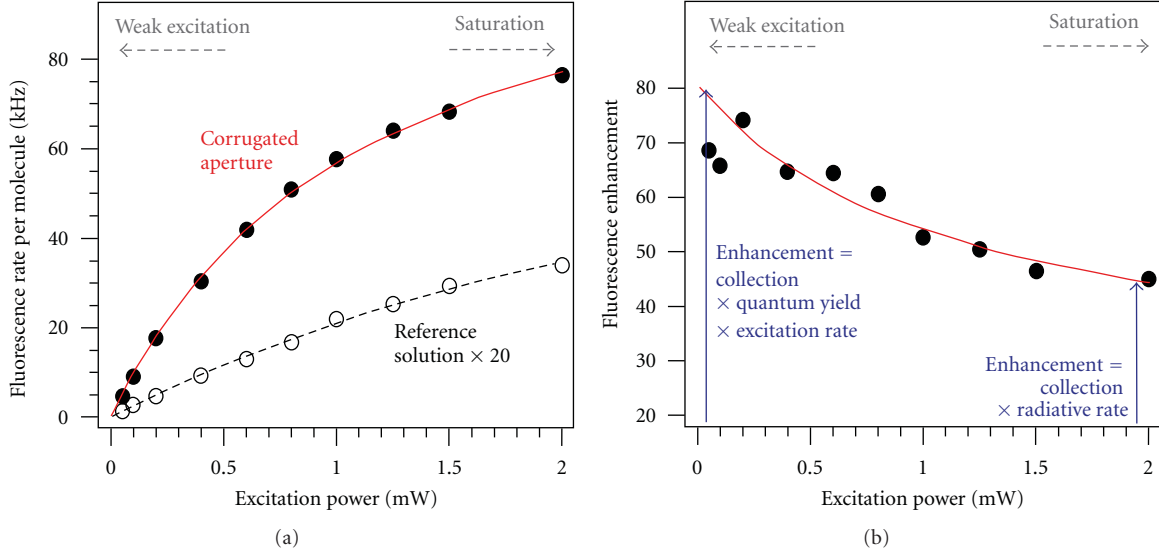


FIGURE 2: (a) Average fluorescence count rate per molecule detected in the case of the corrugated aperture presented in Figure 1 (filled circles) and the reference solution (empty circles). The molecules have a quantum yield in solution of 30% (Alexa Fluor 647), and the numerical aperture used for both excitation and collection is 0.5. (b) Fluorescence enhancement factor for increasing excitation power. The arrows indicate the two extreme cases of weak excitation ($I_e \ll I_s$) and saturation ($I_e \gg I_s$). Figure adapted with permission from [33].

The superscript * denotes the presence of the antenna. In the weak excitation regime, the fluorescence enhancement factor is the product of the enhancements in the collection efficiency, the quantum yield, and the excitation intensity (here we assume that the nanoantenna does not modify significantly the fluorophore's absorption cross section: $\sigma^* = \sigma$).

Equation (4) can be rewritten in a slightly different manner to introduce the gains in the radiative rate k_r^*/k_r and the total fluorescence lifetime reduction k_{tot}^*/k_{tot} :

$$\eta_F = \frac{\kappa^* k_r^* k_{tot} I_e^*}{\kappa k_r k_{tot}^* I_e} = \frac{\kappa^* k_r^* \tau^* I_e^*}{\kappa k_r \tau I_e} \quad (I_e \ll I_s). \quad (5)$$

This equation shows that the fluorescence enhancement factor is proportional to the gains in the radiative rates k_r and *inversely* proportional to the total deexcitation rates k_{tot} . Since $k_{tot}^*/k_{tot} = \tau/\tau^*$ is also the reduction in the fluorescence lifetimes, a strong reduction in the fluorescence lifetimes (sometimes also referred to as Purcell factor) is actually detrimental to the fluorescence enhancement factor. Clearly, the fluorescence lifetimes reduction (Purcell factor) must *not* be confused with the fluorescence count rate enhancement (see also the discussion in [39]). Observing a strong lifetime reduction due to the nanoantenna can be related to an increase in the nonradiative transition rate k_{nr}^* , mostly related to ohmic losses. This is the so-called quenching effect, which is certainly not related to any increase in the fluorescence count rate per emitter.

In the saturation regime, it is evident from (3) that the fluorescence enhancement factor at saturation depends only on the gains in collection efficiency and radiative rate:

$$\eta_F = \frac{\kappa^* k_r^*}{\kappa k_r} \quad (I_e \gg I_s). \quad (6)$$

Interestingly, at saturation of the fluorescence process, the fluorescence enhancement is found independent on the nonradiative transition rate k_{nr} , which means that metal quenching might not be an issue in this particular configuration. At saturation, the sole figure of merit is the ability of the emitter-nanoantenna system to radiate photons into the photonic modes used for detection, which is quantified by κk_r (this rate is sometimes written $k_{em} = \kappa k_r$ [30, 33]). Comparing the enhancement η_F in the saturation regime to the case of weak excitation, it turns out that η_F in the weak excitation regime is larger by a factor $(I_e^*/I_e)(\tau^*/\tau)$, which amounts to the gain in the excitation intensity divided by the fluorescence lifetime reduction. Depending on the interplay between excitation enhancement and quenching losses, high fluorescence enhancement values can be preferentially reached by working in the weak excitation regime (most common cases) or at fluorescence saturation (in the case of strong quenching losses). However, it must be kept in mind that the saturation intensity increases with the reduction of the fluorescence lifetime. Therefore reaching the saturation regime will require more excitation power in the case of strong quenching, that may even induce photodamage to the molecule or to the structure.

Figure 2 illustrates the dependence of the fluorescence enhancement factor on the excitation intensity, in the example case of the corrugated aperture displayed in Figure 1. The fluorescence count rates per molecule in the case of the antenna and the reference solution are presented in Figure 2(a) versus the excitation power, together with numerical fits according to the general expression (1) (the CRM for the reference solution has been multiplied by an arbitrary 20x factor to ease viewing). A transition between the regimes of weak excitation and saturation is clearly seen for excitation powers around 1 mW (excitation made

through a 0.5 NA objective, so the power to reach saturation is significantly higher as compared to focusing with a high NA objective). The transition towards saturation can be quantified by the saturation intensity I_s . For the experiments in Figure 2(a), we found $I_s^* = 1.2 \text{ mW}$ for the antenna and $I_s = 3.4 \text{ mW}$ for the reference solution [33] (in the case of a 1.2 NA objective, the saturation intensities would be $I_s^* = 130 \mu\text{W}$ for the antenna and $I_s = 510 \mu\text{W}$ for the reference solution).

Changing the excitation intensity has a strong influence on the fluorescence enhancement factor, as seen in Figure 2(b). In the weak excitation regime, the enhancement is maximum ($\sim 80\times$ for this example), while it decreases to $\sim 40\times$ when saturation is reached. This can be directly explained by the different contributions of the gains in radiative rate, quantum yield, and excitation intensity. η_F in the weak excitation regime is larger by a factor $(I_e^*/I_e)(\tau^*/\tau) \simeq 2$, which corresponds well to the gain in the excitation intensity (≈ 5.5) divided by the fluorescence lifetime reduction (≈ 2) as measured separately [33].

2.3. Emitter's Reference Quantum Yield without the Antenna.

In this section, we take a closer look at the influence of the emitter's quantum yield $\phi = k_r/(k_r + k_{nr})$ on the fluorescence enhancement factor. The basic question is how shall we choose ϕ for the reference solution (without the antenna) so as to maximize the fluorescence enhancement? Hereafter, the excitation intensity is set to the weak excitation regime $I_e \ll I_s$ (in the saturation regime, the fluorescence enhancement does not depend directly on ϕ , so the discussion is useless).

With the nanoantenna, the quantum yield is modified to $\phi^* = k_r^*/(k_r^* + k_{nr} + k_{abs}^*)$, where a new nonradiative decay route k_{abs}^* is introduced to take into account the ohmic losses into the metal and nonradiative energy transfers to the free electrons in the metal. It is also assumed that the nonradiative rate k_{nr} is not affected by the antenna. After some basic algebra, (4) can be rewritten:

$$\eta_F = \frac{\kappa^* k_r^* I_e^*}{\kappa k_r I_e} \frac{1}{(1 - \phi) + \phi\zeta} \quad (7)$$

with $\zeta = (k_r^* + k_{abs}^*)/k_r$. In the limit of a "poor" emitter $\phi \ll 1$ and $\phi\zeta \ll 1$, (7) resumes to

$$\eta_F = \frac{\kappa^* k_r^* I_e^*}{\kappa k_r I_e} \quad (\phi \ll 1) \quad (8)$$

which is the product of the gains in collection efficiency, radiative rate, and excitation intensity (this value can also be seen as the enhancement factor found at saturation times the gain in excitation intensity).

In the case of a perfect emitter $\phi \simeq 1$, (7) resumes to

$$\eta_F = \frac{\kappa^* I_e^*}{\kappa I_e} \quad (\phi \simeq 1) \quad (9)$$

if we assume that $k_r^* \gg k_{abs}^*$, meaning that the antenna has a large efficiency. Thus for a perfect emitter, the fluorescence enhancement at weak excitation intensity is given by the product of the gains in collection efficiency and excitation

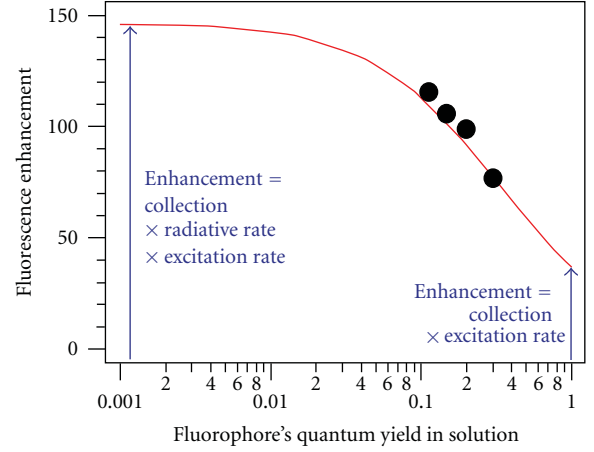


FIGURE 3: Fluorescence enhancement factor versus the dye's quantum yield ϕ in solution (taken without the antenna), in the case of weak excitation. The arrows indicate the two extreme cases of perfect dye ($\phi = 1$) or poor emitter ($\phi \ll 1$). The experimental data is taken from [33].

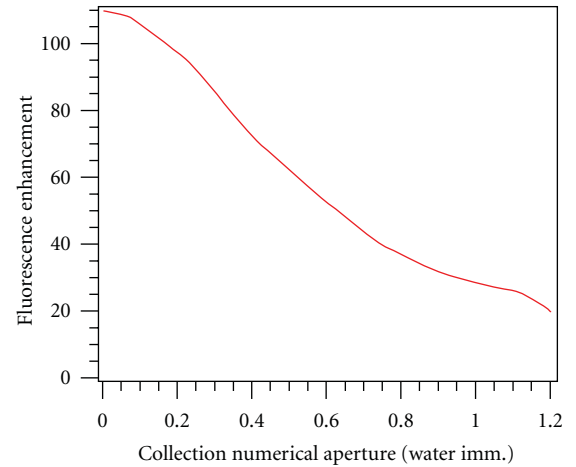


FIGURE 4: Influence of the numerical aperture used for collection on the fluorescence enhancement factor. Computation derived from the experimental data published in [33], in the case of weak excitation.

intensity. The fluorescence enhancement in the case of a poor emitter is larger by a factor k_r^*/k_r , indicating that, in order to maximize the value for η_F , one should preferentially select emitters with rather low quantum yields (as long as the experimental signal-to-noise ratio is sufficiently high to provide for reliable measurements).

Figure 3 illustrates this discussion, based on the modification of the fluorescence properties calibrated in [33]. η_F grows as the reference quantum yield ϕ is decreased, up to a plateau for $\phi < 0.02$. Again, the maximum value for the fluorescence enhancement in this example can be significantly different if a perfect dye is used $\eta_F \approx 35$ or if a poor emitter is chosen $\eta_F \approx 150$.

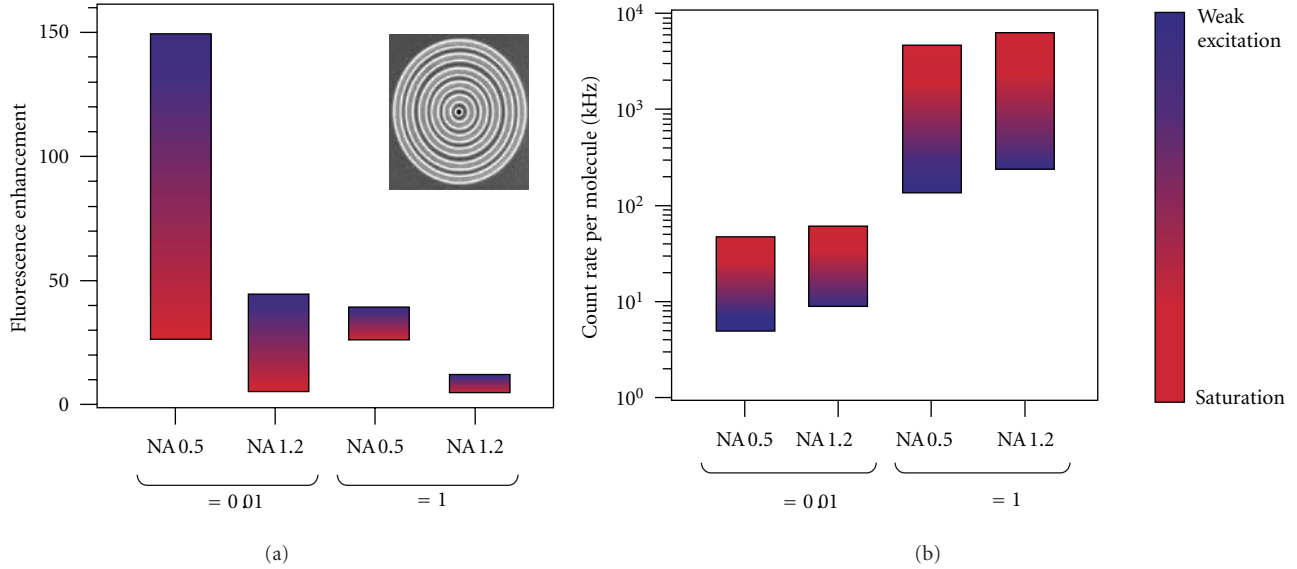


FIGURE 5: Fluorescence enhancement factor (a) and fluorescence detection rate per emitter (b) for different numerical apertures (NAs) used for collection, different quantum yield ϕ of the emitter in solution (in the absence of the antenna) and in the limit of weak excitation (blue) or fluorescence saturation (red). The antenna used here is the corrugated aperture with five grooves described in Figure 1 and calibrated in [33].

2.4. Luminescence Collection Efficiency. All the formulas presented here for the fluorescence enhancement factor are proportional to the gain in collection efficiency κ^*/κ , independently on the choice for excitation intensity or quantum yield. This is a direct consequence that obviously only the photons that are collected by the setup contribute to the detected fluorescence. Therefore, to maximize the fluorescence enhancement factor, one has to maximize the collection efficiency gain κ^*/κ . This can be done by tuning the antenna so as to maximize the directivity [15, 40, 41] and by minimizing the collection efficiency κ used for the reference. In other words, to maximize η_F , an objective with low numerical aperture should be used in accordance with the peak angular emission of the antenna's radiation pattern.

Figure 4 displays the influence of the numerical aperture used for fluorescence collection on the detected fluorescence enhancement factor. The antenna used here is again the corrugated aperture presented in Figure 1. It was found that the fluorescence radiation pattern with the antenna presented a peak in the direction normal to the sample plane with an angular divergence of $\pm 15^\circ$. Figure 4 presents the computed fluorescence enhancement factor integrated over the whole collection NA. Minimizing the collection NA to values below 0.1 maximizes the fluorescence enhancement factor up to values ~ 110 , whereas a large collection NA of 1.2 reduces the effective enhancement factor to ~ 20 as an effect of angular averaging.

3. Discussion

From the aforementioned investigations on the role of the different experimental parameters on the measured fluorescence enhancement factor, a general “rule of thumb” can be

derived: the lower the reference without the antenna, the higher the enhancement factor. In other words, to obtain high enhancement factors, one should preferentially select a weak excitation regime, a dye with low quantum yield and a low collection NA. Of course, this comes at the expense of lower signal (at least for the reference case) and higher noise.

To illustrate the broad range of fluorescence enhancement factors that can be measured using the same nanoantenna design, different computations have been performed using the antenna presented in Figure 1 with either 0.5 or 1.2 NA microscope objective, 0.01 or 1 quantum efficiencies and in the limits of weak excitation or fluorescence saturation. The results are graphically presented in Figure 5(a). In the extreme case of low reference without the antenna (0.5 NA, $\phi = 0.01$, weak excitation), the fluorescence enhancement is maximum ~ 150 , while it is minimum ~ 6 when the reference is the highest (1.2 NA, $\phi = 1$, saturation).

This clearly shows that the fluorescence enhancement factor is *not* an absolute figure of merit for a given nanoantenna. This is in strong opposition with the directivity, which is another figure of merit commonly used to characterize the quality of an antenna design and which can be intrinsic to the antenna (if properly measured [2, 33, 41]).

The fluorescence enhancement factor is an intuitive metric that is commonly used in surface-enhanced (or metal-enhanced) fluorescence. The experimental setup can be adequately tuned so as to maximize the measured values of η_F . However, it should be kept in mind that the final goal in the detection of molecules or the generation of single photons is to realize bright sources out of single quantum emitters [42]. Thus the true figure of merit is not the enhancement factor (“how much do we gain”) but instead the fluorescence count rate per emitter (“how much do we

have”). High enhancement factors should not be confused with bright sources. To illustrate this, Figure 5(b) displays the detected count rate per molecule corresponding to the cases in Figure 5(a). To maximize the detection rate, one has to select the conditions of high collection NA, high quantum yield, and high excitation intensity (saturation). These conditions correspond to the ones leading to the minimum fluorescence enhancement factor in Figure 5(a). Reciprocally, the conditions found for maximum enhancement lead to the minimum detection rates. Taking a low emission for reference and enhancing it (a lot) do not necessarily compensate for the low detection rate to start with. Of course, all this discussion strongly depends on the final application of the nanoantenna-emitter system and the initial photophysical properties of the emitter.

4. Conclusion

This paper has explored the influence of several parameters on the fluorescence enhancement factor with an optical antenna: excitation intensity, emitter’s quantum yield, and collection efficiency. General rules have been derived to obtain high enhancement factors by tuning the experimental conditions without affecting the antenna’s design. Experimental conditions leading to a low reference signal without the antenna should be preferentially selected to maximize η_F . This corresponds to weak excitation regime, dye with low quantum yield and low collection NA. General remarks can be drawn from the discussion: (i) the fluorescence enhancement factor is not an absolute figure of merit for a given optical antenna design, (ii) the fluorescence lifetime reduction (Purcell factor) must not be confused with the fluorescence count rate enhancement, and (iii) high enhancement factors do not necessarily indicate bright photon sources.

Acknowledgments

The author is deeply indebted to many at the Fresnel Institute and the Laboratoire des Nanostructures at the Institut de Science et d’Ingénierie Supramoléculaires. He would like to thank Hervé Rigneault, Pierre-François Lenne, and Thomas Ebbesen for stimulating the early stages of this work, Oussama Mahboub and Eloïse Devaux for fabricating the sample presented in Figure 1, and Heykel Aouani for performing the measurements. The author also would like to acknowledge stimulating discussions with Steve Blair, Davy Gérard, Nicolas Bonod, Brian Stout, and Evgeny Popov. To Nicolas, he owes a special thank for stimulating this work consecutively to the Second Summer School on Plasmonics held on Porquerolles in Fall 2011. Lastly, he would like to thank Didier Wampas for inspiring part of this work. The research leading to these results has received funding from the Agence Nationale de la Recherche, Project ANR-11-BS10-002 TWINS. The research has been conducted in the scope of the CNRS-Weizmann NaBi European associated laboratory.

References

[1] L. Novotny and N. H. van Hulst, “Antennas for light,” *Nature Photonics*, vol. 5, pp. 83–90, 2011.

[2] P. Bharadwaj, B. Deutsch, and L. Novotny, “Optical antennas,” *Advances in Optics and Photonics*, vol. 1, pp. 438–483, 2009.

[3] J. A. Schuller, E. S. Barnard, W. Cai, Y. C. Jun, J. S. White, and M. L. Brongersma, “Plasmonics for extreme light concentration and manipulation,” *Nature Materials*, vol. 9, no. 3, pp. 193–204, 2010.

[4] P. Anger, P. Bharadwaj, and L. Novotny, “Enhancement and quenching of single-molecule fluorescence,” *Physical Review Letters*, vol. 96, no. 11, Article ID 113002, 4 pages, 2006.

[5] S. Kühn, U. Håkanson, L. Rogobete, and V. Sandoghdar, “Enhancement of single-molecule fluorescence using a gold nanoparticle as an optical nanoantenna,” *Physical Review Letters*, vol. 97, no. 1, Article ID 017402, 2006.

[6] O. L. Muskens, V. Giannini, J. A. Sánchez-Gil, and J. Gómez Rivas, “Strong enhancement of the radiative decay rate of emitters by single plasmonic nanoantennas,” *Nano Letters*, vol. 7, no. 9, pp. 2871–2875, 2007.

[7] A. Kinkhabwala, Z. Yu, S. Fan, Y. Avlasevich, K. Müllen, and W. E. Moerner, “Large single-molecule fluorescence enhancements produced by a bowtie nanoantenna,” *Nature Photonics*, vol. 3, no. 11, pp. 654–657, 2009.

[8] Y. Fu and J. R. Lakowicz, “Modification of single molecule fluorescence near metallic nanostructures,” *Laser and Photonics Reviews*, vol. 3, no. 1–2, pp. 221–232, 2009.

[9] M. Ringler, A. Schwemer, M. Wunderlich et al., “Shaping emission spectra of fluorescent molecules with single plasmonic nanoresonators,” *Physical Review Letters*, vol. 100, no. 20, Article ID 203002, 2008.

[10] G. Vecchi, V. Giannini, and J. Gómez Rivas, “Shaping the fluorescent emission by lattice resonances in plasmonic crystals of nanoantennas,” *Physical Review Letters*, vol. 102, no. 14, Article ID 146807, 2009.

[11] R. J. Moerland, T. H. Taminiau, L. Novotny, N. F. Van Hulst, and L. Kuipers, “Reversible polarization control of single photon emission,” *Nano Letters*, vol. 8, no. 2, pp. 606–610, 2008.

[12] H. Gersen, M. F. García-Parajó, L. Novotny, J. A. Veerman, L. Kuipers, and N. F. Van Hulst, “Influencing the angular emission of a single molecule,” *Physical Review Letters*, vol. 85, no. 25, pp. 5312–5315, 2000.

[13] T. H. Taminiau, F. D. Stefani, F. B. Segerink, and N. F. Van Hulst, “Optical antennas direct single-molecule emission,” *Nature Photonics*, vol. 2, no. 4, pp. 234–237, 2008.

[14] S. Kühn, G. Mori, M. Agio, and V. Sandoghdar, “Modification of single molecule fluorescence close to a nanostructure: radiation pattern, spontaneous emission and quenching,” *Molecular Physics*, vol. 106, no. 7, pp. 893–908, 2008.

[15] A. G. Curto, G. Volpe, T. H. Taminiau, M. P. Kreuzer, R. Quidant, and N. F. Van Hulst, “Unidirectional emission of a quantum dot coupled to a nanoantenna,” *Science*, vol. 329, no. 5994, pp. 930–933, 2010.

[16] T. Shegai, V. D. Miljković, K. Bao et al., “Unidirectional broadband light emission from supported plasmonic nanowires,” *Nano Letters*, vol. 11, no. 2, pp. 706–711, 2011.

[17] J. Zhang, Y. Fu, M. H. Chowdhury, and J. R. Lakowicz, “Metal-enhanced single-molecule fluorescence on silver particle monomer and dimer: coupling effect between metal particles,” *Nano Letters*, vol. 7, no. 7, pp. 2101–2107, 2007.

[18] S. Gerber, F. Reil, U. Hohenester, T. Schlagenhaufen, J. R. Krenn, and A. Leitner, “Tailoring light emission properties of fluorophores by coupling to resonance-tuned metallic nanostructures,” *Physical Review B*, vol. 75, no. 7, Article ID 073404, 2007.

- [19] Y. Zhang, K. Aslan, M. J. R. Prevede, and C. D. Geddes, "Metal-enhanced fluorescence: surface plasmons can radiate a fluorophore's structured emission," *Applied Physics Letters*, vol. 90, no. 5, Article ID 053107, 2007.
- [20] G. Colas des Francs, A. Bouhelier, E. Finot et al., "Fluorescence relaxation in the near-field of a mesoscopic metallic particle: distance dependence and role of plasmon modes," *Optics Express*, vol. 16, no. 22, pp. 17654–17666, 2008.
- [21] F. Tam, G. P. Goodrich, B. R. Johnson, and N. J. Halas, "Plasmonic enhancement of molecular fluorescence," *Nano Letters*, vol. 7, no. 2, pp. 496–501, 2007.
- [22] W. L. Barnes, "Fluorescence near interfaces: the role of photonic mode density," *Journal of Modern Optics*, vol. 45, no. 4, pp. 661–699, 1998.
- [23] J. Enderlein and T. Ruckstuhl, "The efficiency of surface-plasmon coupled emission for sensitive fluorescence detection," *Optics Express*, vol. 13, no. 22, pp. 8855–8865, 2005.
- [24] L. Rogobete, F. Kaminski, M. Agio, and V. Sandoghdar, "Design of plasmonic nanoantennae for enhancing spontaneous emission," *Optics Letters*, vol. 32, no. 12, pp. 1623–1625, 2007.
- [25] J. S. Biteen, D. Pacifici, N. S. Lewis, and H. A. Atwater, "Enhanced radiative emission rate and quantum efficiency in coupled silicon nanocrystal-nanostructured gold emitters," *Nano Letters*, vol. 5, no. 9, pp. 1768–1773, 2005.
- [26] G. L. Liu, J. Kim, Y. Lu, and L. P. Lee, "Fluorescence enhancement of quantum dots enclosed in Au nanopockets with subwavelength aperture," *Applied Physics Letters*, vol. 89, no. 24, Article ID 241118, 2006.
- [27] Y. J. Hung, I. I. Smolyaninov, C. C. Davis, and H. C. Wu, "Fluorescence enhancement by surface gratings," *Optics Express*, vol. 14, no. 22, pp. 10825–10830, 2006.
- [28] Y. Liu and S. Blair, "Fluorescence enhancement from an array of subwavelength metal apertures," *Optics Letters*, vol. 28, no. 7, pp. 507–509, 2003.
- [29] D. Gérard, J. Wenger, N. Bonod et al., "Nanoaperture-enhanced fluorescence: towards higher detection rates with plasmonic metals," *Physical Review B*, vol. 77, no. 4, Article ID 045413, 2008.
- [30] J. Wenger, D. Gérard, J. Dintinger et al., "Emission and excitation contributions to enhanced single molecule fluorescence by gold nanometric apertures," *Optics Express*, vol. 16, no. 5, pp. 3008–3020, 2008.
- [31] E. Fort and S. Grésillon, "Surface enhanced fluorescence," *Journal of Physics D*, vol. 41, no. 1, Article ID 013001, 2008.
- [32] L. Novotny and B. Hecht, *Principles of Nano-Optics*, Cambridge University Press, Cambridge, UK, 2006.
- [33] H. Aouani, O. Mahboub, N. Bonod et al., "Bright unidirectional fluorescence emission of molecules in a nanoaperture with plasmonic corrugations," *Nano Letters*, vol. 11, no. 2, pp. 637–644, 2011.
- [34] W. L. Barnes, "Comparing experiment and theory in plasmonics," *Journal of Optics A*, vol. 11, no. 11, Article ID 114002, 2009.
- [35] C. Zander, J. Enderlein, and R. A. Keller, *Single-Molecule Detection in Solution—Methods and Applications*, Wiley-VCH, Berlin, Germany, 2002.
- [36] J. R. Lakowicz, *Principles of Fluorescence Spectroscopy*, Springer, Berlin, Germany, 3rd edition, 2006.
- [37] R. Brouri, A. Beveratos, J. P. Poizat, and P. Grangier, "Photon antibunching in the fluorescence of individual color centers in diamond," *Optics Letters*, vol. 25, no. 17, pp. 1294–1296, 2000.
- [38] A. Beveratos, R. Brouri, T. Gacoin, A. Villing, J. P. Poizat, and P. Grangier, "Single photon quantum cryptography," *Physical Review Letters*, vol. 89, no. 18, Article ID 187901, 4 pages, 2002.
- [39] A. F. Koenderink, "On the use of Purcell factors for plasmon antennas," *Optics Letters*, vol. 35, no. 24, pp. 4208–4210, 2010.
- [40] T. H. Taminiau, F. D. Stefani, and N. F. Van Hulst, "Single emitters coupled to plasmonic nano-antennas: angular emission and collection efficiency," *New Journal of Physics*, vol. 10, Article ID 105005, 2008.
- [41] H. Aouani, O. Mahboub, E. Devaux, H. Rigneault, T. W. Ebbesen, and J. Wenger, "Plasmonic antennas for directional sorting of fluorescence emission," *Nano Letters*, vol. 11, no. 6, pp. 2400–2406, 2011.
- [42] K. G. Lee, X. W. Chen, H. Eghlidi et al., "A planar dielectric antenna for directional single-photon emission and near-unity collection efficiency," *Nature Photonics*, vol. 5, no. 3, pp. 166–169, 2011.